CLAUS Cloud Archive User Service

Final Report

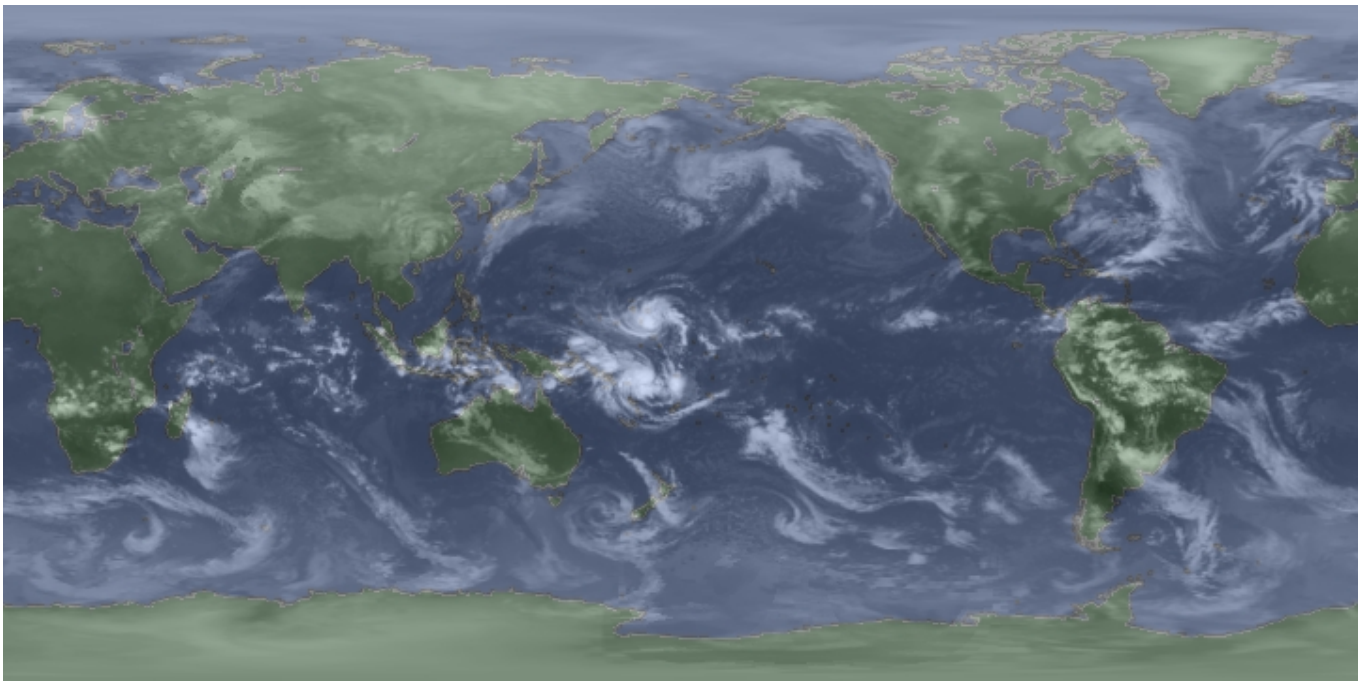

Prepared by the CLAUS Consortium under the co-ordination of the Environmental Systems Science Centre, The University of Reading, England.

CLAUS is an EC Shared Cost Action Project, part-funded under Area 3.3 (Environment and Climate) of the Fourth Framework Programme, which is co-ordinated by the EC Centre for Earth Observation.

Contents

A Introduction

This report describes the activities of the CLAUS Consortium during the period 1st April 1997 to 31st October 1999. It is an edited version of the Final Report (Contract: ENV4-CT96-0356) submitted to the European Commission.

Following the end of the project, ESSC continued to develop the processing methodology and introduced rigorous quality control techniques to improve significantly the quality of the data in the archive. Virtually all of the problems encountered with the source data, described in this report, have therefore now been resolved.

A major policy change involving the third objective, i.e. dissemination of data from the Archive, has been the decision to bank the Archive at the British Atmospheric Data Centre at the end of the project, rather than attempting to do this from within the CLAUS Consortium, because of resource limitations.

This section outlines the objectives of the project, its scope and relevance to the Fourth Framework, the membership of the CLAUS consortium, and lists the customer requirements and reports on how these were met. Subsequent sections (B, C and D) report on the three main objectives listed below. Sections E and F contain a discussion of the project and conclusions, respectively.

1 Objectives

The goal of the Cloud Archive User Service (CLAUS) Project was to provide climate modellers with ready access to a long-term archive of global brightness temperature data. The primary purpose of the archive was for the validation of General Circulation Models, although other applications were anticipated.

To achieve this goal three major objectives were established:

1. Data Set Provision:
   To create the archive using remotely sensed satellite data from the ISCCP level B3 (reduced resolution radiance data) products, covering the period 1983 - present.

2. Validation:
   The archive is to be tested by the participating climate research groups in an operational environment over an extended period. Following an initial testing phase, modifications are to be made to the processing methodology in consultation with these customers.

3. Data Access:
   The archive, and descriptions of the methods used to create it, are to be made freely available over the network, using the CEO European Wide Service Exchange (EWSE) to advertise their availability.

2 Context

2.1 European Climate Research

Global climate modellers and climate researchers throughout Europe and beyond require suitable data (as provided by CLAUS) in order to compare observed data and their own model outputs. Such comparisons would allow the models to be improved.

Until now most of the research into comparing observational results with models has been using data produced from World Weather Watch, and has not used global image data from satellites. Satellite image data have mainly been used for local studies to improve model parameterisations of individual parts of the model, rather than for global model validation. The fourteen year (and continuing) CLAUS archive will allow much more extensive validation than has been attempted before, and will enable hitherto unrealisable improvements to be made to the models. In particular, it is known that most current GCMs produce a relatively poor description of the cloud field. Provision of the CLAUS archive will enable steps to be taken to improve the understanding of clouds, which is central to the improved understanding of climate and changes therein.

One important benefit of the validation activity will be a much better understanding of the natural variability of the climate on the annual and decadal time scale. The applications of this improved scientific knowledge are considerable. For example, it will improve our ability to make predictions about the effects of anthropogenically induced climate changes on similar time scales. Currently, the difficulties inherent in separating natural from anthropogenic change make it very difficult to establish appropriate mitigating strategies and hence for model results to be useful at the policy setting level.

2.2 Relevance to the EC IVTH Framework Environment and Climate Programme

This Project falls completely within the scope of the EC IVth Framework Environment and Climate Programme (FECP).

The first objective of the FECP is to understand the basic processes underlying environmental change, in particular those of the climate system. This project provides one means for climate researchers to work towards this objective in relation to the increased potential to validate GCMs.

The third objective of the FECP is to contribute to the technological development necessary for environmental observation, monitoring and research with particular attention to applied space technologies. This project was fully in line with this objective in that it used state-of-the-art technology to process and archived a new data set derived from satellite observations.

3 The Consortium

The CLAUS Consortium comprised six academic or research organisations, who were both customers for the resulting service and full partners in the project. The main r le of these organisations was to test the usefulness of the data in GCM validation.

A commercial company, National Remote Sensing Centre (NRSC), were sub-contracted by ESSC, who co-ordinated the project, to develop and implement the archive system. The organisations involved, and their respective r les were:

Environmental Systems Science Centre (ESSC), UK

- Project co-ordination
- Develop and specify the data processing algorithms
- Application of feature tracking software to the data, specifically to look for artefacts introduced by the data processing methodology

Centre National de Recherches M t orologiques (CNRM), France

- Apply the archive data to the validation of climate simulations generated with the most recent versions of the Arpege-Climat GCM
- Assess the ability of the CLAUS data for the validation of diurnal and inter-annual variations simulated by the GCM

Laboratoire de M t orologie Dynamique (LMD), France

- Define, develop and implement algorithms to perform space-time analyses of the CLAUS brightness temperature data associated with cloud cover variability
- Use the CLAUS-VIEW software to test and use the data, along with the different algorithms for climate research and climate model evaluation and development, concentrating on convective cloud fluctuations in the Tropics

Max-Planck- Institut f r Meteorologie (MPI), Germany

- Use climate simulations to study the impact of observed sea surface temperature on atmospheric circulation

UK Universities Global Atmospheric Modelling Program (UGAMP), UK

- Co-ordinate the testing activities
- In collaboration with the UK Hadley Centre, use the data in the Unified Model as part of the Atmospheric Model Inter-comparison Project (AMIP II)

European Centre for Medium-Range Weather Forecasts (ECMWF), International.

- Use the latest versions of the ECMWF Models to compare the existing ISCCP data-sets with the CLAUS archive

National Remote Sensing Centre Ltd. (NRSC), UK

- Design, develop and implement the data processing, archive and dissemination systems
- Establish, operate and maintain the archive

4 Main Customer Requirements

The main customer requirements were identified at the start of or during the course of the project: these were met in the most part by the time the project ended. The major requirements (italicised), and the degree to which these were satisfied, are discussed below.

4.1 The Archive

The main customer requirement is the production of, and access to, the archived data. This should be of an appropriate quality and in a format suitable for comparing with the results of GCMs. To be compatible with existing GCMs, the resolution of the data should be 0.5° by 0.5° in latitude and longitude, and three hours in time. The dataset should also be contiguous wherever possible, to avoid gaps and discontinuities that might affect certain types of analyses, e.g. feature tracking.

The data should be accessible directly by geographic regions and/or time range, and optionally in Hovm ller format, without the customer having to perform unreasonable levels of processing. The data should be freely available, with small amounts of data being transferred via ftp and larger volumes by post on Exabyte tapes.

During discussions amongst the Consortium members, it became evident that quality information at the grid point level, in addition to that available at the meta-data level, will also be important. The reason for this is due to the variable coverage, in both space and time, of the source data, which if ignored can sometimes lead to undesirable artefacts in subsequent analyses of the data. As a consequence, two types of quality data were added to the archive, one indicating the satellites contributing to each grid point and the other reflecting the level of spatial and temporal interpolation that is applied to the data value.

NRSC encountered unforeseen problems in the operational processing of the data. As a result, data were generated for a shorter period and delivered later than envisaged. Table 1.0 (page 26) shows the periods generated successfully by NRSC and the periods generated by ESSC using the demonstration software.

4.2 Feedback from Validation Exercises

Another important requirement is for the results of the initial validation exercise to be fed back to the other members of the Consortium, in particular ESSC and NRSC, so that any remaining artefacts or other problems can be identified and corrected, or at least minimised, as soon as possible. Given the large size of the archive (10 Gbytes), it was essential that this process be carried out in a timely manner. The results of the final validation are also to be made available to the wider community so that they may appreciate what can, and cannot, be done with the data.

Because of the problems with operational processing only one year of data was available for the initial validation exercise, although six years were eventually available towards the end of the project for the final validation activities. However, the results obtained using the initial set of data showed that the data were of acceptable quality. Closer examination by MPI (Page 80) revealed the presence of a few residual artefacts caused by the use of insufficient limb darkening correction, which was subsequently rectified. The

effect of missing data, e.g. from the geostationary satellites, was examined by CNRM (Page 24).

One of the major problems encountered with the ISCCP data was the variable quality of some of the data, particularly from GOES-7. This mainly took the form of mis-navigated imagery, which because of the operational nature of this project, was solved by simply discarding such data. This problem is discussed on Page 19.

4.3 Data Access

Data access is a less important requirement for the testing centres during the operational testing phases, since initially they will receive data directly via Exabyte tape. However, other customers requesting data will be, by definition, reliant on the data access system established by the Project. For this reason, the testing centres will act as 'guinea pigs' in using the Web-based access mechanism once it was in place.

Once data were available operationally most of the test cents were able to order and download data. However, the speed of the link to NRSC was not sufficient for large quantities to be downloaded *via* ftp and recourse had to be made to Exabyte transfer.

At the conclusion of the project the data were offered to the British Atmospheric Data Centre for dissemination to other users. The data, and associated documentation, are (at the time of writing) being banked at BADC.

4.4 Data Analysis Tools

There is a clear need for a set of tools to enable customers to perform basic operations on data extracted from the archive. These should take the form of Unix-based utilities that should enable users to perform basic statistical analyses of the data and present the results in a straightforward manner. There are clear advantages in developing the tools within the CLAUS Consortium, since this will reduce the risk of duplication of effort (re-inventing the wheel) and will ensure that other customers are made more aware of the limitations of the data.

LMD, who have experience in developing such tools, took the lead on this activity. The set of tools they developed, 'CLAUS-VIEW', is described on Page 143. CLAUS-VIEW was distributed to and tested by the other customers.

4.5 Documentation

Full documentation should be made available describing the processing methodologies employed, along with the results of the validation exercises, so that other climate groups and the wider general community may appreciate the capabilities and limitations of the data.

The results of the validation exercises are made available through this report. More detailed information is being made available through papers submitted to scientific journals in the Meteorology/climate area.

B The Archive

The activities involved in creating the archive were split into three main sub-tasks: accessing the data from EOSDIS, processing it using purpose written software, and archiving the resulting products using a commercial database system. The following sections describe the main activities involved in carrying out these tasks.

1 Data Acquisition

ISCCP level B3 data, up to June 1995, were received from EOSDIS early in the project. These data were stored in a secure physical archive at NRSC, where they were catalogued to facilitate their ingest during the operational processing phases.

During the course of the project, EOSDIS released revised calibration tables for converting between radiance values and brightness temperature. These were incorporated into the data processing database system and used to regenerate some of the data. Comparison with the old calibration values showed differences that would not seriously affect the outcome of the validation exercises.

As discussed in the next section, occasional problems with the quality of the source B3 data were encountered. ESSC were in regular contact with EOSDIS and GISS (who process the data products) to resolve these. Overall, ESSC were impressed with the efficiency of EOSDIS. In particular, their response to queries about the data, and the turnaround around time between requests for data and their reception, were excellent.

2 Data Processing

The data processing activities were split between ESSC and NRSC. ESSC developed the processing algorithm for converting the source B3 data into the final image products. NRSC took this algorithm and implemented it in an operational system, adding software to handle the large volume of data and to disseminate it *via* the Web.

2.1 Data Processing Methodology

The processing methodology adopted in the project was highly modular (Figure 1). This enabled changes that might result following the validation exercises to be carried out by the Testing Centres, or in other improvements by ESSC to the processing algorithms during that time, to be implemented as efficiently as possible and with minimal impact on the other processing steps.

To help with the development of the processing methodology and its specification, ESSC wrote demonstrator software to experiment with different interpolation and re-sampling techniques and to understand the characteristics of the source data. Examples of the output from this software, and initial attempts to improve certain aspects of the process, are presented below. In addition to helping to specify the algorithms, this software also provided a useful benchmark to compare against the operational version implemented by NRSC.

2.1a Interpolation methodology

The most important module in the data processing chain is the Re-sampling Module. This operates in two modes, which can be run one after the other or separately. The first is the spatial sampling mode, which re-samples the level B3 source data for a user-specified period onto a uniform 0.5° latitude/longitude grid for each three-hourly time step. The temporal interpolation mode then fills in any gaps caused by incomplete satellite coverage or missing data using the preceding and succeeding images, or ones beyond these if these also have gaps.

The approach adopted in the CLAUS project for the spatial interpolation step is similar to that of Salby *et al.*, and results in a similar output. However, it differs in two major respects:

First, interpolation is carried out directly onto the sphere using spherical kernel estimators (Hodges, 1997). In contrast, Salby *et al.* used two projections covering the equatorial and polar regions. These were then re-sampled onto a latitude/longitude grid. The approach used in CLAUS avoids both the re-sampling step and, more importantly, the variable sampling region size that is inherent when interpolating onto projected planes.

Second, interpolation is performed in a hierarchical manner, so that the data are sampled near-optimally according to their spatial density. In contrast, Salby *et al.* filled in small data voids by interpolating over the surrounding grid points. The CLAUS method avoids this double re-sampling by using three levels of interpolation, with kernel radii of 0.5, 1.0 and 1.5 degrees. At each grid point, the point density ρ is computed for each level. The corresponding data value $\langle T \rangle$ is then taken from the level having the highest data

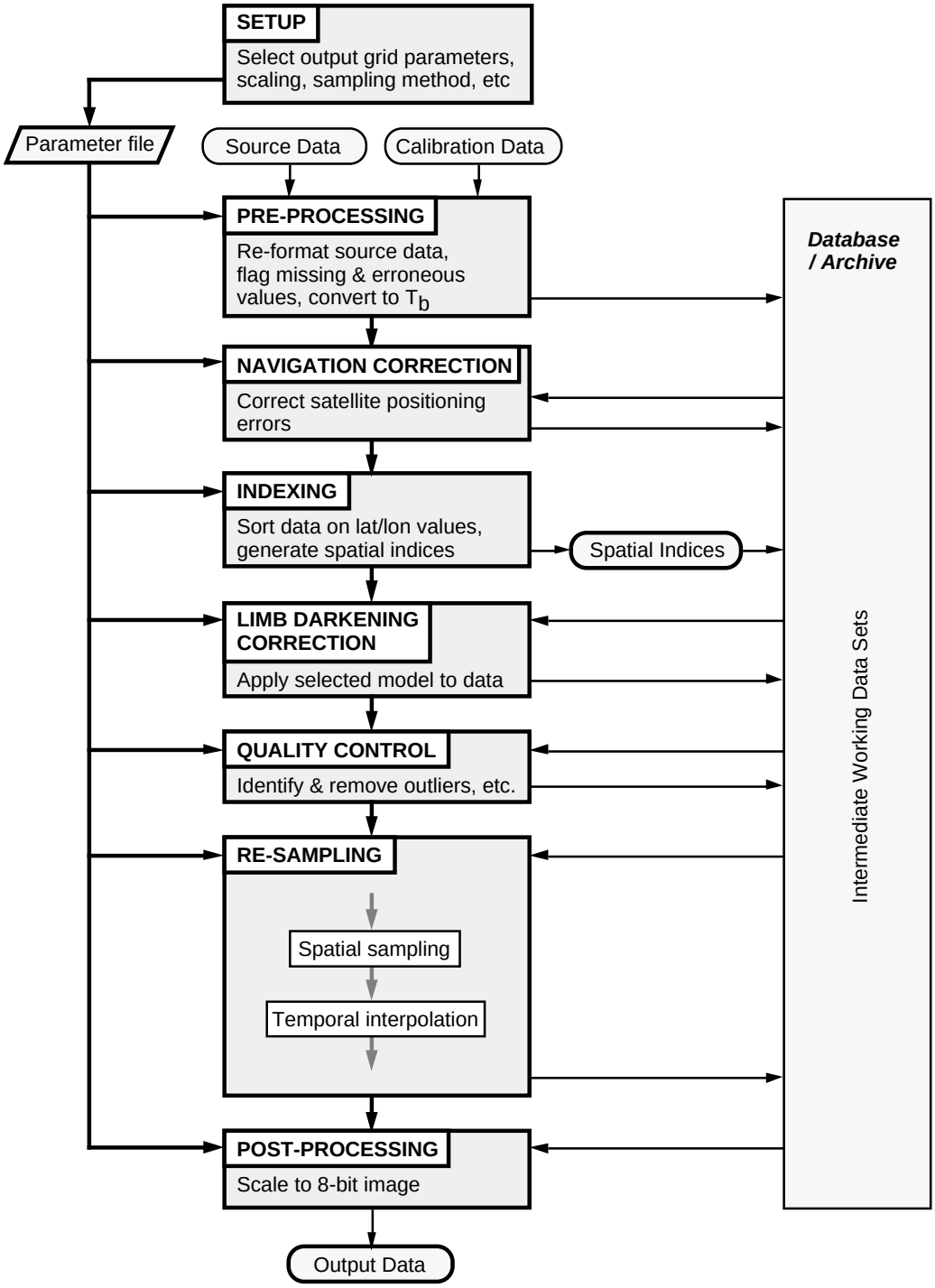

Figure 1: Schematic of CLAUS data processing chain.

density. If this exceeds a pre-defined threshold, otherwise the grid point is flagged as 'missing'.

<T> is computed according the following weighting scheme:

$$\langle T \rangle = \bullet \; w_z w_s w_t \, T_i \; / \bullet \; w_z w_s w_t$$

-where:

$w_z = \gamma(\phi)$ - limb brightening correction factor (defined in next section).

$w_s = c\,(k_i.k_j - 1) / \pi(c-1)^2$ - spherical kernel estimator, with c determined by kernel radius; k_i and k_j are the unit vectors from the Earth's centre to the data and grid points.

For polar orbiting satellites:

$w_t = 1 - |t - t_0| / 1.5$ if $|t - t_0| < 1.5$ - temporal weighting to decrease contribution from polar satellites away from nominal three-hourly time step t_0

else $= 0$

For geostationary satellites:

$w_t = 1$

The data density is determined using the spatial weightings:

$\rho = \sum w_s / N$ - N is the total number of data points.

The limb brightening factor w_z is used to reduce discontinuities at the overlap of geostationary and polar satellites coverages (see next section).

An example of the spatial interpolation process is shown in Figure 2 for three consecutive time steps. Note that the holes in the polar regions, caused by the lack of polar orbiter data, precess so that they can normally be filled in during the temporal interpolation stage. These holes are actually quite small, but appear large due to the latitude-longitude projection. The data re-sampling process is complicated by limb darkening, which affects spatial interpolation, and the diurnal cycle and cloud motion, which affect temporal interpolation.

2.1b Limb Darkening

Limb darkening arises from the dependency of cloud temperature on height, so that at increasing off-nadir satellite the received radiation comes preferentially from higher parts of the Earth's atmosphere. The effect is to make the edge of the Earth, *i.e.* the limb, appear cooler and therefore darker at the wavelengths used in CLAUS (approximately 10.5-13 m).

A number of observational and theoretical studies, *e.g.* Minnis *et al.* (1984), have shown that limb darkening is also a function of land cover type and cloud distribution. However, a reasonable approximation used both in CLAUS and by Salby *et al.* is to approximate the variation in received radiance (L) using a simple geometric function based solely on look angle (ϕ):

$$L(\phi) = \gamma L(0)$$

- where $\gamma = 1$ if $\phi < 11°$; else $\gamma = 1.00067 + 0.03613 \ln \cos(\phi)$

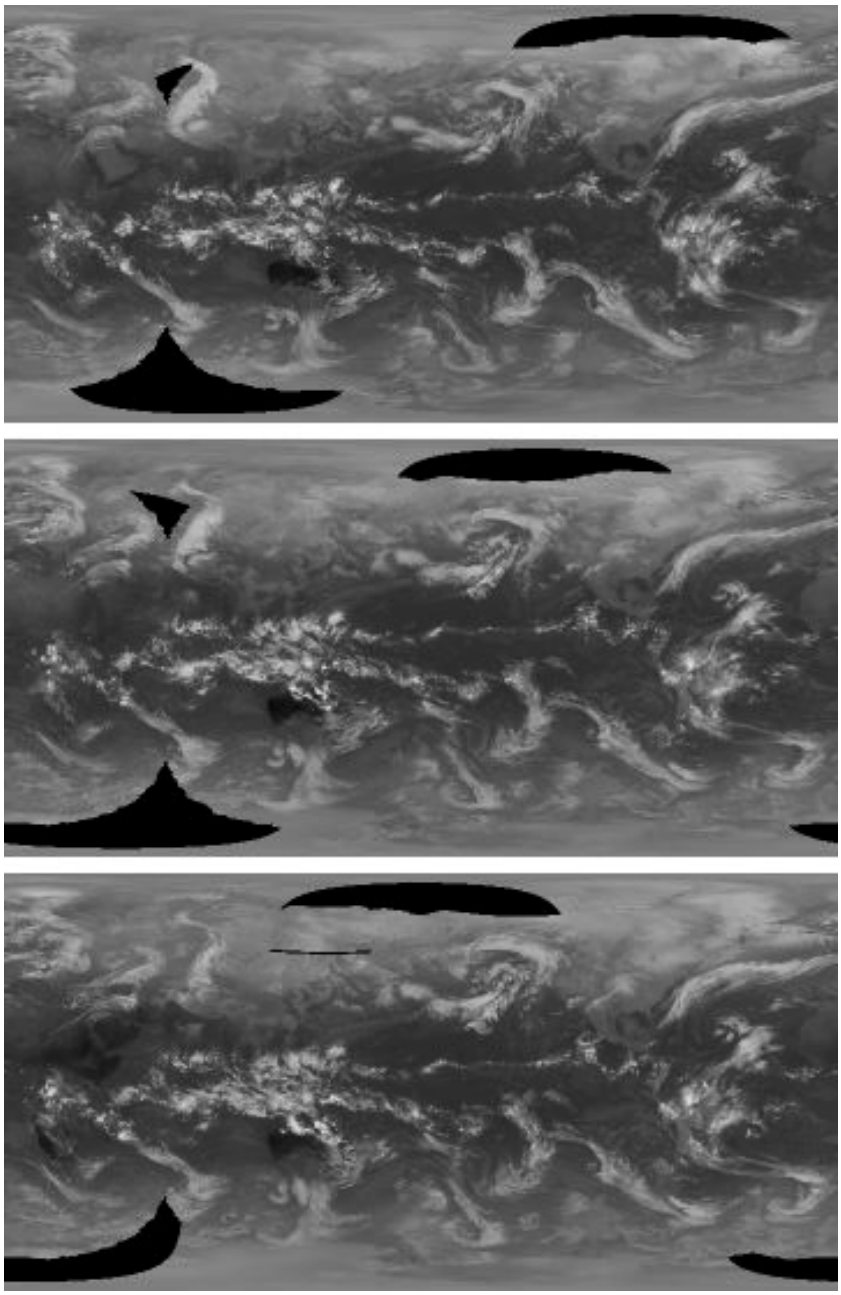

Figure 2: Example of spatial interpolation of three consecutive time steps. The holes are due to incomplete polar orbiter coverage.

Since the input and output data are brightness temperatures, it is necessary to convert these to and from radiance values. This is carried out using the look-up tables supplied by EOSDIS with the source data.

Another problem arising from off-nadir look angles is its effect on perceived cloud distribution. For example, a polar orbiting satellite might look vertically downwards through a gap in high level cloud to lower and therefore warmer clouds (or even the land or sea surface), whereas a geostationary satellite looking at the same point in the upper

atmosphere, but with a large look angle, may just see the high level cloud. To reduce this effect CLAUS is using the solution adopted by Salby *et al*., which is to weight the data by a function based on the viewing angle. This gives greater weight to, for example, the data from polar orbiting satellites, although it can lead to slight discontinuities at the edges of polar orbiter tracks where the adjacent data are from the edges of single geostationary satellite coverages - particularly at high latitudes and over the Indian Ocean.

Diurnal Cycle

The method used in the operational system to perform temporal interpolation is simple linear interpolation, as used by Salby *et al*. However, this can result in brightness discontinuities due to diurnal changes in the cloud, land and sea temperatures. This effect is most pronounced in the equatorial and tropical regions, especially near sunrise and sunset.

Cloud Motion

Other discontinuities arise from changes due to cloud motion (at large scales) and cloud genesis and lysis (at smaller scales) between successive time steps. The former generally appears as a lateral 'shear' across the edge of the data hole.

Improvements to Temporal Interpolation Technique

Further techniques were investigated to minimise the effects of these phenomena, and more importantly, reduce their impact on the results of applications that are especially susceptible to discontinuities. The approach was based on separating out diurnal effects from changes due to cloud motion. This was accomplished by dividing each spatially interpolated image into regions that are cloud-free land, cloud-free sea and cloudy (Figure 3).

For cloud-free land areas the temperature variation is, to a first approximation, due just to the diurnal cycle. This can be represented by a series of 'cloud-free' images produced by selecting the highest temperature for each grid point from a fourteen-day period (Figure 4). Missing values in an image can then be interpolated using a sinusoidal fit through the corresponding points in these images.

Cloud-free sea areas have the smallest diurnal cycle and missing values can be interpolated reasonably satisfactorily using linear interpolation across the neighbouring images.

For clouds, the approach is more complicated owing to their motion. Moreover, their behaviour varies with latitude: in equatorial regions smaller scale structure dominates, with rapid evolution of individual features. This makes temporal interpolation in these areas difficult, although this is partly offset by the lower incidence of holes. At higher latitudes however, cloud structures tend to be larger and evolve relatively more slowly. This behaviour is more amenable to treatment by one of a number of image processing based techniques. The method investigated here is based on one used in MPEG encoding of digital image sequences, namely block motion compensation.

First, block matching of the images on either side is performed in the neighbourhood of each data void. This results in a set of vector displacements, which are then used to perform an initial linear interpolation of the missing values. Any residual variation is due to the diurnal cycle and this is removed by normalising the values locally using a mean fit to the surrounding area (Figure 5):

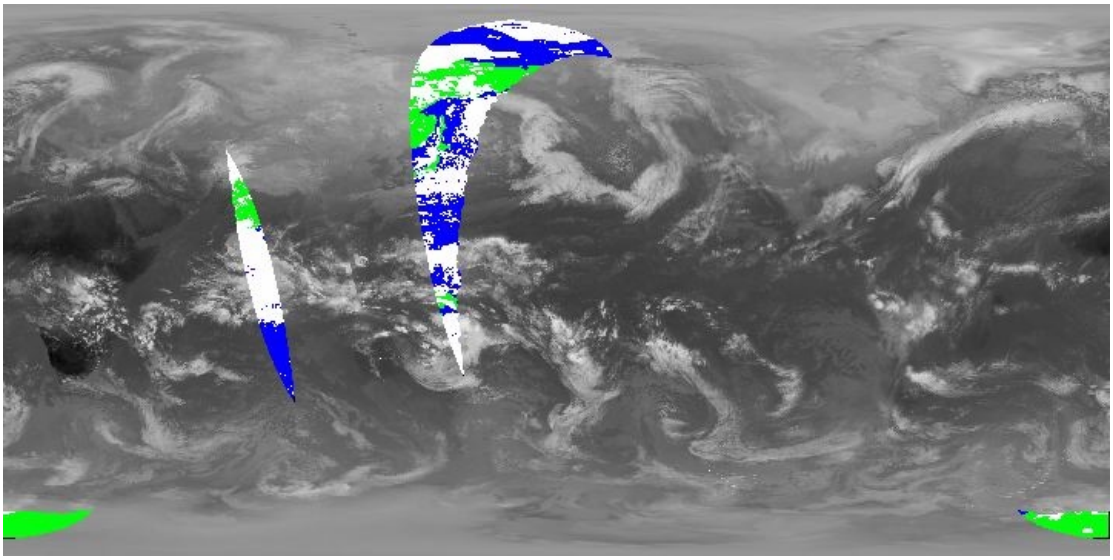

Figure 3: Holes in spatially interpolated image classified into cloud-free land (green), cloud-free sea (blue) and cloud (white).

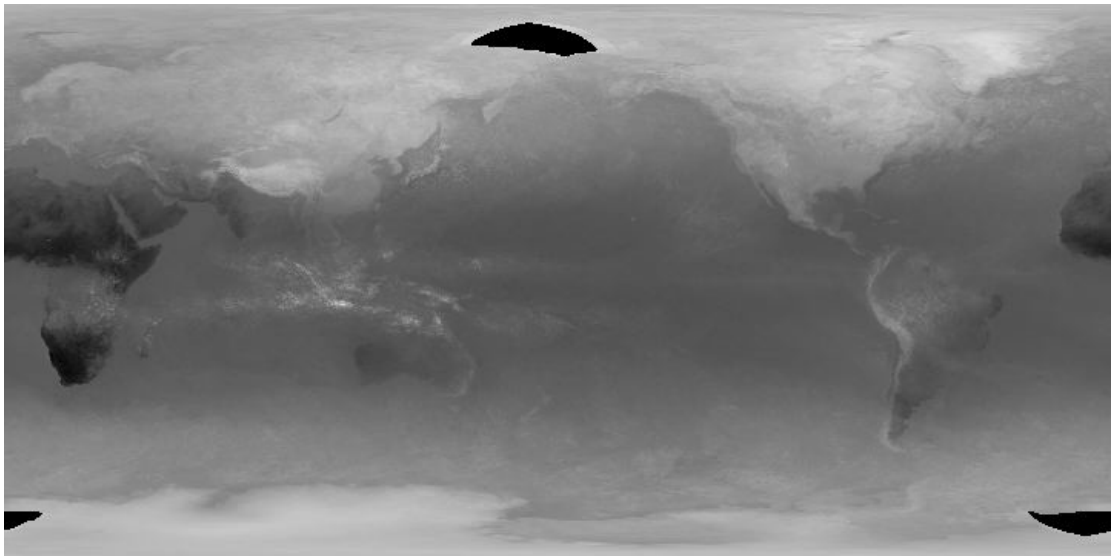

Figure 4: Cloud-free global image for 00.00 UT in January 1984, produced by taking maximum temperatures over a fourteen-day period at the same time each day.

$$I_i^t = (I_i^{t-1} + I_i^{t+1})/2 - \langle I_j^{t-1} + I_j^{t+1} \rangle_a/2 + \langle I_j^t \rangle_a$$

- where I is the intensity (converted from brightness temperature) and the superscripts refer to the current, preceding and succeeding images.

Figure 6 shows the end result of applying these spatial and temporal interpolation techniques.

Although there are sometimes a few residual anomalies, particularly with missing images from geostationary satellites, the results appear better qualitatively than the GCI product of Salby *et al*.

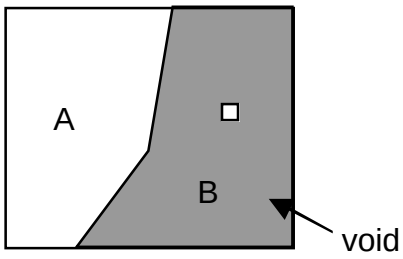

Figure 5: Local area used to correct for diurnal variation at a void in a cloudy region

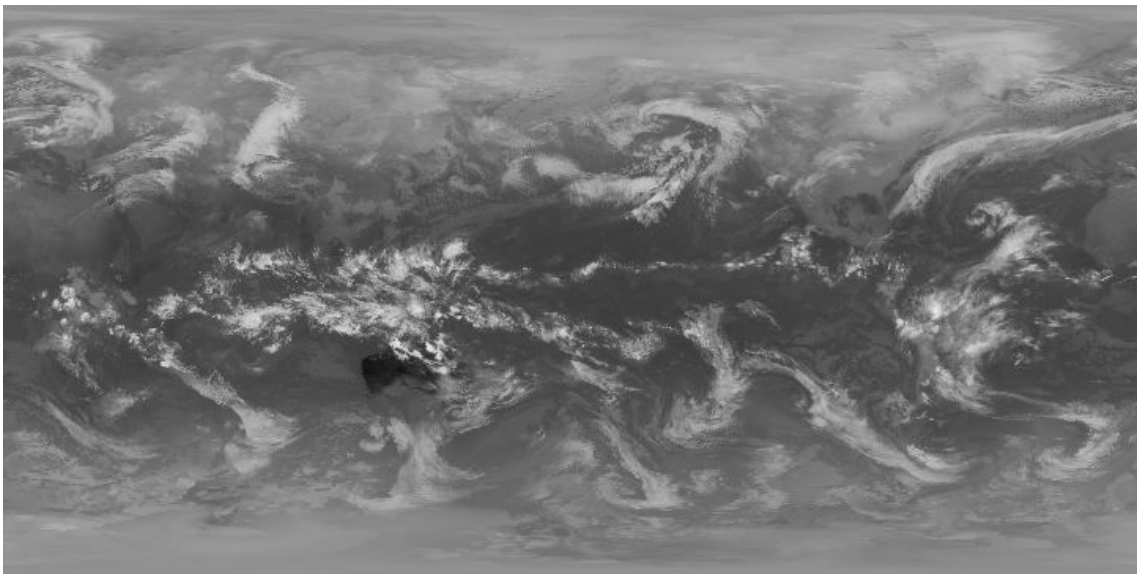

Figure 6: Fully spatially and temporally interpolated image for 1/1/1984 at 06.00 UT.

Animation Products

One method for performing visual quality control checks that has proven invaluable is to display a month s worth of images as an MPEG loop. This reveals very clearly most of the problems with both the interpolation process and the source data itself. For example, although the ISCCP documentation states that all satellite images are corrected for navigation errors, there are clearly a few that are not. These are mainly from GOES-7, the images from which exhibit a pronounced 'nodding' effect. It would appear from visual inspection of several MPEGs that images with deviations beyond a certain limit are not corrected properly. At present, these data have to be identified visually and reprocessed, with any resulting gaps filled using (linear) temporal interpolation. This situation was clearly unsatisfactory and hence discussions were held with GISS (the processing centre of the EOSDIS operation) to resolve this problem.

The MPEGS are felt to be so useful that they may be placed in the archive as browse products for customers to preview the data they are interested in.

Quality Data

As part of the interpolation and image generation process, two associated quality information images are produced for each brightness temperature image. Both are stored as PGM (Portable Grey Map) files to facilitate manipulation and display.

The first contains information on which satellites contribute to each grid point. This is held as a series of bit flags in a byte field (Figure 7), with the names of the satellites held in a separate meta-data file. Generally, six satellites are used, with the two spare bit flags being used when the satellite configuration alters, for example when GOES-W ceased functioning in 1987 and METEOSAT replaced it temporarily, or when a new satellite became operational but the old one remained for a short period.

Figure 9 shows the Contributing Satellite information corresponding to the example image shown in Figure 6, expressed using a colour lookup table. (Although in principle there could be 256 combinations and therefore 256 different colours, there are only about 30 combinations in reality due to the satellite positions and orbits).

S							
7	**6**	**5**	**4**	**3**	**2**	**1**	**0**

Figure 7: Contributing Satellite flag structure.

Bit	Satellite Series
0	GMS
1	METEOSAT
2	GOES-E
3	GOES-W
4	NOAA1
5	NOAA2
6	spare1
7	spare2

Table 1: Contributing Satellites indices.

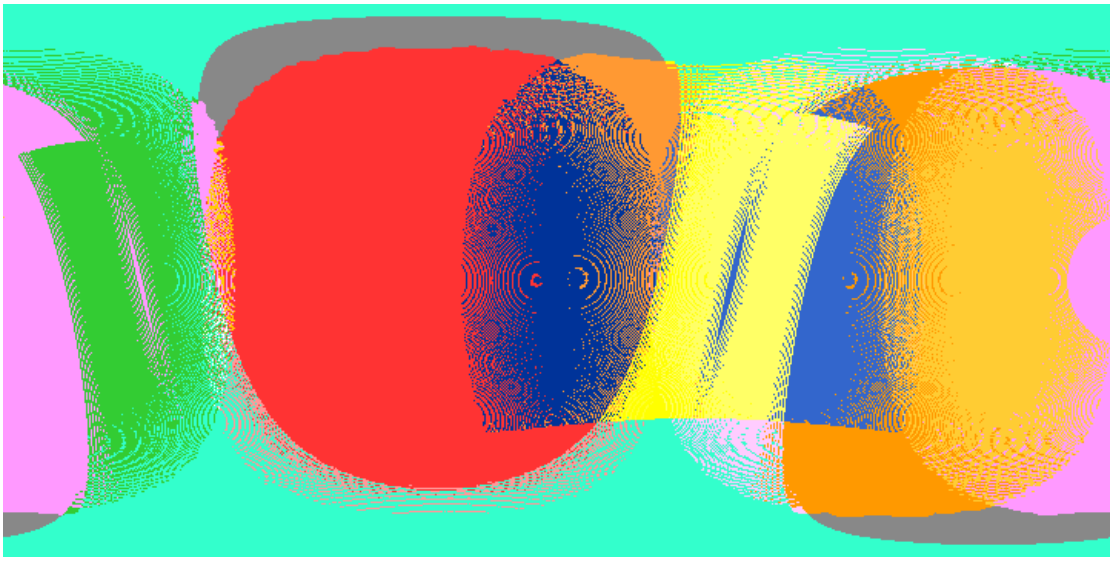

Figure 4: Satellite Contribution Information. Each different colour represents a single satellite or where two or more overlap.

The second image (Figure 9) is used to represent the reliability of the interpolation employed at each grid point. Each byte in the image is split into three parts. The first part holds the mean cosine of satellite zenith angle **Z** (scaled to span the range 1.0 0.1), the second part holds the sampling/interpolation level **I** (see Table 1), and the last part holds the missing data flag **M** (1=missing, 0=present). The three components are arranged so that the higher the combined byte value, the lower the reliability of the corresponding brightness temperature value.

M	**I**			**Z**			
7	**6**	**5**	**4**	**3**	**2**	**1**	**0**

Figure 8: Structure of Interpolation Level quality byte.

Value	Interpolation level
0	primary spatial
1	secondary spatial
2	tertiary spatial
3	primary temporal
4	secondary temporal
5	reserved
6	reserved
7	reserved

Table 1: Values of Interpolation levels

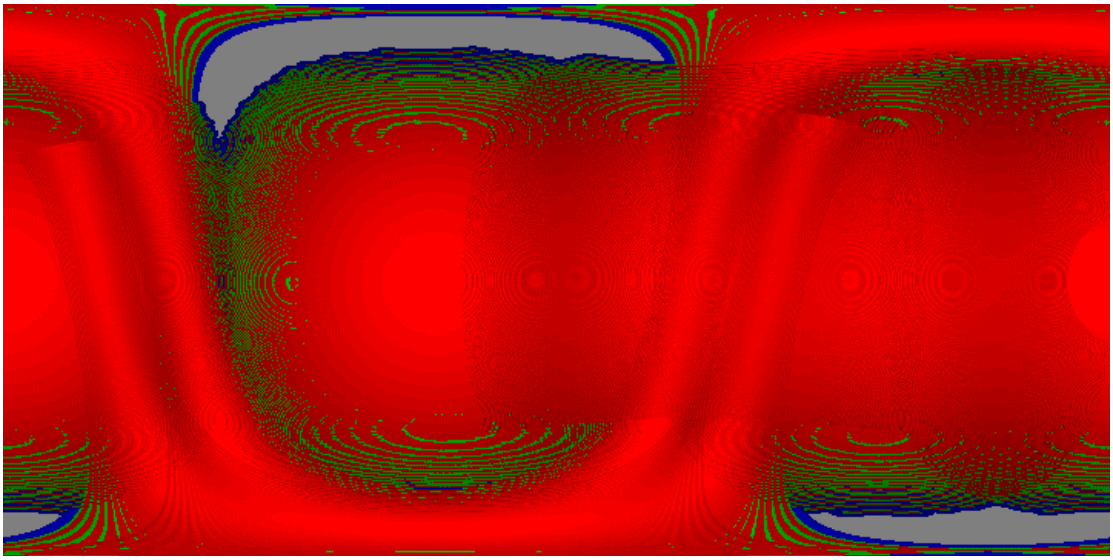

Figure 9: Interpolation Quality Information: Colours are used to denote the degree of smoothing in the spatial (red=primary, green=secondary, blue=tertiary) and temporal (grey) interpolation processes. Intensity of the colour indicates the off-nadir angle (bright=nadir).

3 Data Archive System

The data processing, archiving and dissemination systems all operated on the same hardware configuration (Figure 1). To maintain consistency between product generation and data dissemination these two processes were never run simultaneously, which meant that data were not always available for downloading. However, since processing was normally carried out overnight this had little impact on customers.

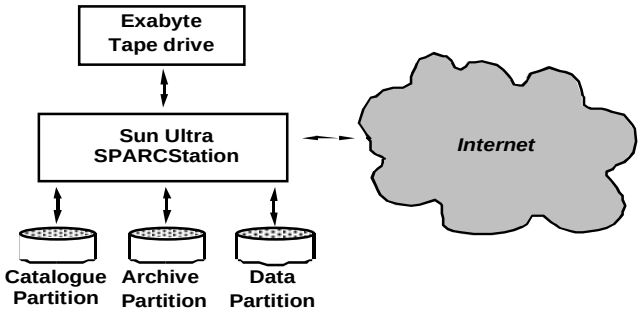

Figure 1: CLAUS Hardware Architecture.

Meta-data describing the data, and other information used in processing the data were catalogued in a SYSBASE relational database system. The database table design and table entity relationship diagrams are shown in Figure 2. These tables were implemented using the ACCESS commercial database system. The catalogues used for search and retrieve functionality were designed to be fully CIP compatible to enable data searching and ordering using either EWSE or INFEO.

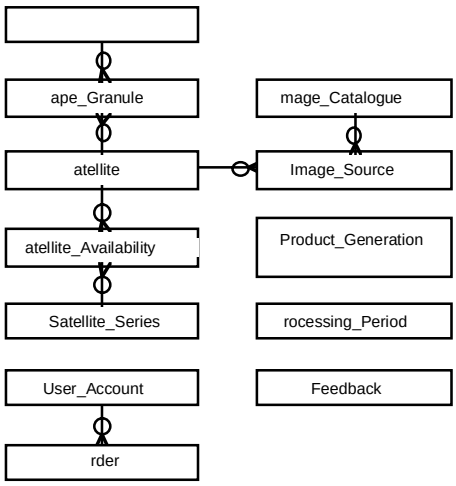

Figure 2: CLAUS Archive Entity Relationship Diagram.

4 Operational Processing and Archiving

4.1 The Processing and Archive System

Once the archive infrastructure and processing systems were implemented on the CLAUS workstation the processing of the data could proceed. These activities were carried out independently of the data delivery system since initially data were distributed to the testing centres directly *via* Exabyte tape.

The Customer Requirements exercise identified two main arrangements for the Brightness Temperature (BT) data:

Latitude/Longitude/Time: This is the normal arrangement, in which the data values can be considered to be arranged in a series of images ordered in time sequence.

Longitude/Time/Latitude: This is the Hovm ller format, used in studies of cloud evolution as a function of latitude.

Salby *et al.* stored data in both arrangements. However, the CLAUS archive spans an order of magnitude longer time series (>15 years compared with 1 year). An analysis of the additional processing necessary showed that was possible to generate the BT data in Hovm ller format on demand reasonably efficiently.

To help with this process the BT data are stored internally within the archive in files corresponding to one day, *i.e.* eight images. Customers are able to request data by time range and/or geographical limits, datasets are generated automatically for dispatch as contiguous sequences (in either latitude-longitude or Hovm ller format as appropriate). The accompanying quality information is also supplied in the same order as the BT data.

4.2 Operational Processing

Operational processing by NRSC commenced soon after the completion of the first validation exercise by the testing centres. Table 1 (Page 22) shows the time period of the B3 data processed by the end of the project.

The processing operation was designed to work on three months of data at a time. This required reading in B3 data from Exabyte tapes from EOSDIS. Depending on the number of satellites available at the time, the number of tape loads varied between eight and twelve. The time taken to load data from each tape was typically 30 minutes, so the time to load data from a three-month period was typically one working day. However, problems with this approach were encountered when tape errors occurred, necessitating re-processing of the entire three-month period.

An unforeseen problem that was not noticed until a substantial amount of data had been processed, was the variable quality of the source data. Although comprising only a few percent of the images, this led to the presence of occasional undesirable artefacts in the products. The main satellites for which this problem happens is the GOES series, which reveal systematic errors in image navigation (i.e. assignment of latitude-longitude values to each pixel) of several consecutive images each month or errors in image rectification. Both of these errors generally show up as a bright (cold) arc where off-planet pixels have

been assigned erroneous latitude-longitude values. Because the original design of the operational processing system did not include quality control checks, many of these artefacts appeared in early versions of the archive.

CLAUS Archive - Status as at end of Project												
	Jan	Feb	Mar	Apr	May	Jun	Jul	Aug	Sep	Oct	Nov	Dec
1983												
1984												
1985												
1986												
1987												
1988												
1989												
1990												
1991												
1992												
1993												
1994												
1995												

Key:

- = data not available
- = data available but unprocessed
- = data processed by NRSC
- = data processed by ESSC

Table 1: Status of the operational processing activities of the CLAUS archive by the end of the Project.

C Validation Activities

The original project timetable called for the validation activities to commence after an initial batch of data had been produced. However, at the first Interim Meeting of the Consortium the testing centres felt that it might be instructive to experiment with the existing Salby GCI data. This data set was therefore made available by ESSC to the testing centres *via* ftp and Exabyte. It was also recognised that this minor modification to the project plan would give the testing centres an opportunity to practice handling data sets of the format and size that would be emerging from CLAUS.

This decision proved well justified. Apart from some initial problems with transferring data *via* ftp and loading it onto their computer systems, the testing centres had little difficulty in manipulating the data using their existing software, and therefore looked with confidence to handling the full CLAUS data-set. Some unexpected results also emerged during the analysis of this data. For example, two testing centres discovered independently possible artefacts with the Salby dataset arising from the sampling method employed, which revealed a mismatch with reference coastlines.

Due to the possible problems with the Salby data set, and the fact that it is of a different grid size (512 by 512) to that of CLAUS (360 by 179), the Consortium agreed at its second Interim Meeting that it would be sensible to generate a small subset of the CLAUS archive for further experimentation. Rather than bring forward the implementation of the operational system, ESSC produced and distributed one year's worth of data (for 1992) using its demonstrator software.

The results of the validation activities presented here are based on the operationally produced data that were available at the time, plus the data for 1992 generated by ESSC.

Centre National de Recherches M t orologiques (CNRM) [1]
with
Ecole Nationale de la M t orologie (ENM) [2]

PI: *J.F. Royer[1]*

Contributors: *M. Belamari[1], J.-P. C ron [2], L. Chaumat[1], J.-F. Gu r my[2] , C. Piriou[1], J.-L. Redelsperger[1], J.-F. Royer[1], S.Tyteca[1]*

1 Overview

The CLAUS database has been used at CNRM for studying the diurnal and intraseasonal variability of convection, and for their validation in climate simulations performed with the Arpege-Climat general circulation model (GCM). The fine resolution (5 km) window brightness temperatures (WBT) images from the GMS satellite stored in the TOGA-COARE database for the four-month period 1st November 1992 to 28th February 1993 over the west Pacific region 10°S-10°N 135°E-175°E have been used for a validation of the WBT produced by the CLAUS algorithm over the same period. An excellent agreement between the two datasets has been found until 16th January 1993. The lack of the GMS data in the subsequent period has been used to study the impact of the temporal interpolation method used for filling regions with missing satellite data. It has been found that the temporal interpolation leads to a systematic effect on the medium range of the histograms, but has only a small effect on the estimation of the high-convective cloud cover.

The CLAUS archive has been used for identifying deep convective clouds with temperature colder than specified thresholds and computing monthly and seasonal statistics of their three-hourly fractional cover. Similar diagnostics have been introduced in a long-term climate simulation with the Arpege-Climat for the period 1983-1992. The results for the year 1992 have been compared to the CLAUS statistics in order to study the diurnal variation of convection. Using a threshold of 215 K, which reveals the presence of deep tropical convection, it has been shown that the geographical distribution and mean value of the simulated convective clouds was in reasonable agreement with the CLAUS observations, but that the amplitude of the diurnal variation of convection, together with the phase difference between ocean an continent are underestimated by the GCM. Sensitivity experiments to several parameterisations in the GCM have been unable to correct significantly this kind of systematic error in the model diurnal cycle. These conclusions have been confirmed by computing from the CLAUS brightness temperatures indirect measures of convective activity such as the OLR or the convective precipitation (DCA). The convection in the model appears to respond too rapidly to the diurnal variations of the surface variables and some mechanisms are missing for slowing down and retarding its response.

A study of the intraseasonal variations of convection has been carried out using two subsets of the total CLAUS dataset, namely a first case covering the West Pacific during January 1984 and a second one covering West Africa during the monsoon season of 1992. The results obtained on the West Pacific have shown that the set of statistical

methods used is appropriate to quantify the space-time variability of the CLAUS brightness temperature, and that this region was characterised during January 1984, in the synoptic scale, by westward propagating convective systems along 10°S that tend to change their direction of propagation toward the east at 175°E, along 20°S. For the 1992 West African monsoon case, it has been shown that the convection is characterised by four main modes of variability. Two modes correspond to westward propagating convective systems (associated to African Easterly Waves), with variance maxima located along 10°N over the continent east of 0° and over the Atlantic; the two other modes correspond to standing convective systems, with variance maxima located over the southern Sudan and over the north-western Zaire. The same analysis done with the OLR computed by the ECMWF model has shown this model tends to exaggerate the coupling between the AEWs and the convection. A preliminary study seems to indicate that the use of a CAPE closure in the convective scheme, instead of the moisture convergence closure, tends to alleviate this discrepancy in seasonal simulations carried out with the Arpege-Climat GCM.

2 Comparison of CLAUS data to those of the GMS satellite in the TOGA-COARE archive

J.F. Royer, L. Chaumat, C. Piriou, JL Redelsperger

During the intensive observation period (IOP) of the international field program Tropical Ocean and Global Atmosphere (TOGA) Coupled Ocean-Atmosphere Response Experiment (COARE) a comprehensive dataset of unprecedented scope and quality has been collected over the western Pacific warm pool (Webster and Lukas, 1992). As part of the International TOGA-COARE (Coupled Ocean and Global Atmosphere) experiment intensive observation period (IOP) which has taken place in the West Pacific Ocean from 1st November 1992 to 28th February 1993, high resolution infrared data from the Japanese Geostationary Meteorological Satellite GMS-4 have been stored and reprocessed by the Australian Bureau of Meteorology (BoM, Melbourne) and the University of Wisconsin. The data have been converted to a common McIDAS-X file format, and processed via a graphical software package called MERLIN (available through the University of Wisconsin-Madison) and stored in the TOGA-COARE database maintained at CNRM (C. Piriou, 1996) over the 4000x2000 km region of the experiment (135-175°E, 10°S-10°N). Information about the TOGA-COARE database at CNRM is available at: http://www.cnrm.meteo.fr/toga-coare/. Detailed information on the GMS-4 dataset is available on the TOGA-COARE Web site (Velden, 1994). An analysis of satellite observations and descriptive overview of the evolution of the large-scale cloud conditions during the four-month period of the IOP can be found in Velden and Young (1994).

The high spatial (5 km) and temporal resolution (hourly) of these data, and their high quality, since they have been carefully checked and re-navigated when necessary at BoM/Wisconsin, offers a convenient opportunity for a comparison with the data produced over these periods by the CLAUS algorithm. The GMS infrared data can be

extracted from the CNRM TOGA-COARE database as a series of three arrays of dimension 888 x 444 giving the window brightness temperature (WBT) at 5 km spacing, the longitude and latitude of the pixels for each satellite image. The WBT data are available most of the time at hourly intervals on the half hour over the whole period, with only a few missing images and a small data gap from 11th to 13 th January 1993 due to satellite re-calibration.

In order to facilitate comparison with the CLAUS radiance the 5 km GMS data have been processed in two different ways. First we have re-gridded the fine resolution data onto the 0.5° grid CLAUS grid in order to summarise their information in a convenient way over the TOGA-COARE domain 135-175°E 10°S-10°N. This has been done by computing spatial averages over all the 5 km pixels falling inside each 0.5° square as determined by their longitude and latitude. The computed averages are the mean BT, its standard deviation, the fractional coverage of pixels with BT less than two selected thresholds (235 K and 215 K). We are aware that alternative ways of re-gridding such as sub-sampling could be used and may have some advantages in preserving the histogram of the BT distribution, but on the other hand they would have the drawback of producing multiple possible alternative gridded data, and thus higher sampling fluctuations. The mean and standard deviation appear as the most objective and economical way of summarising the first moments of the distribution of the fine resolution data. However the spatial averaging may have an impact on the histogram, and thus we have included in the inter-comparison a computation of the histogram of the fine resolution 5 km data and of the 0.5° averaged data to be compared with the histograms of the CLAUS data.

As a typical example illustrating the differences between the fine resolution data, their 0.5° average, and the CLAUS data, we have chosen the image from the 12 December 1992 at 02h30 (Figure 1). This image is at the end of a developing and westward-travelling convective disturbance from 10th-12th December, which has previously been described and illustrated by Velden and Young (1994). A large convective cloud system is clearly apparent, with a number of embedded very deep convective cells with cloud top temperatures below 200 K. The convective cluster is surrounded by a zone of scattered shallow convective clouds of smaller horizontal extension over a sea surface background warmer than 290 K (Figure 1(a)). The spatial averaging at 0.5° resolution (( )1b) has the expected effect of blurring the fine-scale structure of the cloud distribution while keeping the main cloud clusters, and the CLAUS imagery at target time 03h00 (Figure 1(c)) is visually very similar to the 0.5° averaged image. In order to outline the differences between the CLAUS and GMS images at the same 0.5° resolution their difference (image C minus image B) has been displayed as Figure 1(d). It can be seen that the CLAUS WBT are within 5 K of the averaged GMS temperature over most of the area and tend to be sometime colder over the deep convective areas, and warmer over the clear and shallow convective region. However, this difference map points out mainly the excellent agreement between the CLAUS and averaged GMS data. As the GMS data are available every hour while the CLAUS data are sampled only every three hours it is interesting to look at the effect of the observation time on the difference between CLAUS and GMS. For this we have computed the difference between the same CLAUS image (Figure 1(c)) and the 0.5° averaged GMS half an hour later at 03h31 (Figure 1e) and an hour and a half later at 04h23 (Figure 1(f)). It can be seen that the magnitude of the difference is

markedly amplified with the time shift between the CLAUS and GMS image. Point differences in excess of 30 K, both positive and negative, appear as a consequence of the deformation and displacement of the convective cells. The position of the positive anomalies at the western margin of the deep convective clusters and negative anomalies at their eastern side is consistent with the general westward displacement of the cloud systems during this convective episode (Velden and Young, 1994). The three figures illustrate very well that the differences between the CLAUS and averaged GMS data appear more sensitive to small time shifts between the images than to the averaging or sampling method. It is interesting to note that the CLAUS image is closer to the GMS image in the preceding half hour than to the one in the subsequent half hour, which will be shown later to be generally the case.

In order to quantify the overall distance between the CLAUS and GMS images we have computed the spatial root mean square (RMS) of the difference maps, which we term the 'RMS distance'. The RMS distances corresponding to images in Figure1(d, e and f) are respectively 3.0, 9.6 and 14.4 K. The steep increase of RMS distance with the time shift between images shows that it is a very sensitive indicator of spatial deformations in the cloud field. However this very sensitivity makes it less suitable for detecting possible more subtle biases in the WBT temperatures between the two datasets.

In order to monitor the overall distribution of the WBT temperatures we have computed histograms and cumulative histograms over the domain of study. As the WBT data from the GMS and CLAUS imagery can only take a set of discretized values (<256), due to their original 8-bit coding, we have taken care to define the histogram intervals separately for the two data sets to correspond to the mid-point between the neighbouring discrete values, and have normalised the histogram density by dividing by the width of the interval so as to obtain comparable quantities. As an example we have displayed in Figure 2(a) the histograms corresponding to the images in Figure 1(a-c). The histogram corresponding to the 5 km data is rather smooth due to the large number of 5 km pixels. It shows a major peak at about 295 K, decreasing very sharply on the warmer side before 300K (corresponding to surface temperature), while it decreases more gradually on the cold temperatures side due to the presence of low stratus or shallow convective clouds. There is a kind of plateau between 260 and 220 K produced by the uniform distribution of convective clouds at various stage of development, and a decrease between 220 and 180 K produced by comparatively rare very deep convective cells. The distributions for the 0.5° data are noisier due to the smaller number of data points, it can be seen that they follow the same general shape. However some effect of the averaging can be noticed in that the GMS 0.5° data tend to have slightly smaller frequencies at temperatures colder than 220 K, and slightly larger frequencies in a broad band of medium temperature between 240 and 290 K, as can be expected from the averaging over partially cloudy grids. This effect is seen more clearly on the cumulative histogram Figure 2(b), which can be interpreted as the fraction of the domain occupied with clouds colder than the temperature given in abscissa. The spatial averaging reduces by a few percent the frequency of cold clouds, and increases the frequency of low clouds below 270 K. The cumulative histogram is nearly identical to the 5 km data distribution for the very cold clouds below 215 K, and to the averaged 0.5° set for temperatures warmer than 260 K, and lies between the two in the intermediate range. As a measure of the distance between

two histograms we have used the integral over the temperature range of the squared difference of their cumulative density. The distances in Figure 2 are 0.21 between GMS 5 km and GMS 0.5°, 0.14 between CLAUS and GMS 5 km, and 0.11 between CLAUS and GMS 0.5°, confirming the visual impression that CLAUS lies between the other two, and closer to the averaged data over a wider temperature range. By construction, the histogram distance is insensitive to cloud displacements inside the domain, and thus is comparatively less affected by shifts in the time of the observation of the images. For example, for the GMS image at 04h23 the histogram distances are 0.23 between the two GMS resolution, 0.20 and 0.19 between CLAUS and GMS at fine and coarse resolution. The RMS and histogram distance measure different properties and will be both useful for characterising the differences between the CLAUS and GMS datasets.

From all the 5 km GMS images available in the TOGA-COARE database we have computed 0.5° averages and histograms. We have then compared them with the nearest in time CLAUS images using the above defined distances so has to produce a time series summarising the agreement between the two datasets (Figure 3). The horizontal axis in Figure 3 represents the day number starting at 1st November 1992 until 28th February 1993. The RMS distances display a rather uniform behaviour until day 67 (16th January), then increases suddenly to higher values. We will call the first time span from 1st November to 16th January 21 h period 1 , and the following period until February 28 th period 2 . We will show later that this time series has enabled us to detect an unexpected data loss in the preliminary CLAUS analysis procedure, so that the data in period 2 are unrepresentative of the general characteristics of the CLAUS algorithm. The values of the RMS distance in period 1 confirm the particular results for 12th December presented in Figure 1. The RMS values are generally clustered around three different values, a smaller value close to 4 K, a medium value of 8 to 10 K and a larger value between 10 and 15 K. The different clusters correspond to different time shifts between the CLAUS target time and GMS observation times, with the larger values for a shift of one and a half-hour. While the smaller values corresponding generally to the GMS observation half an hour before the CLAUS time are rather stable over the whole of period 1, the other two clusters have fluctuations which are related to the general level of convective activity over the domain of study. During periods of low convective activity, the clouds have warmer cloud top temperatures, and thus the cloud displacements between the observation times produce smaller contrast with the surface and hence smaller differences and RMS, while the converse is true in periods of high convective activity. The histogram distance between the averaged and fine resolution GMS data (solid curve in Figure 3(b)) fluctuates between about 0.1 to 0.3K during both periods. During period 1 the histogram distance between CLAUS and 5 km GMS varies in about the same range, which shows the same satisfactory level of agreement as in Figure 2. On the other hand, during period 2 the histograms of CLAUS become much more different than the GMS histograms, confirming the change seen from the RMS distance.

In order to find the cause for the deterioration of the CLAUS analysis in period 2, we have made use of the quality data produced by the CLAUS algorithm, which summarises in condensed form information about the interpolation method and satellites used in the interpolation (Hodges et al., 2000). The quality data have made readily apparent that the GMS satellite had not been taken into account after 16 January, due probably to an error

in tape manipulation. Though this is an error that will be easily corrected by reprocessing this whole period, we have found interesting to use the erroneous results for period 2 to investigate further the effect of a missing geostationary satellite on the interpolation. We have thus computed separate statistics for period 1, which is truly representative of the overall quality of the CLAUS algorithm and for period 2, which indicates how this quality is degraded at times when a geostationary satellite is missing and only polar orbiting satellites are available for carrying out the analysis. As the polar orbiters cross over a particular region at well defined times it has been found suitable to perform an analysis over a diurnal cycle. Over the TOGA-COARE region the polar orbiters are NOAA-PM and NOAA-AM. The maximum coverage of over 60% of the area is at 09h and 21h for NOAA-PM, and 06h and 18h for NOAA-AM (Figure 4(a)) and is roughly similar in period 1 and period 2. The coverage of GMS is 100% over period 1, except at 03h due a few missing images at this time on particular days, while due to some error in processing it is completely absent from period 2. The interpolation method is method 0 (primary spatial) during period 1 with a small contribution of method 4 (primary temporal) for the missing images at 03h (Figure 4(b)). During period 2 the interpolation method alternates between primary spatial interpolation over the tracks of the NOAA-PM and NOAA-AM satellites (more than 70 % of the area at 06, 09, 18 and 21 h) and temporal interpolation in between (mostly at 00, 03, 12 and 15 h). There is only a very small and marginal contribution of methods 2 and 3 (secondary and tertiary spatial interpolation). The RMS distance for period 1 (Figure 4(c)) confirms the increase of the distance with the time shift seen in Figures 1 and 3. The smallest distances of about 4 K are found for the GMS images in the half-hour preceding the time of the CLAUS image, while the medium distance of 8-9 K is found for the succeeding half hour. The only exception occurs at 15h where this pattern is reversed. The largest distances of 12-13 K are found for a separation of 1.5 hours, with the exception of 00, 06 and 18h for which a medium distance is found. This reduction in the distance after 06 and 18h could be due to the influence of the NOAA-PM or NOAA-AM satellites. It can be seen that the minimal RMS distances are found at the times where the polar orbiters cover only a very small fraction of the area just before 12 and 24 h, and the largest distance 1h30 after 12. In the two-hour time span starting half an hour before twelve where the RMS increases by a factor of three. For period 2 the RMS varies from minimal values of about 11 K at the times when the polar orbiter data are available for a spatial interpolation method over a large fractional area of the domain at 06, 09, 18 and 21h, to larger values of about 16 K when no satellite data are available and CLAUS data are made by temporal interpolation at 00 and 12h. It may be noticed that the minimal RMS resulting from the spatial interpolation of the polar orbiters is comparable to the RMS resulting from a time shift of 1.5 hour in the GMS data. The histogram distance in Figure 4(d) has a nearly constant value of 0.2 K between the averaged and fine resolution GMS data (curve a) and identical values in period 1 (a1) and period 2 (a2). For period 1 the distance between CLAUS and the high-resolution data (curve b1) has similar values, which increase slightly after 09 and 21 h, while the distance with the averaged GMS data (curve c1) decreases slightly between 06-09h and 18-21h. This behaviour could be due to the inclusion in the CLAUS spatial interpolation of the NOAA data producing a kind of averaging making the histogram closer to that of the 0.5° averaged GMS than to the original 5 km histogram.

For the second period a marked variation of the distance is found according to the interpolation method. The CLAUS histograms are systematically closer to the averaged GMS histograms than the fine resolution ones, and the histograms are more similar when the NOAA data are interpolated spatially (06-09h and 18-21h) than when the temporal interpolation is applied (00-03h and 12-15h). In order to illustrate the effects of the interpolation method on the histograms (Figure 5) we have computed separate histograms over the grid points where NOAA data are available and taken into account in the CLAUS images (curves A) and grid points where the NOAA data are absent (curves B). The computation has been made also over the same regions for each 0.5° GMS image closest to the CLAUS image (30 minutes before the CLAUS image except at 15h). For period 1 a very close agreement is found between the CLAUS and GMS cumulated histograms. The taking into account of the NOAA data in the CLAUS analysis (curve CLAUS A) has only a very small effect, which tends to produce slightly cooler temperatures (not more than 1-2K) in the lower levels, perhaps due to a slightly different calibration. The histograms over period 2 seem to confirm that the NOAA data used to produce curve CLAUS A increase the frequency of cooler temperatures (about 5 K) when compared to GMS data (curve GMS C), and thus give a higher fractional cloud cover at a given temperature threshold, when compared to the GMS data. In the absence of NOAA data (curve CLAUS B), the interpolation method is mainly temporal and has a very important effect on the histogram in reducing the frequency of temperatures colder than 260 K and increasing the frequency of low level temperatures between 260 K and 290 K as expected from an averaging of cold cloud tops with warm surface temperature. The deformation in the histogram is very similar to that obtained by computing a histogram on the average of two GMS maps 6 hours apart. The overall increase in histogram distance between CLAUS and GMS data over period 2 is thus the combination of two factors: the different calibration of the NOAA satellites and the averaging effect of the temporal interpolation between two maps to fill the data gaps. While the two effects are additive for temperature higher than 240 K and tend to increase the frequency of middle and low clouds, it should be pointed out that they tend to compensate for colder temperatures. Thus estimations of cold convective clouds will remain accurate on average, though with a tendency to oscillate between successive maps between larger values for spatial interpolation of NOAA data, and lower values for temporal interpolation in the absence of these data. This is exactly what is observed on Figure 6 giving time series of cloud covers below 215 K and 235 K thresholds, and the mean WBT temperature. It can be seen that the CLAUS mean WBT, which is so perfect agreement with the GMS during the first period, becomes colder by a few degrees after 17th January (day 78) as expected from the change in histogram analysed on the previous figure. The cold convective covers remain in excellent agreement throughout the whole period, but the CLAUS cloud cover appears to fluctuate more than the GMS one after this date.

The conclusion emerging from this comparison is that an excellent agreement has been found between the GMS satellite and the data produced by the CLAUS algorithm over the TOGA-COARE period from 1st November to 16th January during which the CLAUS algorithm has been run correctly. An inadvertent omission of the GMS satellite from the CLAUS analysis in the subsequent period has been found useful to study the impact of occasional gaps in geostationary satellite data on the quality of the analysis. It has been found that when polar orbiting satellite data are available the effect on the RMS distance

between maps is not worse than a time shift of about 1h30. The effect on the histogram is different according to the interpolation method, with temporal interpolation having the effect of reducing the high convective cloud cover and increasing the medium and low cloud cover. However, as the compensation between these two effects occurs near 240 K it should not be of much consequence for methods that track cold convective clouds with nearby thresholds.

3 Validation of the diurnal cycle of convection simulated by the ARPEGE-Climat model using the CLAUS dataset for 1992

J.F. Royer, M. Belamari, L. Chaumat, S. Tyteca

The approach adopted for the study of the diurnal cycle of convection is based on the application of temperature thresholds to the brightness temperatures both in the CLAUS dataset and in the simulations with the Arpege-Climat GCM, so as to define a fractional cloud cover for the coldest and highest convective clouds. From a literature survey three widely cited thresholds at 235 K, 215 K and 208 K have been chosen. The window brightness temperatures (WBT) at 0.5° resolution produced by the CLAUS algorithm have been used to compute a monthly mean partial cloud cover on a 2.5° grid, giving the fractional coverage of clouds with radiance temperature smaller than each chosen threshold, separately for the eight three-hourly target observation times, in order to describe the diurnal cycle of convection. This algorithm, first developed and tested on the Salby dataset for January 1984, has then been applied to the CLAUS dataset for 1992, so as to produce a monthly mean partial thresholded convective cloud cover for this year. Seasonal averages for the conventional seasons (DJF, MAM, JJA, SON) have then been computed. The diurnal cycle of convection has been summarised by computing the amplitude and phase of the first diurnal harmonic of the partial cloud cover from the three-hourly means. As an example of the results the seasonal mean 215K-thresholded cloud cover and its first diurnal harmonic variation for boreal winter (DJF) and summer (JJA) are displayed in Figures 7 and 8. The resulting climatology shows clearly the seasonal evolution of convection with a displacement of the convective clouds concentrated along the intertropical convergence zone towards the summer hemisphere. The maps obtained show well defined patterns without any apparent discontinuities that could result from the use of different satellites, even over the Indian Ocean region. The diurnal cycle of convective clouds shows a marked contrast between land and ocean. The relative amplitude of the diurnal cycle is higher over the tropical continents than over the oceans. There is also a marked phase difference with maximum convection occurring generally in the early morning over the oceans, and in the late evening over the continents. Such results are fully consistent with the previous studies on the diurnal cycle of tropical convection.

Similar diagnostics have then been implemented in the ARPEGE-Climat GCM (D qu et al., 1994; Stephenson et al., 1998) in order to compute fractional cloud covers based on the same temperature thresholds. The partial cloudiness computed from the convective

cloud parameterisations of the GCM in the vertical layers with temperature lower than the specified thresholds, are combined and accumulated over three-hourly periods so as to give a thresholded fractional cloud cover comparable to that computed from the CLAUS dataset. A long-term integration this version of ARPEGE-Climat with the new cloud diagnostics has been performed for the period 1983-1995 using observed monthly mean sea surface temperatures. Monthly and seasonal statistics for the three thresholded cloud covers for the year 1992 have been computed and compared to the similar diagnostics from the CLAUS dataset. The comparison shows that, while the mean fractional cloud cover is only slightly underestimated in the model simulation (Figures 9 and 10:top), the amplitude of the first harmonic of the diurnal cycle is smaller than observed particularly over the continents (Figure 9 and 10:middle). The contrast in the phase between oceans and continents is strongly underestimated by the model (Figures 9 and 10:bottom), with convection occurring several hours earlier over the continents than is observed from the brightness temperature (Figures 7 and 8: bottom).

In an attempt to understand what physical parameterisations could play a part in the lack of contrast of the convection between ocean and continents in the model several sensitivity experiments have been performed. We have first tried to improve the contrast in the mixing length used for the computation of boundary layer turbulent fluxes by implementing in the model a diagnostic computation of the boundary layer (BL) height based on the use of a critical bulk Richardson number, as proposed by Troen and Mahrt (1986). This diagnostic BL height is then used as a height scale in the specification of the analytic mixing length profile. This diagnostic computation of the BL height has given more contrasted boundary layer thickness over oceans and continents, and resulted in an overall improvement of the cloud cover, but only over the oceanic areas in the northern mid-latitudes, and had basically no influence on the diurnal cycle of convection. An essential parameter in the convection scheme is the entrainment rate of environmental air used for the computation of the convective cloud vertical profile. By dimensional arguments it has long been known that the entrainment rate should be inversely related to the average radius of the convective cells. Making the assumption that the horizontal size of the convective cells is proportional to the boundary layer thickness we have introduced a dependence of the entrainment rate on the diagnosed boundary layer height so as to take into account the contrast between ocean and continents. Simulations have made with several values of the proportionality factor have shown that the use of a larger entrainment rate with a variable boundary layer height could give a mean fractional cloud cover in better agreement with the observed one, but without any significant improvement in the phase of the diurnal cycle. As an example of the results the seasonal mean 215K-thresholded cloud cover for summer (JJA) 1992 are displayed in Figure 11 for two values of the entrainment factor (a small value of 0.125 with a fixed BL height, and a larger value of 0.185 with diagnosed BL height), and compared with the results obtained from the CLAUS dataset (Figure 11:bottom). The larger entrainment rate used in the second experiment (EN2) and the use of a variable boundary layer height give a mean fractional cloud cover, which is in better agreement with the observed one. However, the improvement in the phase of the diurnal cycle is only marginal. We have implemented a new diagnostic summarising the vertical decrease of the cloud cover in term of a characteristic temperature scale (temperature decrement for which the fractional cloud cover is decreased by e^{-1}). The comparison of this temperature scale between the

Arpege-climat simulations and the CLAUS data (Figure 12) shows that in the simulated clouds are more homogeneous in height and generally extend higher than the observed ones.

In order to understand better the lack of agreement between the phases of diurnal cycle of the high convective cloud fractions diagnosed in the Arpege-Climat GCM and those observed from the CLAUS dataset, we have made several attempts to modify the computation of the high clouds fraction in the GCM. Initially, this fraction was based not on the total cloud cover, but on the convective fraction n_c only. In the Arpege-Climat parameterisation the convective cloud cover n_c is assumed to be simply proportional to the liquid water content of the layer:

$$n_c = \alpha_{nc}\, q_{cc}$$

- with an empirical proportionality coefficient $\alpha_{nc.}$ The liquid water content q_{cc} of the convective cloud is computed diagnostically in each model layer from the vertical derivative of the convective precipitation flux F_{pc} by the following relationship (JM. Piriou, Arpege Documentation, CNRM):

$$q_{cc} = q_{cx}\,[\,1 - \exp(\,-\,g\,\alpha_c\,\{dF_{pc}/dp\}\,\Delta t\,/\,q_{cx}\,)]$$

- where g is the acceleration of gravity, Δt is the time step, q_{cx} and α_c are two adjustable parameters representing respectively the maximum liquid water content, and the inverse of a time scale for condensed water precipitation. These two parameters have been chosen empirically by fitting the simulated zonally averaged total cloud liquid water profiles to observed values.

The stratiform cloud cover n_s is computed by the statistical cloud scheme described in Ricard and Royer (1993). The total cloud cover n in a layer is computed as the maximum of the convective and stratiform cloud cover:

$$n = \max(n_c, n_s)$$

An experiment in which we have used the total cloud cover instead of the convective cloud cover has shown that this leads to a large overestimation of the fractional cold cloud cover at all the chosen thresholds, as a consequence of the large stratiform cloud cover due to water vapour detrainment near the top of the convective clouds. This is a consequence of the low water vapour content of these cirrus-type clouds, which produces only a very small emissivity in the infrared, giving a much-reduced effective cloud cover. It was noticed that the stratiform cloud cover simulated by the model has a very different diurnal cycle compared to the convective cloud cover, due to the longer persistence of the stratiform clouds, and this gives a phase in better agreement with the phase of the high cloud cover diagnosed from the CLAUS data. This might suggest that the stratiform part of the cloud cover could play some part in the observed diurnal phase diagnosed from the satellite brightness temperatures. However, the computation of their influence on the brightness temperature diagnosed in Arpege-Climat would need to take better into account their radiative properties since they cannot be assumed to radiate as blackbodies at low water contents.

As a complement to the previous straightforward approach, which consists in computing in the GCM a cold cloud fraction comparable to a similar diagnostics from the observed dataset, we have tried the indirect approach of using the brightness temperatures of the CLAUS dataset to produce fields of OLR and convective precipitation that can then be compared to standard GCM fields. For the OLR field, we have applied the following empirical equation (Ellingson and Ferraro, 1983) relating the radiance brightness temperature T_b in the IR window to a flux equivalent temperature T_F:

$$T_F = T_b\ (a + b\ T_b),$$

- where *a* and *b* are empirical coefficients. We have taken: $a \sim 1.2$ and $b \sim 1.2\ 10^{-3}$, based on an average of the values quoted in Table 1 of Ohring et al. (1984).

The Outgoing Longwave Radiation (OLR) and the equivalent temperature are then by definition related by the blackbody radiation law:

$$OLR = \sigma\ T_F^{\ 4}$$

- where σ is the Stephen-Boltzmann constant.

This computation of the OLR, applied to the brightness temperatures in the 0.5° grid of the CLAUS dataset and averaged over a coarser 2.5° grid, gives values of average OLR (Figure 13:top) that are in good agreement with OLR climatologies. The convective regions covered by cold cloud tops appear as minima with OLR values below 260 W/m^2. The OLR computed by the radiative scheme of the GCM (Figure 13:bottom) has a very similar structure with however an underestimation of the low OLR values, consistent with the underestimation of the cold convective fractional cloud cover noticed previously. We have also applied the relationship used to derive the OLR values from the brightness temperature to the temperatures of the cloud layers in the Arpege model using the total cloud cover (Figure 13:middle). The excessively low values obtained for the OLR in the convective regions confirm that the stratiform cloud cover needs first to be reduced by taking into account its emissivity in this computation. The phase of the diurnal variation of the OLR showing the hour of the minimum OLR, in order to agree with the phase of maximum convection (Figure 14:top), displays a marked contrast between the convective areas where the minimum OLR occurs between 12 and 24h local time, and the non-convective areas where the minimum OLR occurs in the early hours of the morning. The model OLR (Figure 14:bottom) reproduces this contrast rather well over the continents where the minimum OLR occurs in the late evening over the convective regions. However over the oceans the model does not reproduce the phase contrast between the convective and non-convective regions.

We have derived from the CLAUS brightness temperature a convective precipitation estimate based on the Deep Convective Activity (DCA) index of Hendon and Woodberry (1993). The DCA index is computed by applying a 230 K threshold to the brightness temperatures T_b:

$$DCA = 230\ K - T_b \quad \text{for } T_b < 230\ K\ ;\ \text{and } DCA = 0 \text{ otherwise.}$$

DCA is then averaged and transformed to precipitation by the conversion factor 0.87 mm (3 hours)$^{-1}$ (unit DCA)$^{-1}$. The resulting map (Figure 16:top) gives a mean rainfall rate in good agreement with other climatologies of tropical precipitation, as well as with the rainfall simulated by Arpege-Climat (Figure 15:top). The relative diurnal amplitude is comparable to the simulated one over the continents but larger over the oceans. The diurnal phase (Figure 16:bottom) is very similar to the phase of the 215 K fractional cloud cover (Figure 8:top) and gives a later maximum delayed to the late evening over the continents when compared to the GCM simulation (Figure 15:bottom). Over the oceans the maximum occurs also later in the early morning than in the simulation. The diurnal cycle of the convective rainfall of the model shows a similar contrast with a marked diurnal cycle over continents, and a very small diurnal amplitude over oceans. The maximum convective precipitation peaks in the beginning of the afternoon over the continents while over the oceans the maximum occurs in the middle of the night. The phase of the diurnal cycle of convective precipitation is thus quite different over the oceans than that of the deepest convective clouds that have a maximum in the afternoon.

Diagnostics of the diurnal cycle for other surface variables have been incorporated in the GCM, in particular precipitation, surface temperature, evaporation and cloud cover. As expected, the amplitude of the diurnal cycle of surface temperature was found to have a marked geographical variation and to be largest in the cloud free areas, and to be reduced by the development of convective clouds in regions affected by the intertropical convergence zone or monsoon circulations. The phase of the diurnal cycle of temperature is rather uniform over the continents with the maximum occurring in the afternoon between 12 and 16h local time. The surface evaporation simulated by the model has a strong diurnal variation larger than 2 mm/day over the continents in the regions of large convective precipitation. The maximum evaporation is directly affected by the diurnal variation of the solar radiation that provides the required source of latent heat, and peaks over these areas at about midday. Over desert areas the evaporation and its diurnal variation are naturally very small and tend to their maximum a few hours before noon. The surface evaporation reaches its highest values over the tropical oceans, but has a very small (less than 0.7 mm/day) diurnal variation with a rather consistent phase with a maximum in the morning hours before 8h local time. As the surface temperature is fixed in the model this diurnal variation is probably due to the accumulation of the nocturnal cooling of the atmosphere, which tends to destabilise the lower layers of the atmosphere and thus to enhance turbulent fluxes, with a maximum at about sunrise.

In conclusion, the CLAUS dataset has been used to compute monthly mean fractional covers of high convective clouds. The diurnal cycle of convection has been summarised by computing the amplitude and phase of the first diurnal harmonics of the partial cloud cover from the three-hourly means. The analysis of a long-term integration (over the period 1983-1995) of ARPEGE-Climat with the new cloud diagnostics has been compared with the similar cloud monthly and seasonal cloud diagnostics from the CLAUS dataset for the year 1992. This comparison has shown that, while the mean fractional cloud cover is realistically simulated by the model, the amplitude and phase of the first harmonic of the diurnal cycle is not correctly reproduced. Some modifications were attempted in the computation of the convective and stratiform cloud properties used

in the Arpege-Climat GCM, but their impact was rather modest and was not able to alter significantly the major deficiencies identified in the diurnal cycle of the GCM. These conclusions have been confirmed by computing from the CLAUS brightness temperatures indirect measures of convective activity such as the OLR or the convective precipitation (DCA). The diagnostics of the convective cloud fraction in the model would need to be improved by taking into account the radiative properties of the stratiform clouds, which seem to play some part in the phase of the diurnal variation of the high convective cloud cover diagnosed from the brightness temperature. The main conclusion that can be drawn is that the convection in the model appears to respond too rapidly to the diurnal variations of the surface variables, and that some mechanisms are missing for slowing down and retarding its response. Potential candidates could be a turbulent kinetic energy scheme, which could introduce some inertia in the response of the boundary layer, or a more stringent criterion for the triggering of convection. Both schemes are currently in development for inclusion in Arpege-Climat and will be tested for their potential impact on the diurnal cycle.

4 Intraseasonal space-time variability of brightness temperature: observation versus simulations

Jean-François Guérémy and Jean-Pierre Céron (ENM/UFR/UMT)

This work has been carried out using two subsets of the total CLAUS dataset, namely a first case covering the West Pacific during January 1984 and a second one covering West Africa during the monsoon season of 1992. The main goal of the work done at UMT was to identify the intraseasonal space-time variability of the brightness temperature (both observed and simulated) with the help of a hierarchy of objective statistical tools used in a previous study (Ceron and Gueremy, 1999), going from a global (in space and time) to a more local perspective. The scientific issues addressed by this work are first the possible ability of the statistical tools to identify the variability, and second, the nature of the observed variability together with the validation of the simulated variability.

4.1 January 1984 over the West Pacific

The preliminary Salby data sample for January 1984 (three-hourly GCI radiance temperature data) provided by ESSC has been used in this study. An equatorial West Pacific domain has been considered (100°E to 170°W, 10°S to 20°N). First, the variability has been analysed globally on the space-time domain. This is done with the help of a Space Time Spectral Analysis (STSA), which provides a space-time spectrum, and a spatial representation of the time variance for different time spectral windows (such as the diurnal cycle, the synoptic and intraseasonal time band). Moreover, the STSA allows a partition of the variance produced in one hand by standing perturbations and on the other hand by travelling ones. Then, a Complex Empirical Orthogonal Function Analysis (CEOFA) has been used on time filtered data (synoptic time band) in order to get a more precise view of the variability (decomposition on several modes associated to

a spatial representation of the space module and phase speed together with a time representation of the time module). Second, the variability has been analysed locally, taking into account the results of the first step. This is done with the help of a Wavelet Analysis (WA) on the first complex principal components. The WA that gives a time frequency spectrum.

The results obtained have shown that these statistical diagnoses are appropriate to quantify the space-time variability of the brightness temperature, even at the relatively high resolution used here. These results can be summarised as follows. The space-time spectra have shown that there exist three significant time domains of variability, the diurnal, synoptic (2 to 10 days) and intraseasonal (above 10 days) time domains. The spatial representation of the diurnal time variance clearly shows maxima on land regions. The emphasis has been put on the synoptic time domain and more precisely on two regions characterised by variance maxima in this time domain. These two regions are the SE zone (South of the equator and East of Australia; 6°S - 20°N and 150°E - 150°W) and the NW zone (North of the equator and West of the Philippines; 1°N - 16°N and 122°E - 178°W).

For the first region, the STSA has allowed a clear space partition between the westward propagating waves (in the north) and the eastward propagating waves (in the south) (Figure 17). The mapping of the phase speeds by the CEOFA method gives a more complete picture; indeed, it appears as a change in curvature of the phase speed vectors from the East to the West in the western part of the region (Figure 18). Moreover, the areas of disorganised phase speeds correspond well to the areas of significant standing wave variance given by the STSA. The WA applied on the first two CPCs has shown that there exist oscillations with two main superimposed periods, one around 4 days and the other around 6 days (Figure 19).

For the second region, the interpretation is less clear. Nevertheless, the combined use of the STSA and the CEOFA has shown that the first CEOF mode mainly includes travelling oscillations whereas the second mode mainly includes standing oscillations.

The results obtained on the Salby dataset show that this set of statistical methods is appropriate to quantify the space-time variability of the brightness temperature, even at the relatively high resolution used here. The same analysis has therefore been applied to the processed radiance data produced in the CLAUS project, specifically on the subset covering the 1992 West African monsoon.

4.2 The 1992 West African monsoon

In this study, we have used a space-time spectral analysis to investigate the space variability of the CLAUS brightness temperature (BT) during the 92 African monsoon season. At the same time, we have applied the same method to the outgoing longwave radiation (OLR) from the ECMWF reanalysis in order to assess the quality of this dataset compared the CLAUS information, which is more realistic because it comes from a more direct measurement (satellite radiometer). The method we have applied has been already tested on BT fields in a previous study (see above), and it has been shown that it was suitable for this kind of work (investigation of the space-time variability). The space-time domain chosen is the following: May to October 1992 in time (184 days), over an

African domain in space (40°W/5°S to 40°E/35°N), for the smallest resolution of the 2 datasets (6h, 1°x1°; the CLAUS dataset has been averaged to this resolution). The ECMWF OLR fields are in fact forecasts fields (6 hourly averaged, between 06 to 12, and 12 to 18) from the reanalyses.

First, we have plotted the space-time spectra. The same pattern has been observed for the normalised power densities of travelling oscillations for both the BT and the OLR (Figure 20). We can notably notice maxima of power density for the 3-5 day (around 4 and 5 days mainly, i.e., for the time harmonics 45 and 37) and 20-60 day (around 30 and 50 days mainly, i.e., for the time harmonics 6 and 4) bands, for westward travelling oscillations. Then, we put the emphasis on these two bands. Thus, we have plotted the spectra for the 3-5 day band in terms of the zonal and meridional wavenumbers (not shown). It appeared that the ECMWF OLR presents a space structure characterised with too small a scale along the meridians and too large a scale along the parallels.

Second, we have plotted the time variance for the two space-time spectral windows defined with the help of the spectra. Figure 21 shows these plots for the synoptic (3-5 days) window concerning westward travelling oscillations, for the month of August. The maxima of variance give the location where the convection is significantly modulated by the African easterly waves (AEWs). This plot gives further details on the discrepancies already mentioned previously. Indeed, the ECMWF OLR variance tends to be too large over the eastern part of the domain, whereas it tends to be too weak over the northern side of the Sahel. The former discrepancy is observed for all the months of the season, whereas the latter is mainly observed during the second part of the season. The fact that the ECMWF OLR variance tends to be weak over the northern side of the Sahel indicates that the convective precipitation (associated to the synoptic variability) simulated by the ECMWF model will be too weak over that region.

Concerning the CLAUS BT standing wave variance for the 20-60 day time window (low frequency oscillation, LFO), it appears (Figure not shown) that we have maxima of variance over West Africa which might due to the modulation of the AEW activity by the LFO, with an extension over the Sahara due to cirrus, and another maxima over Uganda due to the direct modulation of convection by the LFO over this mountain area. For the CLAUS BT westward travelling wave variance, one can notice that the main maxima over west Africa is collocated with the synoptic wave maxima, indicating that the westward travelling part of the LFO modulates the activity of the AEWs, and as a consequence, the convection itself. The ECMWF OLR standing wave variance shows that its intensity is too weak relatively to the travelling part, by comparison to the CLAUS data; moreover, the maxima over the East African highlands does not exist. The pattern of the westward travelling part of the LFO is reasonably reproduced by the ECMWF OLR data, even if the variance seems to be too weak over the west Sahel.

The preceding study has been extended by the use of a Complex Empirical Orthogonal Function (CEOF) analysis. In order to refine the physical interpretation of the CEOF decomposition, we have developed a rotation method of CEOFs, which has been applied in this study. We have also applied the CEOF analysis to the outgoing longwave radiation (OLR) from the ECMWF reanalysis in order to assess the quality of this dataset compared the CLAUS information. For each grid point of the space domain, we have filtered the time series of the two dataset, keeping the information in the band 2.5 to 6

days, with the help of a fourth order Butterworth filter. The time band has been chosen according to the results of the Space-Time Spectral (STS) analysis, in order to put the emphasis on the synoptic variability, mainly due the African Easterly Waves (AEWs).

Figure 22 (resp. Figure 23) presents the mapping of the time variance associated to the first four rotated CEOFs of the CLAUS (resp. ECMWF) dataset. These first four rotated CEOFs of both datasets represent each a significant part of the total variance. Concerning the CLAUS data, one can notice that the variance maxima are located over the western Sahel and its coastal region, the south of Sudan, the Atlantic and finally the western part of equatorial Africa, respectively for the first four rotated CEOFs. According to the previous STS analysis, the CEOF 2 and CEOF 4 correspond mainly to standing or eastward travelling phenomena, whereas the CEOF 1 and CEOF 3 correspond to westward travelling phenomena (i.e., the AEWs). This result might be confirmed by the mapping of the phase speeds associated to the CEOF modes (not shown here). In this case, the rotation method appears to be really interesting in so far as it allows us to discriminate amongst different physical phenomena. Concerning the ECMWF data, one can notice a rather good resemblance of the variance patterns associated to CEOF 1 and COEF 2 to the CLAUS variance patterns associated to CEOF 3 and CEOF 1 respectively, even if the ECMWF CEOF 1 variance is relatively too large (that is too much variance over the Atlantic for the ECMWF OLR). However, there is a lack of variance in the ECMWF data over the Sahel (CLAUS CEOF 1), and particularly over the south of Sudan and the western part of equatorial Africa (respectively CLAUS CEOF 2 and CEOF 4); moreover, the ECMWF data present an excess of variance over the south of Chad (ECMWF CEOF 4, which corresponds in the STS analysis to westward travelling phenomena).

Figure 24 shows the time series of the Complex Principal Component (CPC) modulus (which gives the time amplitude modulation) for the ECMWF CEOF modes 2 and 1, and for the CLAUS CEOF modes 1 and 3; these couples of modes have been chosen because of their resemblance, as mentioned above. Intraseasonal variability appears in these time series, with a more regular period (of around 30 days) for the first couple of CPCs, corresponding to the continental and close to the coast AEW mode. It is worth to note that the previous STS analysis showed variance maxima in the 20 to 60-day band over the regions concerned by these two modes, indicating a link between this intraseasonal variability and the intraseasonal modulation of the synoptic activity. Unfortunately, the time phase of this intraseasonal modulation is not very well reproduced by the ECMWF reanalysis compared to the CLAUS dataset (our reference), especially for the second couple of CPCs.

Further to the work already done using a global (over the all season) perspective (work described above), we have investigated the space-time variability of the two datasets using a local perspective. First, we have looked at a particular time period of the season characterised by the propagation of an African Easterly Wave (AEW) associated during part of its life cycle to an intense convective system. Second, we have started to apply a Moving Complex Empirical Orthogonal Function (MCEOF) analysis. First, we have looked specifically at the period starting August 17th 1992 to August 25th, period of time during which an AEW crossed Africa from the East to the West between 10°N and 15°N. Our goal was to check if we will notice the same discrepancies between the CLAUS BT

dataset and the ECMWF OLR dataset than those that appeared using the global perspective; we were also willing to relate the convection traced with the help of the BT or the OLR to the wind field in order to try to understand these discrepancies. Figure 25 shows the CLAUS BT field superimposed on the wind at 700 hPa from the ECMWF ERA dataset (top) together with the ECMWF OLR field superimposed on the same wind field (bottom) for August 21st at 12Z (August 17th at 18Z and August 21st at 18Z are not shown). An AEW clearly appears the 17th of August at 18Z with a cyclonic circulation centred on the border between Chad and Sudan followed by an anticyclonic circulation. Associated to this AEW, the ECMWF OLR field presents a local minimum (that is a signature of deep convection) in the centre of the cyclonic circulation that does not exist in the CLAUS BT field. This particular event illustrates one of the discrepancies that we have noticed in the global perspective study, that is the fact that the ECMWF OLR field is characterised by westward travelling variance over Sudan and Chad, which does not exist in the CLAUS BT field. On the 21st of August, the cyclonic circulation of the AEW is located over the eastern part of Nigeria. At 12Z, the ECMWF OLR field presents a local minimum located one more time in the centre of the cyclonic circulation that does not exist in the CLAUS BT field. At 18Z, the local minimum of the ECMWF OLR field is still located at the latitude of the cyclonic circulation but ahead (East) of its centre, whereas the CLAUS BT field shows a local minimum in the North-East of the cyclonic circulation. What happens on the 21st of August illustrates another discrepancy that we have noticed in the global perspective study, that is the fact that the ECMWF OLR field is characterised by a lack of westward travelling variance North of 12°N over the Sahel. Furthermore, there is an indication that the convection is triggered too early in the ECMWF model (see Figure 25); this specific defect of the GCM has been pointed out by other participants of the CLAUS project. Finally, it appears that the two discrepancies illustrated by this particular event seem to be related to the fact that the ECMWF GCM tends to produce convection which is unrealistically located too close to the centre of the cyclonic circulation of the AEWs over our region of interest. A modification of the convective scheme closure assumption is being tested in the frame of another UE project (WAMP) in order to tackle this problem, while a modification of the convective scheme triggering assumption is also being tested in order to remedy the diurnal phase discrepancy.

Second, we have developed a Moving Complex Empirical Orthogonal Function (MCEOF) software using our CEOF software already used and a Gaussian window in order to localise the signal. Then, after some validations, we have applied the software to the 92 CLAUS dataset. As an example, we have extracted using the MCEOF analysis the Local Modes over a period beginning the 8th of September and ending the 14th of September. This period is characterised by a synoptic wave that grows on the western part of the African continent and propagates over the Atlantic. As expected the patterns of the Local modes (sampled every 24 hours) clearly show this behaviour. Interestingly, the space phase field catches the propagation in the behaviour of the isophase lines over regions of large mode values. This result is shown on Figure 26, where one can see the local modes at the beginning (top), in the middle (middle) and at the end (bottom) of the previous period. The variance isolines indicate the intensity of the phenomena that is strongest at the beginning of the period while the intensity decays at the end over the Atlantic Ocean. The arrows indicate the phase speed of the Local Modes and always

show a westward propagation of some meters per seconds. A development of a clustering method of the modes is in progress in order to get the life cycle of the waves and to be able to deeply study the growing, mature and decaying stages of such phenomena.

Finally, we have carried out seasonal simulations using ARPEGE-climat (Meteo-France climate GCM) for the 1992 monsoon season, one control simulation and another simulation where we have just changed the closure assumption of the convection scheme (a CAPE closure has been taken into account, instead of a Moisture Convergence (MC-closure). A Space-Time Spectral Analysis (STSA) has been performed on both daily OLR and precipitation fields. Those fields have been chosen as proxy fields in order to investigate the space-time variability of convection. Moreover, we are able to compare the simulated OLR variability to that of the observed OLR derived from the CLAUS dataset. The first results are the following. We have noticed a significant reduction of the OLR variance in the 3 to 5 day band in the CAPE simulation versus the MC one; this reduction gives a variance intensity which seems to be in accordance with that of the observed OLR field; this means that the convection is less coupled to the AEWs for the CAPE closure compared to the MC closure.

More work needs to be done in order increase the number of the simulated seasons and to diagnose more precisely the nature of the differences of the two simulations in terms of convection variability. We need also to use a secondary variable computed from the brightness temperature itself, such as the high cloud cloudiness to better assess the quality and the failure of the simulations versus the observation, following the work done at CNRM/GMGEC/UDC, described in a previous paragraph.

In conclusion, the results obtained on the West Pacific have shown that the set of statistical methods used is appropriate to quantify the space-time variability of the brightness temperature, even at the relatively high resolution used here. Second, it has been shown that this region was characterised during January 1984, in the synoptic scale, by westward propagating convective systems along 10°S that tend to change their direction of propagation toward the east at 175°E, along 20°S. Concerning the work done on the 1992 West African monsoon, it has been shown that the convection is characterised by 4 main modes of variability. Two modes correspond to westward propagating convective systems (associated to African Easterly Waves), with variance maxima located along 10°N over the continent east of 0° and over the Atlantic; the two other modes correspond to standing convective systems, with variance maxima located over the southern Sudan and over the north-western Zaire. The time evolution of the two former modes is characterised by an intraseasonal modulation. The same analysis done with the ECMWF simulated OLR (short-range forecasts from the reanalysis dataset) has shown that the ECMWF model tends to exaggerate the coupling between the AEWs and the convection. A preliminary study seems to indicate that the use of a CAPE closure in the convective scheme, instead of the moisture convergence closure tends to remedy that discrepancy for seasonal simulations carried out with the CNRM GCM.

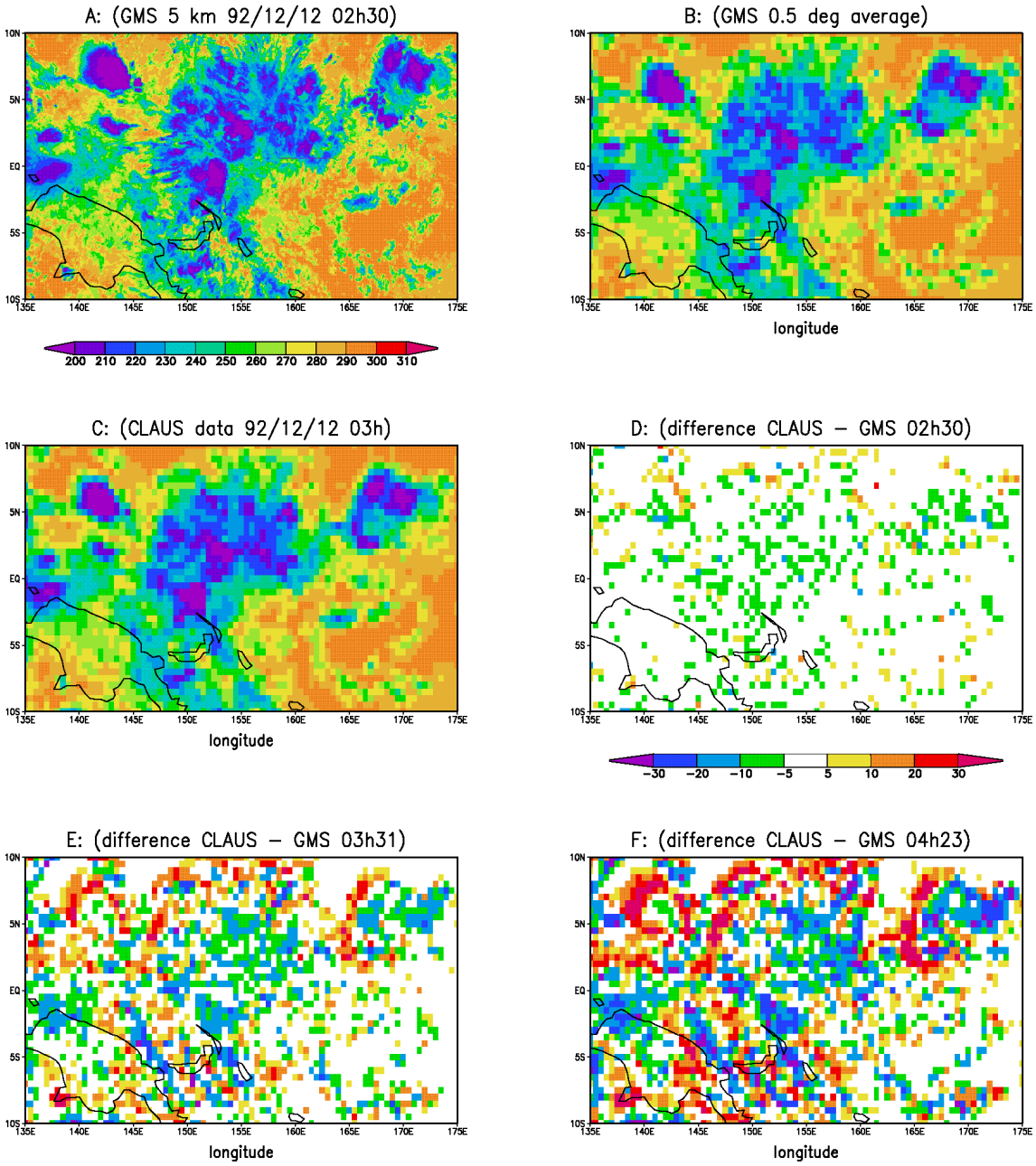

Figure 1: Window brightness temperature (WBT) over the TOGA-COARE region as observed from GMS and in the CLAUS dataset for 12 December 1992: **a**: GMS fine resolution 5 km image at 02h30 as stored in the TOGA-COARE database. **b**: Image obtained by averaging the WBT in the previous image over 0.5° latitude-Longitude boxes. **c**: WBT over a 0.5° grid from the CLAUS dataset for target time 03h00. **d**: Difference between CLAUS and GMS temperatures (image (c) minus image (b)). **e**: Difference between CLAUS (03h00) and the next GMS 0.5° averaged image at 03h31. **f**: Difference between CLAUS (03h00) and the following GMS image at 04h23. The colour scales are shown under image A for WBT, and image D for the difference and apply also to the following two images.

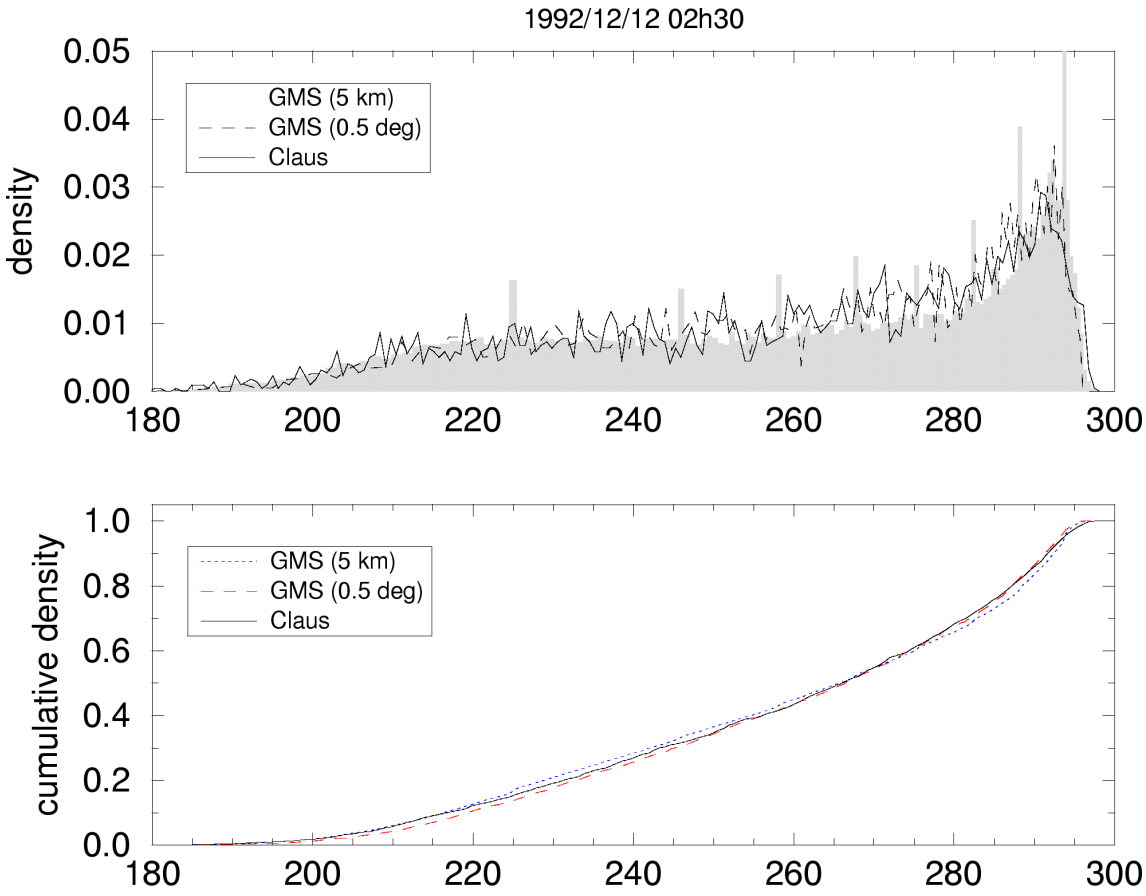

Figure 2: Histograms: (**a: top**) and cumulative histogram (**b: bottom**) of the brightness temperatures from Figures 1a-c. The histogram from Figure 1a (5 km GMS) is shown in a grey shading or dotted line, those of Figure 1b (0.5° averaged GMS) as a dashed line, and those of Fig 1c (CLAUS) as a solid line. The density in the histogram has been normalised by dividing the frequency in each interval by the width of the interval, and is expressed in K^{-1}.

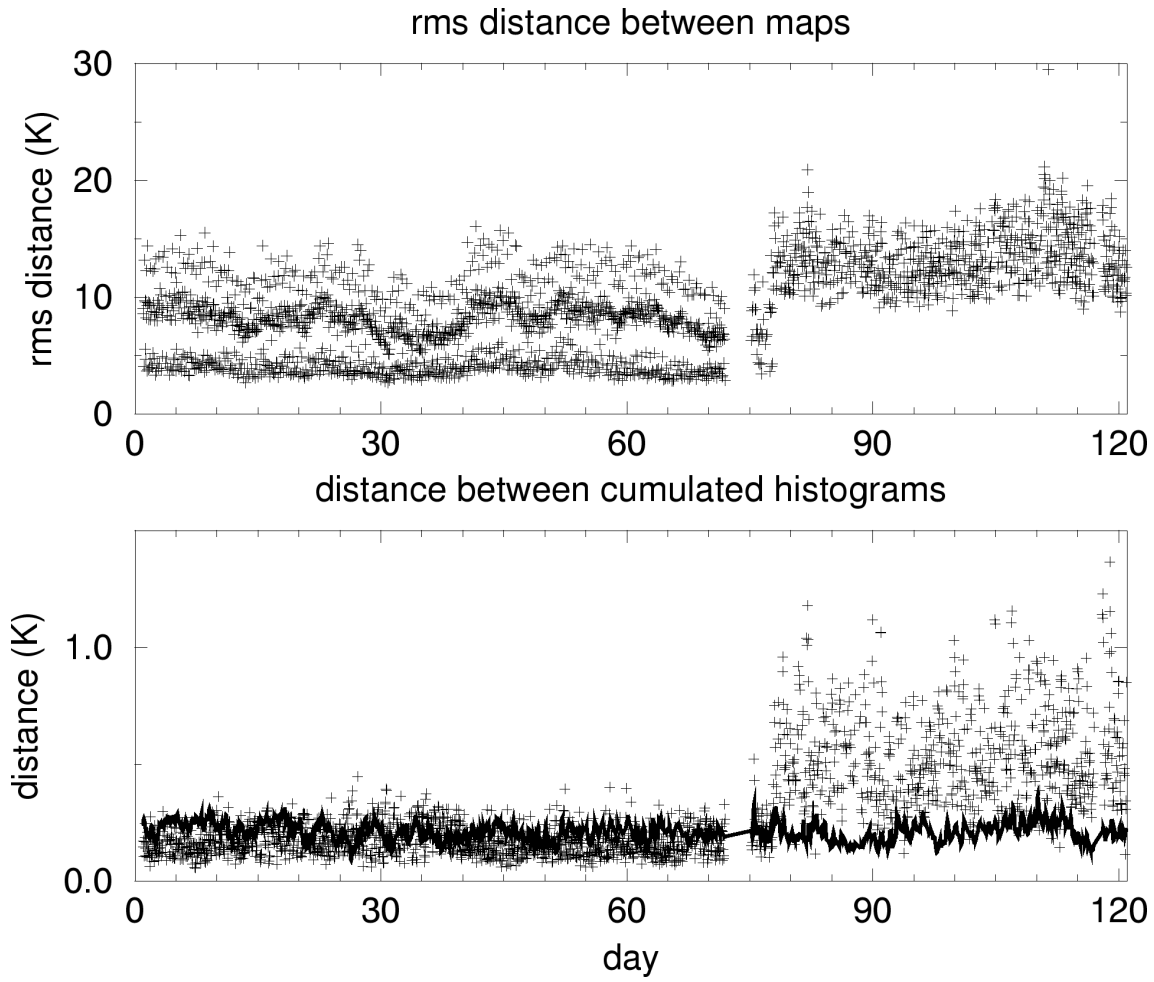

Figure 3: Evolution as a function of time of the distance (in K) between the GMS data and the closest in time CLAUS image. The time is indicated in days with day 1 representing 1 November 1992. Top: RMS distance between the 0.5° averaged GMS and CLAUS data (crosses). Bottom: distance between cumulated histograms (as defined in text). The solid line represents the distance between the GMS histogram at 5 km resolution and the histogram of the 0.5° averaged GMS grids. The crosses are for the distance of the 5 km histogram with the CLAUS histogram. (The empty area between days 73 -75 is due to missing GMS images in the TOGA-COARE database).

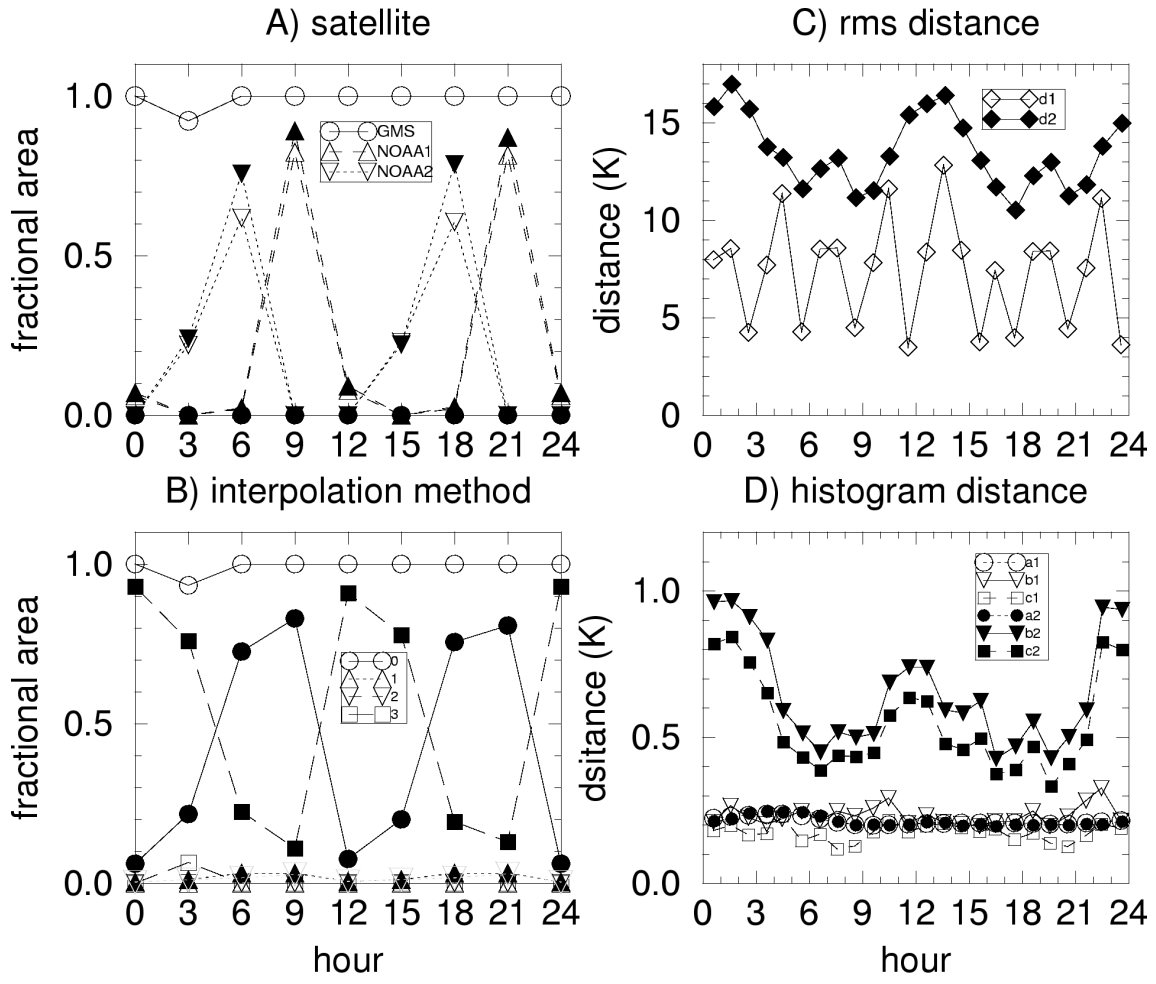

Figure 4: Diurnal variation (as a function of the hour in universal time) computed over period 1 (empty symbols) and period 2 (filled symbols). **a**: fractional area of the TOGA-COARE domain covered by different satellites used in the CLAUS interpolation (GMS : circles; NOAA-PM: triangle up; NOAA-AM: triangle down). **b**: fractional area of the domain in which the different interpolation methods have been used by the CLAUS algorithm (circle: method 0, primary spatial; triangle up: method 1, secondary spatial; triangle down: method 2, tertiary spatial; square: method 4, primary temporal). **c**: RMS distance (in K) between the 0.5° averaged GMS image and the nearest in time CLAUS image for period 1 (d1) and period 2 (d2). **d**: Histogram distances between GMS 5 km and 0.5° images (circles: a1 and a2), CLAUS and GMS 5 km (triangles down: b1 and b2); CLAUS and GMS 0.5° (squares: c1 and c2)

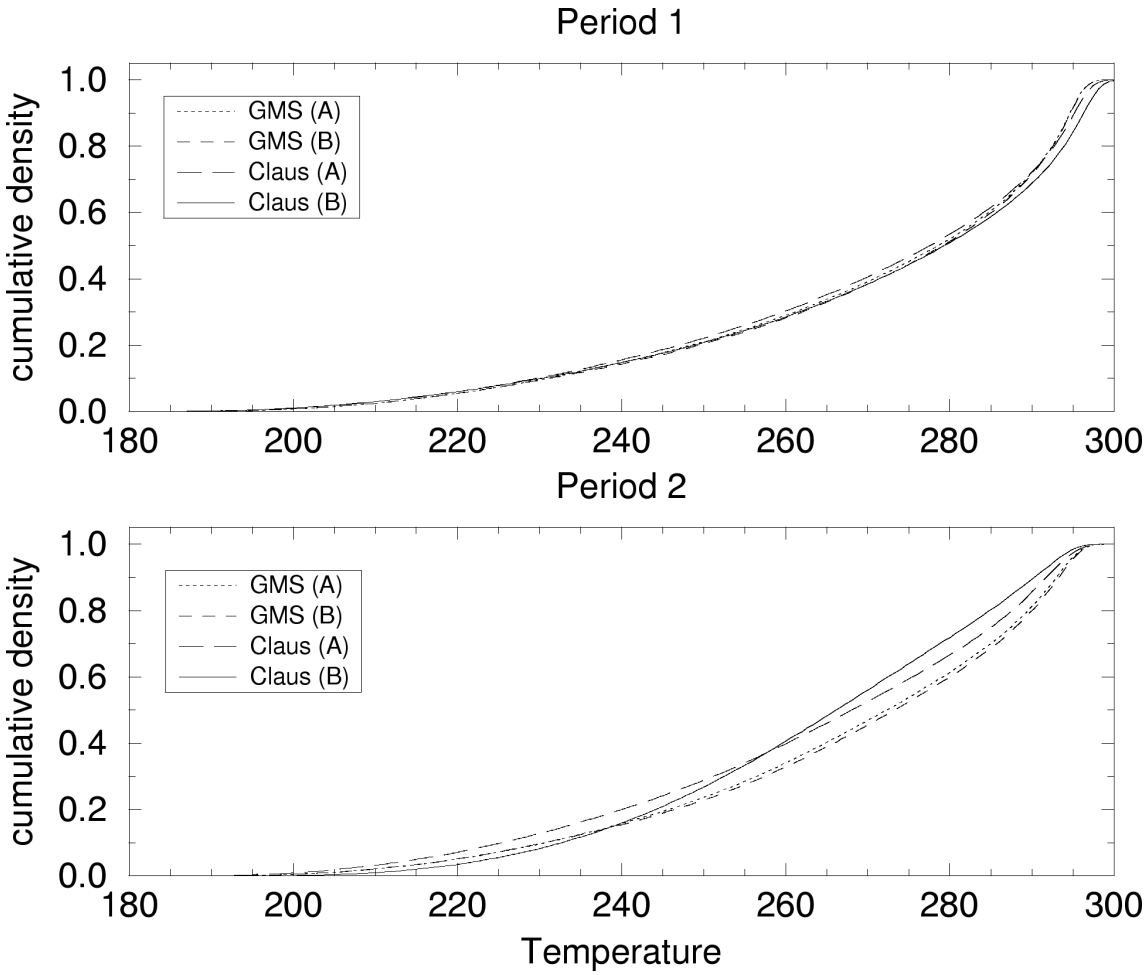

Figure 5: Cumulative histograms over period 1 (top) and period 2 (bottom). The GMS data on a 0.5° grid are represented by the dotted line. The CLAUS histograms have been computed separately over regions where the NOAA satellite data were available (CLAUS A: long-dashed line) and over regions without NOAA (CLAUS B: solid line). For period 1 in the curve CLAUS B corresponds to a spatial interpolation of the GMS satellite, while in period 2 in the absence of both GMS and NOAA it corresponds to a temporal interpolation method. The curve GMS D (short dashes) represents the histogram of the half sum of two GMS maps 6 hours apart to simulate the effect of a temporal interpolation.

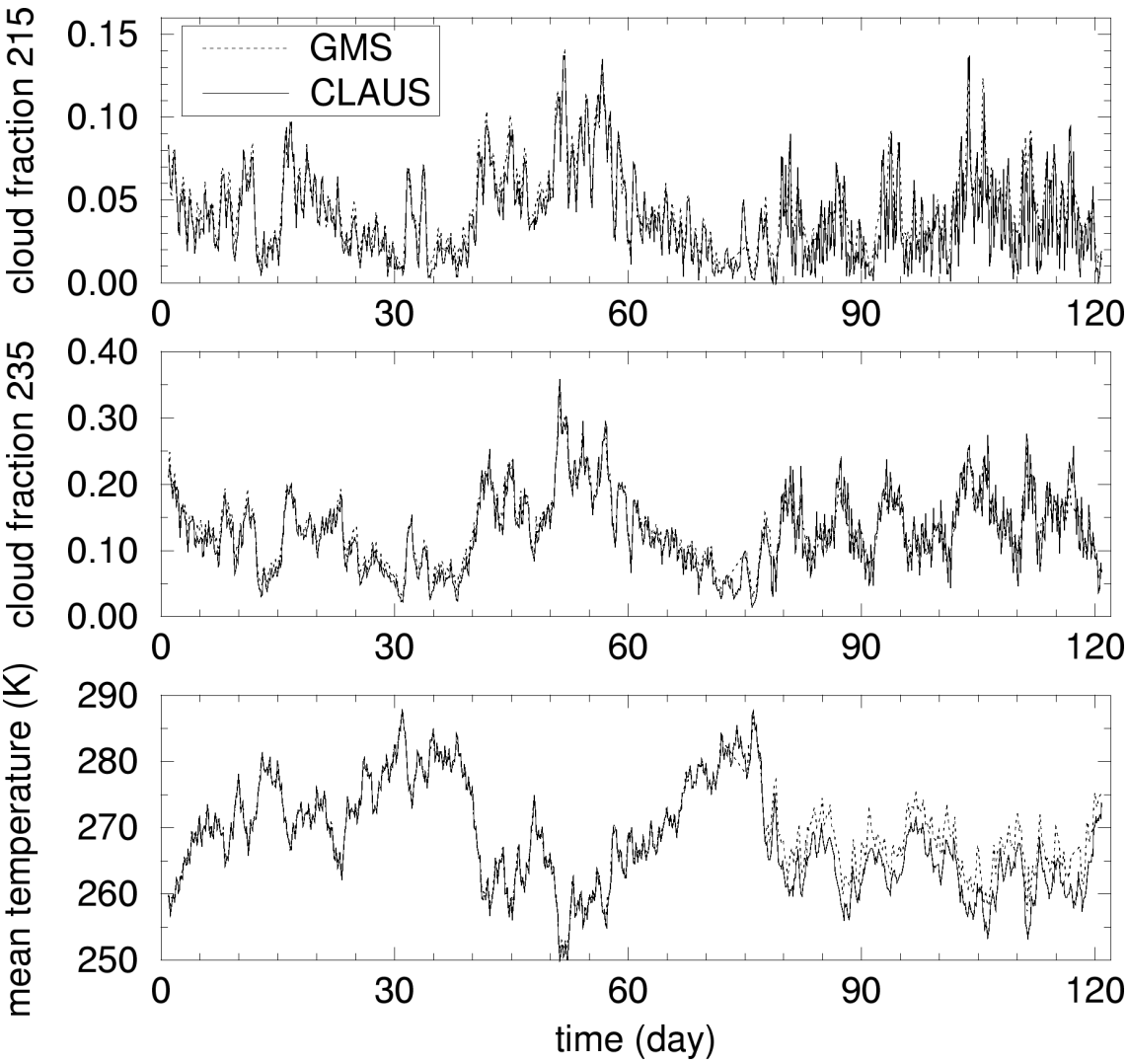

Figure 6: Time series of averages over the TOGA-COARE domain for CLAUS (solid line) and GMS (dotted line) data. **Bottom**: average brightness temperature (K). **Middle**: Fractional cover of clouds colder than 235 K. **Top**: Fractional cover of deep convective clouds colder than 215 K. Time is in days starting at 1 November 1992 (day 1). CLAUS data are given at three-hourly frequency, and GMS data at hourly frequency (except for a data gap between days 73-75)

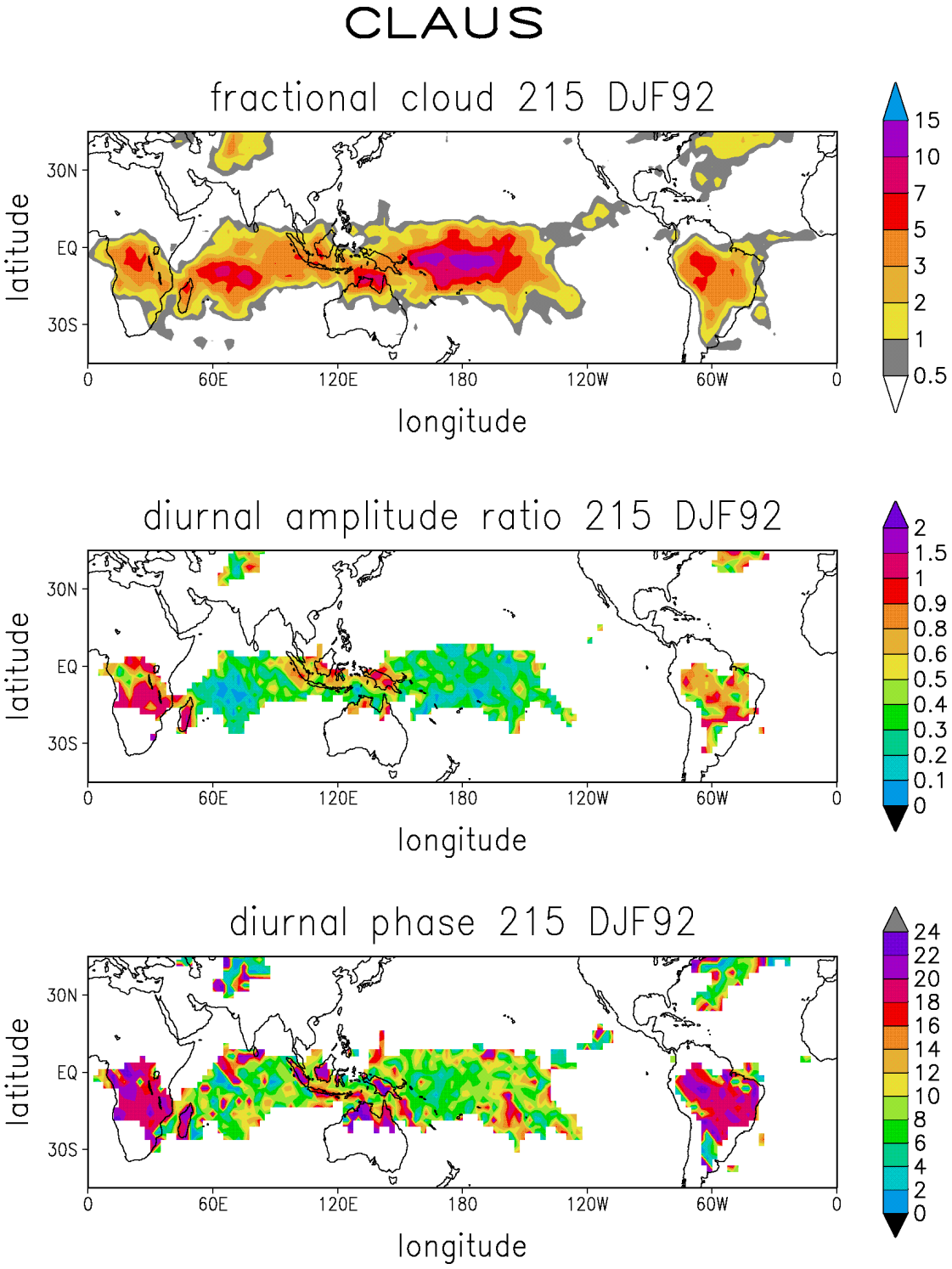

Figure 7: Geographical distribution of the diurnal variation of the fractional convective cloud cover with brightness temperature below 215 K for seasonal mean December-January-February 1992 computed from the CLAUS dataset. **Top**: daily averaged cloud fraction in %; **middle**: relative amplitude of the first harmonic of the diurnal cycle (amplitude of diurnal harmonic divided by mean cloud cover); **bottom**: phase in local time (hours) of the maximum of the first diurnal harmonic.

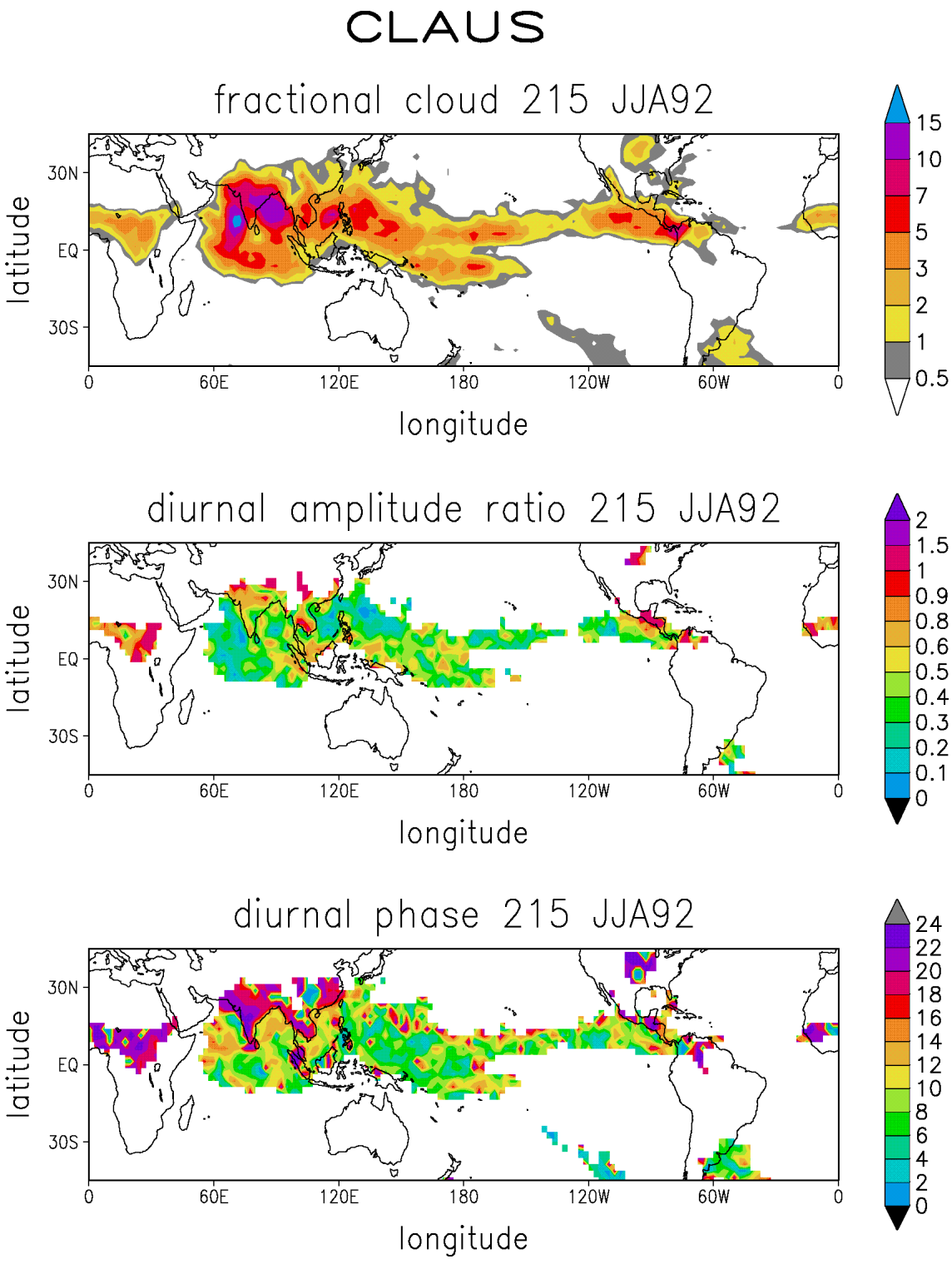

Figure 8: Same as Figure 7, but for seasonal mean June-July-August 1992

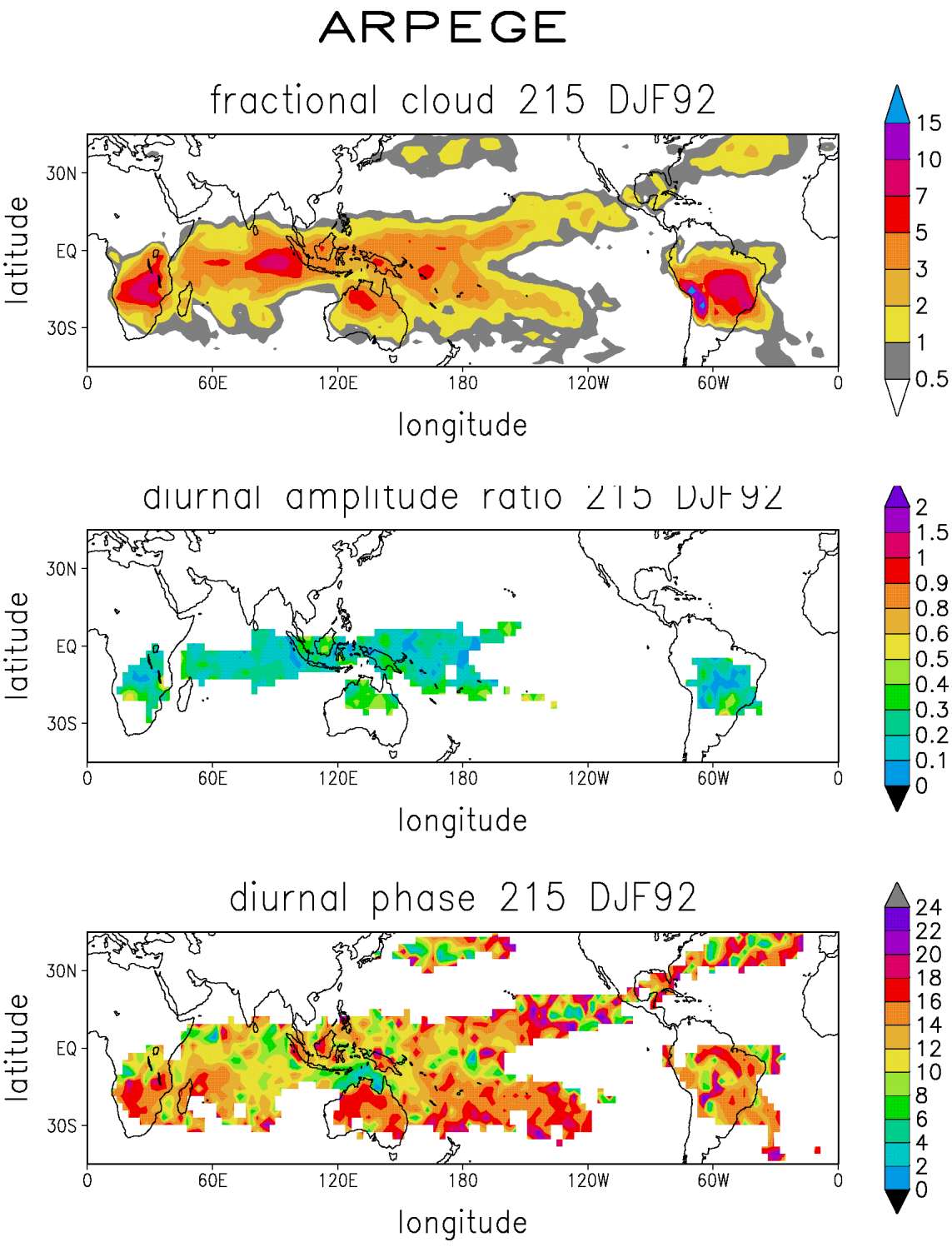

Figure 9: Same as Figure 7, but for the fractional convective cloud cover computed from the Arpege-Climat GCM simulation for DJF 1992

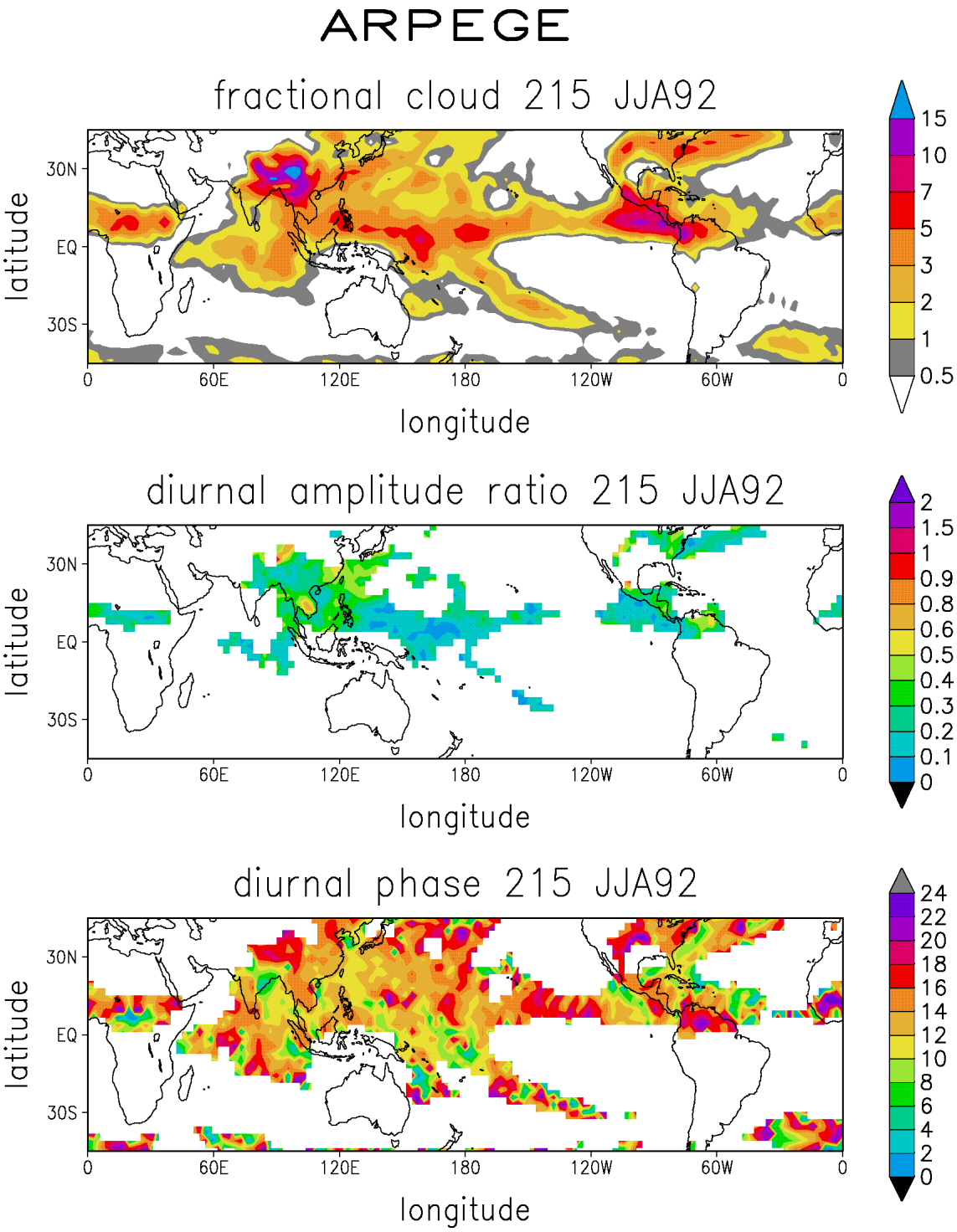

Figure 10: Same as Figure 8, but for the fractional convective cloud cover computed from the Arpege-Climat GCM simulation for JJA 1992.

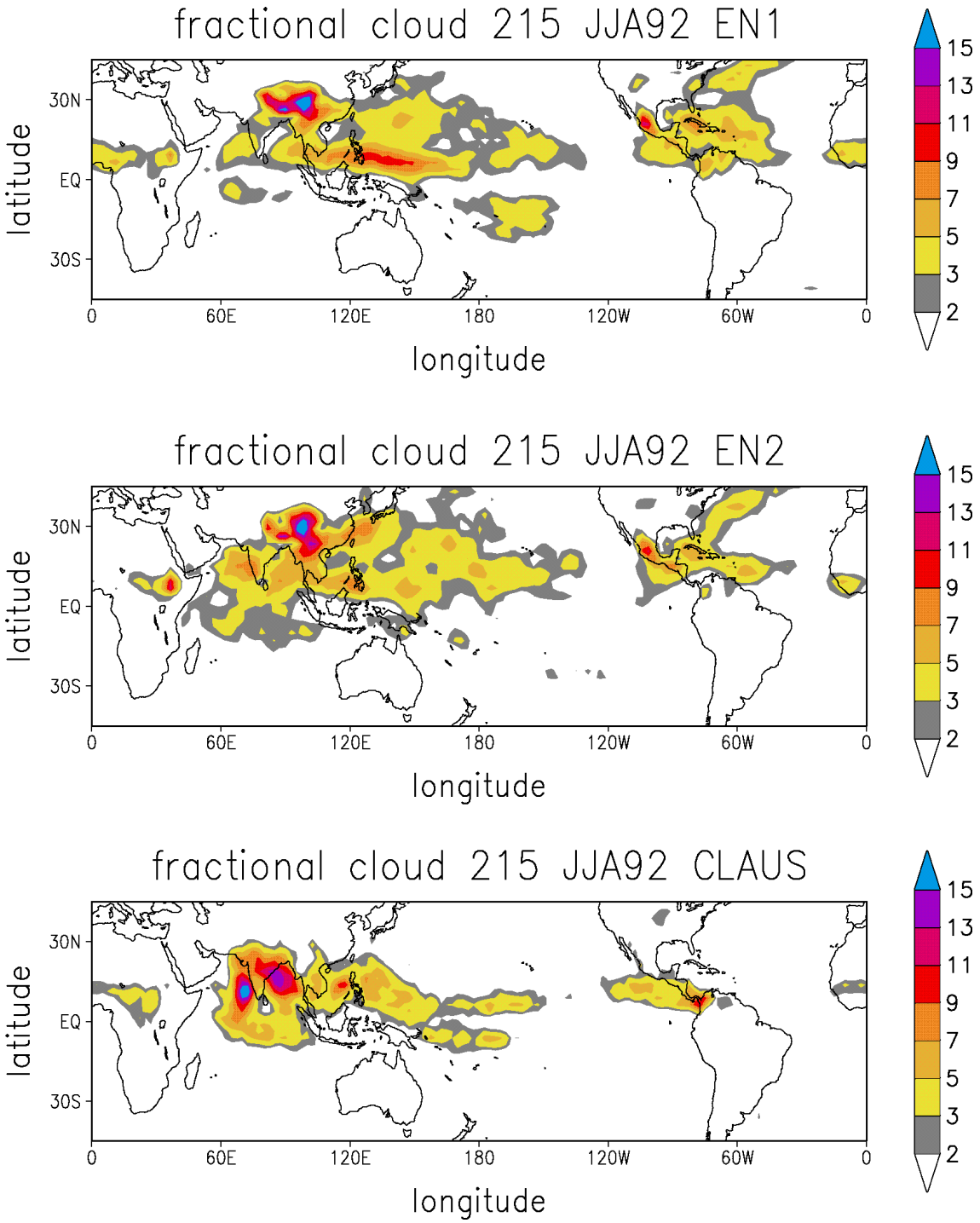

Figure 11: Geographical variation of the seasonal mean fractional cover (in %) of clouds colder than 215 K for the summer (JJA) 1992. **Top**: Arpege simulation EN1 with entrainment factor 0.125 and fixed BL height; **middle**: simulation EN2 with entrainment factor 0.185 and diagnostic BL height; **bottom**: computed from CLAUS dataset

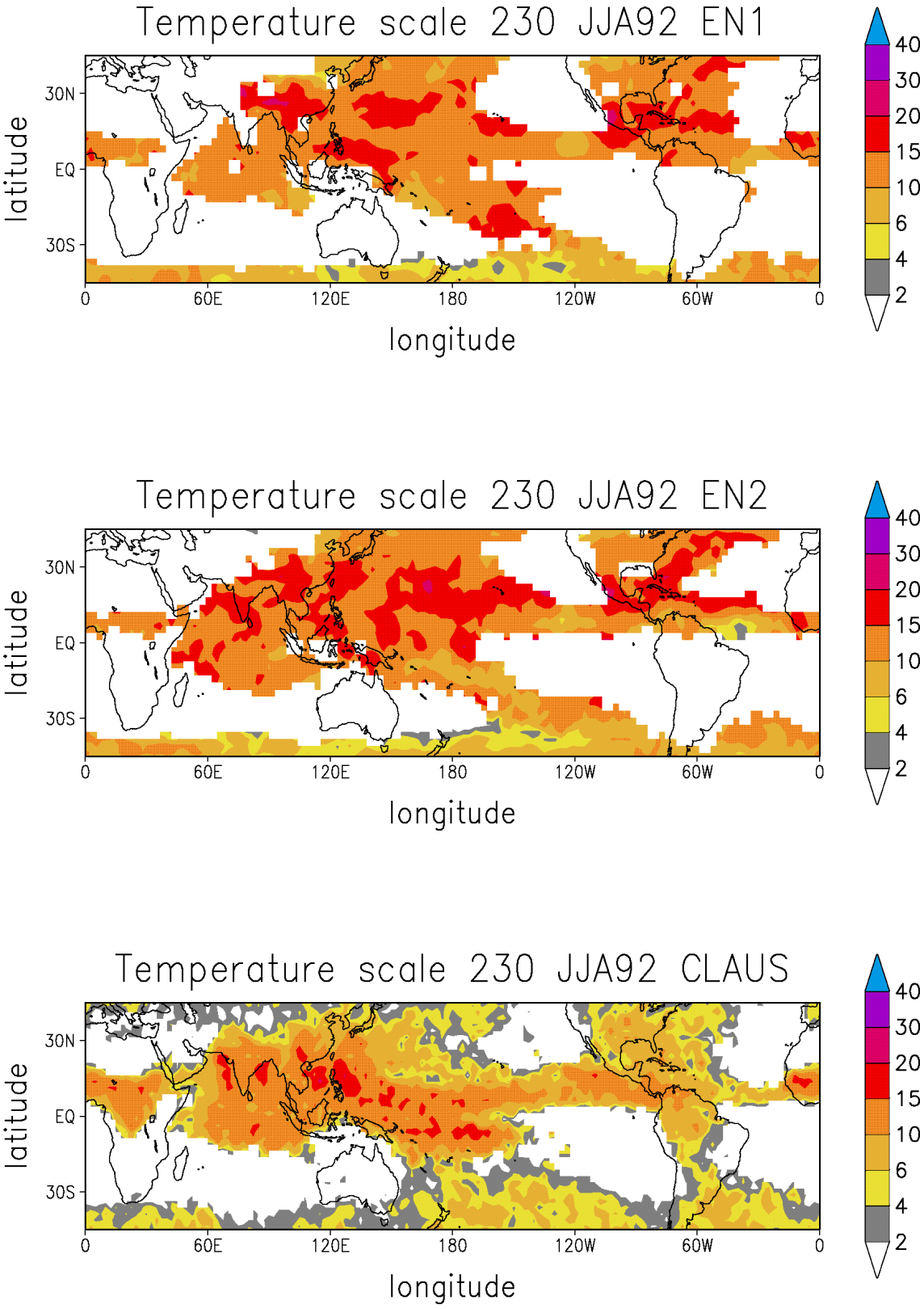

Figure 12: Geographical variation of the seasonal mean temperature scale (in K) of clouds colder than 230 K for the summer (JJA) 1992. **Top**: Arpege simulation EN1; **middle**: simulation EN2; **bottom**: computed from CLAUS dataset

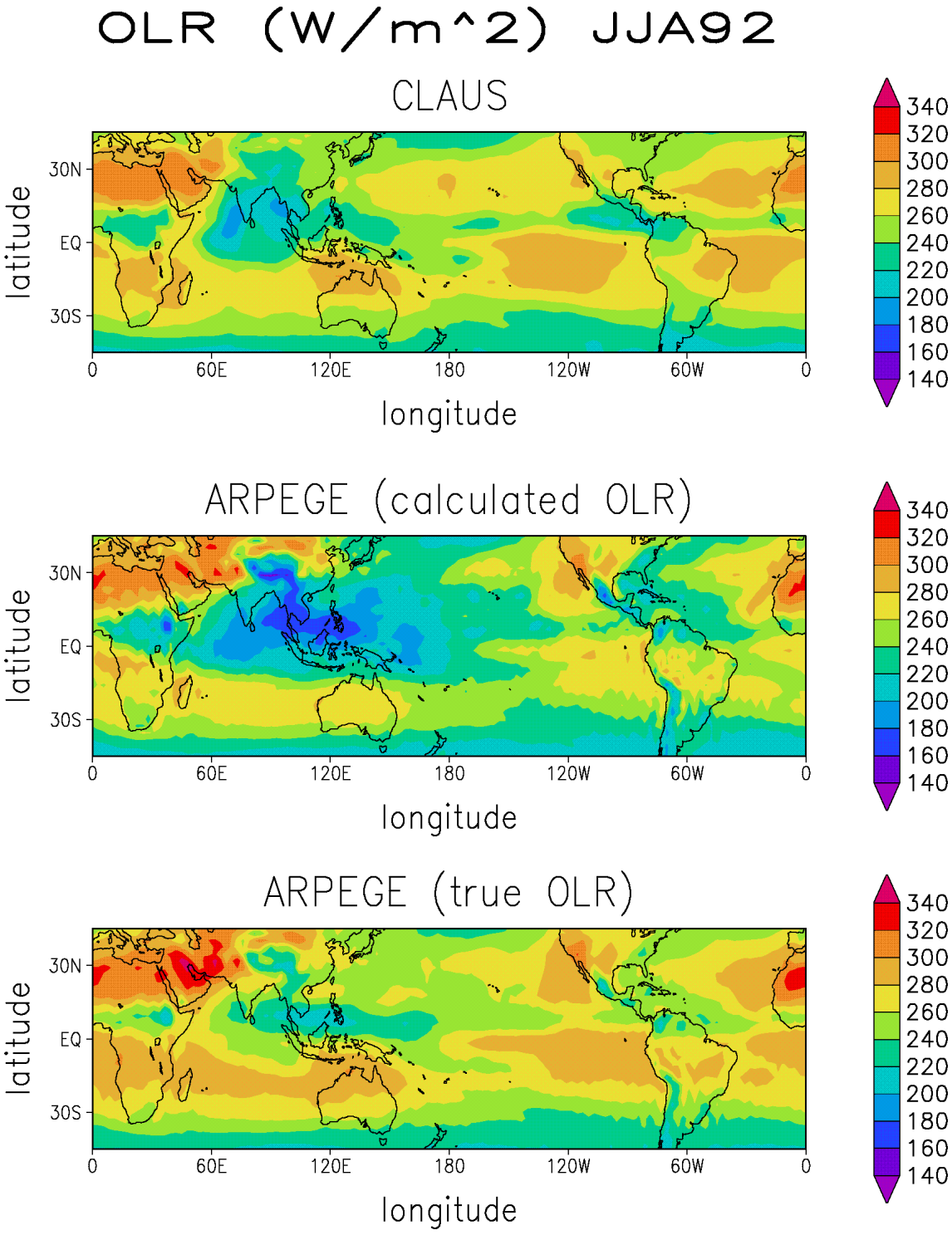

Figure 13: Comparison between the OLR (in W/m^2) for JJA 1992 reconstructed from CLAUS data (**top**), OLR reconstructed from the Arpege-Climat total cloud cover with the same method (**middle**) and the OLR simulated directly by the GCM (**bottom**).

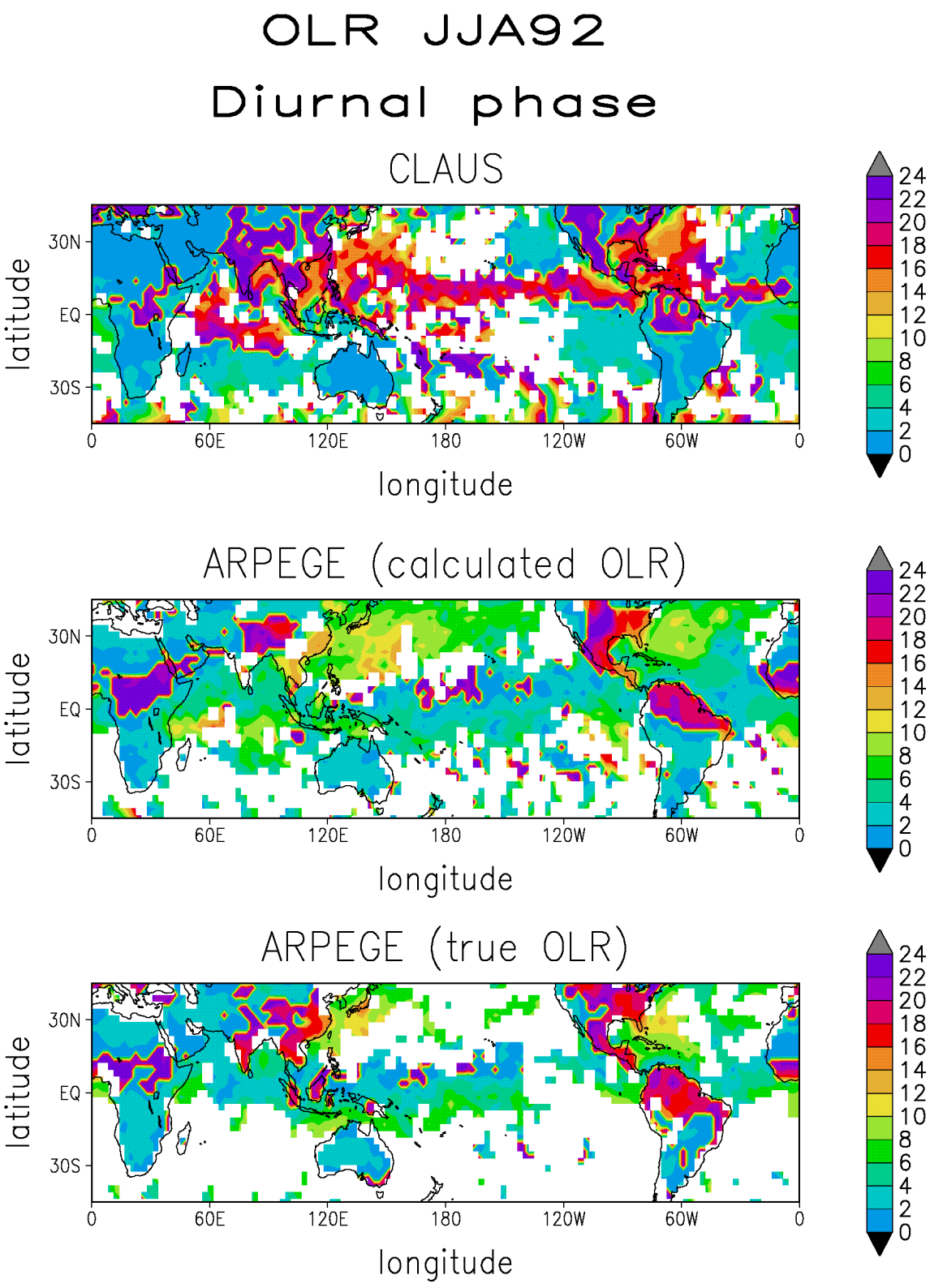

Figure 14: Phase of the first diurnal harmonic (hour of the minimum in local time) for the OLR of the previous figure (**top**: reconstructed from CLAUS data, **middle**: reconstructed from GCM total cloud cover, **bottom**: simulated by the GCM).

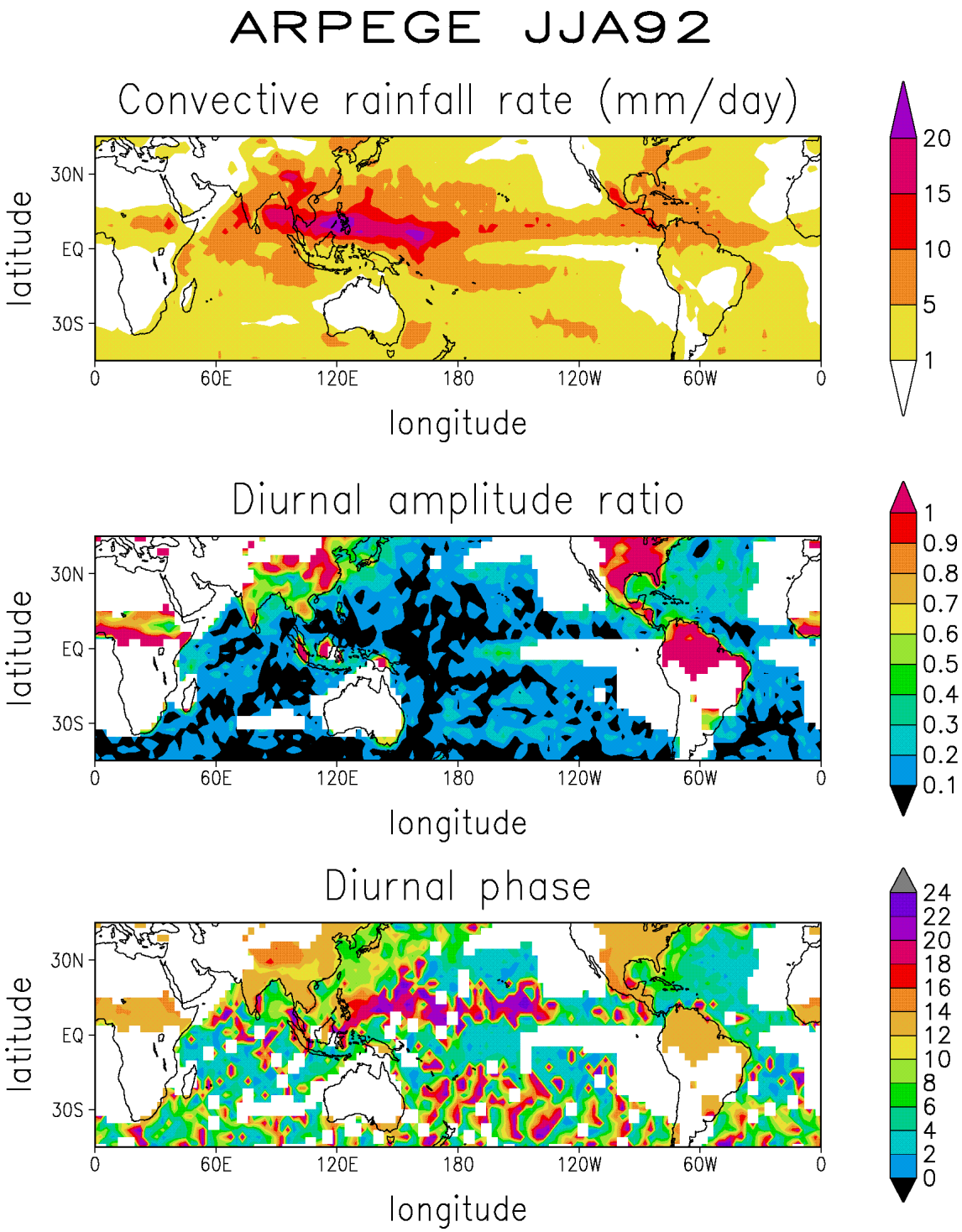

Figure 15: Mean convective rainfall for JJA 1992 simulated by the Arpege-Climat GCM (**top**: in mm/day), relative amplitude ratio (**middle**) and phase (**bottom**: hour of the maximum in local time) of the first harmonic of its diurnal cycle.

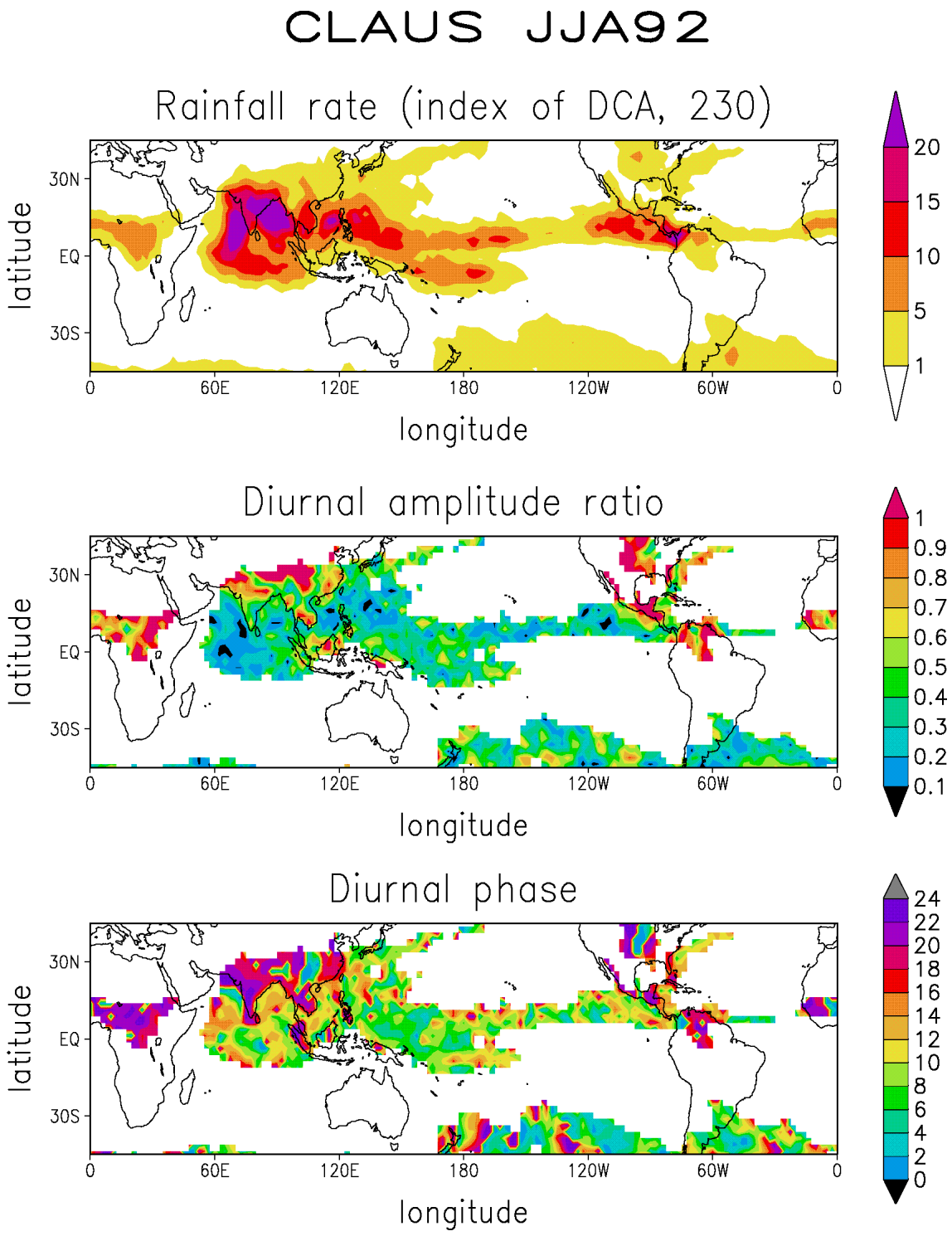

Figure 16 : Mean convective rainfall for JJA 1992 computed by applying the DCA index of Hendon and Woodberry to the CLAUS dataset (**top**: in mm/day), relative amplitude ratio (**middle**) and phase (**bottom**: hour of the maximum in local time) of the first harmonic of its diurnal cycle.

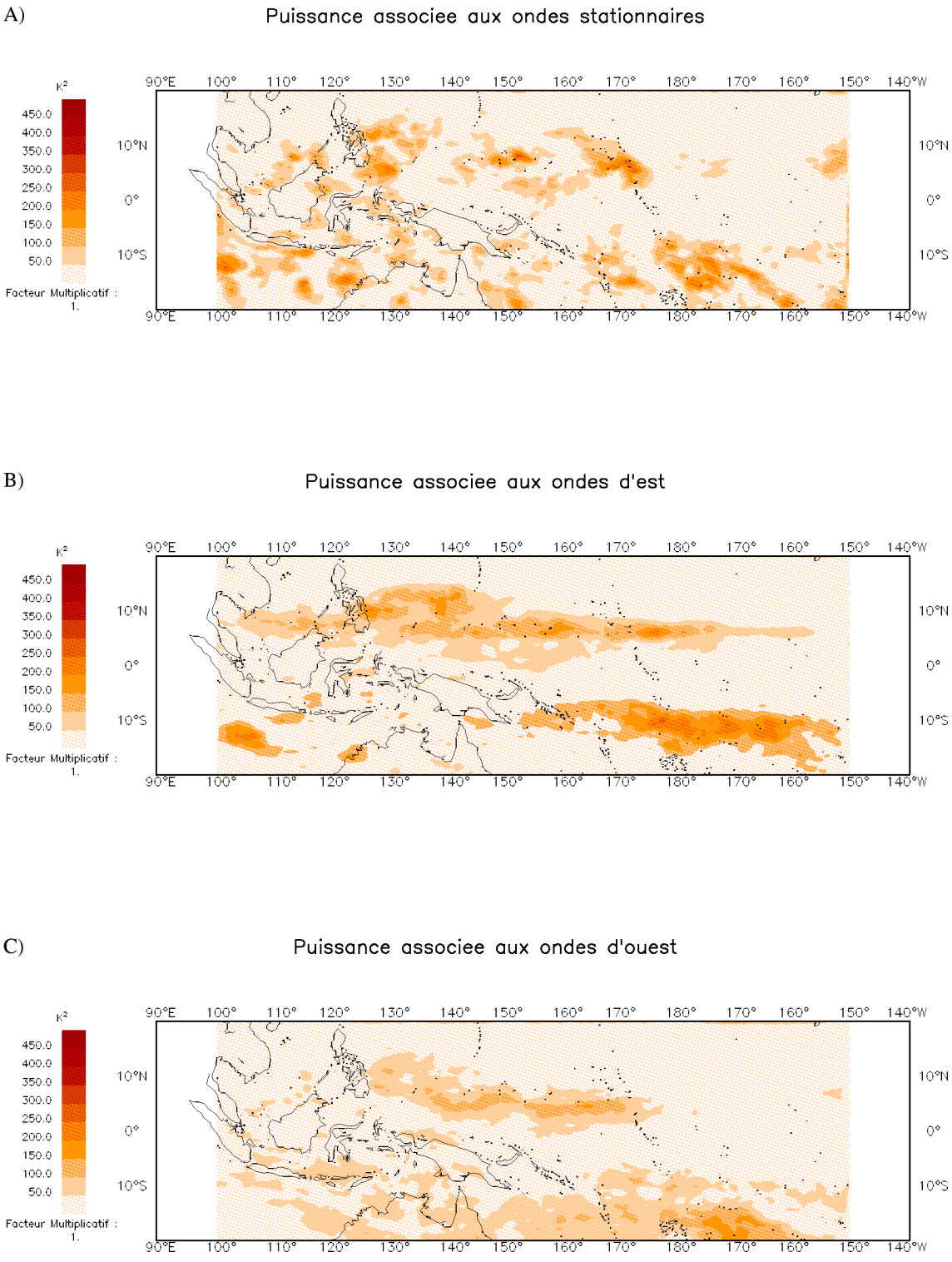

Figure 17: Brightness Temperature (BT) variance in the synoptic time band of standing (**a**), easterly (**b**) and westerly waves (**c**) for the West Pacific during January 1984.

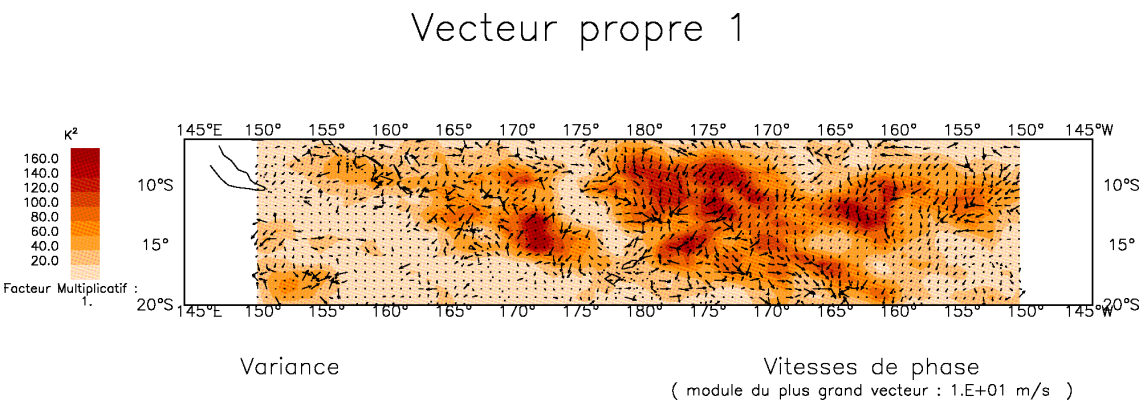

Figure 18: BT variance of the first eigenvector for the SE zone and associated phase speeds (small arrows).

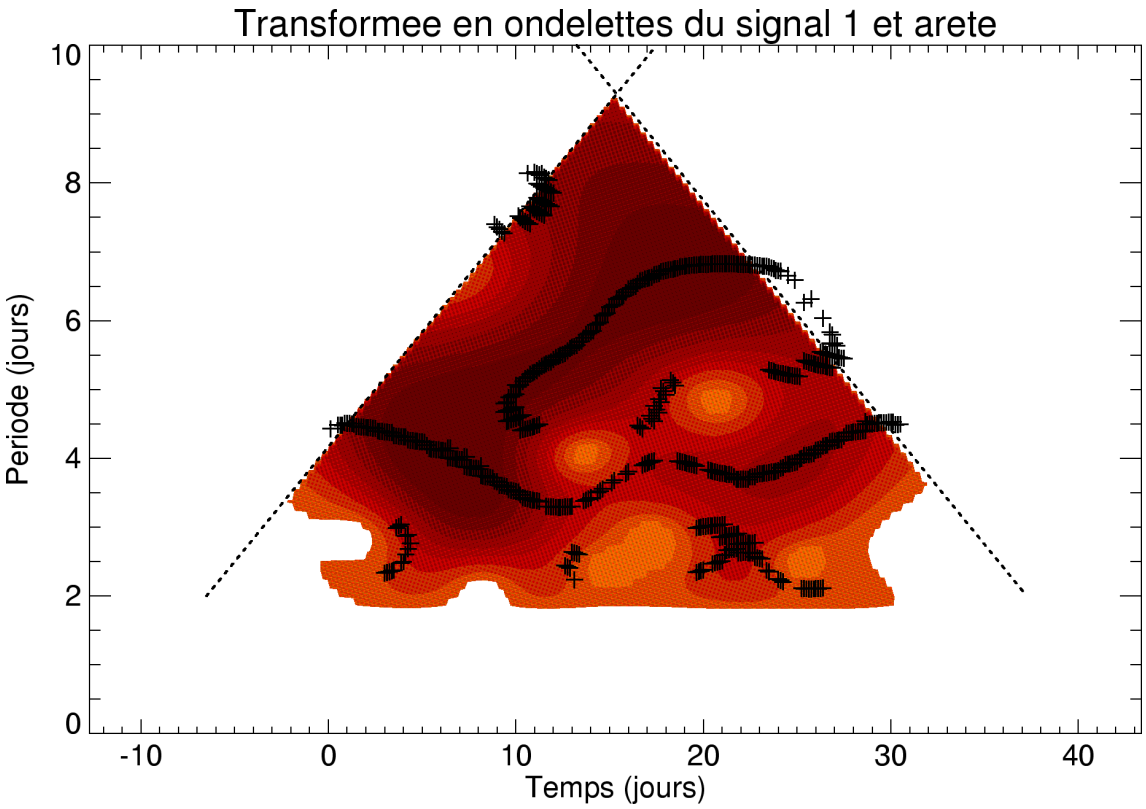

Figure 19: Wavelet analysis representing the variance of the first CPC for the SE zone as a function of time (horizontal axis) and period (vertical axis) in days.

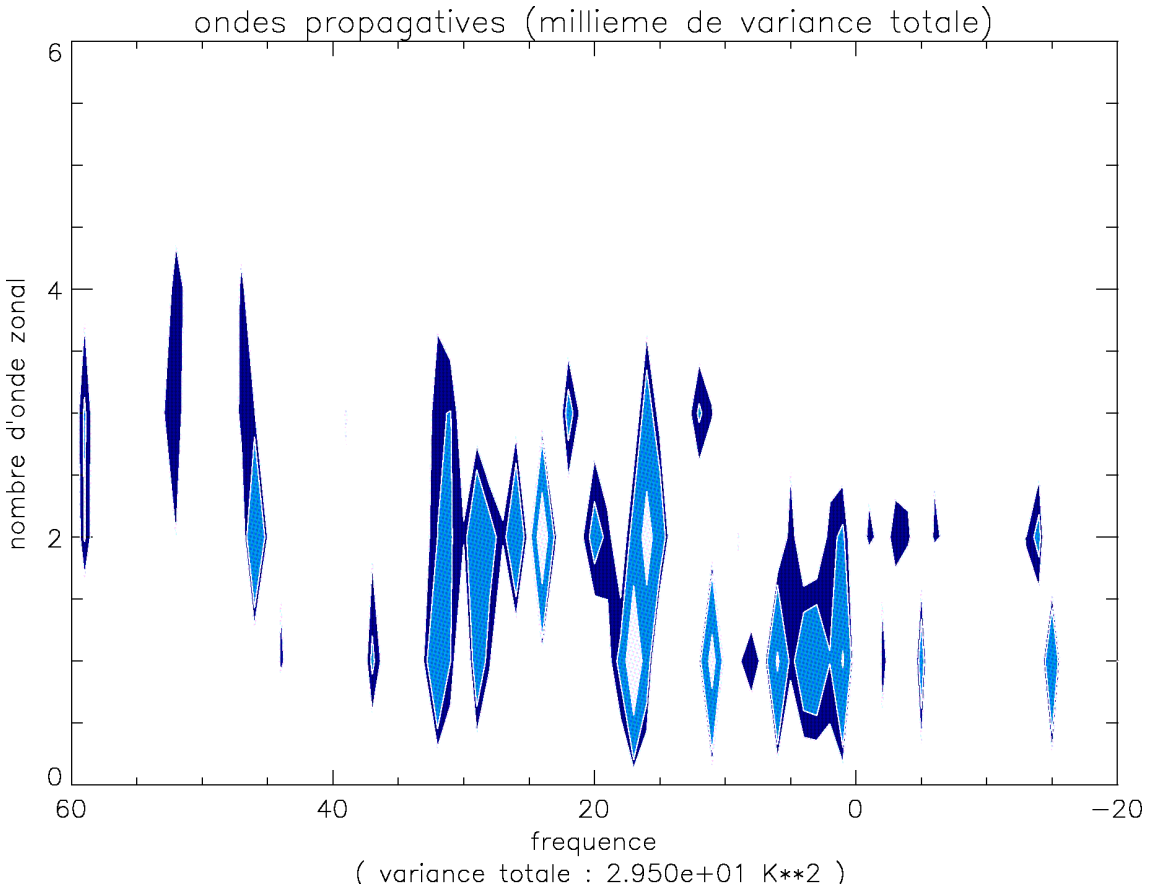

Figure 20: Space time spectra for travelling wave (power densities expressed in thousand of the total variance) for the CLAUS brightness temperature (**a: top**) and the ECMWF outgoing longwave radiation (**b: bottom**), for a West African domain during the 1992 monsoon season.

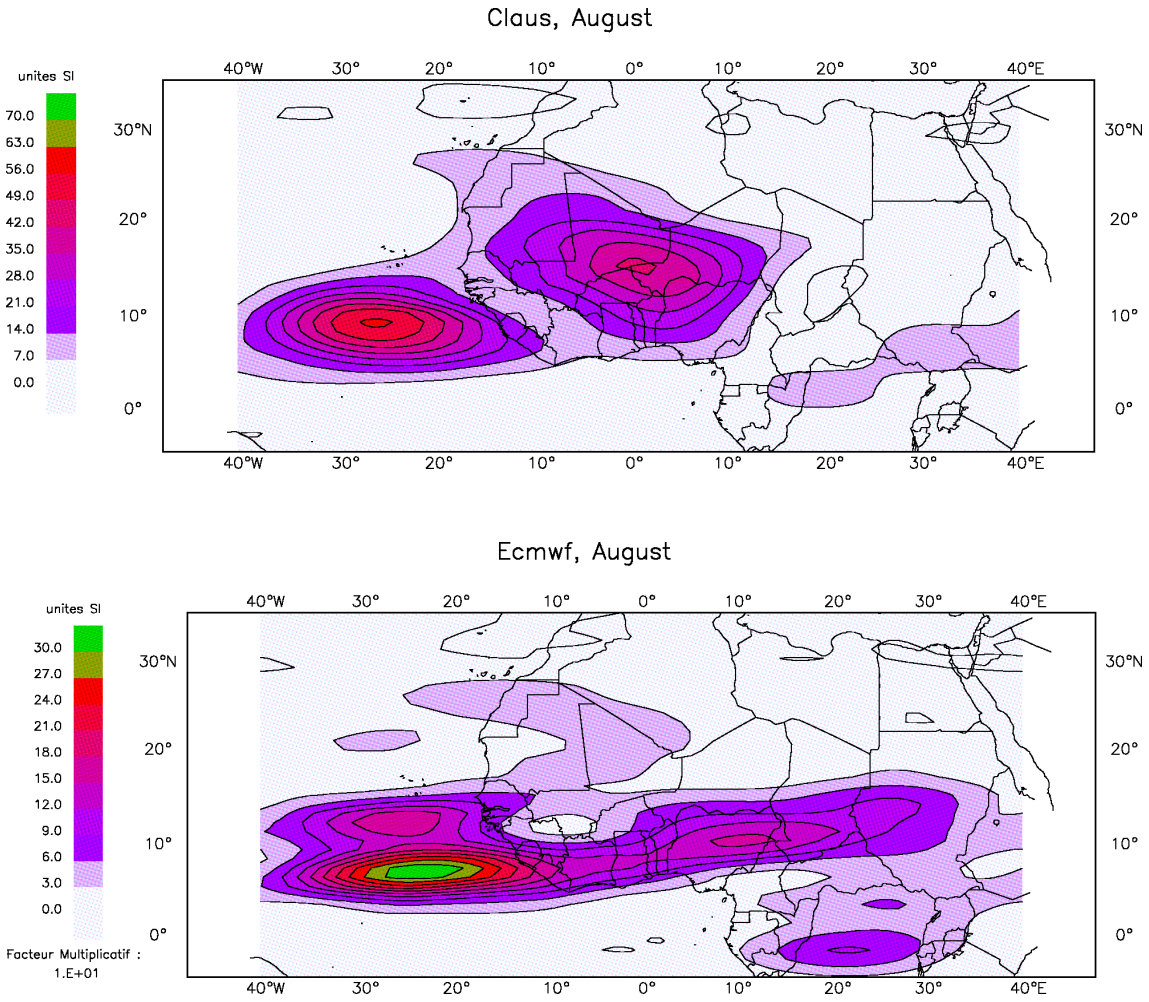

Figure 21: Eastward travelling wave variance for the 3-5 day time window of the CLAUS brightness temperature (A: top) and the ECMWF outgoing longwave radiation (B: bottom), for the month of August 1992.

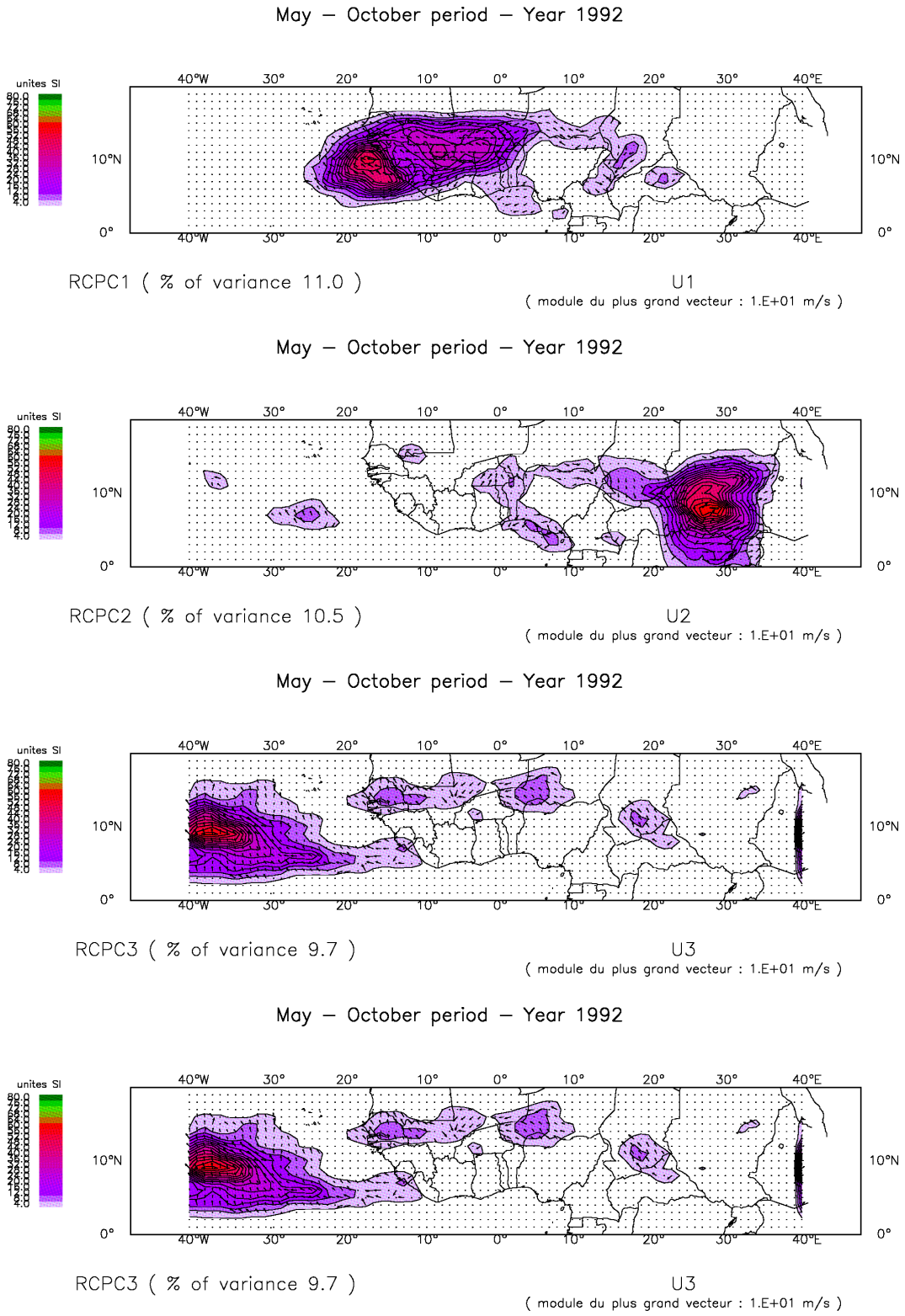

Figure 22: Time variance (May to October 1992) associated to the first four rotated CEOFs (A-D) of the CLAUS dataset (brightness temperature).

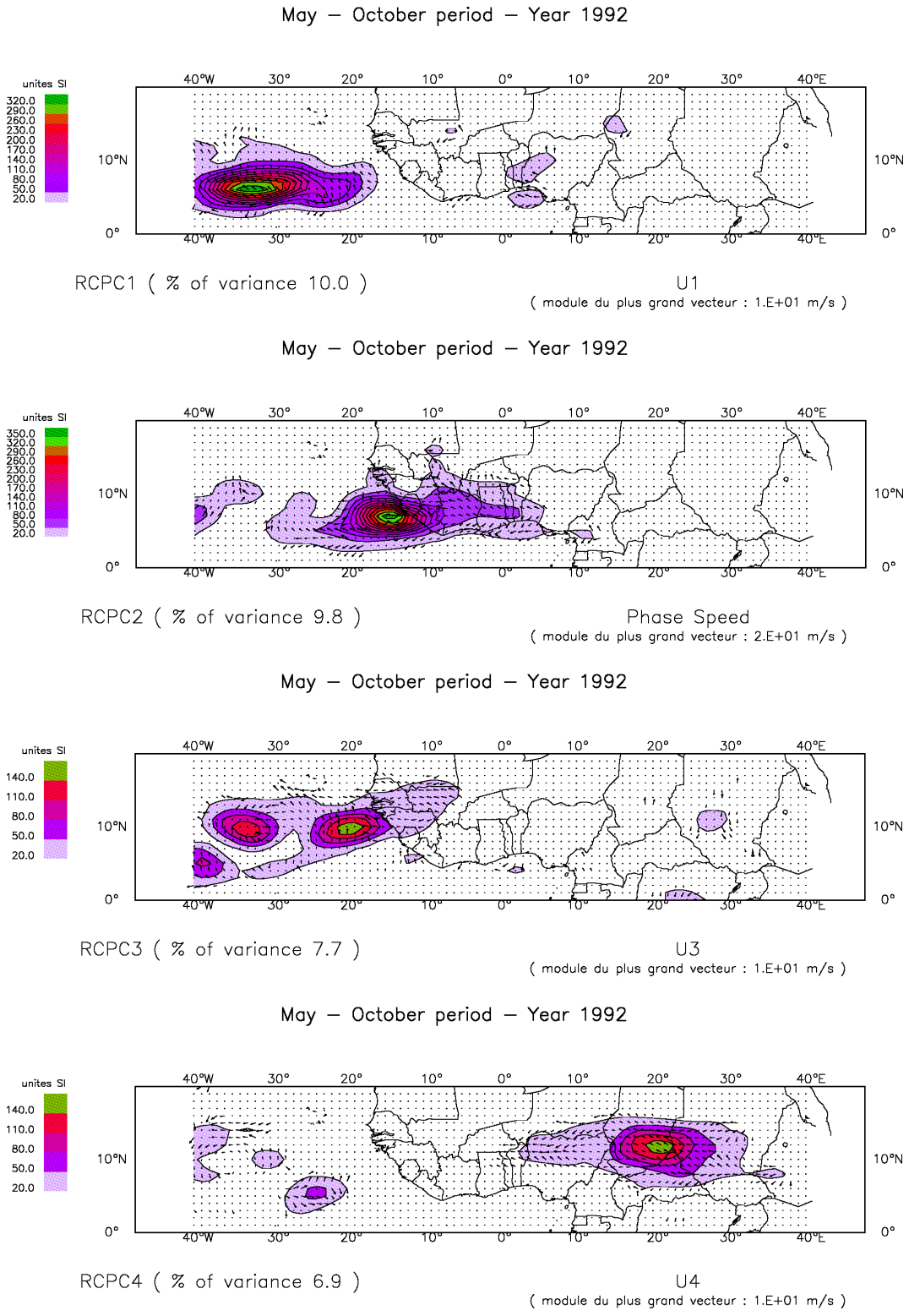

Figure 23: Same as Figure 22, but for the ECMWF dataset (OLR).

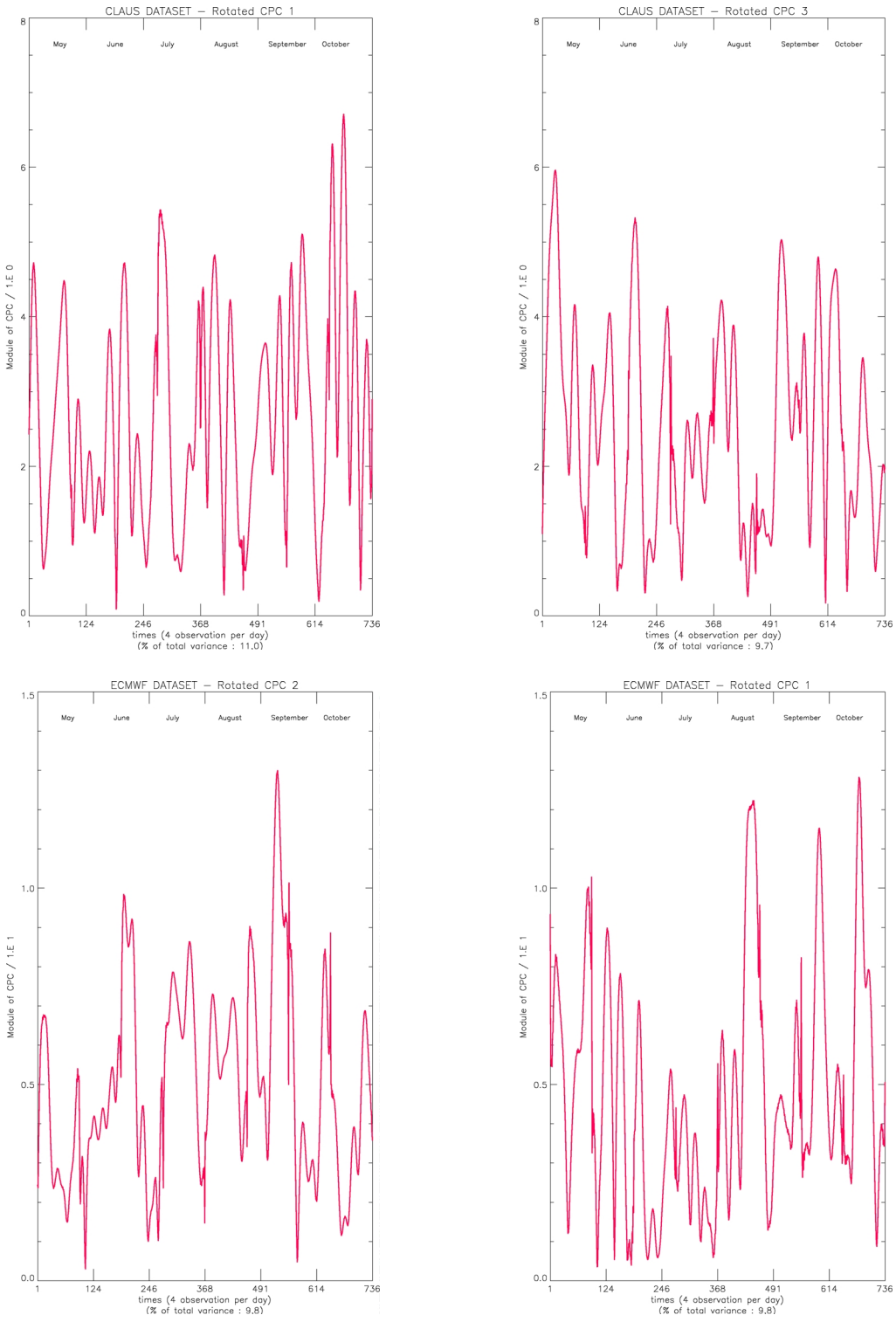

Figure 24: Time series of the Complex Principal Component (CPC) modulus (which gives the time amplitude modulation) for the CLAUS CEOF modes 1 (top left) and 3 (top right), and for the ECMWF CEOF modes 2 (bottom left) and 1 (bottom right).

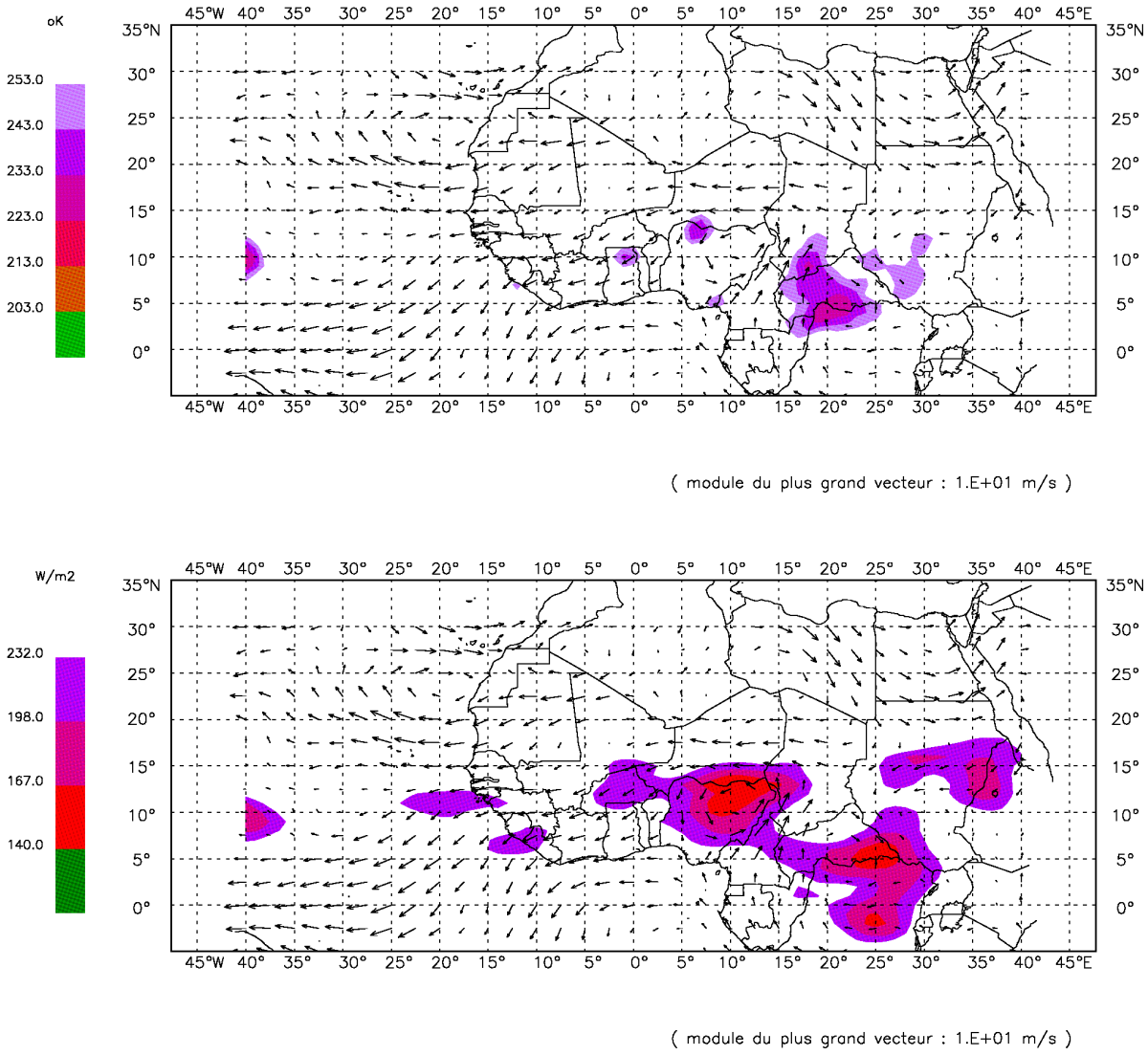

Figure 25: CLAUS BT field superimposed on the wind field at 700 hPa from the ECMWF ERA dataset (top) together with the ECMWF OLR field superimposed on the same wind field (bottom) for August 21st at 12Z.

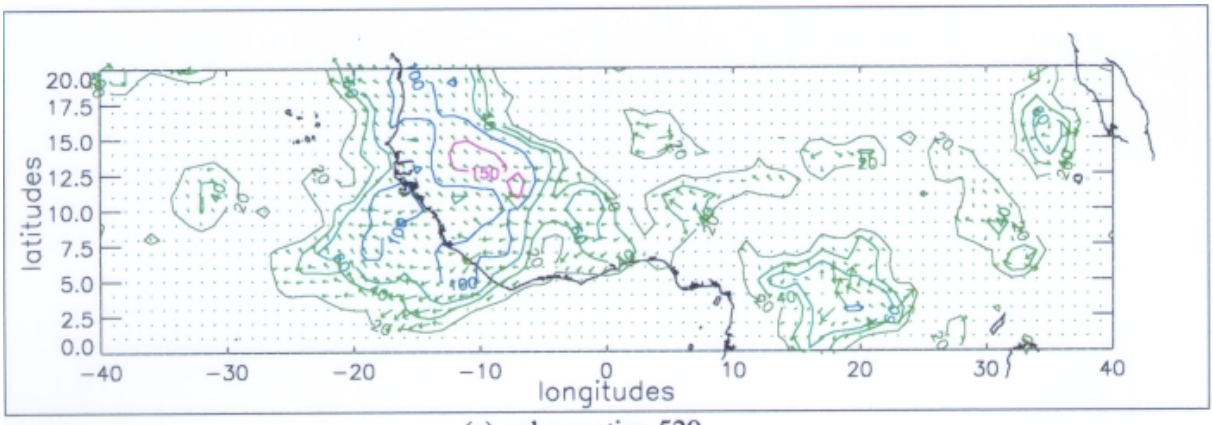

(a) : observation 520

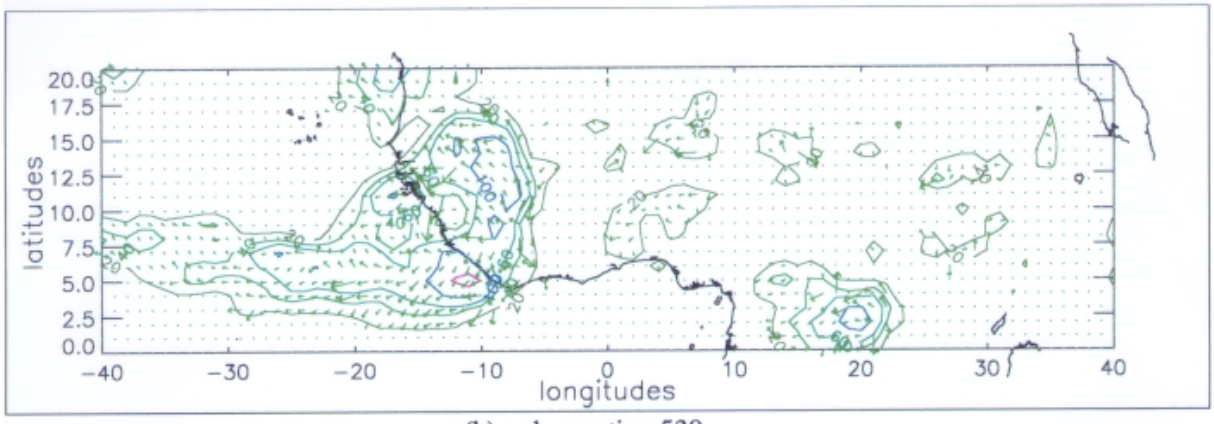

(b) : observation 530

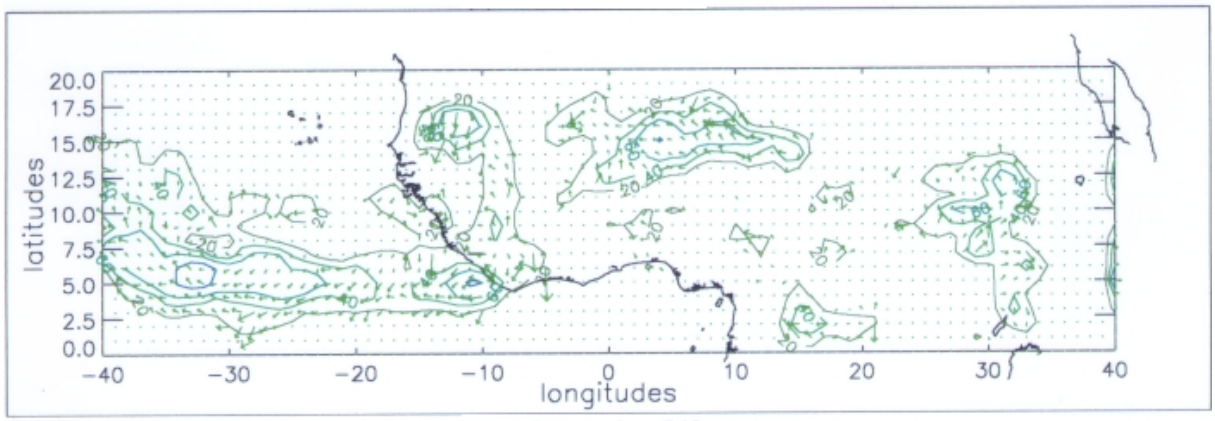

(c) : observation 540

Figure 26: Variance of the first Local Modes (from the CLAUS BT field) superimposed on their phase speed for September the 8th (top), the 11th (middle) and the 14th (bottom).

Laboratoire de M t orologie Dynamique

J.P. Duvel, I. Musat and M. Sabre

Characterisation of the tropical convective cloud clusters

5 Introduction

Deep convective cloudiness in the tropical region exhibits a broad spectrum of temporal and spatial scales. The CLAUS dataset offers the opportunity to analyse globally the variability of the characteristics of the convective cloud clusters at time scales from diurnal to interannual, including thus also intraseasonal oscillations and modulations by wave perturbations. The results presented in this report are based on the equivalent Blackbody temperature (EBBT) or brightness temperatures (BT) of the CLAUS data set for 1985, 1987 and 1992. The aim of this paper is to report the main scientific results obtained on the basis of these three years of data. The aim is also to report on artefacts in the CLAUS dataset due to gaps in the original source satellite dataset or shortcomings in the processing algorithms.

Using the infrared imagery provided by the CLAUS dataset, different classes of clouds may be retrieved by considering a simple threshold of the BT. For a very cold threshold (i.e. lower than 215-220 K), the effect of semi-transparency, brokenness or atmospheric emission/absorption above the cloud tops is small. The BT is thus very close to the real temperature of the cloud top. For a warmer threshold, there is a mixing between high and cold broken (semi-transparent) cloud and warmer but thick clouds. A given class at a given threshold thus corresponds to a mixing of different cloud types. However, for a relatively cold threshold in the tropics (i.e. lower than 250-260 K), all the retrieved cloudiness may be considered to originate from the deep convective activity. The cloud cover at this threshold is thus a tracer of this convective activity.

The seasonal variation of this mean cloud fraction is briefly analysed in Section 5. Section 6 also reports an analysis of the characteristics of the convective cloud cluster, in particular their size distribution and their vertical extension.

6 CLAUS data analysis

6.1 The cloud fraction

The mean cloud fraction at a given BT threshold (s) for a given region and a given time step is defined as the ratio between the number of pixels $N_s(t)$ with BT smaller than the threshold S and the number of pixels of the region. The regional and temporal mean cloud fraction C_s at a given threshold (s) is:

$$C_s = \frac{\sum_{t=1}^{T} N_s(t)}{N.T}$$ Equation 1

- where T is the total number of time-steps (or images) considered.

In this study a threshold of 255K (called hereinafter the reference threshold) is selected to characterise the cloud ensemble resulting from the convective activity. This will be called the convective cloudiness in the following. This cloud ensemble may be due either to semi-transparent and broken cirrus clouds or to the top of mid-level clouds (i.e. typically cumulus congestus or alto-cumulus clouds). A threshold at 255 K corresponds to the value used by Roca and Ramanathan (1999) to study the convective cloud clusters over the Indian Ocean. Other thresholds were used previously to study the convective cloudiness over Africa and the Atlantic Ocean (253 K in Duvel, 1989, 1990; Machado et al, 1992) or over the Indian Ocean (260 K in Kulkarny et al., 1997). A BT of 255K represents a cloud top around 8 km for a standard tropical atmosphere and a cloud emissivity close to 1. The cloud fractions presented here are made on grid boxes of 5 by 5 degrees (i.e., N=100 CLAUS pixels).

The mean cloud fraction with a threshold s=255 K for the four seasons and for three years 1985, 1987 and 1992 is reported in Figure 1. The seasonal migration of the inter-tropical convergence zone (ITCZ) is well depicted, especially for the continental regions of Africa and South- and Central-America and for the Indian region strongly influenced by the strong seasonal migration related to the Indian monsoon. This seasonal mean high cloud fraction obviously depicts the seasonal migration of the convective activity related to the solar declination. During Northern Hemisphere (NH) winter the maximum high cloudiness is located south of the equator over the Indian Ocean, corresponding to the "winter" monsoon. Over the Pacific ocean, the high cloudiness is concentrated over the western and central Pacific during NH winter and is more extended in longitude during NH spring and summer in relation with a stronger convective activity west of Central-America. The separation between the south pacific convergence zone (SPCZ) and the Pacific ITCZ is more prominent during NH summer and autumn.

Estimating the interannual variability by simply computing the standard deviation of the seasonal mean cloud fraction for the three years (Figure 2), the largest value appears over the central pacific in NH winter and spring, in relation with the interannual variation between 1985, 1987 and 1992. This variability of the eastern edge of the maximum cloud fraction above the pacific is mostly due to the El Ni o years of 1987 and 1992 compared to 1985. More generally, maximum values of the standard deviation are located around maxima of the mean cloud fraction; for example North and South of this maximum near 70°E for the Indian Ocean during NH winter or Northwest-Southeast above India during NH summer.

Concerning the quality of the CLAUS dataset, there is no obvious artefact in these seasonal mean distributions of the high cloudiness, even for the Indian region, despite the stronger temporal sampling and the higher mean viewing angle resulting from the lack of data from the geo-synchronous satellite INSAT. There is also no obvious artefact on the standard deviation fields.

6.2 Seasonal variation of cloud clusters characteristics

A cluster at a BT threshold (s) is defined by the area covered by adjacent pixels with brightness temperature colder than this BT. For each image the identification of the clusters is followed by the calculation of their characteristics, i.e. the longitude and the latitude of the centre of mass (centroid) of the cloud, the area at the reference threshold (s) and the area at a colder threshold (c). Because of the large variety of observed cluster shapes, we compute an equivalent radius R_e of a cloud cluster assuming a circular shape. The equivalent radius is then only a characteristic of the cloud cluster area. The clusters are distributed in classes of equivalent radius for the reference threshold of 255 K. The clusters are also classified according to the area they cover at a colder threshold (c) compared to their area at the reference threshold (s=255 K). To this end, for each time step (t) (or each image) a vertical shape parameter $V_S(t)$, defined as:

$$V_s(t) = \frac{N_c(t)}{N_{255}(t)} \qquad \text{Equation 2}$$

is calculated. This V_s parameter is assumed to account for the intensity of the "convective activity" for a given cluster. If V_s is close to 1, the surface of the cluster at the colder threshold (c) is similar to the surface at 255 K and this may be interpreted as an active cluster with mainly a convective part (i.e. relatively thick and extended stratiform part). For an intermediate value of V_s, a larger part of the cluster at 255 K is composed of semi-transparent or broken cirrus and/or by mid-level clouds, revealing the degree of dissipation of the high convective cloudiness. If V_s is equal to 0, the cluster at the reference threshold (255 K) does not reach the colder threshold and it is supposed to represents only mid-level clouds or broken/semi-transparent cirrus. The results presented below correspond to the threshold c=235 K. This threshold represents the deep convective cloudiness (Duvel, 1989; Chen et al, 1996).

For the tropical belt (35°N-35°S) during NH winter 1992, the surface covered by the convective cloudiness is maximal for the small clusters and decreases almost linearly as the equivalent radius increase (Figure 3). The geographical distribution of the centre of mass for small, medium and large cloud clusters (Figure 4) for this same season exhibits three preferential areas for the large systems over the western Pacific, the Indian Ocean and south America. Centres of mass of these large cloud clusters are located close but south of the Equator. Over Central Africa, no clusters are larger than 1000 km for this threshold and this season, suggesting a weaker convective activity compared to the Indo-Pacific region and South America. Another striking result is the lack of large systems over the Indonesian region. These facts will be discussed in more detailed in the following sections. The distribution of V_S for c=235 K exhibits a sharp maximum for V_S between 0.5 and 0.6 (Figure 5). The distribution decreases very rapidly for larger V_s, with only a small portion of the whole cloud coverage with very active clusters (V_S >0.6). On the other hand, there is a more progressive increase of the surface fraction from very small V_s to the maximum between 0.5 and 0.6. Also, there is a relatively large portion of the cloud clusters with BT<255 K that have no part that reaches the level BT=235 K (the category with $V_S < 0$).

The clusters may also be classified according to their equivalent radius (R_e) and vertical shape (V_s) parameters. These R_e-V_s classes give, in a certain way, a 3-dimensional view of the organisation of the convective cloudiness between the two thresholds considered (255K and 235K). On the average for the tropical belt and for JFM 1992 (Figure 6), the cloud coverage at 255K is concentrated on two main classes for V_s between 0.5 and 0.6 and for R_e around 700 km and R_e around 1500 km. Two striking results appear on this figure. First, the very active cloud clusters (i.e. V_s>0.6) are nearly uniformly distributed for almost R_e classes between 150 and 1500 km (with a small tendency for maximum convective activity for R_e between 300 and 900 km). Second, there is no large and inactive clusters and V_s tends to decrease with R_e. The clusters at 255K that do not reach the level 235K are all concentrated for R_e lower than 600km. Relatively large clusters at 255K that do not reach the level 235K may characterise either large fields of broken/semi-transparent cirrus or large fields of mid-level clouds (As, Ac).

From the distribution shown in Figure 6, nine classes of R_e - V_s are defined with three classes of surface (R_e < 500 km; 500< R_e < 1000 km and R_e > 1000 km) and three classes of vertical shape between 255 and 235K (V_s < 0.5, 0.5 < V_s < 0.6 and V_s > 0.6). An absolute frequency of clusters belonging to a given R_e-V_s class for each region of 5x5 degrees is computed. The absolute frequency of a given R_e-V_S class is defined as:

$$F_a = \frac{\sum_{t=1}^{T} N_{rv}(t)}{N.T} \qquad \text{Equation 3}$$

- where N_{rv} is the number of pixels of the region belonging to a cloud cluster of the R_e-V_s class. This parameter gives the probability that a pixel of a given 5X5 grid box is part of a convective cloud cluster in a given class of R_e and V_s. The geographical distribution of this absolute frequency is then computed for each of the nine classes.

On the average for the three NH winter seasons (JFM 85, 87 and 92; Figure 7), the largest and more active convective cloud clusters are observed mainly over the Indo-Pacific region south of the equator. Inspecting each year separately (not shown), the maximum convective activity is located over the western and central Pacific during the El Ni o years (1987 and 1992) and over the Indian Ocean during the "normal" year 1985. These locations of the largest convective cloud clusters well correspond to region of maximum amplitude of the intraseasonal oscillation during winter (Lau and Chan, 1988; Salby and Hendon, 1994; Goulet and Duvel, 2000).

For the three NH winters (JFM), the south-eastern part of the South America is characterised by large clusters but with average or low V_s. Over South-America, it is interesting to note the change of the cloud cluster characteristics from small and relatively inactive clusters north-west (including the effect of the Andes) to the largest and more active systems south-east. Surprisingly, the convective clusters above Central Africa are smaller and less active than above South-America with a maximum frequency for medium R_e and average V_s. Relatively small and less active cloud clusters also cover the Indonesian islands.

For the NH summer (JJA; Figure 8), the largest and more active convective cloud clusters are obtained over and south of India, in evident relation with the Indian Monsoon. Nearly

all the clusters with a radius larger than 1000 km at BT=255 K are obtained over this region. Clusters with medium radius are obtained over eastern and western Pacific Ocean. The Indian monsoon region and north-west pacific are the two regions with an intense intraseasonal oscillation during NH summer (Lau and Chan, 1988; Goulet and Duvel, 2000). As for the winter case, the Intraseasonal oscillation thus appears to be related strongly to the largest and the more active cloud clusters of the whole tropical belt. The smallest and the less active convective clusters are located above Africa and Central America and the Indonesian Islands.

This result tends to demonstrate that the largest and more active convective cloud clusters are rather observed over oceanic regions, in apparent relation with the regions of maximum intraseasonal activity. By contrast, the continental regions are rather characterised by smaller and less active cloud clusters. This may be explained by the regular (i.e. diurnal) release of the conditional instability over the continental regions, and the relatively rapid adjustment of the surface and of boundary layer. These rapid adjustments apparently inhibit the development of very large and long living convective perturbations. India during the monsoon and the south-east part of South America during local summer appears as two exceptions.

On the basis of this analysis, it is difficult to extract evident artefacts in the CLAUS data. Even the strong data sampling around the Indian longitudes does not give evident biases in the results. The complete validation of the CLAUS algorithm above this region will however require a more detailed study and comparison using for example the Meteosat-5 measurements (since 1998).

6.3 Diurnal variation of cloud clusters characteristics

An example of the diurnal variation of the cloud cluster characteristics is presented in Figure 9. This example is obtained for the region of the South America that is highlighted in Figure 4. The diurnal variation of the convective clusters over this region mainly concerns the radius classes larger than 1000 km, with a maximum cover and a maximum diurnal modulation for V_s around 0.5 and R_e between 1250 and 1500 km. Curiously, the diurnal modulation of the surface covered by small and medium clusters is not very important. The convective activity is minimal between 0900 and 1200 LT. This minimum is characterised by a small cloud cover (at this 255 K threshold) for all categories of R_e and V_s. For this period of the day, a second class of cluster appears for V_S around 0.4 and R_e around 750 km. This most probably corresponds to a mixing between new developing convective clouds and cloud fragments of older clusters that already appear at 0600 LT for R_e around 1000 km and V_S=0.4. The maximum vertical development of the cloud clusters is obtained around 1800 LT with many clusters having a V_s larger or equal to 0.6. The value of V_S progressively decreases between 1800 and 0900 LT.

The diurnal variations above the west Pacific is much more complex (Figure 10). There is no clear hour of minimum convective cloud cover. There is a concentration of clusters with radius between 1500 and 1750 km and these clusters are more active (i.e. more vertically developed with a maximum of the distribution for V_s=0.7) around 0900 LT.

The less active period of the day is around 2100 LT with most of the clusters with V_s around 0.5. However, the largest clusters are also observed at this hour.

7 Conclusions

These preliminary results on the statistical distribution of the convective cloud clusters using the CLAUS dataset are very encouraging. No significant bias, due to temporal and spatial interpolation or to the angular correction, was found for this particular diagnostic. This preliminary study shows the very large potential of the CLAUS dataset to better describe and understand the characteristics of the deep convection above all the tropical belt, even over the Indian Ocean region where no data from geo-synchronous satellite were currently available. These characteristics include the mean distribution of the convective cloudiness but also its variability at different time scales from diurnal to interannual. Also, the CLAUS dataset makes it possible to study the variability of the cloud clusters geometrical characteristics (horizontal and vertical extension) for the whole tropical belt.

There is no doubt that the entire CLAUS dataset - extending from 1983 to the present - will give a very interesting and more general view of the interannual variability of the cloud cluster characteristics (i.e. Figures 7 and 8). In addition, while no results on this subject are presented here, there is no doubt that the CLAUS dataset will give a good statistical view of the life cycle (duration, direction of propagation, change in the geometrical properties) of the large cloud clusters by using cloud tracking techniques.

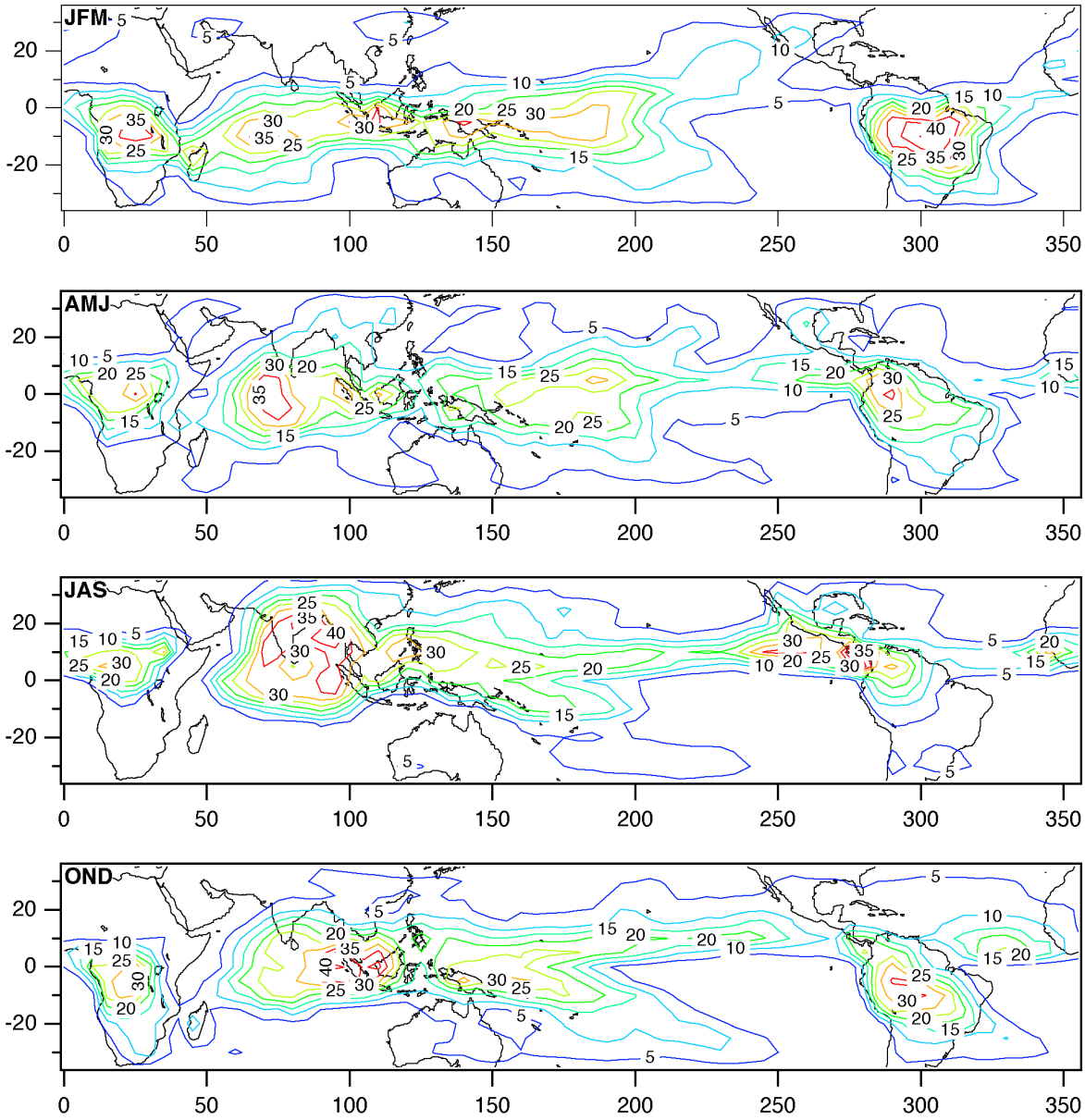

Figure 1: Mean cloud fraction for a BT of 255 K and for the four seasons. Average for three years (1985, 1987 and 1992).

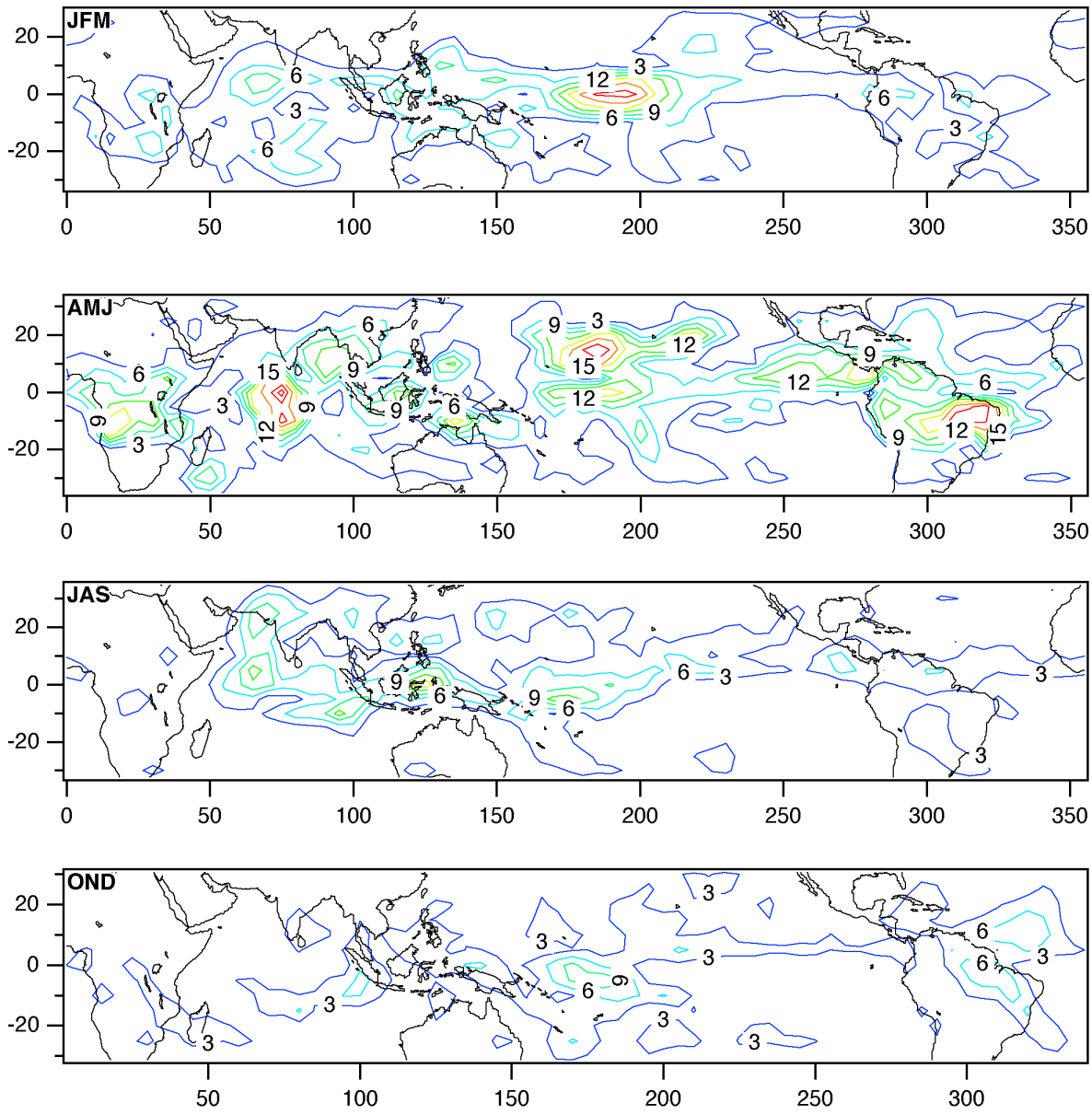

Figure 2: Interannual variability of the mean cloud fraction for a BT of 255 K and for the four seasons among the three years (1985, 1987 and 1992).

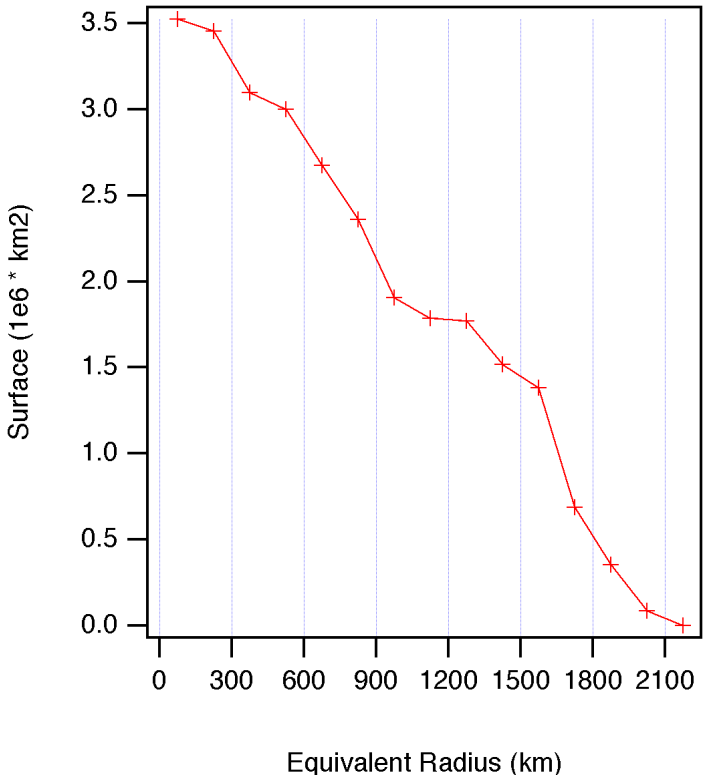

Figure 3: Distribution of the surface covered by cloud (BT<255 K) in different classes of the equivalent radius R_e on the average for the months of January to March 1992 for the tropical belt (35°N-35°S).

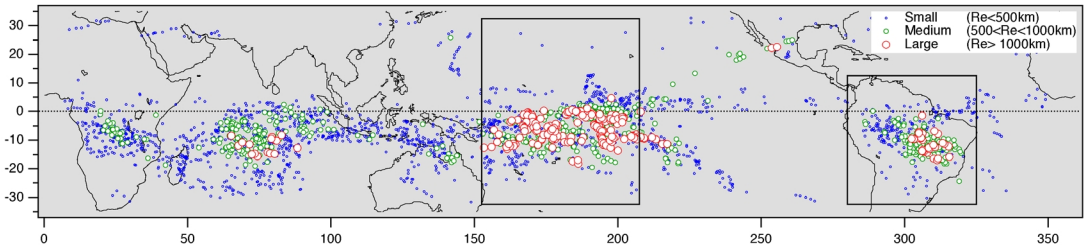

Figure 4: Distribution of centre of mass for the small (R_e<500 km: blue), the medium (500< R_e <1000 km; green) and large (R_e>1000 km; red) clusters for the months of January to March 1992.

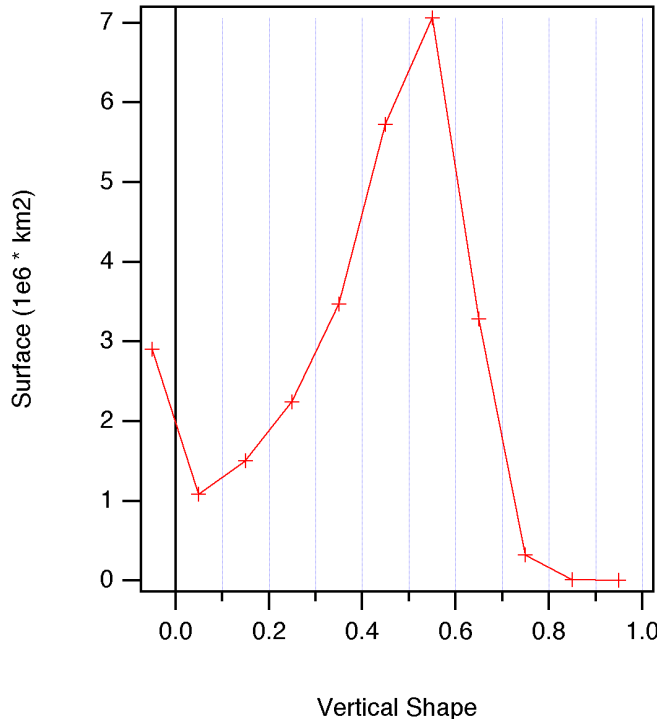

Figure 5: Distribution of the surface covered by cloud (BT<255 K) in different classes of the vertical shape V_s on the average for the months of January to March 1992 for the tropical belt (35°N-35°S).

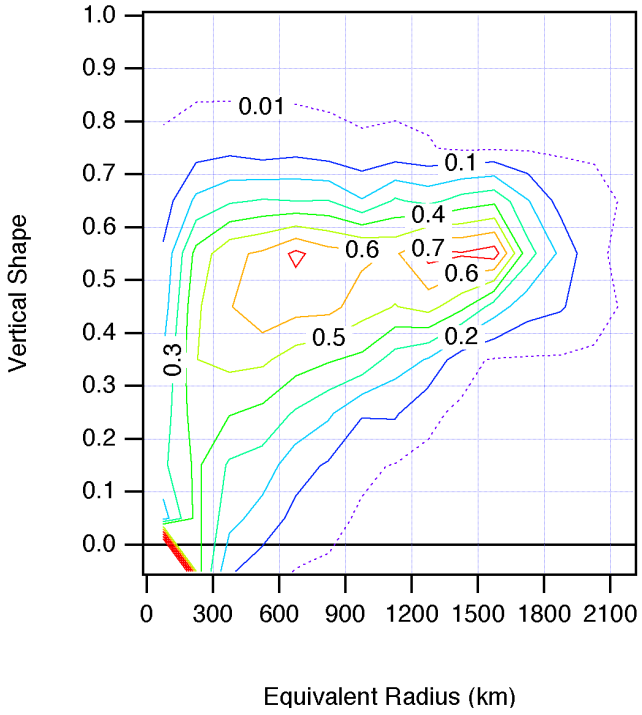

Figure 6: Distribution of the surface covered by cloud (BT<255 K) in different classes of V_s and R_e on the average for the months of January to March 1992 for the tropical belt (35°N-35°S).

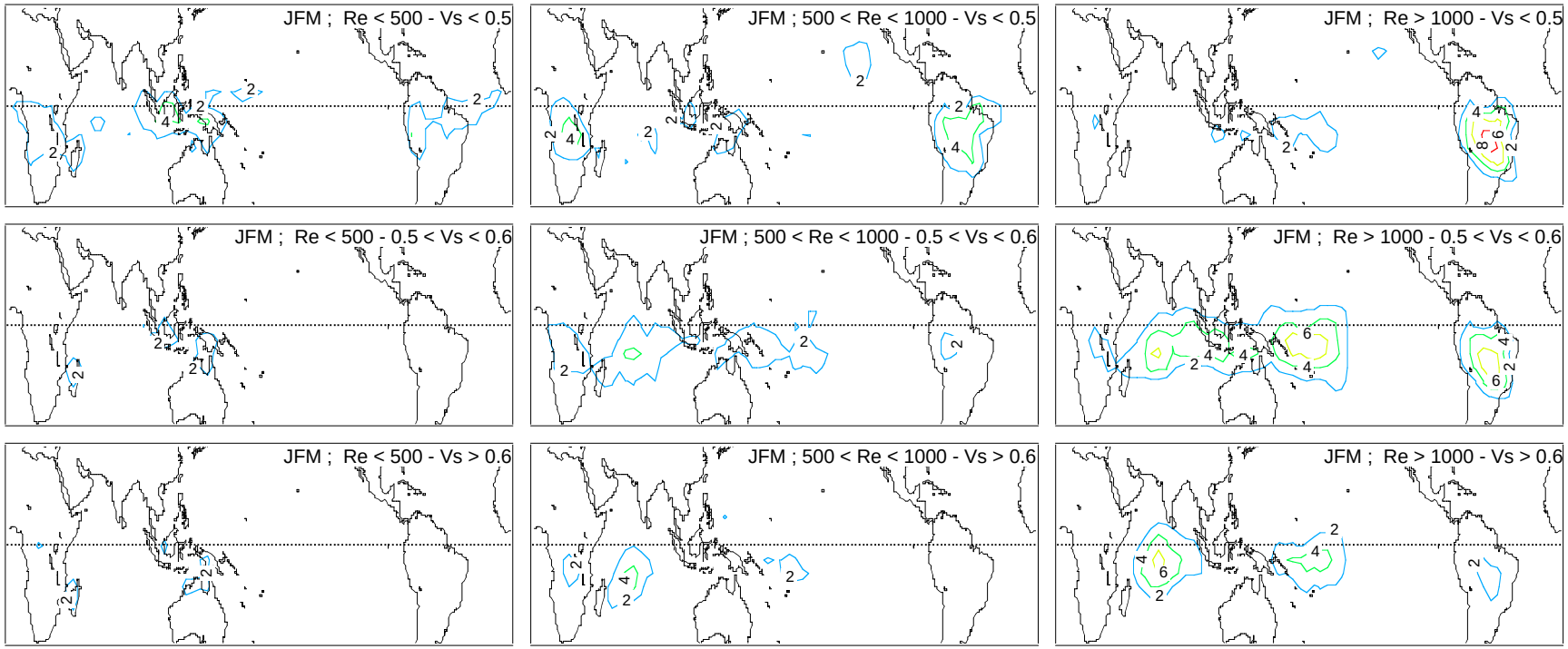

Figure 7: Regional distribution of the absolute frequency (Eq.3) of cloud clusters in different classes of R_e and V_s. Average for January, February and March for three years (85, 87 and 92).

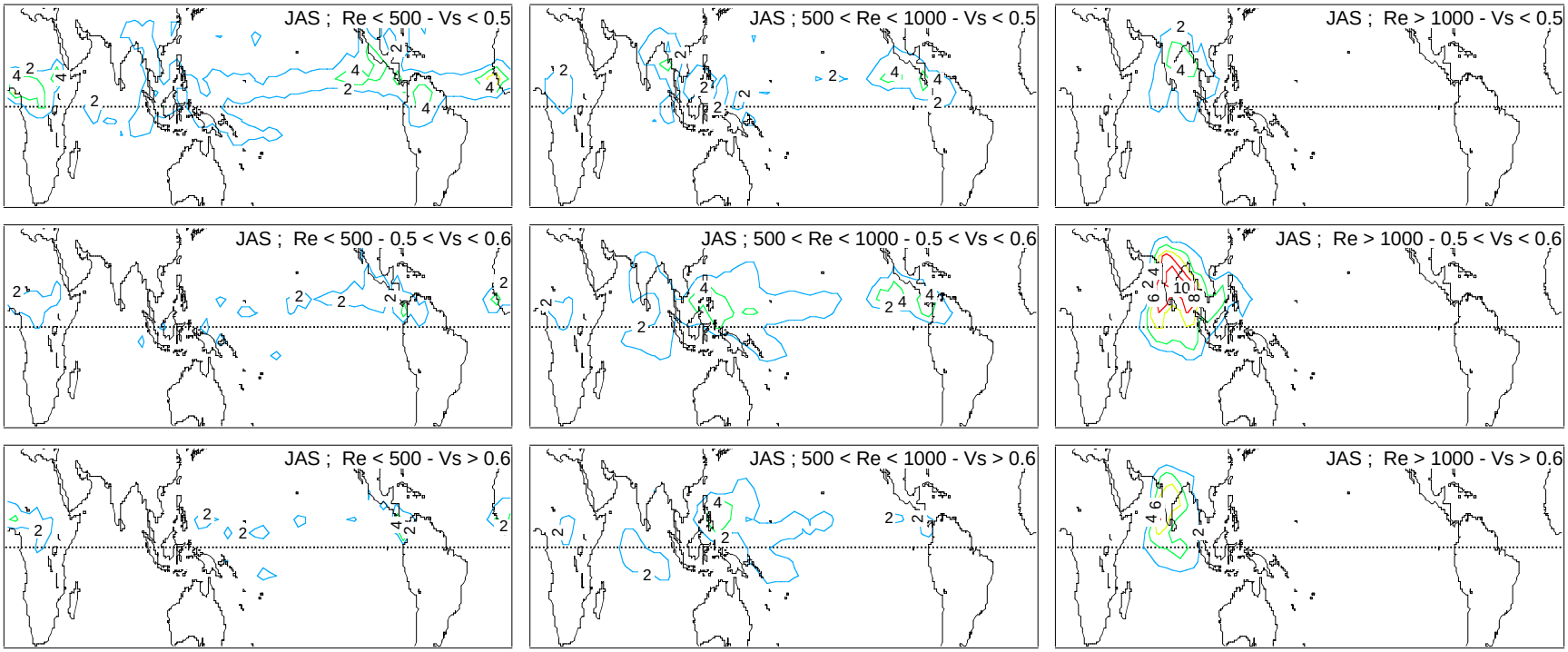

Figure 8: Regional distribution of the absolute frequency (Eq.3) of cloud clusters in different classes of R_e and V_s. Average for July, August and September for three years (85, 87 and 92).

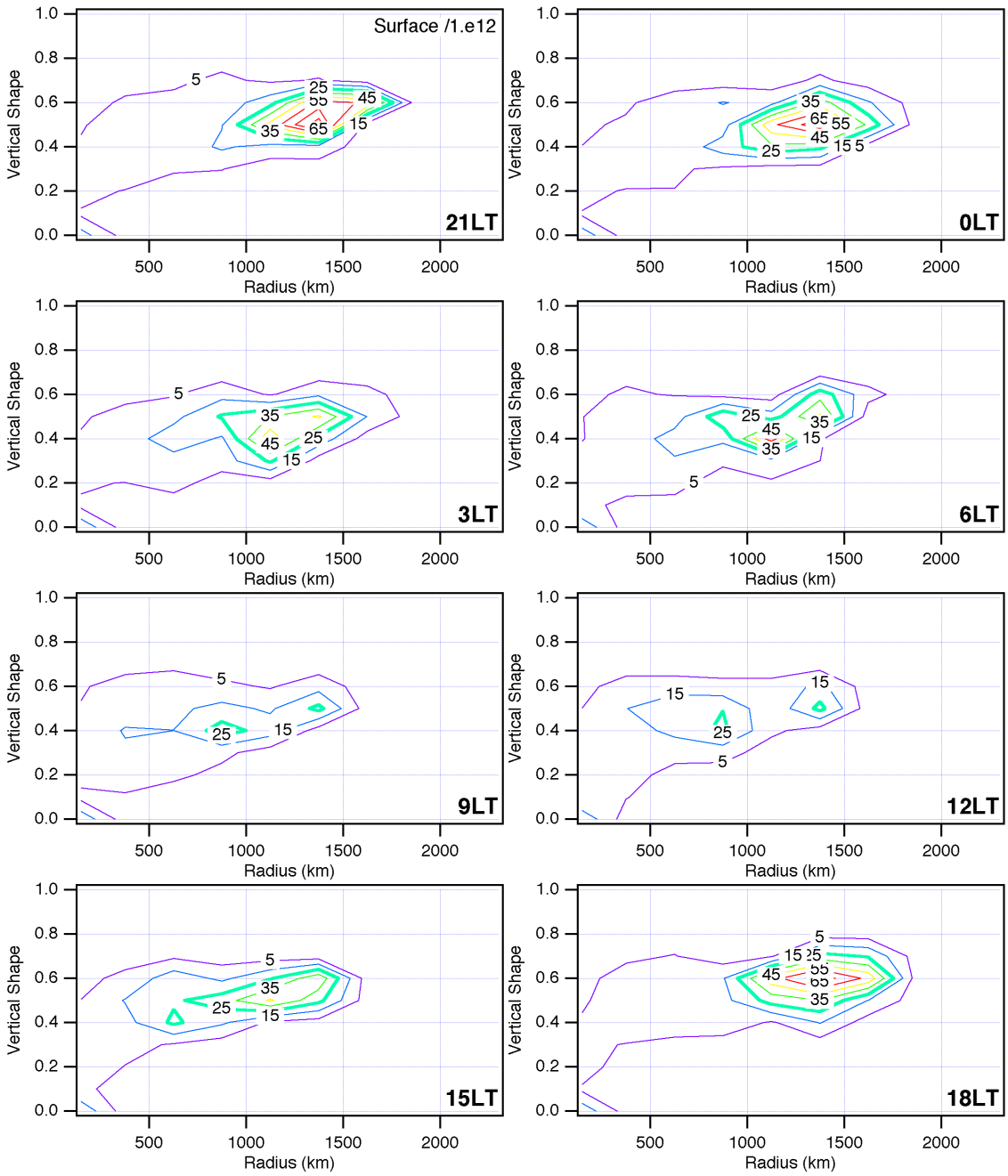

Figure 9: Diurnal variations of the convective cloud cluster characteristics above South America during local summer (JFM 1992).

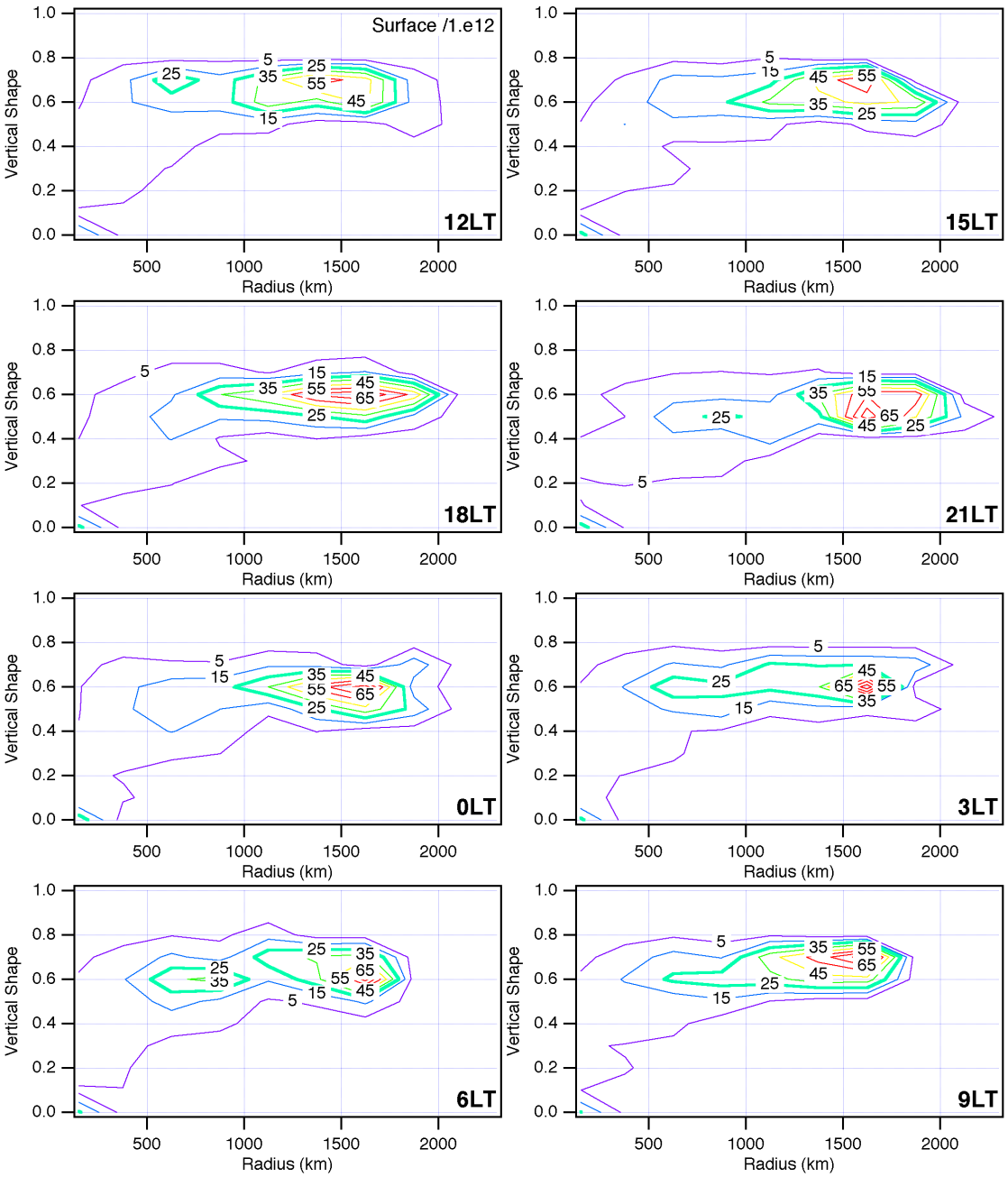

Figure 10: Diurnal variations of the convective cloud cluster characteristics above West Pacific during local summer (JFM 1992).

Max-Planck Institut f r Meteorologie

Validation of Climate Model Parameterisations using the CLAUS Dataset

Andreas Rhodin and Klaus Arpe

8 Introduction

The CLAUS dataset provides brightness temperatures in the atmospheric water vapour window on a high temporal (three-hourly) and spatial (0.5°) scale. Brightness temperatures in the infrared water vapour window (12 m) observed from satellites reflect either cloud top temperatures or surface skin temperatures in cloud free regions and thus may be used for the validation of those parameterisations which reflect cloud processes (convection, stratiform precipitation) and the land surface scheme.

The model to satellite approach is pursued, i.e. the observed parameter brightness temperature is directly compared with the model. Brightness temperature is not a standard model output and thus has to be computed from modelled atmospheric temperature, humidity and cloud cover as well as surface temperature and pressure in a post-processing step. A narrow band radiation model provided by Jean-Jacques Morcrette (Morcrette and Fouquart, 1985) was used for this purpose.

Although the dataset provides information on high temporal and spatial scale it is not easy to make use of this information. Because cloudiness has high spatial and temporal variability, a direct comparison of observed and modelled temperatures is not feasible, especially not for climate runs which are merely driven by observed sea surface temperature and besides that do not reflect actual weather conditions. Thus the frequency distribution of brightness temperature within limited areas is compared.

Results regarding the validation of brightness temperatures derived from the global climate model ECHAM (Roeckner et al., 1996) in T42 resolution and two different model versions (4.0 and 4.5) are presented. Mean values, standard deviations, and histograms of brightness temperature distribution within limited areas were compared (for one year) with those derived from the CLAUS data set. The results for one month are shown as an example.

In order to overcome the difficulty of comparing climate runs with observations the prognostic atmospheric variables were relaxed to the ECMWF reanalyses (nudged) in a further run so that the model results reflect the actual weather conditions. The nudging method allows for a reasonable comparison within shorter time spans. This is especially important for model runs at higher resolution, which are much more expensive. An example is shown for T106 resolution during a four day period. Furthermore, if the performance of the land surface scheme is assessed, a comparison at a single model grid-point makes sense.

The CLAUS data set has also been used for an assessment of the clouds generated by ECHAM in selected synoptic situations (storm event, blocking period) in another study (Bauer, 2000).

9 Approach for Brightness Temperature comparison

There are two basic approaches for comparing results from numerical models to remote sensing data, i.e. the satellite to model and the model to satellite approach:

Satellite to model approach:

> The comparison is made for those quantities that are directly predicted by the model, i.e. distributions of cloud heights, rainfall rates, or surface skin temperatures. This procedure requires some kind of inversion of the remote sensing data.

Model to satellite approach:

> The comparison is made for those quantities that are observed by the satellite, namely brightness temperatures in this case. In this approach the observed quantities must be calculated from the model state variables.

The first approach has the disadvantage that there is generally some ambiguity in deriving the model variables under consideration from the observations. Furthermore, the retrieval of indirectly observed parameters always depends on some model assumptions. Thus in this study the model to satellite approach will be pursued. Because brightness temperature is not a direct model result it had to be calculated from the model output in a post-processing step.

To make use of the detailed information of the CLAUS data set, in spite of the statistical nature of cloud representation in the models, frequency distributions of brightness temperature occurrences were calculated for the CLAUS data set and the model results as well; this method has also been used by Morcrette (1991). The frequency of low brightness temperatures is related to the frequency of clouds with the respective cloud top temperature. The frequency of high brightness temperatures stems from low clouds or from surface skin temperature variations. The latter two mechanisms cannot be distinguished in every case. Figure 1a shows the three regions chosen to calculate brightness temperature frequency distributions. They consist of a dry (Sahara) and a moist (Brasilia) land surface as well as an oceanic (eastern Pacific) region in the tropics.

9.1 ECHAM Model runs

ECHAM version	Run type	Resolution	Period	Run number
4.0	climate	T42	1992	22591
4.5	climate	T42	1992	22876
4.5	nudged	T42	1992	50010ex01
4.0	nudged	T106	12-15 March 1993	58036
4.0	nudged	T42	12-15 March 1993	

Table 1: ECHAM model runs investigated.

Table 1 lists the model runs referred to within this section. The results of two versions of the global model ECHAM in T42 resolution (19 vertical levels) are compared to the

CLAUS brightness temperatures for the year 1992. The runs are performed with the current model versions 4 and with version 4.5, which has been used in the AMIP2 Model Intercomparison Project. The main differences to version 4 are:

- Replacement of the explicit surface scheme by an implicit one (Schulz et al., 1999).
- Changed numerics in the large-scale condensation scheme (Lenderink, 1998).
- Changed values for some parameters in the stratiform cloud scheme.

The next version 5 is currently under development.

Variable	Time Constant (50010ex01)	Time Constant (58036)
logsurfacepressure	1.16E-05/s(1/24h)	1.e-4/s
temperature	1.16E-05/s(1/24h)	1.e-5/s
vorticity	4.63E-05/s(1/6h)	1.e-4/s
divergence	5.79E-06/s(1/48h)	5.e-5/s

Table 2: Time constants corresponding to the nudging coefficients used in this study. In run 50010ex01 the coefficients decreased to zero in the boundary layer.

In order to perform model runs reflecting the actual weather situation a nudging approach (Jeuken et al., 1996) was pursued. Temperature, vorticity and divergence were relaxed to the ECMWF reanalyses. Specific humidity was not relaxed in order to allow the evolution of a balanced state governed by the physical parameterisations of the model. An additional ECHAM 4.5 version run relaxed to the ECMWF reanalysis with nudging coefficients given in Table 2 was performed. Below level 14 (approximately 850 hPa) the coefficients linearly decreased to zero in run 50010ex01 in order to allow an undisturbed evolution of the boundary layer in order to assess the performance of the land surface scheme.

9.2 Climate model runs (T42 resolution, 1 year)

Figure 2 shows observed and modelled mean brightness temperature and standard deviations for March 1992. The observations provided by the CLAUS dataset were averaged to the same resolution as the model results.

The results presented here for March 1992 are valid also for the other months of that year:

- The warm (cloud free) areas over sea are modelled to be too cold (too high cloud cover) in the ECHAM 4.0 run. This aspect is better reproduced in version 4.5.
- The mean brightness temperatures in the cold (cloudy) areas over sea correspond very closely to the ECHAM 4.0 values. ECHAM 4.5 shows slightly lower temperatures in these cases.
- In the tropical areas over land ECHAM 4.0 gives to high brightness temperatures whereas version 4.5 is in better correspondence with the observations.

- The standard deviation of brightness temperature is high in areas with high variations of cloudiness. The standard deviation modelled by ECHAM 4.0 corresponds well with the observation, the differences reflect the differences of the mean value (mean cloudiness) stated above. On the other hand the standard deviation is much higher in the ECHAM 4.5 run, the reason for that will become apparent below.
- The nudged model run (ECHAM 4.5) shows similar results as the climate run, but with following differences:
-
  i) The location of the cloudy region generally corresponds better with observations.
  ii) The main deficiency of this model version, namely the occurrence of too cold areas with too high variance is enhanced.

Brightness temperature frequency distributions were derived for selected areas (Figure 1a) and are presented below for one oceanic area (Pacific region, 160-200°E, 20-0°S) and two land areas (Sahara region, 0-30° E, 15-30° N, and the Amazonia region, 290-310°E, 10-0° S):

2.2a Sahara Region

Figure 3 shows brightness temperature distributions for the Sahara region taken for March 1992. The distribution is dominated by surface skin temperature variations during the diurnal cycle. Averaging the CLAUS dataset to T42 resolution does modify the distribution at the very cold end, because infrequently occurring cold brightness temperatures related to high clouds with small spatial extend are averaged with warmer pixels in their neighbourhood. Averaging the CLAUS data to the T42 resolution mainly results in worse statistics of the frequency distribution histograms because of the smaller number of grid points in the averaging area. Comparison with the ECHAM 4 run shows, that the overall distribution (Figure 4a) is represented very well by the model, mainly the amplitude of the surface skin temperature is too low. The ECHAM 4.5 and the ECHAM 4.5 run relaxed to analyses do not differ significantly from the former besides some excess of high clouds. The relaxed run of course shows temporal coincidence of observed and modelled clouds but the amount of high clouds is still overestimated.

The mean diurnal cycle of surface temperature (Figure 5) is slightly underestimated by the model. Especially the strong peaks at noon are missing. This can only partly be explained by the coarser temporal resolution of the climate run data sets (six-hourly vs. three-hourly). Very low temperatures occur more frequently in the ECHAM 4.5 run.

Figure 6 shows brightness temperature distributions in the Sahara area for each month of the year 1992. It can be seen that the underestimation of skin temperature amplitude is a general feature of the model. Furthermore, there are often too much cloud modelled in this area. Both shortcomings lead to too low values of mean brightness temperatures during the whole year.

2.2b Pacific Region

In Figure 4(b) the brightness temperature distribution in the Pacific region during March 1992 is shown. The distinct peak (at approx. 290 K) results from cloud free situations and reflects sea surface temperature. The long tail to lower temperatures corresponds to cloudy situations with the respective distribution of cloud top temperatures. Averaging the CLAUS data to the T42 resolution changes the shape of the histogram only slightly (blue vs. green line). The distribution becomes slightly broader in its centre but narrower at the tails. The sparse occurrence of very high clouds cannot be reproduced with the low resolution. The overall distribution modelled by the ECHAM 4 physics (orange) follows very closely the distribution of the averaged observations (blue). The ECHAM 4.5 physics lead to a bimodal brightness temperature distribution (red line in bottom right panel) in contradiction to observations. The excess of high clouds is the reason for the high variance of brightness temperatures apparent in Figure 2. The higher number of cloud free events may be due to sampling problems and thus be insignificant. As seen in Figure 7 cloudiness in the averaging area shows considerable variations on a time scale of weeks and sampling climate run results over a period of one month may be not representative. Indeed, in the nudged run (black) the peak corresponding to the sea surface temperature is reduced (Figure 4(b), black line) in correspondence with observations, but the excess of high clouds is further enhanced.

Differences between model and observations are more apparent in the diagrams of the mean diurnal cycle (Figure 8). Observations show a maximum of high cloud tops (temperature lower than 200 K) shortly after midnight (15 UT), of medium height clouds (approx. 220 K) at noon (00 UT), and of lower clouds (250 K) in the late evening. ECHAM 4 yields a maximum of both medium and high cloud tops in the afternoon (06 UT, with less high level clouds at all) and a distinct maximum of lower clouds in the early morning (18 UT), which also appears in the total distribution but is not present in the observations. In ECHAM 4.5 the temporal evolution of cloudiness differs substantially from observations.

Figure 9 shows brightness temperature distributions in the Pacific area for each month of the year 1992. The shape of the distribution is generally reproduced very well by ECHAM 4 with a slight tendency to too much mid-level clouds. There is also a systematic bias of the peak position with the model being colder than the observations.

2.2c Amazonia region

Figure 4c shows brightness temperature distributions for the Amazonia region. The distributions do not show a sharp peak at high temperatures as present over the sea, because surface temperature is much more variable in space and time over land. The time averaged modelled temperature distribution still has a maximum at surface temperature values (orange line) whereas the observation shows a broad distribution due to higher cloudiness (blue). The ECHAM 4.5 parameterisations (red line) reduce the frequency of cloud free situations and are in better correspondence with the observations in this respect, but lead to an excess of high clouds, as over the Pacific region. The nudged ECHAM 4.5 run does not differ significantly from the corresponding climate run.

None of the parameterisations reproduces the observed brightness temperature distribution in this area very well.

The diurnal variations of surface temperature at the high end of the distributions can be clearly seen in the time series (Figure 10) or in the mean diurnal cycle (Figure 11). The observed mean diurnal cycle shows a maximum occurrence of high cloud tops in the early afternoon (local noon corresponds with 16 UT) and of low clouds just before noon, whereas the modelled cloudiness reaches its maximum in the early morning.

Figure 12 shows observed and modelled (ECHAM 4) brightness temperature distributions in the Amazonia region averaged over each month of the year 1992. The overestimation of cloud free periods in the model is a persistent feature during January to April. The correspondence between model and observations is generally better during the other seasons, but the temperatures at the high end of the distribution (surface temperatures) are generally overestimated by the model.

9.3 Summary of results from the three study areas

These comparisons show that brightness temperature distribution over the tropical ocean is quite well represented by the ECHAM 4 model, whereas there are larger differences over land. The ECHAM 4.5 parameterisations show some improvements of mean brightness temperature values, but at the cost of an unrealistic excess of high clouds.

The comparison of climate run results with observations over short time spans (here one year) runs the risk of sampling problems. Comparisons over longer time spans may yield more robust results but the comparison becomes very unhandy, especially if different parameterisations or parameter values shall be evaluated at higher resolutions. Comparison of the nudged run with the respective climate run shows that sampling errors were small for the one-month periods and the relatively large spatial areas. The discrepancies between model results are caused by systematic errors of the model. On the other hand the nudging in this case enhanced the systematic error of the model. Further investigations are required if this shortcoming can be overcome by a further modification of the nudging technique. Studies over shorter periods with a higher spatial model resolution are shown in the next paragraph.

2.3a Model runs relaxed to analyses (T106 resolution, 4 days)

Figure 13 shows a snapshot of brightness temperature at March 14th 1993 as observed (CLAUS) and modelled by the ECHAM 4 model at T106 resolution. The brightness temperature derived from the driving ECMWF reanalyses is shown at the bottom. Observed and modelled cloud patterns correspond relatively well at higher latitudes but differ considerably in the tropics. There are differences in cloud positions between observations and the ECHAM model results, between observations and analysis, and between analysis and ECHAM model results as well. This shows that the approach to compare frequency distributions of cloud top temperatures, instead of cloud top temperatures itself, is still required.

Figure 14 shows the brightness temperature histograms derived from observations (CLAUS) and model results in 2 resolutions (T106 and T42) in the Pacific and Amazonia region during the 4 days period of 12-15th March 1993. In the Pacific region observed

and modelled distributions again correspond quite well, although there are some indications for an excess of low clouds in the T106 resolution not apparent in the climate run comparison. In the Amazonia region the ECHAM 4 T42 run overestimates the occurrence of cloud free situations as in the climate run. The correspondence between observation and model results here improves with the higher (T106) resolution.

10 Comparison at single model grid-points

This comparison of model results and brightness temperature observations was primarily based on frequency distributions because the model does not produce clouds or cloud clusters in the same location as observed. The situation is different if the information on surface skin temperature is explored. In this case a comparison at single pixels may be performed in order to validate the performance of the surface scheme and to extract information on soil parameters.

Figure 15 shows the temporal development of brightness temperature as observed (black line, CLAUS data averaged to a T42 pixel) and modelled (green: total brightness temperature, red: clear sky BT) at a model grid-point in northern Germany (red pixel in Figure 1b), taken from the nudged ECHAM 4.5 run. There is good correspondence between observed and modelled brightness temperature minima during the clear sky period (day 137 to 142), but the model underestimates the diurnal maxima by 5 K. The correspondence is also very good during day 130 to 134 where clouds are present, driven by synoptic systems varying on a time scale of two days. The cloud top temperatures are well reproduced by the model, merely a time lag of approximately 1/2 day is present. The correspondence is worse in the period after day 142 with partial cloudiness due to convective activity.

Further investigations are planned with the ECHAM column model version that reproduces the trajectory of the three-dimensional model (with forcing terms prescribed from a 3-d minus 1-d difference run). Detailed process studies and sensitivity experiments at single grid-points are anticipated and their results may hopefully be generalised for the 3—d model domain. The global coverage of the CLAUS data set allows this kind of investigation to be performed at any model grid-point. Information to drive the column model from the ECHAM 4.5 nudged run has been stored at all the locations indicated in Figure 1b.

11 Assessment of the CLAUS data set quality

The studies described in this report used the CLAUS Version 1.0 dataset. This data set still suffers from insufficient limb darkening corrections, which will be improved in the next release. The shortcomings become apparent if the diurnal cycle or a time series of brightness temperatures is investigated. An example is given in Figure 16. The brightness temperature distribution taken in a domain located over the northern Atlantic shows a variation of cold temperature occurrences at 00 and 03 UT, which can be attributed to the lack of coverage by the NOAA satellites. Similar problems are visible in other situations, for instance in the Caspian Sea area in September 1992.

12 Conclusions

The CLAUS brightness temperature data set provides a lot of detailed information on cloudiness (and surface skin temperature variations), which has been used for the assessment of two different ECHAM model versions. The close relationship of brightness temperature histograms with cloud top temperature distributions in the model to satellite approach allows a more detailed assessment of model parameterisations than comparison with mean values and variances alone. So monthly averaged values of brightness temperature were improved in the 4.5 model version, but partly for the wrong reason.

Comparison with the CLAUS data set clearly shows deficiencies in the vertical distribution as well as in the temporal evolution of cloudiness in the model and differences in the performance of different versions. Nudged runs were performed in order to allow a direct comparison of model results and brightness temperature observations at single model grid-points.

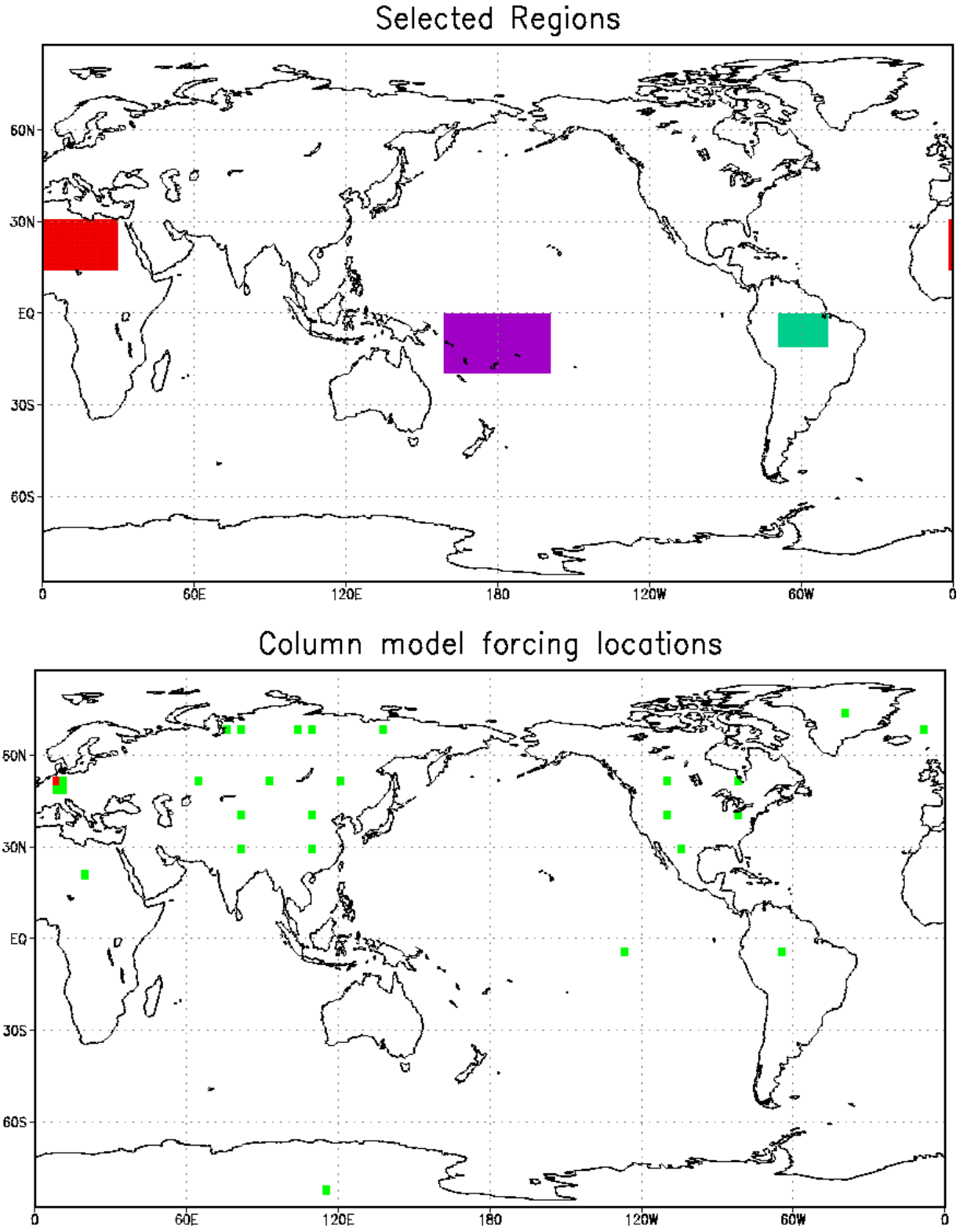

Figure 1: The areas selected for taking brightness temperature frequency distributions are indicated by the boxes in the top panel (a). Column model forcing was prepared for the points indicated in the bottom frame (b).

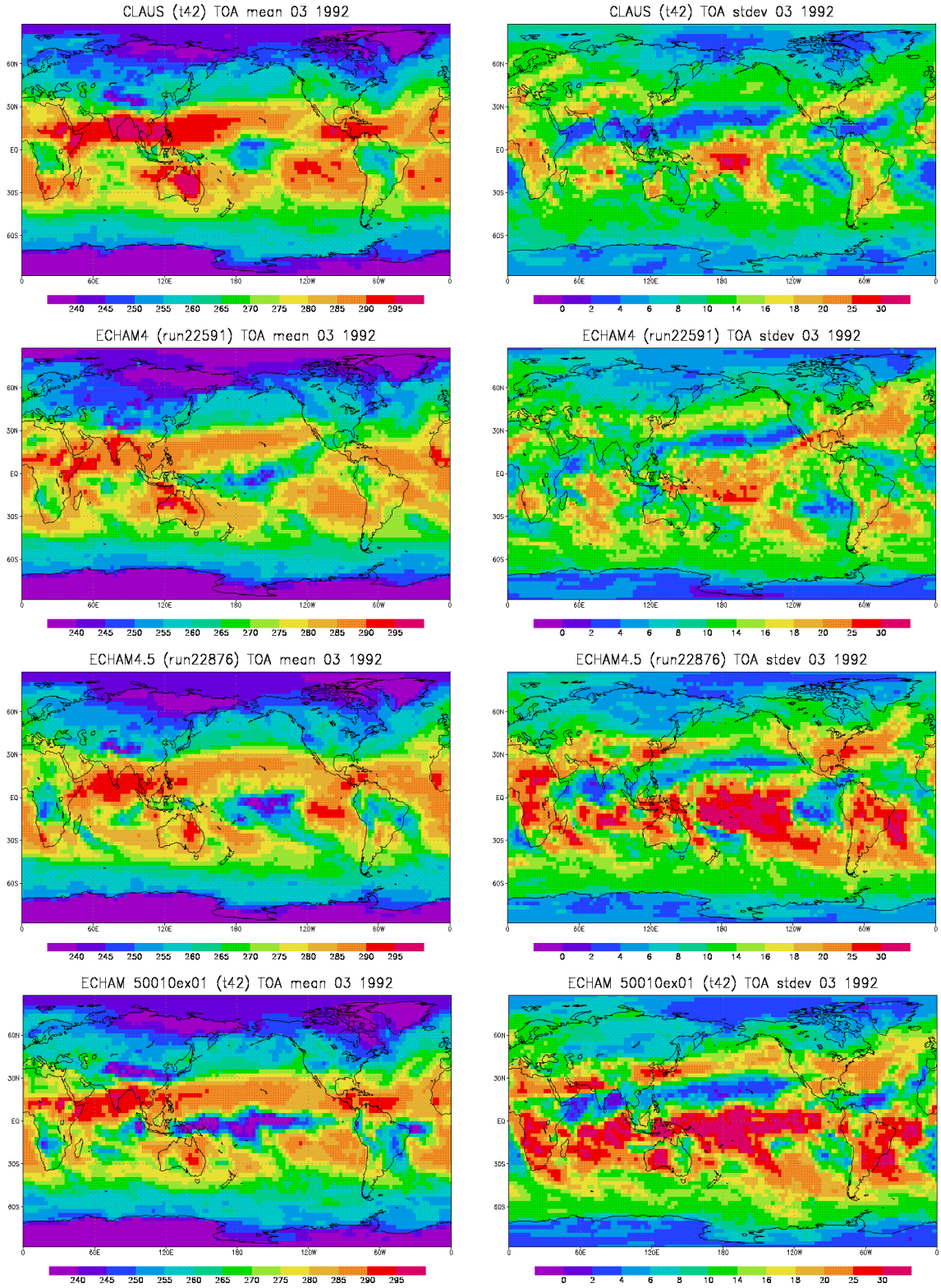

Figure 2: Mean infrared (12 m) brightness temperature for March 1992 (left) and standard deviation (right), observed (CLAUS data set: top row) and derived from climate runs with the ECHAM 4.0 (second row) and ECHAM 4.5 (third row). Results from the ECHAM 4.5 run nudged to ECMWF reanalyses is shown at the bottom.

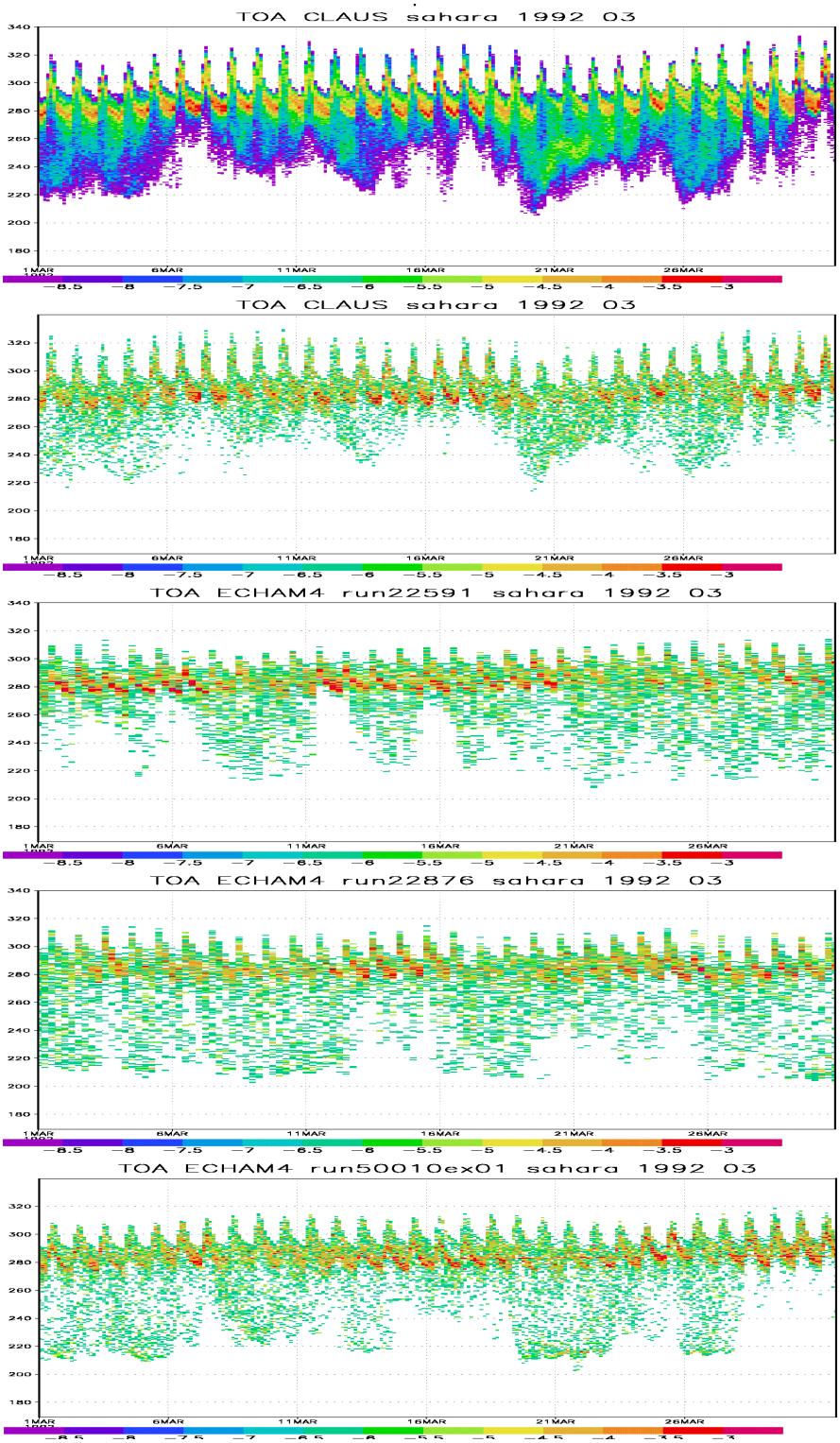

Figure 3: Brightness temperature frequency distribution for March 1992 in the Sahara region (0-30° E, 15-30° N). From top to bottom: a) temporal evolution in the CLAUS dataset with 1/2 degree resolution, b) averaged to a T42 grid and c) in the ECHAM 4 climate run as well as in the d) ECHAM 4.5 climate run and e) the ECHAM 4.5 nudged run. The colour scale is logarithmic to the base 2, a difference of two adjacent colours corresponds to a factor of two in brightness temperature occurrence.

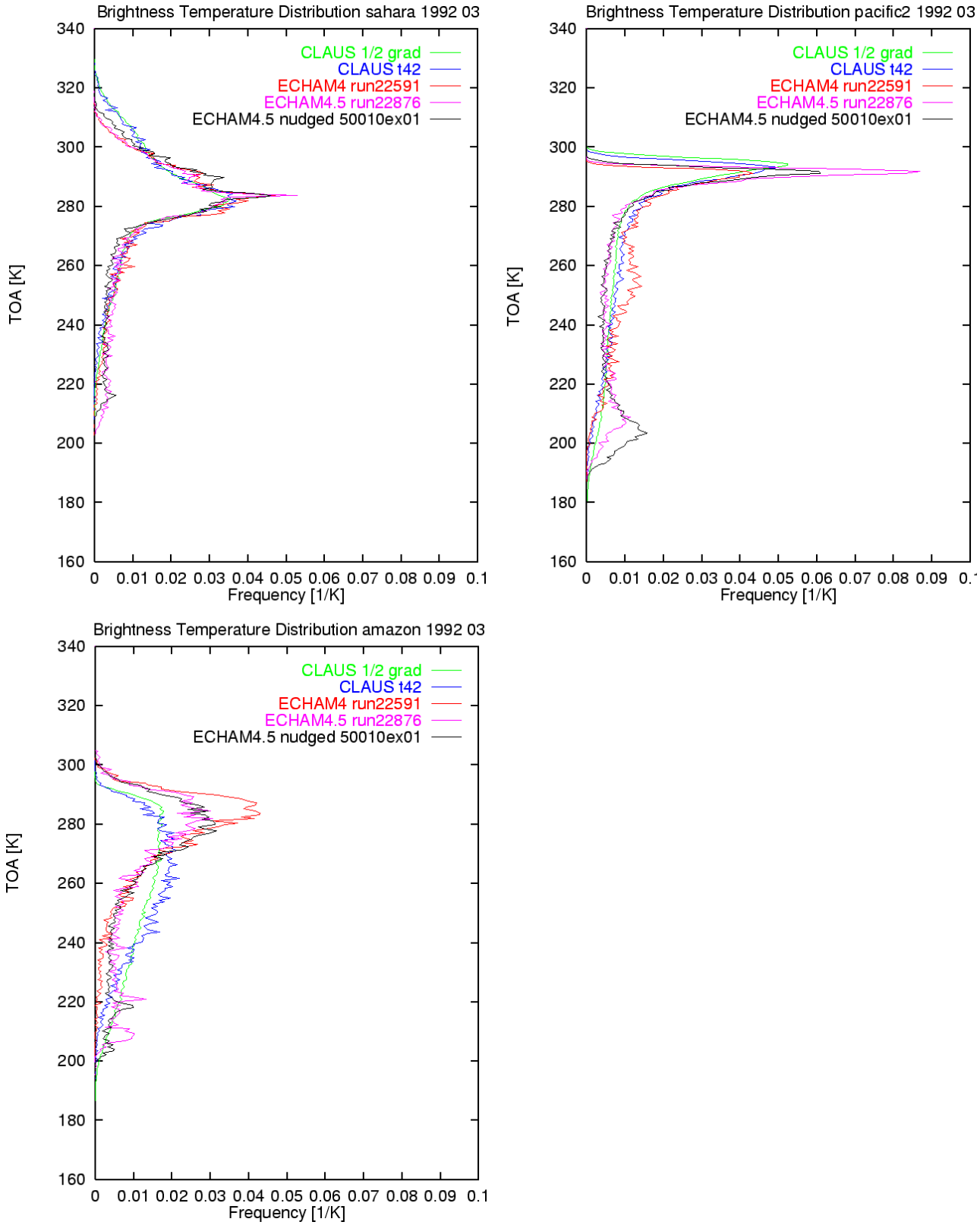

Figure 4: The brightness temperature distribution averaged during March 1992 is shown for a) the Sahara, b) the Pacific and c) the Amazonia region.

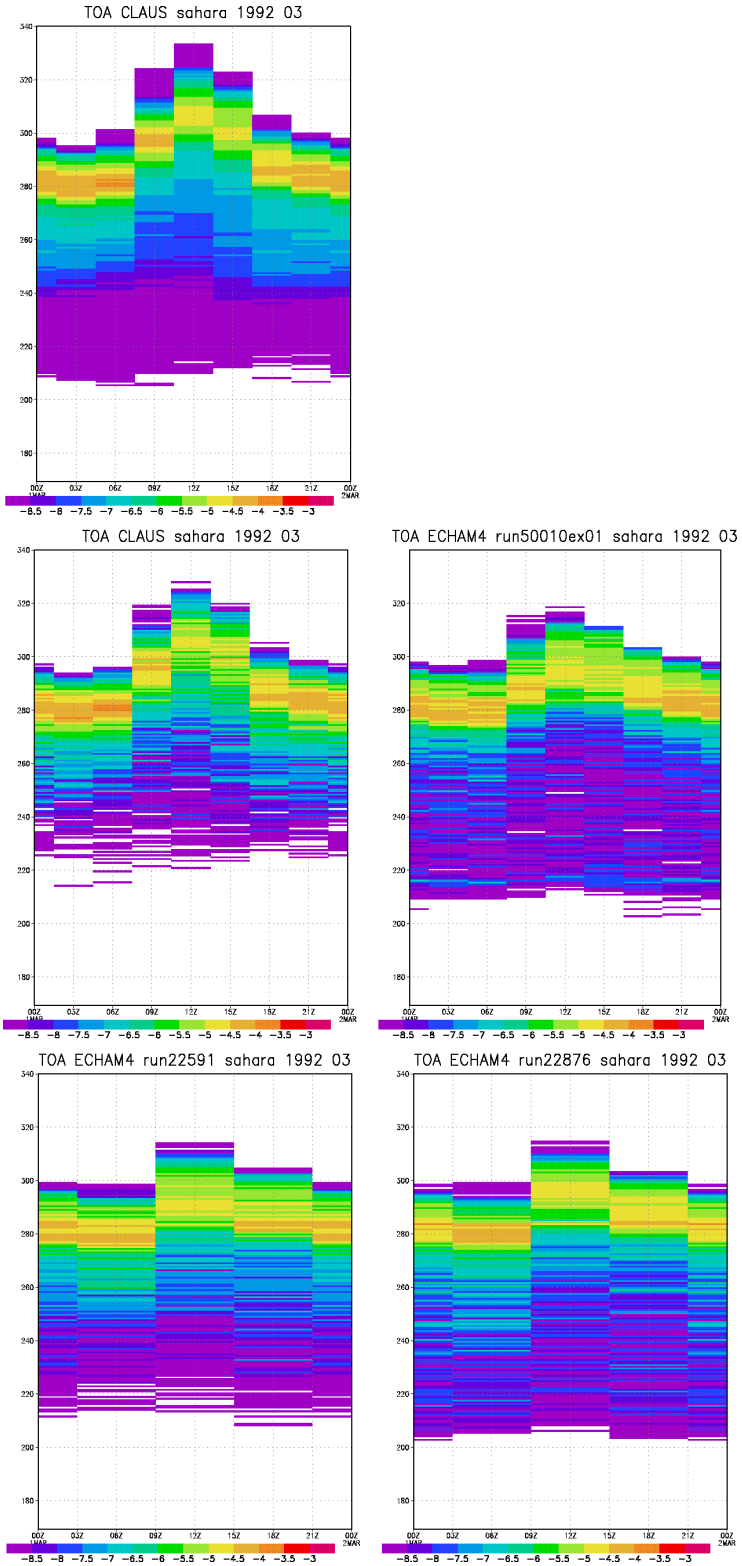

Figure 5: Mean diurnal cycle of brightness temperature distribution in March 1992 in the Sahara region derived by calculating averages for each time of the day, shown from the left to the right, top to bottom: a) CLAUS with 0.5° resolution, b) CLAUS averaged to T42 resolution, c) ECHAM 4.5 T42 nudged (all 3 hourly) run and d) ECHAM 4 and e) ECHAM 4.5 climate run (both six hourly).

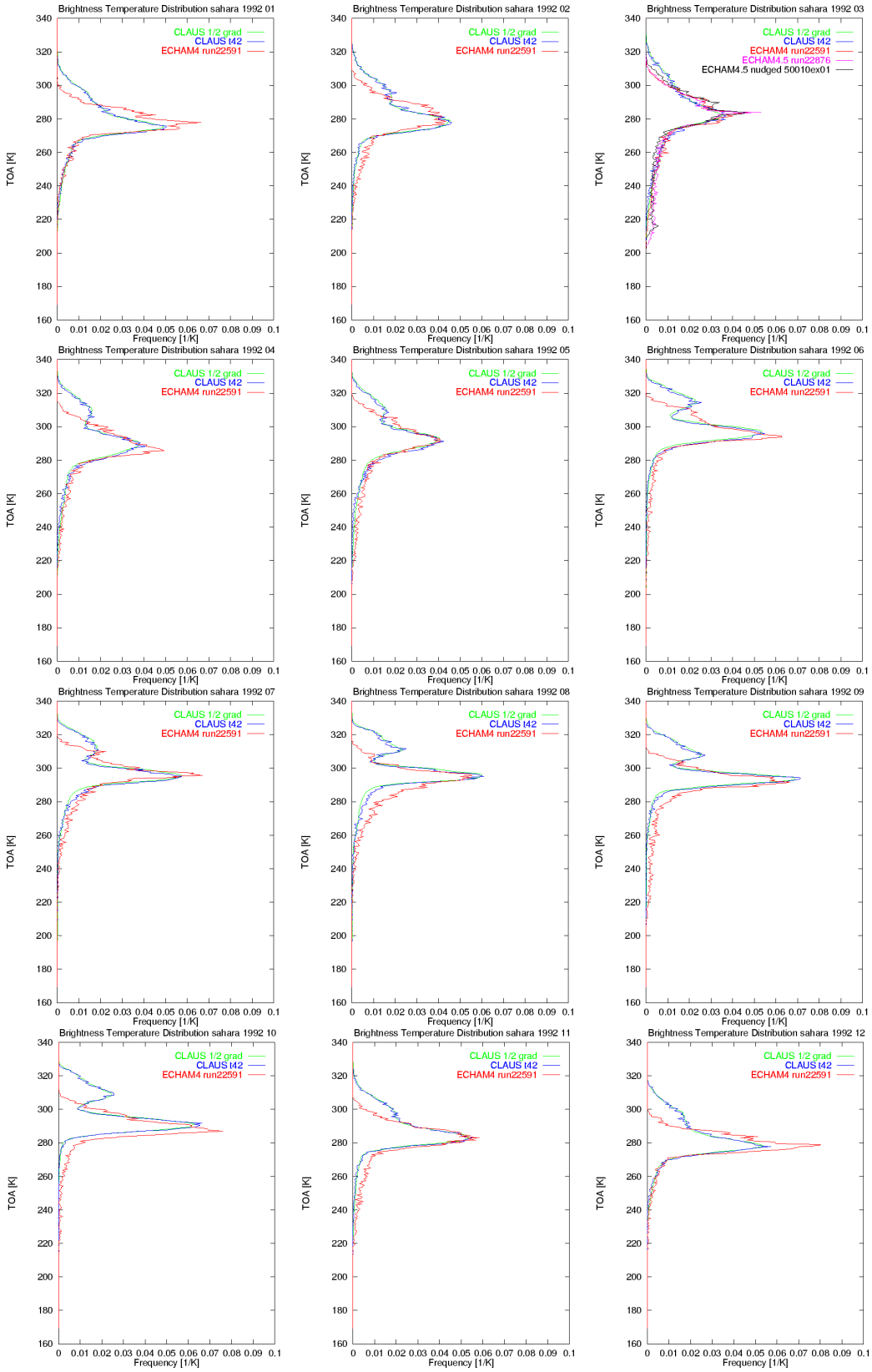

Figure 6: Observed (CLAUS) and modelled (ECHAM 4 climate run) brightness temperature distributions in the Sahara region for each month of the year 1992.

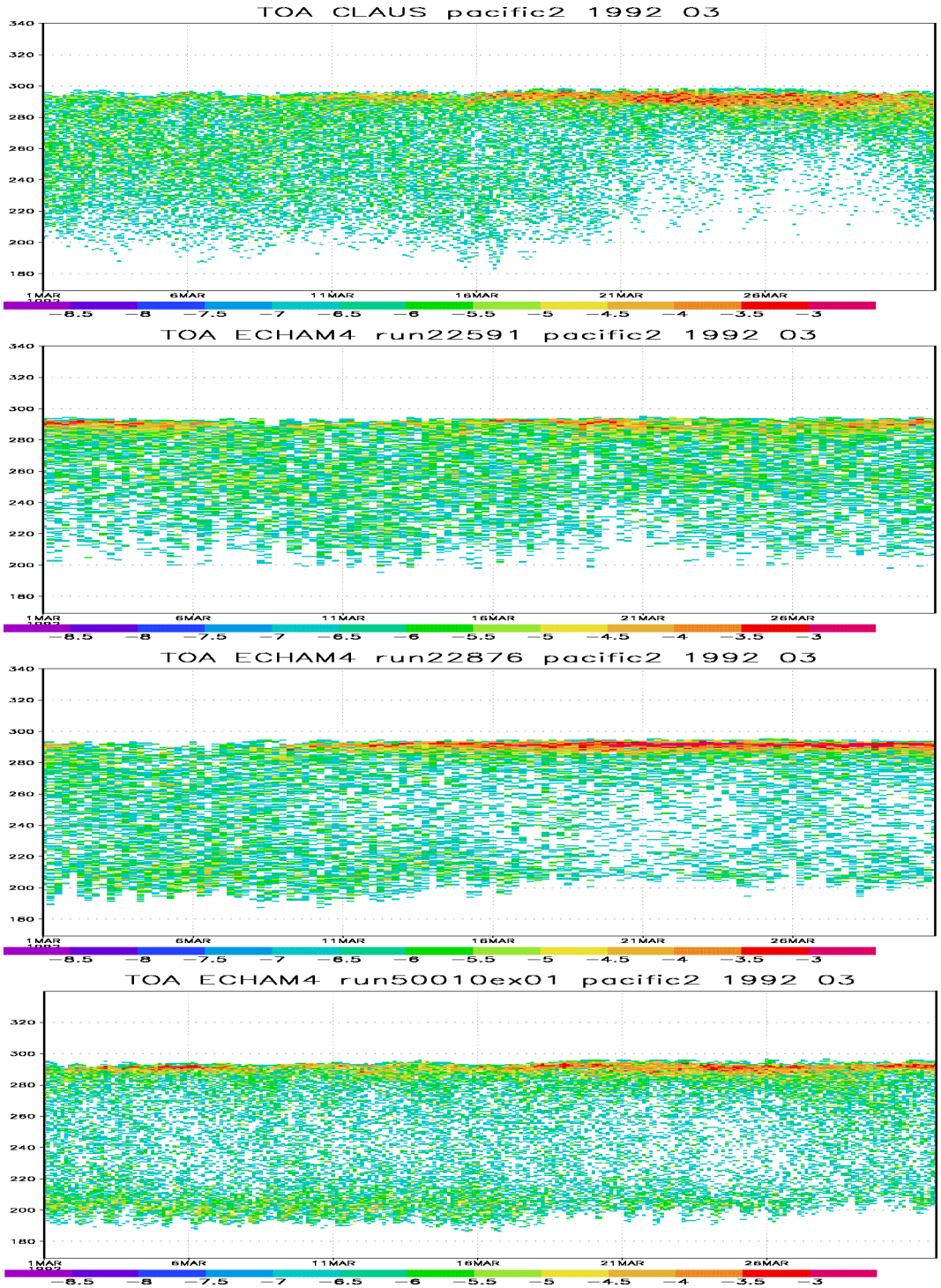

Figure 7: Brightness temperature frequency distribution for March 1992 in the Pacific region (160-200° E, 20-0° S). From top to bottom: a) temporal evolution of the CLAUS data set averaged to a T42 grid, and the b) ECHAM 4 and c) ECHAM 4.5 climate run as well as d) the ECHAM 4.5 nudged run.

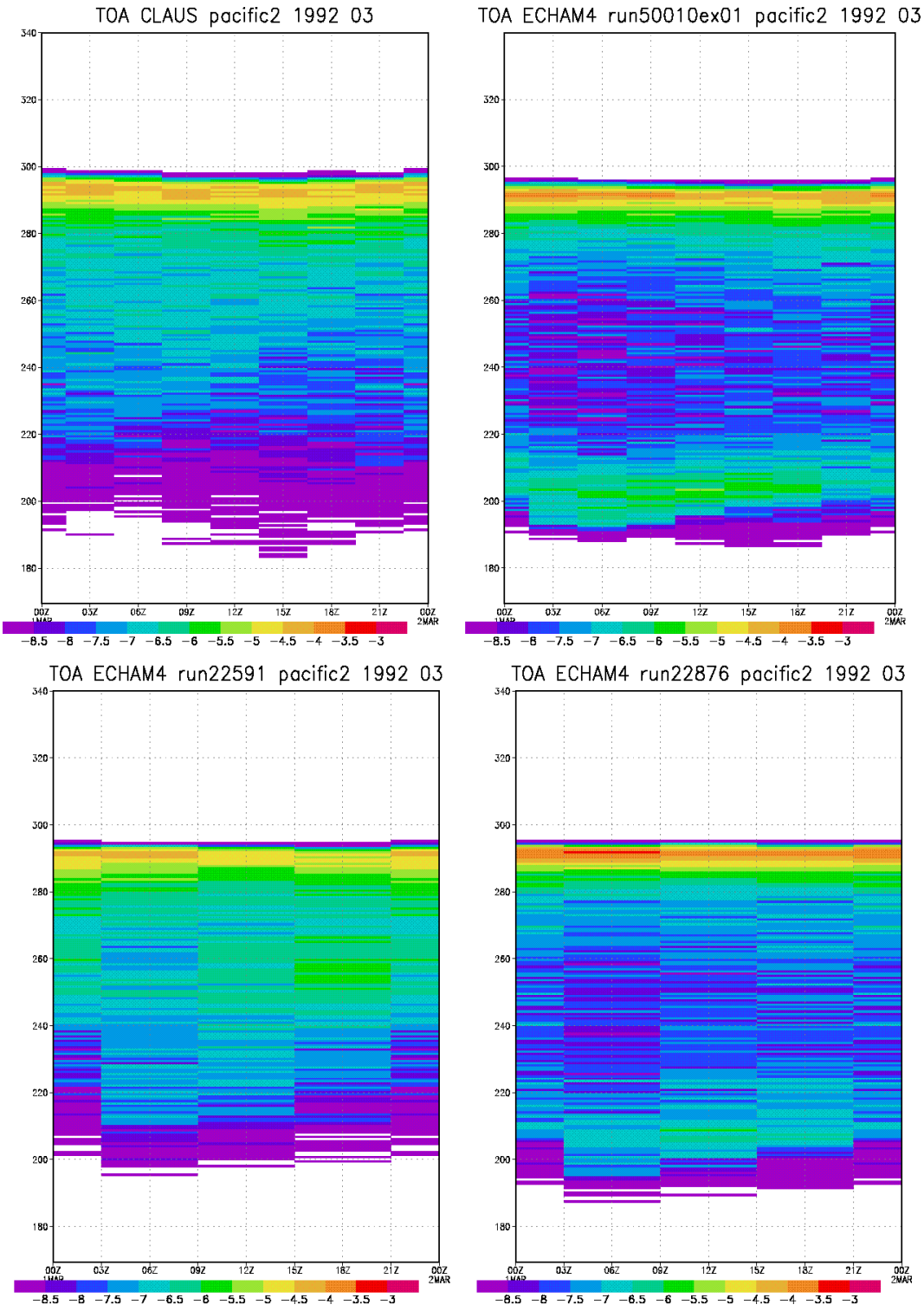

Figure 8: Mean diurnal cycle of brightness temperature distribution in March 1992 in the Pacific region derived by calculating averages for each time of the day, shown from the left to the right, top to bottom: a) CLAUS averaged to T42 resolution , b) ECHAM 4.5 T42 nudged run (both three hourly) and c) ECHAM 4 and d) ECHAM 4.5 climate run (both six hourly).

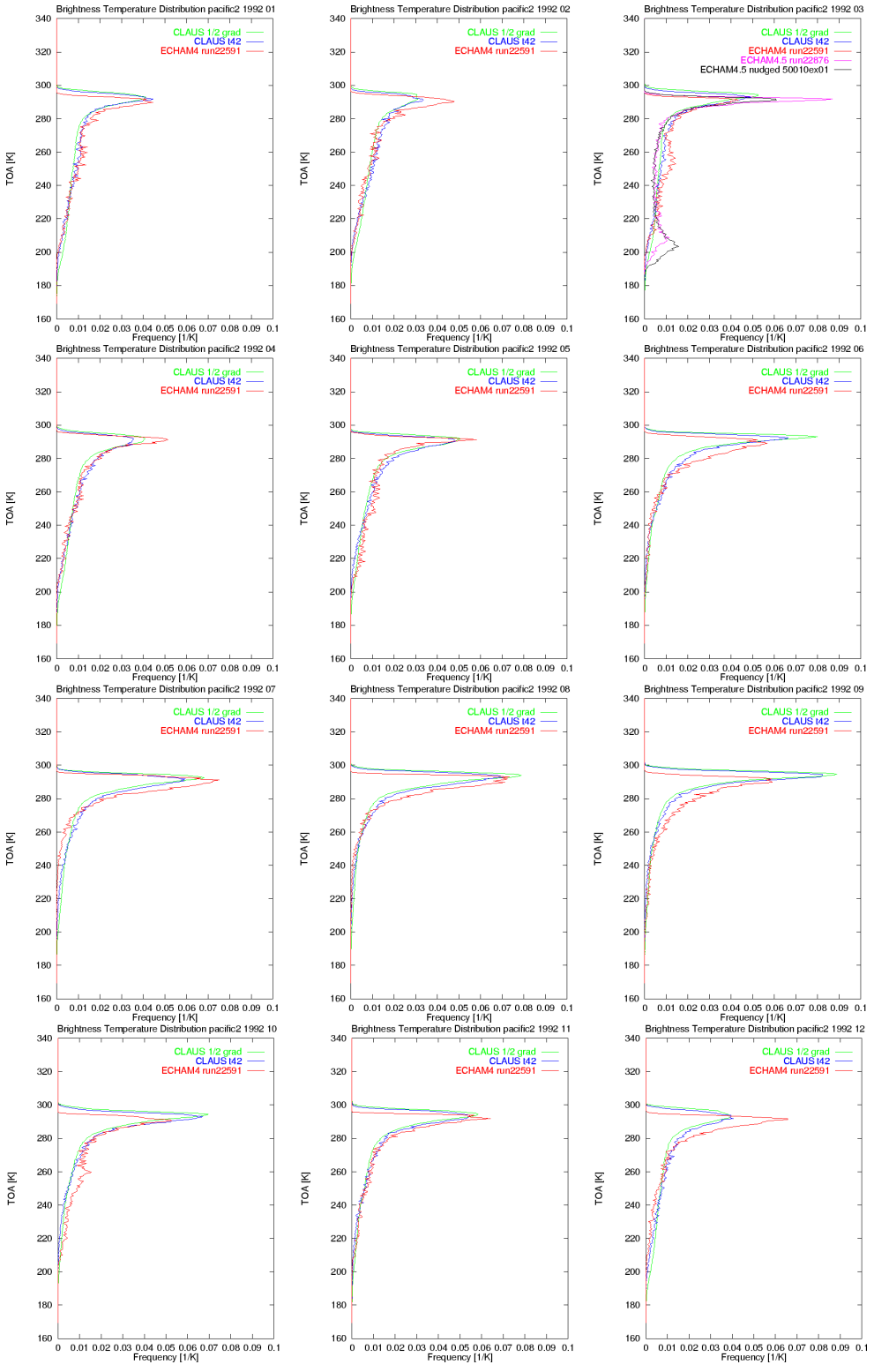

Figure 9: Brightness temperature frequency distribution for each month of the year 1992 in the Pacific region.

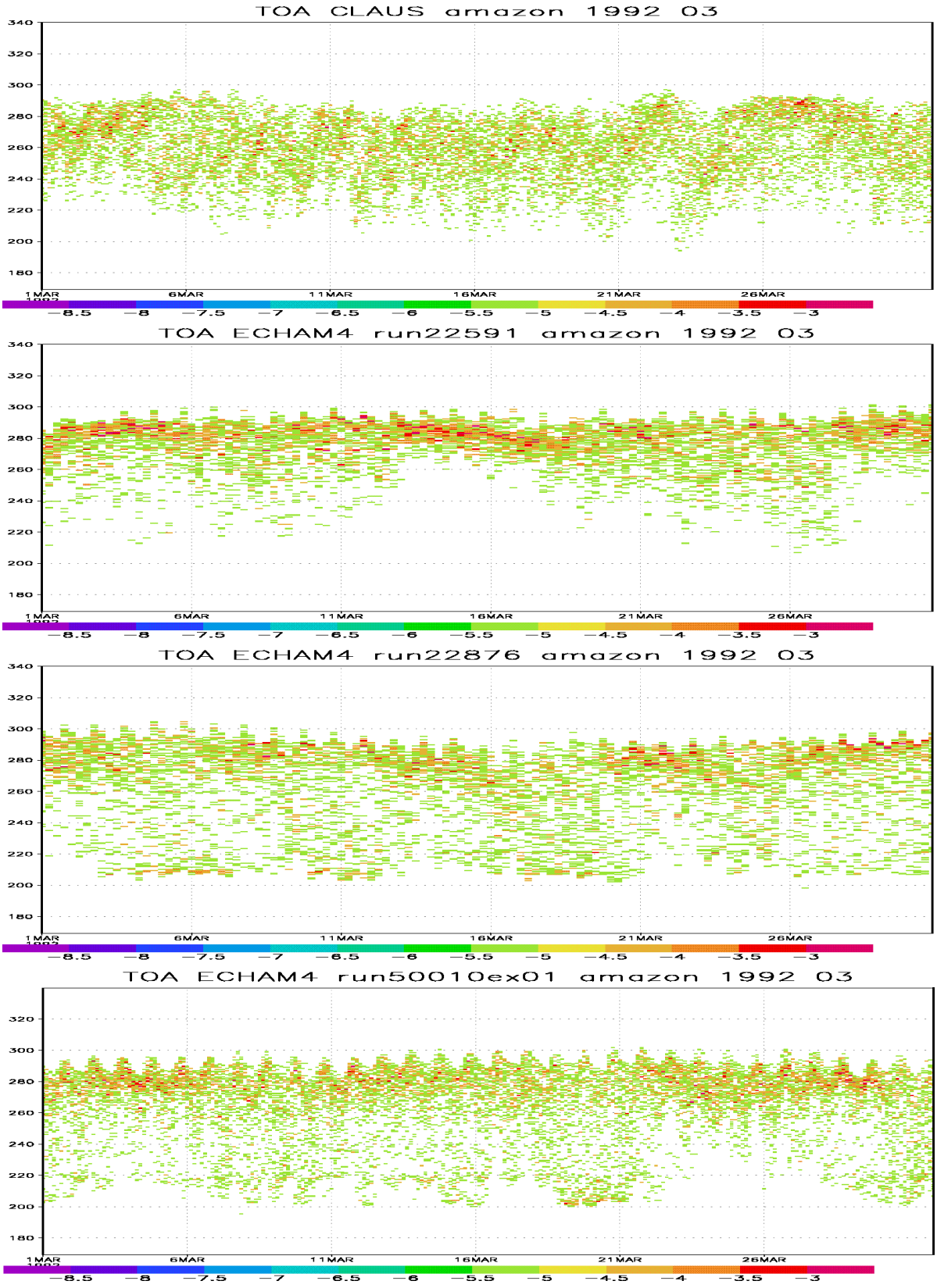

Figure 10: As Figure 7 but for the Amazonia region (290-310° E, 10-0° S).

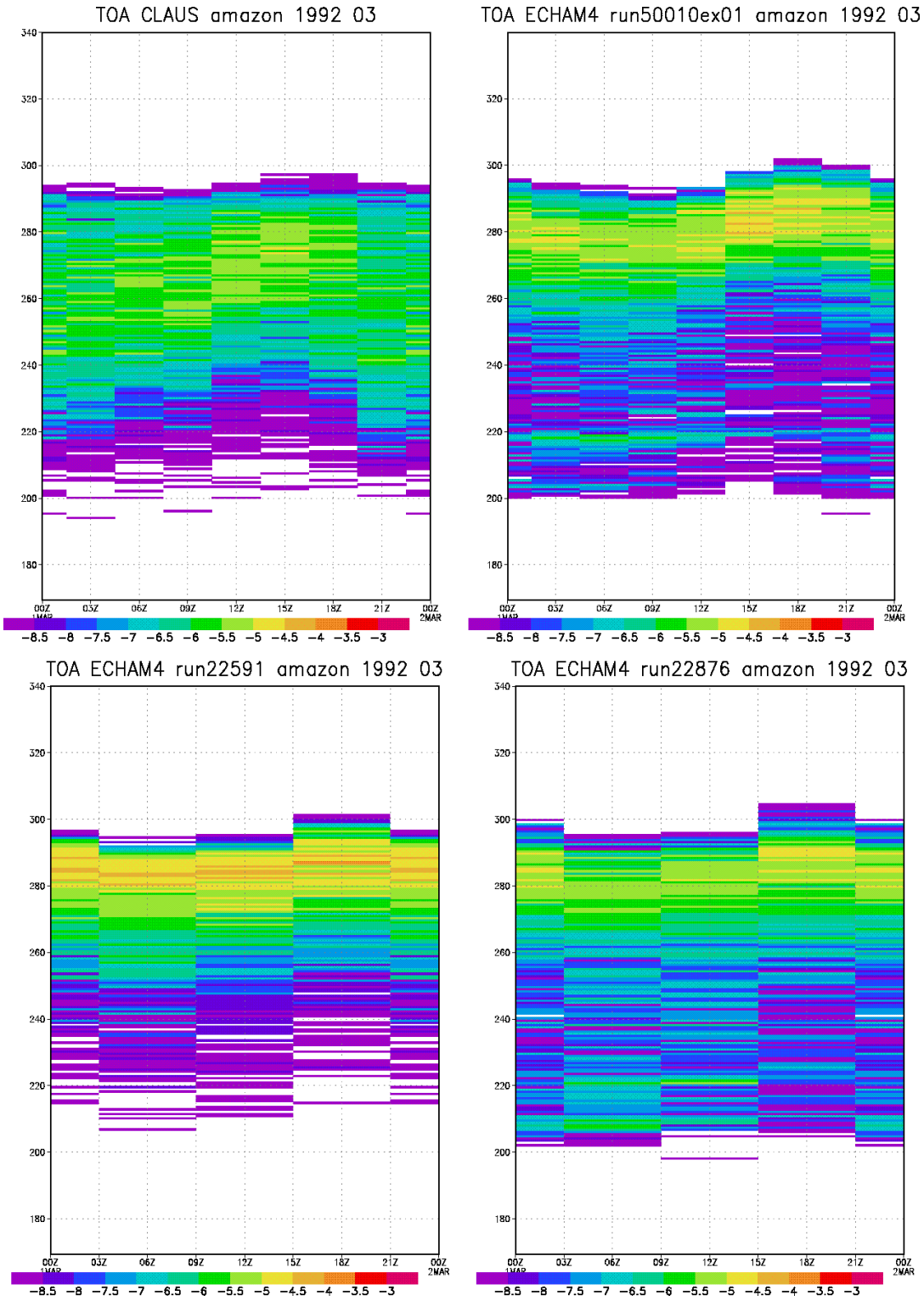

Figure 11: Mean diurnal cycle of brightness temperature distribution in March 1992 in the Amazonia region derived by calculating averages for each time of the day, shown from the left to the right, top to bottom: a) CLAUS averaged to T42 resolution , b) ECHAM 4.5 T42 nudged run (both 3 hourly) and c) ECHAM 4 and d) ECHAM 4.5 climate run (both 6 hourly).

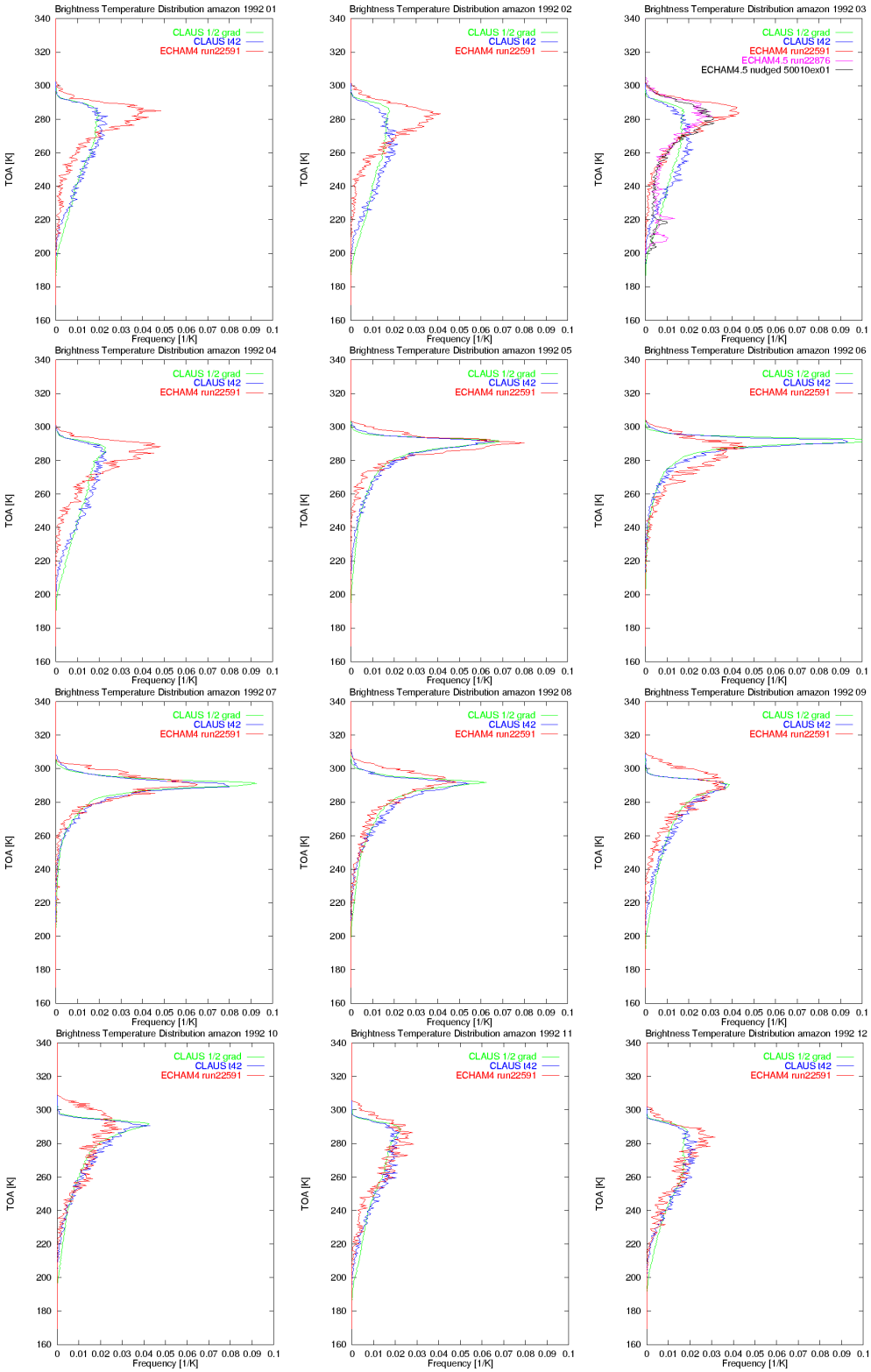

Figure 12: Brightness temperature frequency distribution for each month of the year 1992 in the Amazonia region.

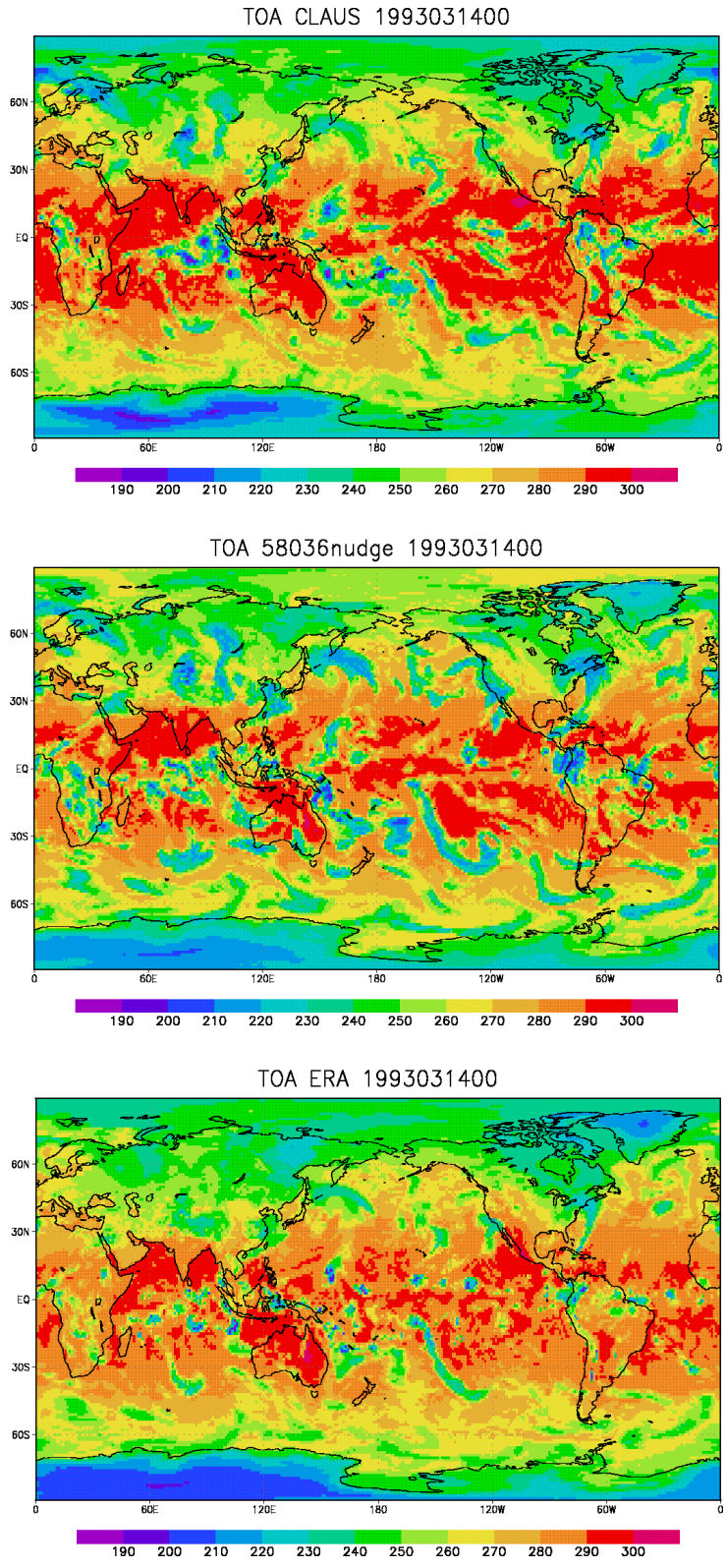

Figure 13: Snapshot of brightness temperature on March 14th 1993 as observed (CLAUS data, top, averaged to T106) and modelled by ECHAM 4 at T106 resolution (middle), nudged to the ECMWF reanalyses (bottom).

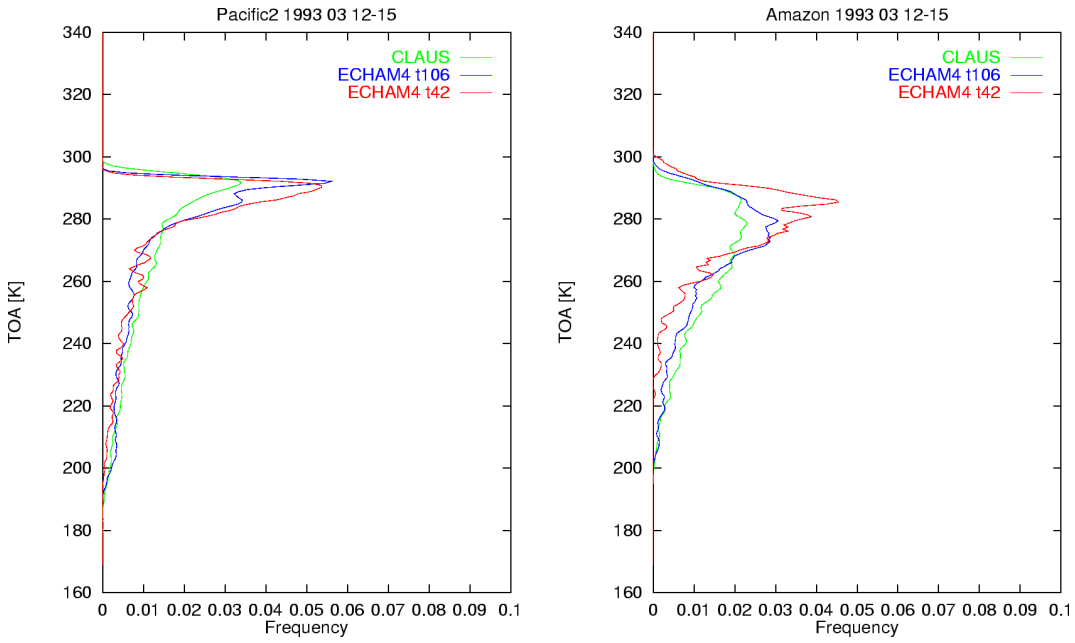

Figure 14: Brightness temperature histograms derived from observations (CLAUS) and nudged ECHAM 4 runs in T106 and T42 resolution in the Pacific and Amazonia region during the 4 days period of 12-15th March 1993.

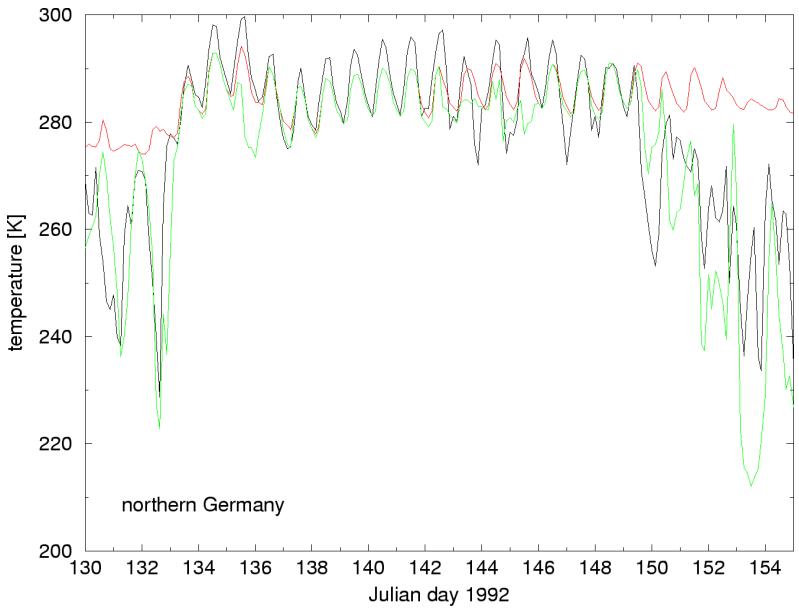

Figure 15: Temporal evolution of brightness temperature from May 9th until June 3rd at a model grid-point located in northern Germany (indicated red in Figure 1b). Observed (black, CLAUS averaged to the T42 model grid point), model derived (ECHAM 4.5 nudged run) total (green) and clear sky (red) brightness temperature.

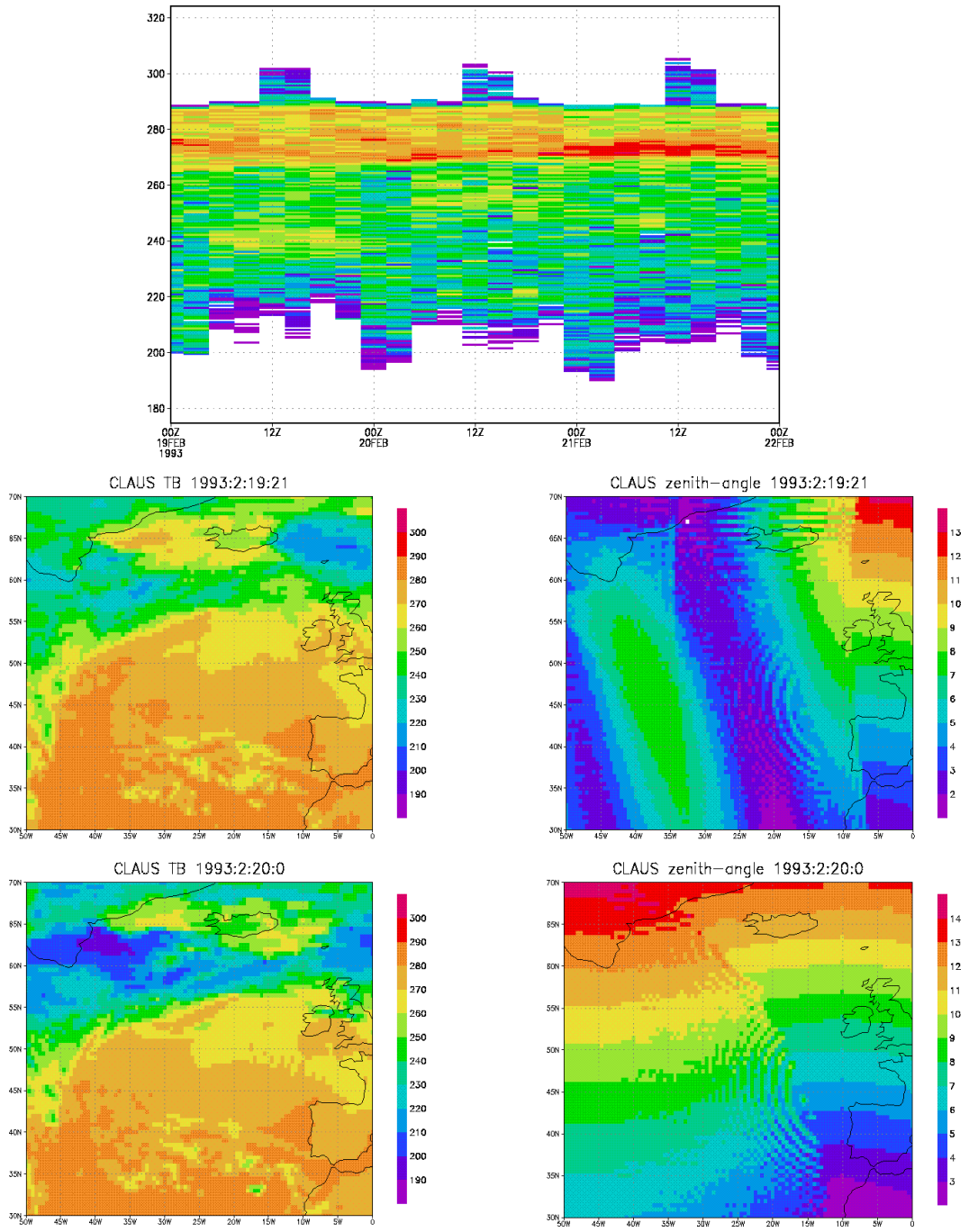

Figure 16: Example of insufficient limb darkening correction: brightness temperature distribution of the CLAUS data set in the domain 50W-0° W, 30N-70° N (top panel). Brightness temperatures at 19.3.1993 21 UT and 20.3.1993 0 UT ([K] left panels) and cosine of the zenith angle (scaled by a factor of 16, right panels).

Centre for Global Atmospheric Modelling [1]

Equatorial convectively coupled waves in CLAUS/ERA data and AMIP II integrations with the UM

Gui-Ying Yang and Julia Slingo

13 Introduction

Tropical convection contains variability on a variety of temporal and spatial scales, ranging from the individual clouds, to the cloud clusters associated with synoptic scale disturbances, to the superclusters or ensembles of clusters. Synoptic activity in the tropics is often associated with waves that can be related to the preferred equatorially-trapped modes of the atmospheric circulation based on shallow water theory (Wheeler and Kiladis 1999). Various modes (inertio-gravity, equatorial Rossby, mixed Rossby-gravity and Kelvin waves) can be detected, in many cases related to the active phase of the Madden-Julian Oscillation (MJO).

The understanding of equatorial waves and their annual variation is crucial for weather forecasting and climate prediction in the tropics and even for prediction in the extra-tropics. The development and maintenance of equatorial waves is important for forecasting hurricanes and typhoons in the tropics. Tropical disturbances may directly migrate pole-wards into the mid-latitude storm tracks or induce a remote response in the extratropics. Organised tropical convection is closely associated with the large-scale teleconnections through intraseasonal oscillation and response to El Ni o Southern Oscillation (ENSO). It has been known for some time that equatorial waves are important for the circulation of the middle atmosphere. Kelvin and mixed Rossby-gravity waves are the predominate disturbances of the equatorial stratosphere. They transport energy and momentum upwards, playing a crucial role in the general circulation of the stratosphere and may be instrumental in exciting the quasi-biennial oscillation (QBO). It has also been recognised that the various temporal and spatial scales of organised tropical convection play an important role in forcing the tropical oceans through variations in the surface stress and energy budget and may be instrumental in the development of ENSO. That being the case, it is important that GCMs are able to represent the convectively-coupled equatorial waves.

14 Identification of equatorial convectively coupled waves in CLAUS and model data

Based on shallow water theory, various modes (inertio-gravity, equatorial Rossby, mixed Rossby-gravity and Kelvin waves) can be detected in the window brightness temperature, using time-space spectral analysis (Hayashi 1982). This method of spectral analysis enables a distinction to be made between stationary vs. moving waves and between eastward vs. westward moving waves. Dependent on the meridional wave number (n),

the theoretical equatorially-trapped modes have structures with convective field symmetric (n odd) or antisymmetric (n even) about the equator (Matsuno 1966).

Figure 1 shows an analysis of the space-time spectra, averaged between 15°N and 15°S of the CLAUS brightness temperature (T_b) for the summer (May to October) of 1992. The space-time spectra for the symmetric and antisymmetric modes have been plotted separately to present n odd and n even modes. The power spectra have been divided by the background power (calculated by smoothing the power of T_b many times with a 1-2-1 filter in frequency and wavenumber) to highlight the dominant equatorial waves (Wheeler and Kiladis 1999). From shallow water theory, dispersion curves for the various modes are computed assuming a specified equivalent depth (h) and a basic state zonal wind (u). In Figure 1, the dispersion curves for a range of equivalent depths between 8m and 90m are shown for various modes (inertio-gravity (IR), equatorial Rossby (ER), mixed Rossby-gravity (MRG) and Kelvin waves); the dispersion curves have been Doppler shifted, assuming a basic state easterly of 3 ms^{-1}.

A similar space-time spectra analysis but for the winter of 1986/87 is shown in Figure 2. For this El Ni o winter a weaker basic easterly of 1 ms^{-1} is used to calculate the dispersion curves.

The two figures clearly demonstrate that tropical convection is organised on preferred space and time scales that coincide with those of theoretical equatorial waves. It is suggested that the tropical convection is indeed closely associated with Kelvin, equatorial Rossby, mixed Rossby-gravity, eastward inertio-gravity (EIG) and westward inertio-gravity (WIG) waves.

The results from the CLAUS data have been used to evaluate the organization of tropical convection in the UK Meteorological Office Unified Model (UM), current version of the atmospheric component of the Hadley Centre Climate Model (HadAM3). The model has a horizontal resolution of 3.75° longitude x 2.5° latitude and vertical resolution of 58 levels (with 25 levels in troposphere, top at 0.1hPa). Figures 3 and 4 show the analysis of the space-time spectra of modelled Outgoing Longwave Radiation (OLR) and vertical velocity (at 500 hPa for AMIP II integration (1979 - 95) with full physics.

The two plots show that the model has very limited wave activity. For OLR (Figure 3) there is no significant power associated with the equatorial waves as suggested by the observed data (Figure 1). It seems that the equatorial wave-related convection is poorly simulated by the OLR in the model. OLR requires link from convection to clouds. As indicated in Figure 4, the vertical velocity at middle troposphere in the AMIP II integration is able, to some extent, to represent the Kelvin, equatorial Rossby and mixed Rossby gravity waves; however, those wave signals are still less significant than observed.

15 The structure of equatorial waves in the CLAUS/ERA data and UM

Using the ECMWF Reanalysis (ERA) the structure of these modes is investigated by the application of appropriate space and time filters. The combination of the ERA and CLAUS data represents a unique opportunity to diagnose the relationship between the

dynamical structure and convective organization of equatorial waves and to evaluate the model.

Figures 5 and 6 give examples of the spatial distribution of the convection and wind fields of equatorial waves for the CLAUS/ERA data and model simulation in 1992 summer. Figure 5 shows the result for the westward mixed Rossby-gravity (MRG) wave (see the filtering box in Figure 1) and Figure 6 for the n=1 equatorial Rossby wave. It is apparent that the wave spatial structure in the observed data is consistent with that of the theoretical shallow water equatorial waves. For the MRG wave, the signal in convective and u fields has maxima off the equator, while the maximum signal of the v field is at the equator. For the n=1 ER wave, the maximum variation in T_b is off the equator with a second maximum at the equator; on the other hand the maximum variation in the u and v fields is at and off the equator, respectively. These are in agreement with the theoretical equatorial wave structures (Matsuno 1966). By comparing the observed results with those of the model, we can see that the model generally represents many features of the wave structures. However, it is apparent that there are some discrepancies between the observations and model. For instance, the second maximum in the convective field for the n=1 ER wave is missing in the model and the convective field is less trapped on the equator. For the MRG wave the spatial patterns for convective v fields in the model is quite different from those of observations.

16 Conclusion

The CLAUS data for Summer 1989 and Winter 1986/87 have been used to identify and characterise the equatorial waves based on time/space spectral analysis. It is shown that the tropical convection is closely related to the equatorial waves. The dynamical structures of these modes have been investigated using ERA data. The consistency between ERA and the CLAUS data has been assessed. The results have been used to evaluate the equatorial waves in AMIP II integrations with the UM. Preliminary results have shown that the model has very limited wave activity. Future work will focus on identifying the causes of this deficiency and assess performance of UKMO Unified Model with different vertical/horizontal resolutions and with changes to physical parameterisations (e.g. convective momentum flux, CAPE closure for convection).

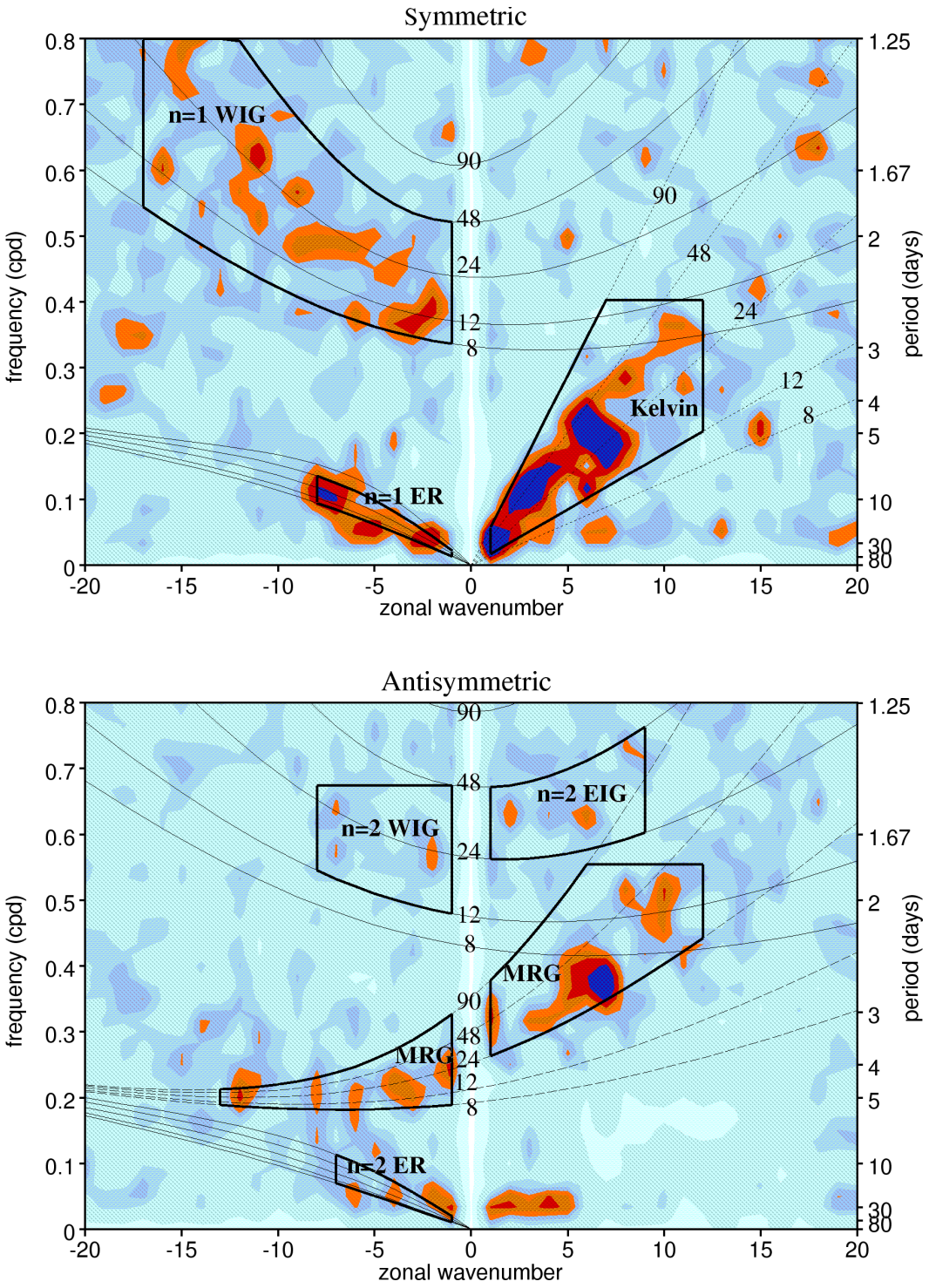

Figure 1: Zonal wavenumber-frequency power spectra divided by background power of the symmetric (the odd meridional mode number n) and antisymmetric (even n) components of CLAUS brightness temperature (T_b) for Summer (May-October) 1992. The power has been averaged over the latitudes 15° N-15° S. Superimposed thin lines are the dispersion curves of the odd and even n equatorial waves for the equivalent depths of h=8, 12, 24, 48 and 90m. The curves have been Doppler-shifted with a 3 ms^{-1} easterly basic state. Thicker boxes show the regions of the wavenumber-frequency domains used in Figures 5 and 6 for filtering of the various equatorial waves.

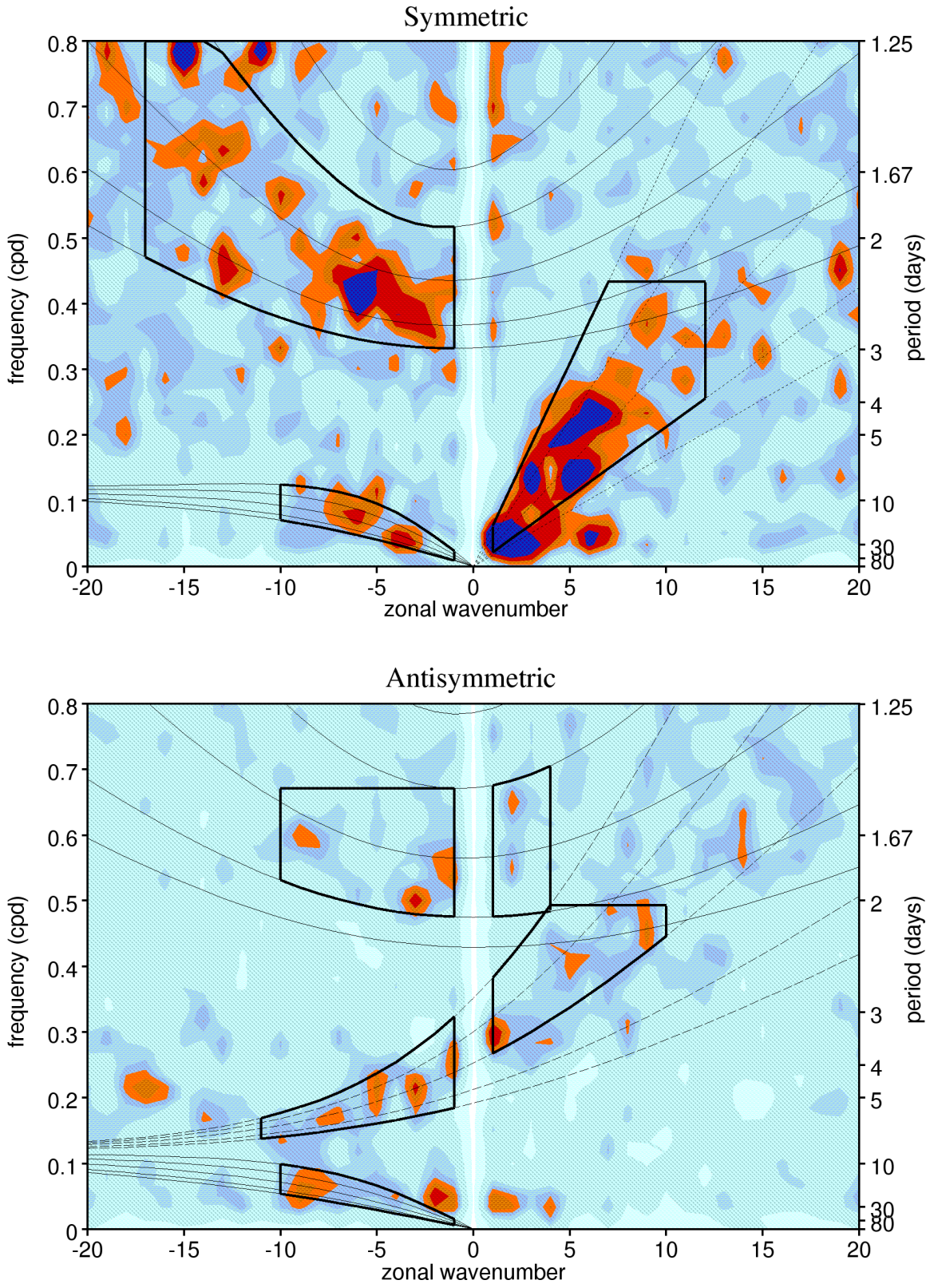

Figure 2: As Figure 1, but for Winter (November-April) 1986/87. The dispersion curves are calculated with a weaker easterly basic state of 1 ms^{-1} and theoretical waves as in Figure 1.

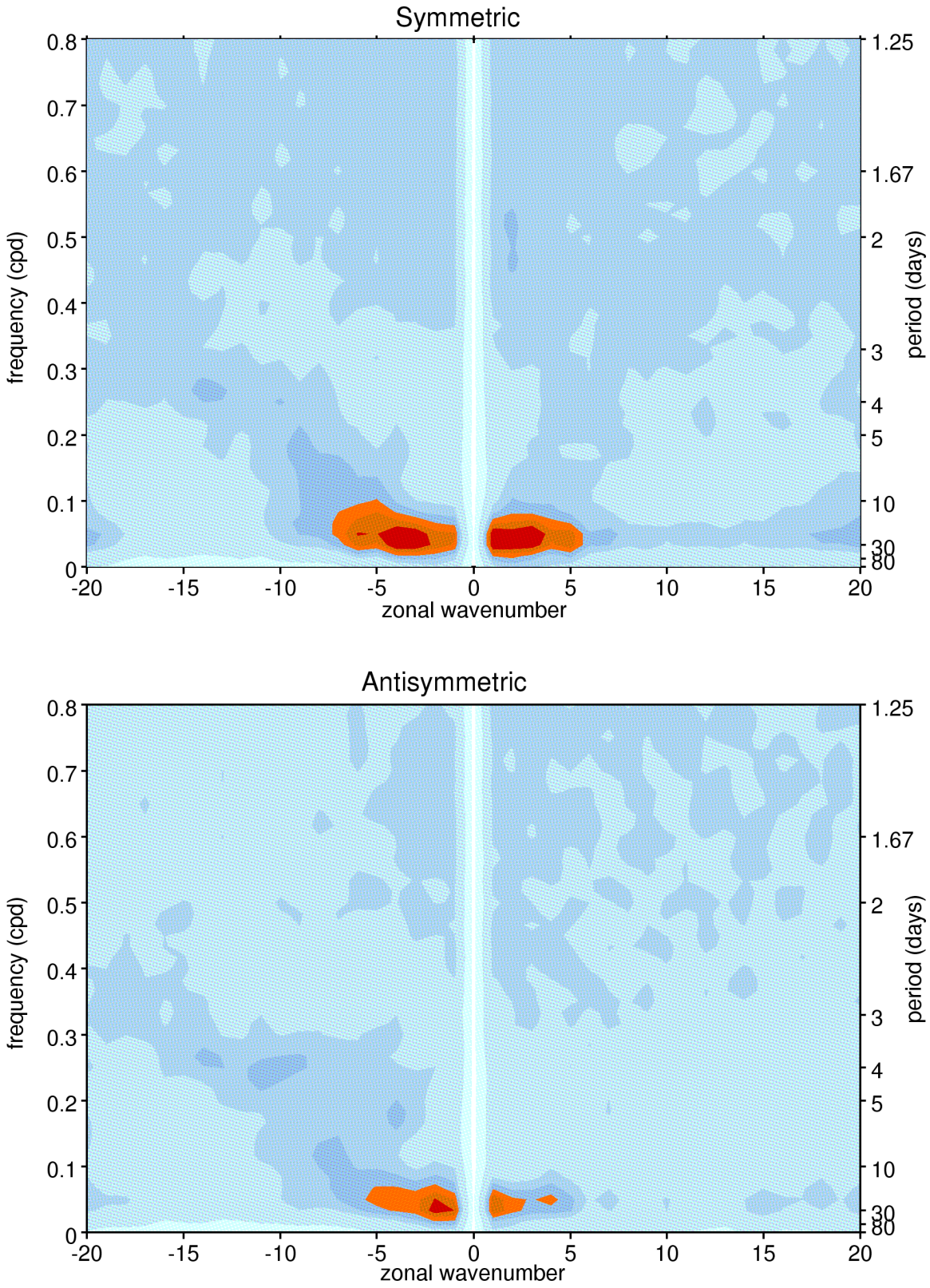

Figure 3: Zonal wavenumber-frequency power spectra divided by background power of the symmetric and antisymmetric components of AMIP II OLR for 15 Summer (May-October) mean over 15° N - 15° S.

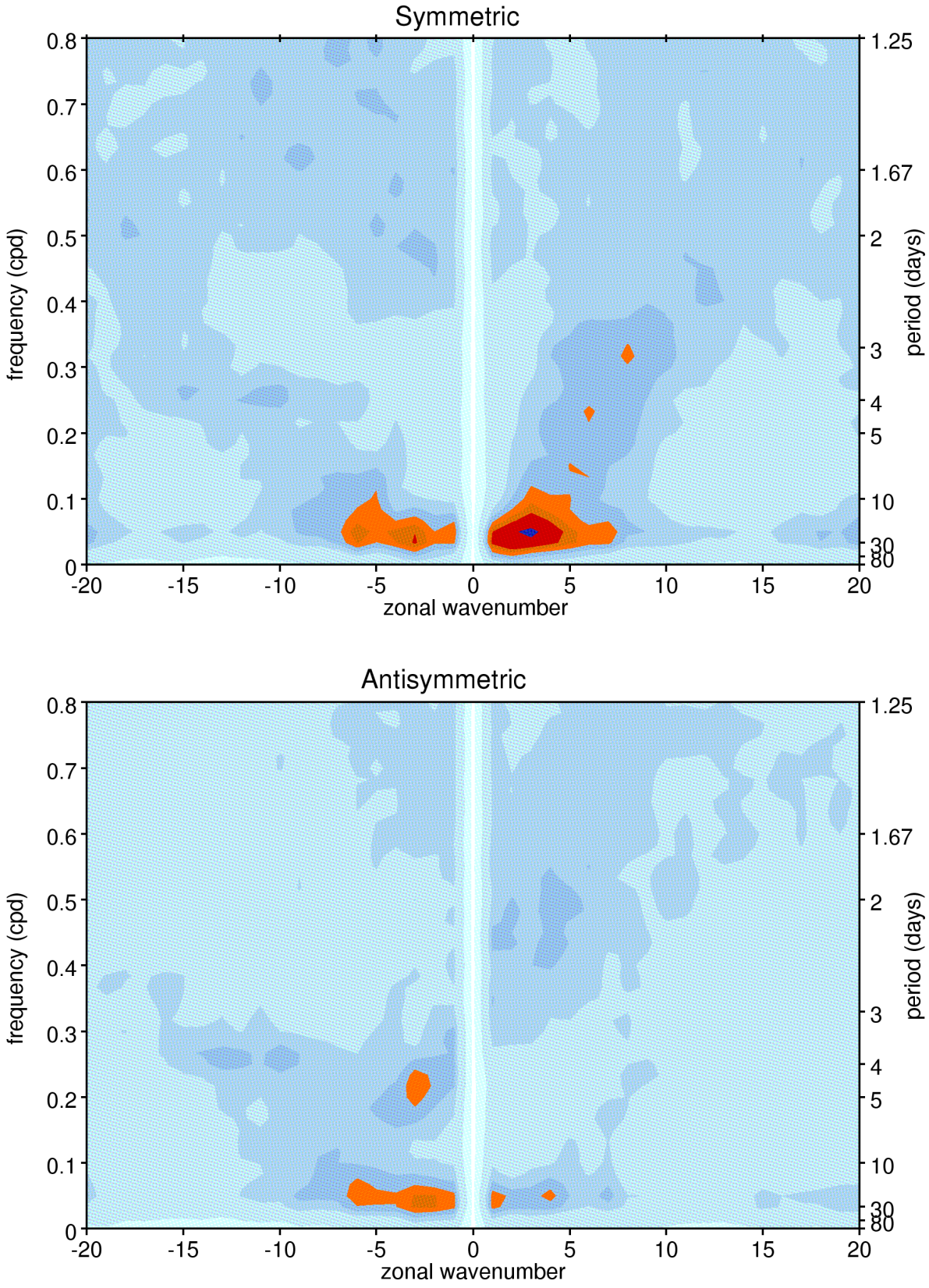

Figure 4: As in Figure 3, but for AMIP II vertical velocity at 500 hPa for 17 Summer mean over 16° N-16° S.

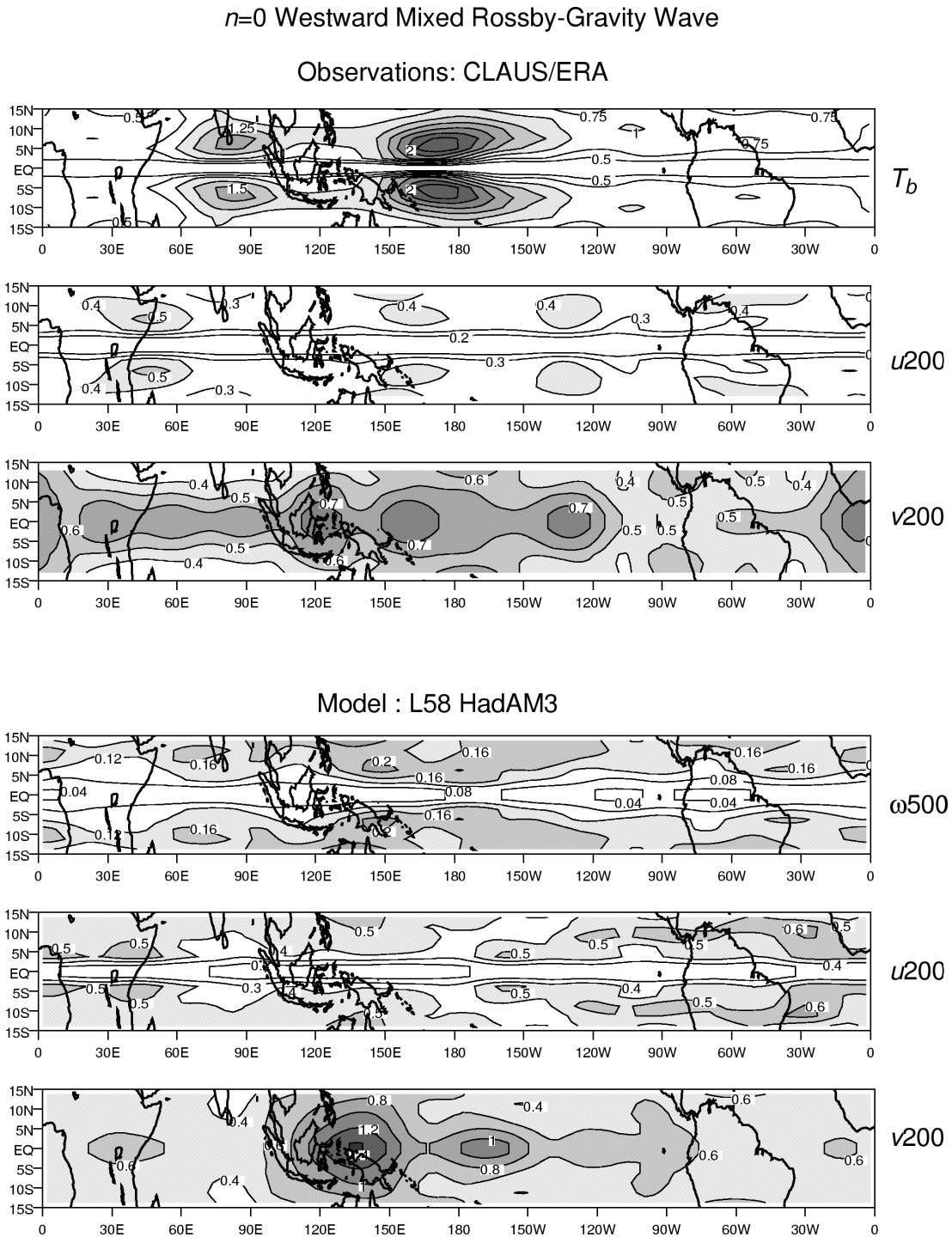

Figure 5: Geographical distributions of the standard deviation of the westward mixed Rossby-gravity (MRG) wave (see the filtering box in Figure 1) in Summer 1992, for observed CLAUS T_b, ERA zonal wind u and meridional wind v at 200 Pha (upper panels), UM modelled vertical velocity at 500 hPa, u and v at 200 Pha (lower panels).

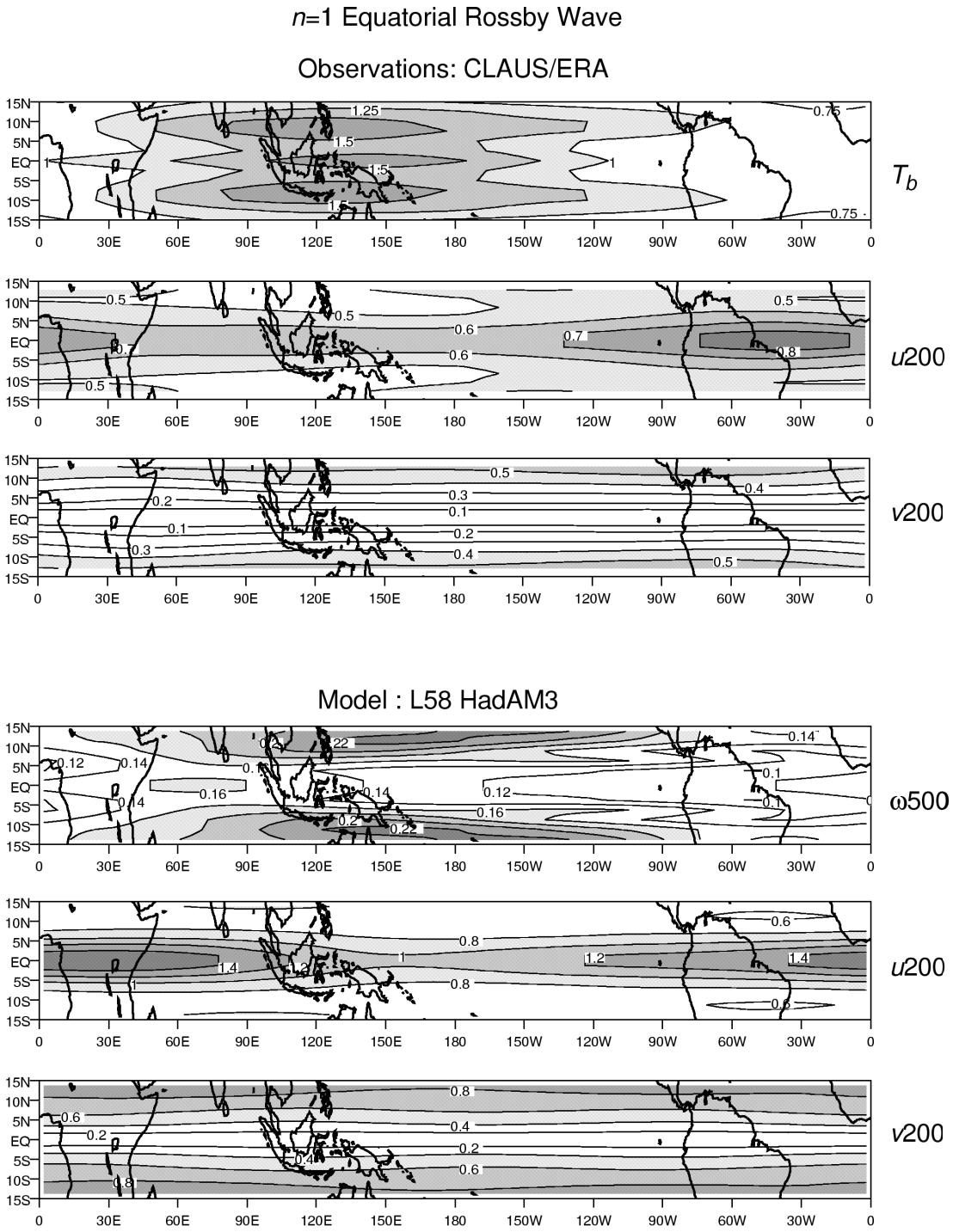

Figure 6: As Figure 5, but for the n=1 equatorial Rossby wave.

Centre for Global Atmospheric Modelling [2]

The Diurnal Cycle in the Tropics

Gui-Ying Yang and Julia Slingo

17 Introduction

The most fundamental modes of variability of the global climate system are the diurnal and seasonal cycles that are associated with large and well-defined variations in the solar forcing. As basic, forced modes of the climate system, the ability of general circulation models to represent these cycles should be a key test of the correctness of any model. On both diurnal and seasonal timescales, the proper representation of the interaction between the various elements of the atmosphere-land-ocean-cryosphere system is crucial for achieving the correct amplitude and phase of these forced modes. In particular, an accurate representation of the diurnal cycle over land and ocean provides a key test of many aspects of the physical parameterisations in a climate model, from radiative transfer and surface exchanges through to boundary layer, convective and cloud processes. It could be argued, therefore, that the simulation of the amplitude and phase of the diurnal cycle provides an ideal test bed for model parameterisations and for the representation of the interactions between the surface, the boundary layer and the free atmosphere.

The diurnal cycle in tropical cloudiness and precipitation has been extensively studied for several decades, but because of the scarcity of observational data, especially over the tropical oceans, these studies have used different data sources and have mostly been confined to limited regions. The earlier studies primarily used surface observations (e.g. Gray and Jacobson 1977; McGarry and Reed 1978; Albright et al. 1981), whilst later studies used various forms of satellite or radar-derived cloudiness and precipitation (e.g. Albright et al. 1985; Hendon and Woodberry 1993; Chang et al. 1995; Chen and Houze 1997; Sui et al. 1997; Garreaud and Wallace 1997). Most of these studies showed that the convective or precipitation maximum tended to occur in the early morning over the open oceans and in the late afternoon/early evening over land. However, some studies also showed an afternoon maximum in precipitation and cloudiness over the oceans (e.g. McGarry and Reed 1978; Augustine 1984; Shin et al. 1991). Janowiak et al. (1994) provided an extensive analysis of the diurnal cycle of cold clouds in the global tropics based on three-hourly geostationary satellite data that have been averaged on to a 2.5° latitude/longitude grid. Their results confirmed the existence of an early morning maximum in the extent of the coldest cloud tops (temperatures < 230 K) but also demonstrated that warmer clouds, typical of mid-level convection, were most prevalent in the afternoon.

In this study, the CLAUS data are used to investigate the diurnal variation of tropical convection (and, by implication, precipitation), cloudiness and surface temperature, and to provide a climatology of the amplitude and phase of the diurnal cycle for all regions of the tropics (30° N-30° S). As an example of the application of the results to model evaluation, a diagnosis of the

diurnal cycle in the Met. Office Unified Model has been performed and the results will be described briefly.

18 The CLAUS dataset

It is important to note here that the radiance resolution (eight bits) of the source ISCCP B3 data used in CLAUS is relatively coarse, so that the precision of the gridded window brightness temperature in the CLAUS dataset is only of the order of 0.7K. This is adequate for diagnosing the diurnal cycle in cumulus convection and land surface temperature, but may not be sufficient to delineate the subtle diurnal variations in sea surface temperatures (SST) and stratocumulus decks. CLAUS data for four winters (December - February 1984/85, 1986/87, 1987/88 and 1991/92) and four summers (June - August of 1985, 1986, 1987 and 1992) are currently available and have been used in this study. All results are based on an average over the four winters and four summers, respectively. There is considerable consistency between the characteristics of the diurnal cycle from year to year, which suggests that four years of data are sufficient to provide a useful climatology.

Figures 1 and 2 show the seasonal mean brightness temperature for northern winter and summer, as well as the total standard deviation of the three-hourly samples and the percentage of the total variance that is associated with intra-diurnal (less than or equal to 1 day) time-scales. The intra-diurnal variance was computed by performing a spectral analysis of the brightness temperature time series at each grid-point and then averaging the power for timescales less than or equal to 1 day. To perform this calculation accurately, it requires a complete time series at each grid point; grid points where this is not the case are therefore treated as missing data in Figures 1 and 2[1].

As expected, the seasonal mean brightness temperature distribution (top panels, Figures 1 and 2) follows the climatological distributions of Outgoing Longwave Radiation (OLR) derived from broadband satellite measurements (e.g. Harrison et al. 1990) and also those of precipitation (e.g. Xie and Arkin 1996), with the coldest temperatures coincident with the minima in OLR and maxima in precipitation. The change in the mean brightness temperature field between DJF and JJA shows the seasonal transition of the Intertropical Convergence Zone (ITCZ) and the movement of the major areas of convection associated with summertime continental convection and monsoons. In both seasons, the highest brightness temperatures tend to occur during summer over the desert areas of Australia and North Africa. High temperatures are also seen in the subsiding, dry, and predominantly cloud-free regions of the subtropical anticyclones.

Comparison of the total standard deviation of the brightness temperature (middle panels, Figures 1 and 2) with the seasonal mean field shows that most of the convective regions, defined by low brightness temperatures, are coincident with regions of large standard deviation. This is in agreement with other observational and modelling studies (e.g. Salby et al. 1991; Slingo et. al 1992). Also it can be seen that for most of the non-convective regions, such as the subtropical anticyclones, the standard deviation is small, the exceptions being the clear sky land regions, where the standard deviation is almost entirely related to intradiurnal timescales (bottom panels,

[1] The percentage variance explained by intradiurnal timescales was only computed for the three summers of 1986, 87 and 92 due to large areas of missing data during the summer of 1985. The winter datasets were all complete.

Figures 1 and 2). Over the deep convective regions of the tropical oceans, intradiurnal timescales only account for between 15 and 20% of the total variability. As shown by several authors (e.g. Salby et al. 1991; Slingo et al. 1994) most of the variability in tropical oceanic convection is associated with synoptic systems (e.g. easterly waves) and intraseasonal phenomena (e.g. Madden Julian Oscillation). For land based tropical convection, the intradiurnal timescales account for much more of the total variance, typically between 30 and 40%.

The results shown in Figures 1 and 2 demonstrate that the CLAUS dataset provides a good climatology of tropical brightness temperature and therefore, by inference, convective activity and land surface temperatures. Through its high temporal sampling and global coverage, it also provides a good measure of tropical variability, in particular the degree to which that variability is associated with intradiurnal timescales. In the following section the methodology used to analyse the coherent diurnal cycle will be described.

19 Methodology for analysing the diurnal cycle

Time series analysis and evolutionary histograms will be used to study the coherent diurnal cycle in tropical convection and land surface temperature. By computing the long term (seasonal) mean for each of the eight times of day (three-hourly intervals), the coherent diurnal variation, which is directly linked to the response of the surface/atmosphere system to the diurnal cycle in the solar radiation, can be obtained. The amplitude and phase of the diurnal and semidiurnal harmonics can then be calculated using Fourier analysis. The phase of the diurnal harmonic indicates the local time of the maximum in the variable considered. Calculation of the semidiurnal and 8-hour harmonics showed that the amplitudes of these harmonics are much smaller, generally about 40% and 15% of that for the diurnal harmonic.

The evolutionary histogram approach, which has been used in several studies for analysing the diurnal cycle (e.g., Morcrette 1991), will be used to show the composite diurnal evolution of convection and land surface temperature over various selected, nearly homogeneous, regions. In an evolution histogram of brightness temperature (T_b), the number of pixels (grid points) within each T_b interval is plotted as a function of time of day. In general, high values of T_b correspond to radiation emitted from at or near the surface, and lower values to radiation emitted from clouds. This technique provides a clear overview of the evolution of surface temperature and convection with time of day. In this study, the evolution histograms are constructed by binning the three-hourly T_b data into 4 K bins. The diurnal variation in the histogram of T_b is identified more clearly by computing the percentage anomaly at each three-hourly interval against the daily mean histogram of T_b. Currently, models do not diagnose a window brightness temperature comparable to that observed by satellites, although algorithms are being developed and implemented. Therefore, for the application of the CLAUS data to model evaluation, it has been necessary to transform the model output and the CLAUS data to common variables. Firstly, the model s Outgoing Longwave Radiation (OLR) has been converted to an equivalent brightness temperature using the relationship between the observed window brightness temperature (T_b) and the flux equivalent brightness temperature (T_f), as proposed by Ohring and Gruber (1984):

$$T_f = T_b (a + b. T_b) \qquad \text{(Equation 1)}$$

- where a=1.228 and b=-1.106*10 -3 K^{-1}. Then T_f is related to OLR by:

$$OLR = \sigma . T_f^4 \qquad \text{(Equation 2)}$$

- where σ is the Planck constant. Secondly, the CLAUS data have been converted to equivalent precipitation on the basis that the coverage of cold clouds (with brightness temperature or equivalent blackbody temperature less than some threshold) is correlated with accumulations of precipitation during some period (e.g., Richards and Arkin 1981; Hendon and Woodberry 1993; Goodman et al. 1993). In this study, a threshold technique for estimating tropical deep convective precipitation, developed by Hendon and Woodberry (1993) and used for studying the diurnal cycle in tropical convection, has been applied to the CLAUS data. Known as the Deep Convective Activity (DCA) index, it relates brightness temperature to an equivalent precipitation rate:

$$DCA = a.(230 - T_b) \text{ for } T_b < 230K \qquad \text{(Equation 3)}$$

$$DCA = 0 \text{ otherwise}$$

- where a = 0.29 mm. hr^{-1} $K^{-1}$and the choice of the 230 K threshold is based on the work of Fu et al. (1990). The seasonal mean precipitation rate produced by applying Equation 3 to the CLAUS data compares well with other precipitation climatologies (e.g. Xie and Arkin 1996). The advantage of converting the observed brightness temperature to an equivalent precipitation rate is that it provides a different view of the diurnal cycle; it delineates the diurnal cycle in deep convection (i.e. cold cloud tops) from that in land surface temperatures.

As already discussed in Section 2 the transient characteristics of convective and non-convective regimes are different, with the variability over clear sky land areas being dominated by intradiurnal timescales (Figures 1 and 2).

20 Observed diurnal cycle in brightness temperature and derived precipitation

20.1 Amplitude and Phase of the Diurnal Cycle

Figure 3 shows the amplitude of the diurnal (24 hours) harmonic in brightness temperature (T_b) and estimated precipitation (DCA algorithm) for northern winter (DJF) and northern summer (JJA), respectively[2]. For both seasons, the largest amplitude of T_b occurs over land clear sky regions, as a result of the large response of the surface temperature to daytime solar heating. The maxima in the amplitude of the diurnal cycle in T_b occur over the Atacama and Namib Deserts in DJF and over Saudi Arabia and the Sahara and Kalahari Deserts in JJA. The convective regions over land (e.g. South America in DJF, Indian subcontinent in JJA, Indonesian Islands) also show large amplitudes for T_b, consistent with the forcing of convection by the diurnal cycle in land surface heating. This is particularly pronounced over north-east India during the summer monsoon season and demonstrates the importance of the diurnal cycle in modulating monsoon

[2] The diagnosis was also completed for the transition seasons, March-May and September-November. The results were similar and will not be shown here.

rainfall. An interesting feature of Figure 3 is the spreading of the diurnal amplitude from land convective regions out over the adjacent oceans, suggestive of complex land-sea breeze effects. This is especially marked around the Indonesian Islands in DJF, and over the northern Bay of Bengal and along the central American and Mexican coasts in JJA.

Over the majority of the tropical oceans, the diurnal cycle is much more subtle and is best captured by the estimated precipitation field which focuses on the variations in the cold cloud amounts. The results shown in Figure 3(c and d) demonstrate that there is a small but significant diurnal variation in oceanic precipitation of the order of 3-6 $mm.day^{-1}$ along the Intertropical and South Pacific Convergence Zones (ITCZ and SPCZ) in both seasons. The amplitude of the diurnal cycle inferred from the CLAUS data is similar to that suggested by Janowiak et al. (1994) and Chang et al. (1995) based on SSM/I data.

The phase of the diurnal harmonic of brightness temperature and estimated precipitation for DJF and JJA is given in Figure 4 in terms of the local time of the maximum. Over clear sky land regions, such as the Sahara, the maximum in T_b occurs consistently about 1-2 hours after the peak in the solar heating, indicative of a slight lag in the land surface heating due to the thermal inertia of the soil. In comparison, over oceanic clear sky/non-convective regions, such as the subtropical anticyclones and the stratocumulus regions off the western seaboards, the maximum in T_b occurs in the mid to late afternoon. However, this result may not be very robust since the amplitude of the diurnal cycle is small and the precision of the raw T_b data is rather poor, due to the packing density of the ISCCP B3 data (see Section 2). Nevertheless, the phase results are entirely consistent with other observations of the diurnal cycle in marine stratocumulus (e.g. Hignett 1991; Bergman and Salby 1996), which have shown a minimum in cloud optical depth/amount in the late afternoon. This has been explained by, firstly, the decoupling of the surface and planetary boundary layers during the day, which leads to a reduction in the surface moisture supply to the cloud layer, and secondly, by the short-wave radiative warming of the cloud layer itself (e.g. Smith and Kao 1996).

The phase of the diurnal harmonic in the estimated precipitation (Figure 4(c and d)), emphasises the timing of the maximum in deep convection. The continental areas show that the maximum in deep convection/precipitation tends to occur in the late afternoon and evening, between 1700 and midnight local time. However, there are some interesting regional variations (e.g. central Africa, 0° - 20°N, in JJA), which suggest that orography may play an important part in modulating the phase of the diurnal cycle. Over Africa, Mesoscale Convective Systems (MCS; e.g. squall lines) are often triggered by orography and elevated daytime heating (e.g. Rowell and Milford 1993; Hodges and Thorncroft 1997). In Figure 3(d), there is a good correspondence between the maxima in the amplitude of the diurnal harmonic and the elevated terrain of the Ethiopian Highlands, the Cameroon Highlands, Jos, Air and the Guinea Highlands. Hodges and Thorncroft (1997) show that these MCSs are typically initiated around 1700 and 1800 hours local time, and that their lifetime varies from a few hours to more than a day. Their propagation, usually westwards away from their source regions, means that the phase of the diurnal harmonic may portray a later and later time as the MCS moves further and further away from its source region. McGarry and Reed (1978) offer this explanation for the near midnight maximum in precipitation that was observed over West Africa during GATE (GARP (Global Atmospheric Research

Programme) Atlantic Tropical Experiment). The results from this analysis of the CLAUS data, combined with the initiation and lifetime of MCSs given by Hodges and Thorncroft (1997), appear to support this explanation.

Similar interactions between orography and diurnal heating are also suggested by the rather complex variations in the phase of the diurnal harmonic over South America, for example along the Andes in DJF. Kousky (1980) describes a detailed analysis of the diurnal rainfall variations over north-east Brazil, which suggests a complex arrangement of land-sea and mountain-valley breezes. The CLAUS results shown in Figure 4 provide further evidence that the phase of the diurnal cycle in precipitation/convection is much more variable than the late afternoon/evening maximum suggested by, for example, Wallace (1975) who related it to daytime boundary layer heating.

Nevertheless, over quite extensive areas of South Africa, South and central America, where orographic influences are small and convection is less well organised than over central and West Africa, there is a strong tendency for the maximum in precipitation/convection to occur between 1700 and 2000 local time. This timing is consistent with the results of Gray and Jacobson (1977) who analysed the incidence of moderate to heavy precipitation using the present weather codes reported by a large number of land surface stations from South America and Africa.

Over the oceans, the phase of the diurnal cycle is very variable, although for regions of deep convection (characterised by low T_b in Figures 1 and 2), away from any influence of land forced diurnal variations, the precipitation tends to peak in the early morning, around 0600 local time, as noted by Janowiak et al. (1994) using satellite measurements of cold clouds. However, this result needs to be treated with caution since there are potential inconsistencies between the actual timing of the precipitation maximum and that inferred from the brightness temperature using Equation 6. Janowiak et al. (1994) present results from in situ measurements of rainfall during TOGA COARE which show that, in disturbed conditions, the maximum precipitation generally occurred near 0300 local time, some three-hours earlier than the maximum extent of cold clouds (T_b <230 K). Gray and Jacobson (1977) also report oceanic precipitation maxima prior to 0600 local time, nearer 0400 local time. Similarly, McGarry and Reed (1978) noted that, over West Africa, the rainfall maxima preceded the convective cloud maxima by up to two hours, which they associated with the spreading out of the convective cloud tops after the peak in precipitation. This apparent discrepancy between the actual and inferred timing of the precipitation maximum is important when satellite data are used to evaluate model behaviour.

The rather variable phase results over the oceanic convective regions are perhaps not surprising bearing in mind the complex diurnal cycles in tropical convection described by Sui et al. (1997) based on TOGA COARE observations. They noted that only the deep, organised convection tended to show an early morning maximum whereas sub-mesoscale convection, typical of suppressed conditions, tended to show a late afternoon maximum, much more similar to land-based convection. They relate this to the diurnal cycle in the ocean skin temperature, which can be pronounced in light wind conditions (e.g. Weller and Anderson 1996). Similarly, Janowiak et al. (1994) noted that, whereas the coldest clouds (T_b <230 K) tended to show an early morning maximum, warmer clouds (T_b >235 K) were most prevalent in the afternoon.

The CLAUS results also suggest that there is a notable difference in the phasing of the diurnal cycle between the Atlantic sector and the Pacific and Indian Oceans. In JJA (Figure 4(b and d)), there is a uniform signal over the Caribbean, Gulf of Mexico and the north west Atlantic of a maximum in T_b near midnight. The most likely explanation is that these regions are dominated by warmer clouds whose behaviour is more similar to the sub-mesoscale cumulus congestus extensively observed in TOGA-COARE (Johnson et al. 1999), and whose diurnal variation is more typical of land-based convection with maximum cloudiness in the late afternoon (e.g. Sui et al. 1997).

A notable feature of the GATE results was the tendency for the precipitation over the ship array (20°W-27°W; 5°N-12°N) to occur in the afternoon (McGarry and Reed 1978; Albright et al. 1981), at odds with the oceanic early morning maximum suggested by Gray and Jacobson (1977). The CLAUS results for JJA show a similar pattern, with an afternoon maximum being more likely east of 30°W (Figure 4(d)).

The spreading of the diurnal cycle from coastal regions out over the surrounding oceans has already been noted in Figure 3. This effect is particularly striking in the phase of the diurnal harmonic. Closer examination of Figure 4 shows coherent diurnal variations propagating away from the coasts of the Indonesian islands in DJF, down the Bay of Bengal in JJA, south westwards away from the Mexican coast in JJA, and off the West African coast in JJA. In many cases these coherent diurnal variations spread out for many hundreds of kilometres. It is clear, particularly from the results for T_b (Figure 4(b)), that the phase of the diurnal cycle over the GATE ship array, noted above, may well be associated with the remote effects of the diurnal cycle over the adjacent West African land mass.

From the timing of the lines of constant phase seen in Figure 4, it is possible to estimate the propagation speed of the signal as it moves away from the coast. Figure 5 shows a close up view of the phase of the maximum brightness temperature over the Bay of Bengal in JJA. Starting from the north-east coast of India, lines of constant phase spread out south eastwards across the Bay of Bengal. The inferred propagation speed is between 15 and 20ms^{-1}, in line with those of coherent disturbances that were observed propagating rapidly southwards over the Bay of Bengal during the recent Joint Air-Sea Monsoon Interaction Experiment (JASMINE; Webster, personal communication). As shown in Figure 3(d), these propagating disturbances generate significant diurnal variations in precipitation over the Bay of Bengal, suggesting that these waves have a fairly deep structure. In fact, the inferred propagation speed is consistent with that expected for a diurnally generated gravity wave whose equivalent depth is 40 metres and whose spatial scale is wavenumber 20. The fact that the lines of constant phase tend to run parallel to the coast in Figure 5 suggests that this coherent diurnal variation is probably triggered by the diurnal cycle over the land. Figure 3(d) has already shown a maximum in the diurnal amplitude of precipitation over north east India; its spatial scale is about 10°, consistent with the inferred gravity wave spatial scale noted above.

The lines of constant phase around the islands of Indonesia in DJF (Figure 4(a and c)) suggest a complex system of diurnally varying convection over the Maritime Continent. Here the inferred propagation speed away from the islands is slower than over the Bay of Bengal case, being typically nearer 10 ms^{-1}. Again, the signal is evident for many hundreds of kilometres, for

example, north-eastwards of New Guinea in DJF (Figure 4(a) and (c)). Similarly, the lines of constant phase spreading away from the Mexican coast in JJA also suggest a slower propagation speed than seen in Figure 5 for the Bay of Bengal. If the signal is associated with a gravity wave, then the slower speed is probably indicative of a shallower wave, more typical of a sea/land breeze effect. This is consistent with the amplitude of the signal in precipitation/deep convection being weaker for the Indonesian Islands and Mexican coast than for the Bay of Bengal (Figure 3).

During the Winter Monsoon Experiment (WMONEX), pronounced diurnal variations around Borneo were observed (Houze et al. 1981; Williams and Houze 1987), similar to those described here. A morning maximum in convection was noted off the north west coast of Borneo which Johnson and Kriete (1982) interpreted as an interaction between the N.E. monsoon flow and the night-time land breeze off Borneo. They noted that the structure of the disturbance was very similar to a squall line, much as was observed over the Bay of Bengal during JASMINE. In addition, Mapes and Houze (1993) have commented on the afternoon maximum in convection over the islands of the Maritime Continent with a related, but lesser peak over the surrounding seas during the night and morning. The results from this analysis of the CLAUS data show that these coherent diurnal variations around the islands are widespread and ubiquitous, indicating that diurnally forced sea/land breezes and their influence on organised convection may be an important component of the hydrological cycle and energy budget of the Maritime Continent.

20.2 Evolution histograms for selected regions with different characteristics

To investigate the diurnal cycle in more detail for particular regions with different characteristics, evolution histograms have been constructed. Based on the seasonal mean field T_b and its variability (Figures 1 and 2), various regions have been selected whose characteristics are nearly homogeneous and which represent different climatic regimes (e.g. deep oceanic convection, clear sky land). Figures 6 and 7 show the evolution histograms of T_b over three[3] particular regions for DJF and JJA, respectively. These have been constructed as described in Section 3; since the areas chosen cover a minimum of 1200 data points which are sampled over 3 months and over the four years available, the histograms are well sampled. These results complement those shown earlier for the diurnal harmonic and demonstrate how well the diurnal cycle can be represented by a harmonic analysis. They also show the more general characteristics of the diurnal cycle for a particular climatic regime and are therefore particularly useful for model evaluation.

For clear sky land conditions (Figures 6(a) and 7(a)), the evolution histograms confirm that the maximum brightness temperature occurs just after noon, consistent with the phase of the diurnal harmonic in T_b seen in Figure 4. However, the evolution histograms suggest that the minimum T_b occurs between 0400 and 0600 hours local time, just before dawn, with a diurnal range in T_b of typically around 30 K. This timing of the maximum T_b and the evolution of T_b , as shown in Figure 6(a) and Figure 7(a), are in agreement with the detailed study of the diurnal cycle over Kansas, observed during the First ISLSCP (International Satellite Land Surface Climatology

[3] Several others were also studied but will not be shown here since the results are very similar.

Project) Field Experiment (FIFE) and described by Betts and Ball (1995). They report a minimum 2m temperature just before sunrise, between 0500 and 0600 hours local time and a maximum temperature 1-2 hours after local noon.

Comparison of the land convection with the land clear sky examples (Figures 6(a,b) and 7(a,b)) demonstrates, as expected, the importance of the warming of the land surface in triggering convection. Over both S. America in DJF and central Africa in JJA, deep convection develops in the late afternoon and reaches a maximum in the evening. Thereafter the histograms suggest that the clouds decay during the early morning hours, dissipating at or just before sunrise. This allows the land surface temperatures to increase in the morning hours, and the whole cycle repeats itself. Again, these results are broadly consistent with the phases of the diurnal harmonics of T_b and estimated precipitation shown in Figure 4.

Even though the amplitude of the diurnal harmonic in T_b is small over the tropical oceans (Figure 3), the size of the sample used to construct the evolution histograms has enabled a clear signal of the diurnal cycle in deep convection to be identified (Figure 6(c) and Figure 7(c)). As suggested by the phase of the diurnal harmonic in estimated precipitation (Figure 4), which focuses on cold clouds, the evolution histograms confirm that deep convection tends to peak during the early morning. The coldest clouds, with T_b near 200 K, always occur preferentially between 0200 and 0600 hours local time. Where the convection tends to be slightly less deep (T_b between 200 K and 220 K) the maximum occurrence of cold clouds is slightly later, between 0600 and 1000 hours local time. This is typical of the Atlantic ITCZ in JJA and the SPCZ in DJF.

The histograms also show that the very coldest clouds occur over the West Pacific in DJF, consistent with the maximum height and coldness of the tropopause, as diagnosed by Highwood and Hoskins (1998). Conversely, convection in the Atlantic ITCZ is never as deep as over the West Pacific; the coldest T_b over the Atlantic is typically 10-20 K warmer than over the West Pacific. Again, this result is consistent with the lower/warmer tropopause over the Atlantic (Highwood and Hoskins 1998).

The histograms for regimes with oceanic deep convection (Figures 6(c) and 7(c)) also show that, while the deepest clouds are most prevalent in the early morning, middle and low level clouds appear most commonly during the afternoon and evening. This result is consistent with the characteristics of the diurnal cycle in mesoscale and sub-mesoscale convective events reported by Rickenbach (1996) and Sui et al. (1997) based on TOGA-COARE measurements. Rickenbach (1996) showed that sub-mesoscale clouds typically extend only to the mid-troposphere, near the freezing level inversion (Johnson et al. 1999) and have their maximum amounts during afternoon and evening, much more typical of land based convection. This is in contrast to the larger, mesoscale convective systems whose cloud tops often reach the upper troposphere. These systems display an early morning maximum in precipitation, consistent with the behaviour of the cold clouds, as identified by the CLAUS precipitation algorithm and seen in the phase of diurnal harmonic (Figure 4(c and d)). Similarly, Sui et al. (1997) describe the diurnal cycle in convection as one in which warm cumuli occur preferentially in the morning, convective showers in the afternoon, and organised convection, with heavy precipitation, at night. They note, in agreement with other studies, that the afternoon convective showers are

most evident in undisturbed conditions, typical of the suppressed phase of the Madden Julian Oscillation.

21 Example of the use of CLAUS data to evaluate the simulated diurnal cycle

As noted in the Introduction, the ability of a GCM to simulate correctly the phase and amplitude of the response of the land-ocean-atmosphere system to the diurnal cycle of solar radiation should be an important test of physical parameterisation schemes. Here we show an example of the application of the CLAUS data to the evaluation of the diurnal cycle simulated by the climate, atmosphere-only version (HadAM3) of the Met. Office Unified Model (UM). To provide similar statistics on the diurnal cycle, the UM was integrated for a year with observed SSTs for 1991/92; three-hourly diagnostics of OLR and precipitation were archived. Consequently the sample size from the model is rather limited, but future studies will focus on examining the diurnal cycle in the model in much more detail.

A full description of the model and its basic climate can be found in Pope et al. (2000). It contains a comprehensive suite of physical parameterisations, including state-of-the-art radiative transfer (Edwards and Slingo 1996), a fully interactive soil and vegetation land surface scheme (Cox et al. 1999) and a mass-flux convection scheme, which is closed on buoyancy and includes convective momentum transport (Gregory et al. 1997). As described by Pope et al. (2000), this version of the UM provides a reasonable simulation of the tropical precipitation and circulation, although it still tends to underestimate the rainfall over the Maritime Continent and to overestimate the rainfall over the western Indian Ocean. These deficiencies are common to earlier versions of the UM and appear to be associated with the representation of the complex land-ocean system that exists around the Indonesian Islands. In this study, the horizontal resolution of the model is 3.75° longitude by 2.5° latitude, its typical climate resolution. Versions of the model with 30 (L30) and 19 (L19) vertical levels have been evaluated. Since the results were found to be insensitive to vertical resolution, only those from the L30 version will be presented here.

The previous section has described the observed behaviour of the diurnal cycle in radiation and convection in the CLAUS data. In this section, similar diagnostics will be presented based on the OLR and precipitation fields generated by the UM. To allow direct comparison with the CLAUS results, the model s OLR has been converted to an equivalent brightness temperature using equations (1) and (2). When considering the model results, it is important to note that, whereas precipitation and T_b are uniquely related in the analysis of the CLAUS data through the use of Equation 3, the same does not necessarily apply in the model. Variations in OLR, and hence equivalent T_b , will depend on how well the model s cloud scheme relates to the convection scheme.

The amplitudes of the diurnal harmonic in the simulated equivalent T_b and precipitation for DJF and JJA are shown in Figure 8. In comparison with the results from CLAUS (Figure 3), the model has successfully simulated many aspects of the amplitude of the diurnal harmonic.

The spatial patterns are slightly different which may be associated partly with systematic errors in the model s basic climate (Pope et al. 2000), and partly with the limited sample size. The amplitudes of the diurnal harmonic in equivalent T_b are generally well captured over the clear sky land areas of North Africa, but are underestimated for Australia, particularly during southern winter. The diurnal amplitude in precipitation over continental convective regions, such as South Africa in DJF and central Africa in JJA, is generally well captured. Obvious discrepancies are over the islands of the maritime continent in DJF and over the Indian monsoon region in JJA. The model has failed to capture the pronounced diurnal cycle over northern India, but has simulated rather large amplitudes in equivalent T_b over the Arabian Sea and Bay of Bengal (Figure 8(b)), which are not co-located with those in precipitation (Figure 8(d)), nor seen in the CLAUS results (Figure 3). Over the open oceans, the model appears to have slightly overestimated the amplitude of the diurnal harmonic in equivalent T_b but underestimated it in precipitation, although the limitations of the CLAUS results should be noted, since they rely on simple algorithms to relate T_b to precipitation.

The phase of the diurnal harmonic of equivalent T_b and precipitation from the UM is shown in Figure 9. In comparison with the CLAUS results (Figure 4), it is evident that the UM poorly simulates the phase of the diurnal harmonic of the equivalent T_b and precipitation in the tropics for both seasons. The most marked discrepancy occurs for convective regimes. According to Figure 9, for land convective regimes, the diurnal maximum in the simulated precipitation occurs before noon, instead of in the late afternoon and evening as indicated in the CLAUS data (Figure 4). The model is more successful at simulating the time of maximum equivalent T_b, which is generally in the mid-morning in agreement with the CLAUS results. A notable exception is over Brazil in JJA where the model gives a near midnight maximum in equivalent T_b, which is quite different from any of the other land convective regions.

The UM also advances the timing of the simulated diurnal maximum in oceanic precipitation which appears around midnight, in contrast to the estimates from the CLAUS data where the maximum convection occurs typically about 6 hours later in the early morning. Even allowing for the likelihood that the phase results for precipitation, estimated from the CLAUS data, may be later than reality by up to three-hours (e.g. Janowiak et al. 1994), it is clear that the UM produces a diurnal maximum in precipitation that is too early in the day. There is also a lesser discrepancy over land clear sky regions, where the model gives a maximum in equivalent T_b coincident with the peak in solar heating, 1-2 hours earlier than that observed in the CLAUS data.

Using three-hourly diagnostics of equivalent T_b from the UM, evolution histograms typical of continental and oceanic convection have been constructed in a similar manner to those based on T_b from the CLAUS dataset. Although the histograms are not nearly as well sampled as in the CLAUS results (coarser grid, one year only), the results nevertheless reveal systematic errors in the model. Figure 10 shows three examples of the histograms for land convective regimes, which are characterised by a precipitation maximum near noon in Figure 9. All show a very similar behaviour that does not compare well with the CLAUS results shown in Figures 5 and 6. As soon as the land surface begins to warm up in the morning, convection is initiated, which reaches to the mid-troposphere. Soon after, the convection extends to the upper troposphere with the

lowest values of equivalent T_b typically occurring in the mid-afternoon, compared to the evening in the CLAUS data.

For oceanic convection (Figure 11), the histograms are quite noisy since the diurnal cycle is quite weak and therefore difficult to sample. Nevertheless, the results given in Figure 11, for two oceanic convective regimes, again show similar characteristics, which support the phase results shown in Figure 9. The deepest convection tends to occur in the late afternoon in the model compared with the early morning in the CLAUS data (Figure 6 and 7).

22 Discussion and Conclusions

The CLAUS multi-year, high spatial and temporal resolution global dataset of brightness temperature has provided a unique opportunity to carry out a systematic investigation of the diurnal variation in convection and radiation over the whole tropics. The characteristics of the diurnal cycle described by the CLAUS data agree with previous observational studies cited in the Introduction. Whereas those studies were mostly for limited regions and short time samples, the CLAUS results have demonstrated the universality of the characteristics of the diurnal cycle for land vs. ocean, clear sky vs. convective regimes. They have also shown some interesting regional variations indicative of the effects of complex land-sea and mountain-valley breezes, as well as the life cycle of mesoscale convective systems.

A striking result from the analysis of the CLAUS data has been the extent to which the strong diurnal signal over land is spread out over the adjacent oceans, probably through gravity waves of varying depths. These coherent signals can be seen for several hundred kilometres and in some instances, such as over the Bay of Bengal, can lead to substantial diurnal variations in convection and precipitation. Over the complex system of islands that make up the Maritime Continent, these coherent signals in the diurnal cycle represent important land-sea breeze effects, which may play a crucial role in the heat and moisture budget of this key region for the tropical and global circulation.

The results have shown that the diurnal cycle for various tropical regions with different characteristics is substantially different. The largest amplitudes of the diurnal harmonic of T_b occur over the clear sky continents with a maximum in T_b in the early afternoon, 1—2 hours after the maximum in solar heating. For convective regimes, the diurnal amplitude is larger and more spatially consistent over the continents than over the oceans. For both DJF and JJA, oceanic deep convection tends to reach its maximum in the early morning, while continental convection typically peaks in the evening.

The phase of the diurnal harmonic suggests that the mechanisms for the observed diurnal variation in convection over land and ocean are very different. The diurnal cycle of convection over land is basically a low level thermodynamical response to the radiative heating cycle.

During the day, solar heating over land surface increases the lower tropospheric temperature (and moisture) and hence instability, leading to development of convection, the resulting convective precipitation maximum tending to occur in the evening. In contrast, radiative cooling of the land surface at night enhances the stability, suppressing convection, and leading to a minimum in the early morning. This idealised view of the diurnal cycle over land is modified by local orography

and by the initiation, propagation and decay of mesoscale convective systems, such as squall lines.

For deep oceanic convection, which typically peaks in the early morning, the situation is much more complicated, and there may be several mechanisms responsible for the behaviour of the diurnal cycle. The first involves a direct radiation-convection interaction (Randall at el. 1991). At night, infrared cooling at the cloud top is greater than at cloud base resulting in destablization of the upper troposphere, leading to cloud development with a maximum occurring in the early morning; during the day, warming at cloud top due to solar absorption increases the stability and therefore restricts convective activity.

The second possible mechanism involves the cloud vs. cloud free radiation difference in the horizontal (Gray and Jacobson 1977). The radiative cooling of the cirrostratus at upper tropospheric levels is greater than the radiative cooling in the surrounding less cloudy or clear sky regions, whereas during the day the situation is reversed. This day-night differential heating cycle results in a daily variation in the horizontal divergence field which may give rise to a diurnal variation in convective activity. Recently, Liu and Moncrieff (1998) used an idealised two-dimensional cloud resolving numerical model to simulate the diurnal variation of tropical oceanic deep convection. The model gave a predawn maximum and late afternoon minimum in convection intensity for highly organised as well as less organised convection. Liu and Moncrieff (1998) concluded that this diurnal variation was primarily controlled by the direct radiation-convection interaction; the cloud vs. cloud free radiation difference was of secondary importance.

However, Chen and Houze (1997) have suggested that the mechanism for the diurnal cycle of tropical oceanic deep convection involves a rather complex surface-cloud-radiation interaction, not just a cloud-radiation interaction. They argue that the cloud-radiation interaction mechanism can only partially explain the diurnal cycle of the tropical oceanic deep convection. It does not explain why the large scale convective systems, which contribute most to the observed night-to-dawn maximum in cold cloud cover and precipitation, usually start preferentially in the afternoon, a time which is unfavourable in terms of atmospheric radiative processes. Chen and Houze (1997) point out that surface and near-surface thermal variables relevant to convective variability, (i.e. skin sea surface temperature and surface air temperature), consistently reach their maximum in the afternoon, and that the phasing of the diurnal cycle in these variables is favourable to the afternoon initiation of convective systems. Some of these convective systems, under optimal environmental conditions, continue to grow and reach their mature stage some time later during the night and early morning.

Chen and Houze (1997) also suggest that besides the nature of the underlying surface, an additional factor affecting the diurnal cycle in tropical deep convection is the life-cycle of cloud systems themselves. Because the life-cycle of large convective systems can take up to a day, they leave the boundary layer filled with air of lower moist-static energy and a cloud canopy that partially shades the ocean surface from the sunlight the following day. Since the surface conditions are unfavourable for another round of widespread convection, the next day s convection tends to occur in neighbouring regions unaffected by the previous convective systems. They call this spatial variability of the diurnal cycle of the large convective systems

diurnal dancing which may trigger and phase-lock with westward propagating inertio-gravity waves of similar two-day period.

The example of the use of the CLAUS data in the evaluation of the Met. Office Unified Model has demonstrated that the model has considerable difficulty in capturing the observed phase of the diurnal cycle in convection. This has been noted also in numerical weather prediction applications of the model (Ringer 1998). This may suggest some fundamental difficulties in the model s physical parameterizations. Possible candidates to be considered are the land surface scheme and its response to solar heating, the planetary boundary layer and its communication with the surface and the free troposphere, the convection scheme and its response to near surface buoyancy.

However, some of the problems in the phase of the diurnal cycle in the UM may be related to the technical implementation of the radiation scheme. Comprehensive radiation calculations are computationally demanding and, in common with many other AGCMs (see Phillips, 1994), the UM only calls the full radiation scheme every three-hours. At intermediate timesteps, a simple radiation calculation is made, based on the short-wave and longwave fluxes from the full radiation calculation. To allow for the diurnal variation in the incoming solar radiation, the short-wave fluxes are adjusted by the solar zenith angle on the intermediate timesteps but the clouds and the temperatures essentially remain fixed between the three-hourly calls to the full radiation calculation. This may have serious implications for the diurnal cycle, particularly over land where the surface temperature should respond rapidly to the diurnal cycle in solar forcing. Also the use of fixed clouds essentially means that the cloud field can be on average 1.5 hours out of phase with the solar forcing.

To investigate how much of the discrepancy between the observed and simulated diurnal cycles might be explained by the technical implementation of the radiation code, a year s integration was performed in which the full radiation calculation was made every timestep, and hence was as accurate as possible. In terms of both the amplitude and the phase of the diurnal harmonic, the results were quite similar, except over clear sky land (desert) regions where the time of maximum inferred brightness temperature was 1-2 hours later, in better agreement with the CLAUS data. This is well demonstrated in Figure 12(a and(b). With the standard 3-hourly calls to the full radiation calculation (Figure 12(a)), the model has produced its warmest land surface temperatures before noon, due the imbalance between the solar heating and the longwave cooling. When the radiation is calculated accurately (Figure 2, the shape of the evolution histogram is much closer to the observed behaviour (c.f. Figure 8(a)), with the warmest temperatures occurring in the early afternoon. As is also evident in Figure 12(a and b), the amplitude of the diurnal cycle is slightly reduced with the full radiation calculation.

For land convective regimes, the implementation of an accurate radiation calculation has had little impact on the model s major systematic error in the phase of diurnal cycle in precipitation. The rainfall still occurs preferentially before noon. However, the evolution histogram shown in Figure 12(c) does suggest that the detailed behaviour of the diurnal cycle is affected by the accuracy of the radiation calculation. There is now a more gradual evolution of the cloud field and the tendency for large amounts of middle level cloudiness to appear suddenly just before noon has been removed (c.f. Figure 10). Nevertheless, the fact that the model s rainfall still

occurs preferentially before noon suggests that there are fundamental shortcomings in the response of the surface, boundary layer and convective parameterizations to the diurnal cycle in short-wave heating.

The implementation of an accurate radiation calculation has also had little impact on the simulated diurnal cycle in oceanic convection. Returning to the results of Chen and Houze (1997) discussed above, it is clear that the Unified Model (and indeed other atmospheric GCMs) may lack potential key ingredients to produce the correct diurnal cycle in convection over the oceans. Firstly, the model uses a fixed SST and so there is no allowance for diurnal variations in skin sea surface temperature such as was observed during TOGA-COARE (e.g. Weller and Anderson 1996). These variations in skin temperature can be large (>1 K), particularly in light wind, undisturbed conditions (e.g. Webster et al. 1996), and appear to be important for triggering convection. Secondly, the model s convective parametrization involves an instantaneous adjustment and is therefore unlikely to represent the gradual growth of a convective system as described by Chen and Houze (1997). It is possible that the convective parametrization may need to carry a history of the life-cycle of the cloud systems, suggesting major changes in our current approach to convective parametrization.

This paper has shown the considerable potential that diurnal cycle diagnostics possess for demonstrating model deficiencies. The results support the argument that, as a basic, forced mode of the climate system, the ability of general circulation models to represent the diurnal cycle should be a key test of the correctness of any model. Future research will involve a more detailed analysis of the diurnal cycle in the Unified Model, as well as experimentation with a hierarchy of models, including a cloud resolving model, to investigate the coupling between the surface, boundary layer and free troposphere on diurnal timescales.

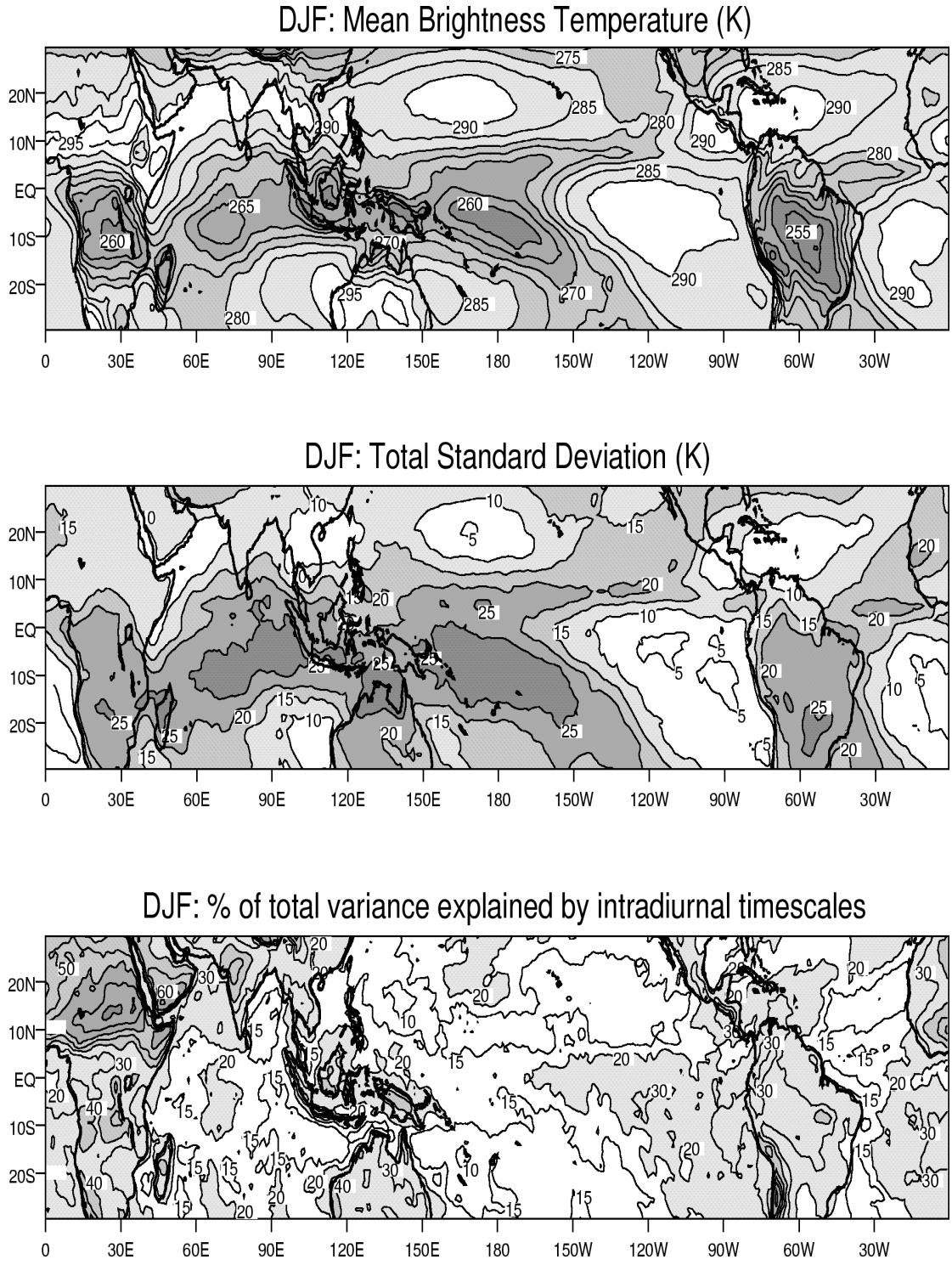

Figure 1: Seasonal mean brightness temperature (K), total standard deviation (K) and % of total variance explained by intradiurnal (<1day) timescales for December-February.

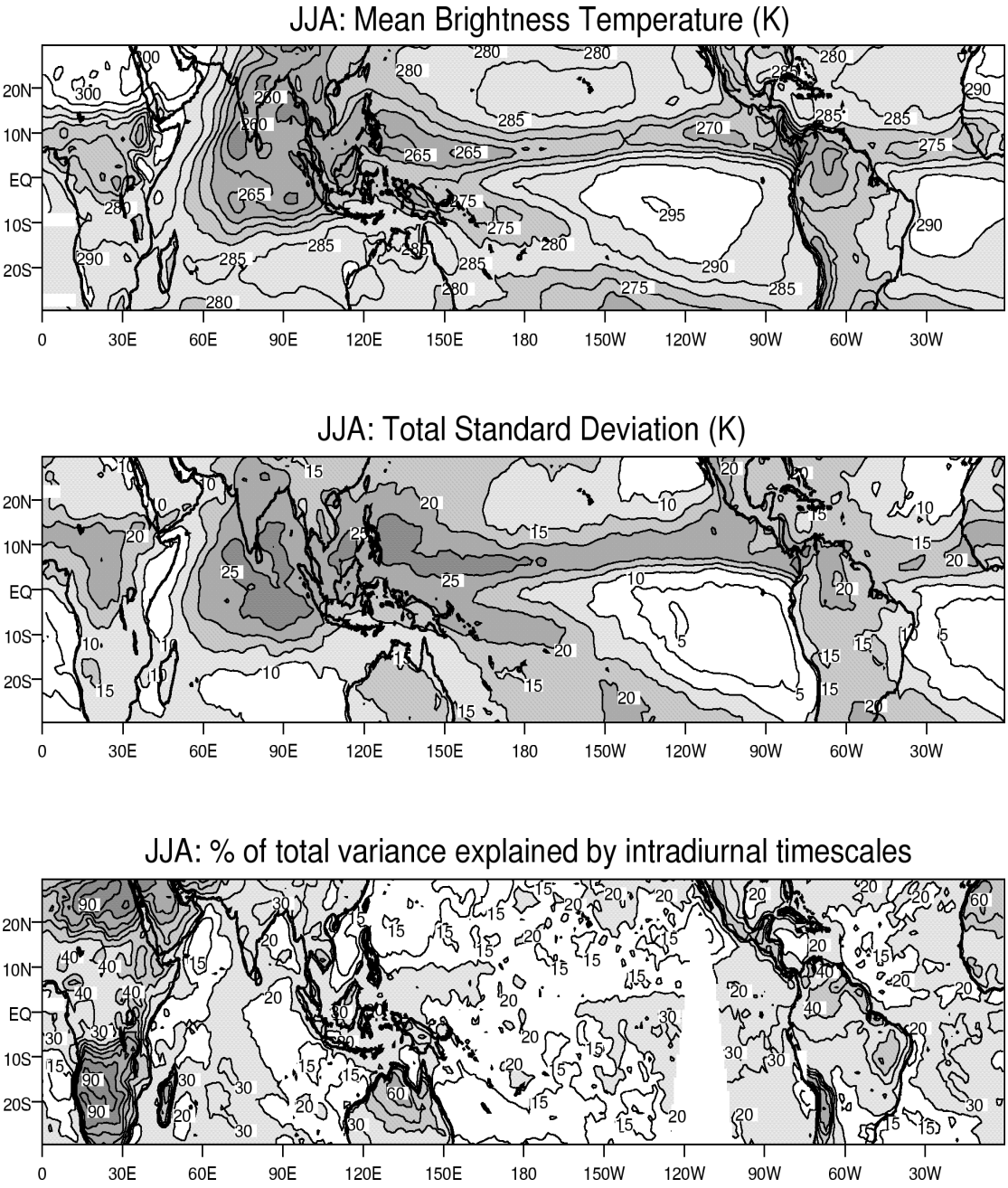

Figure 2: As Figure 1, but for June-August.

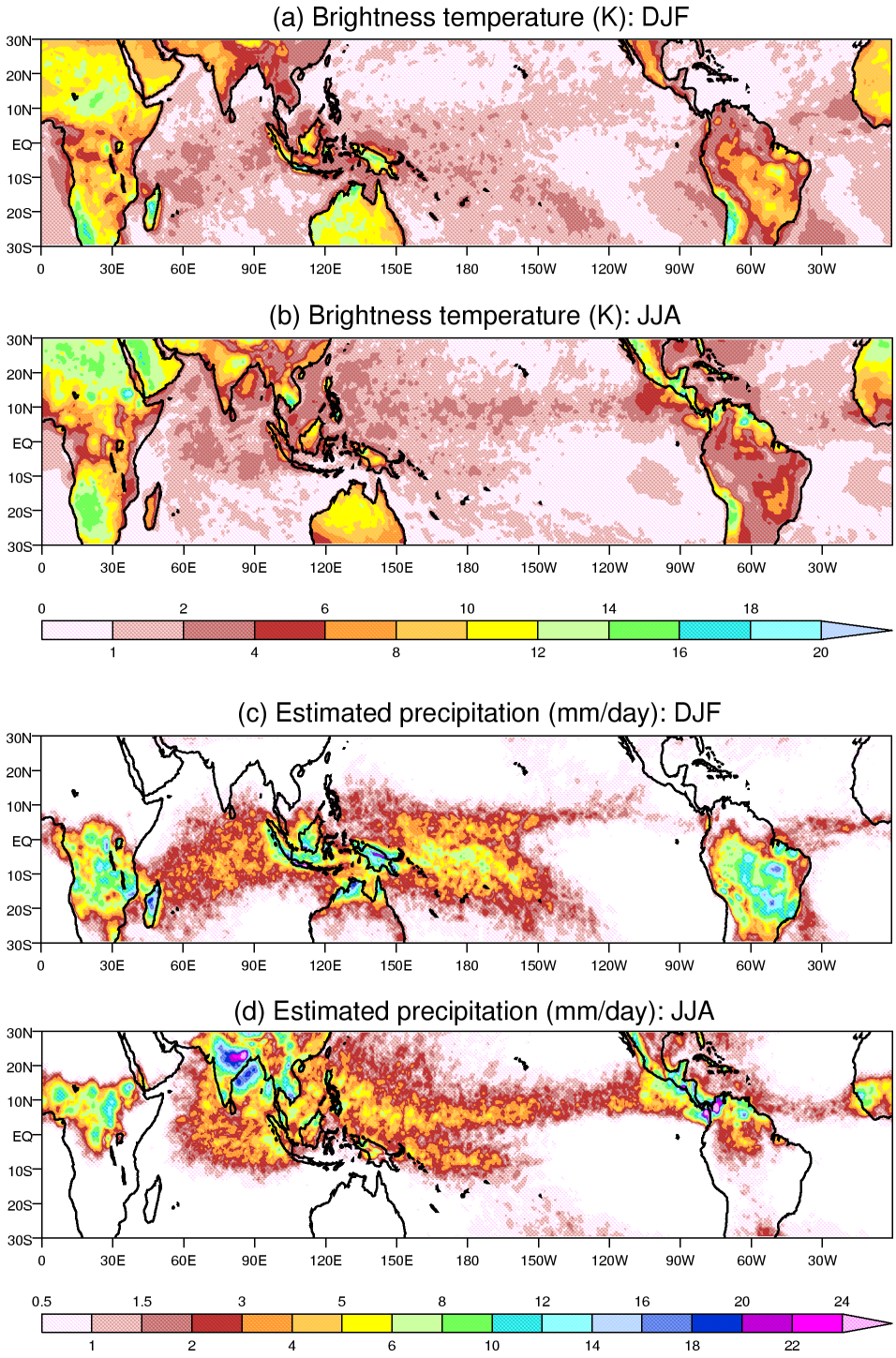

Figure 3: Seasonal mean amplitude of the diurnal harmonic in brightness temperature (K) and estimated precipitation (mm.day^{-1}) for DJF and JJA.

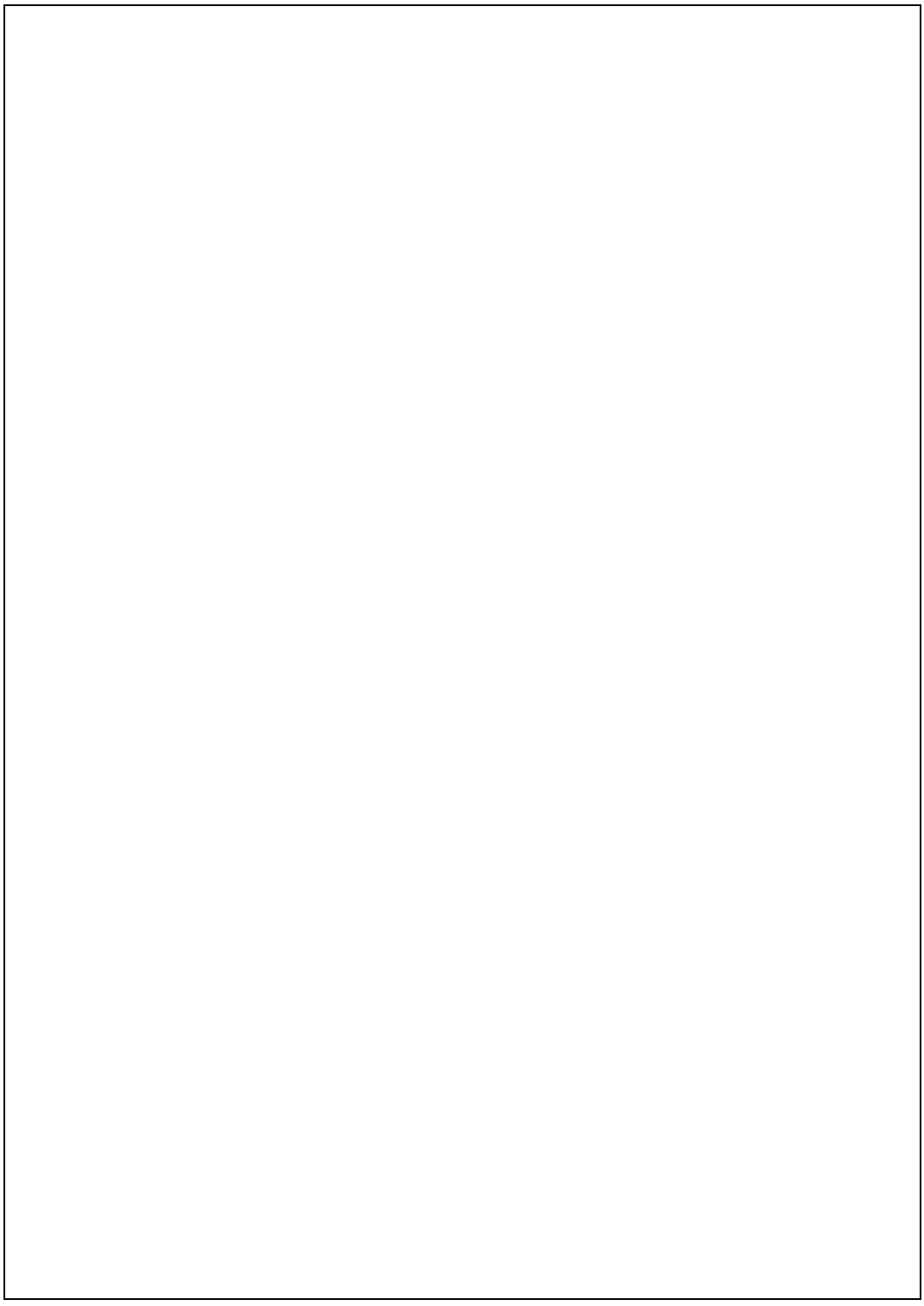

Figure 4: Seasonal mean phase of the diurnal harmonic of brightness temperature and estimated precipitation for DJF and JJA. Local time of the maximum is given.

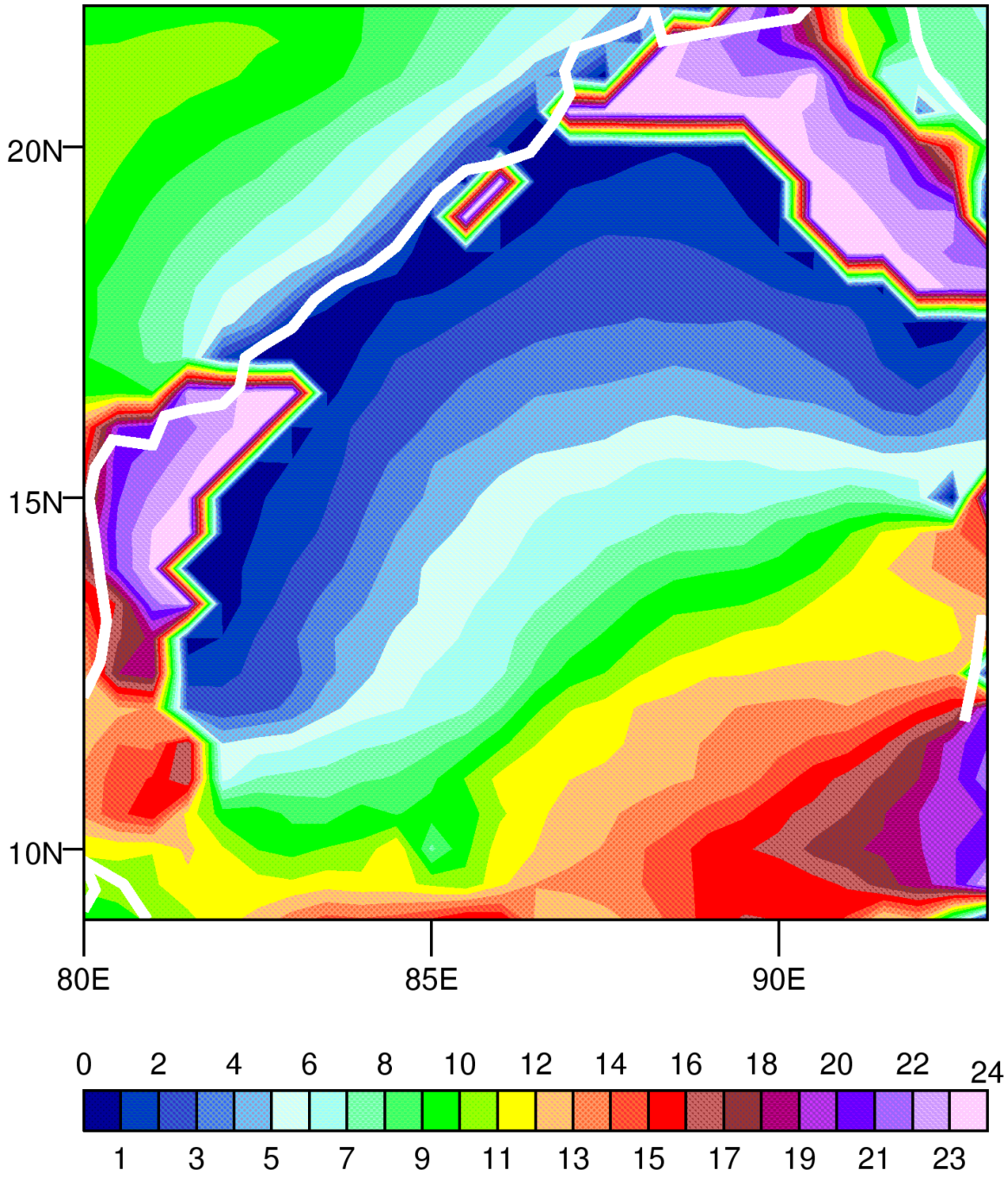

Figure 5: Phase of the diurnal harmonic of brightness temperature over the Bay of Bengal in JJA in terms of the local time of the maximum. The coastline is marked in white.

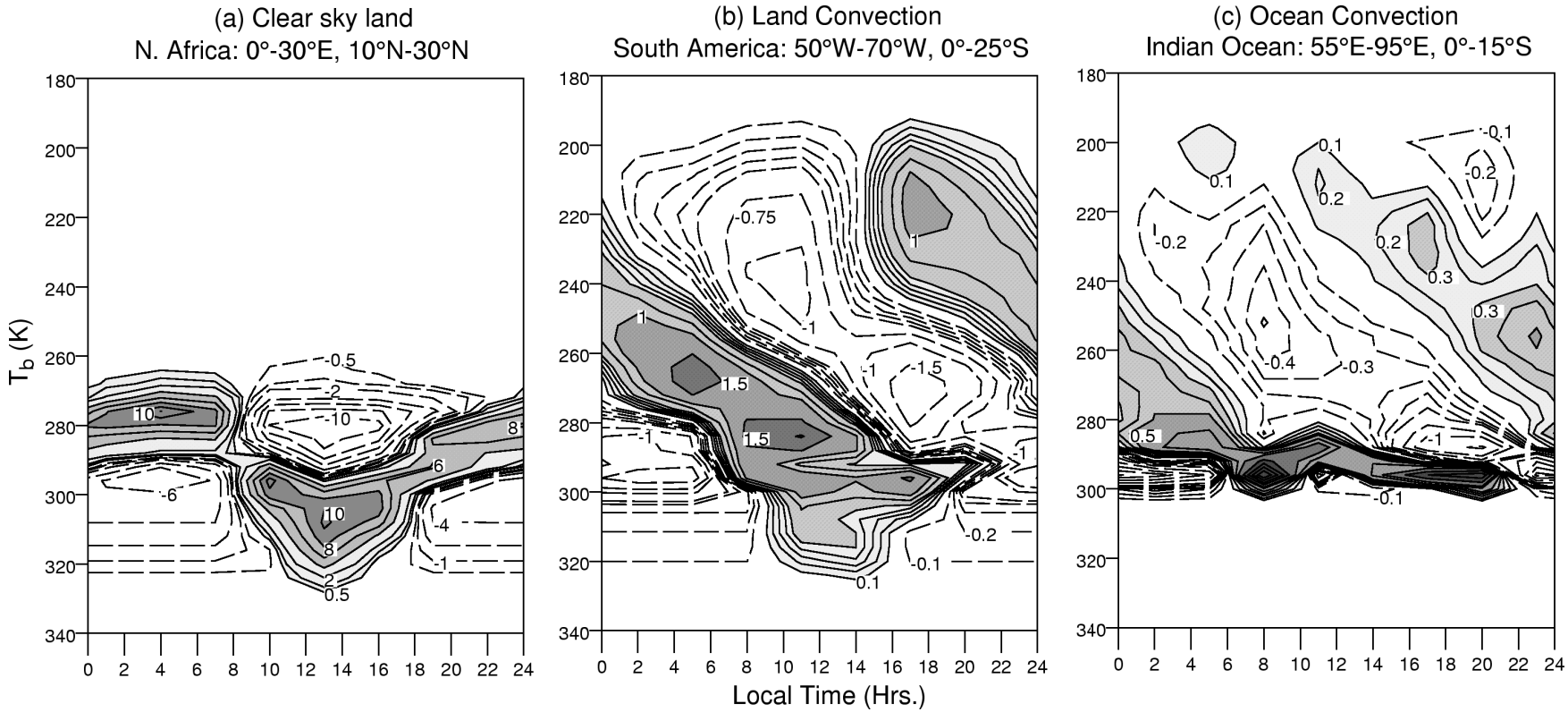

Figure 6: Seasonal mean evolution histograms of the diurnal variation in brightness temperature for DJF. The contours represent % departures from the daily mean histogram of brightness temperature.

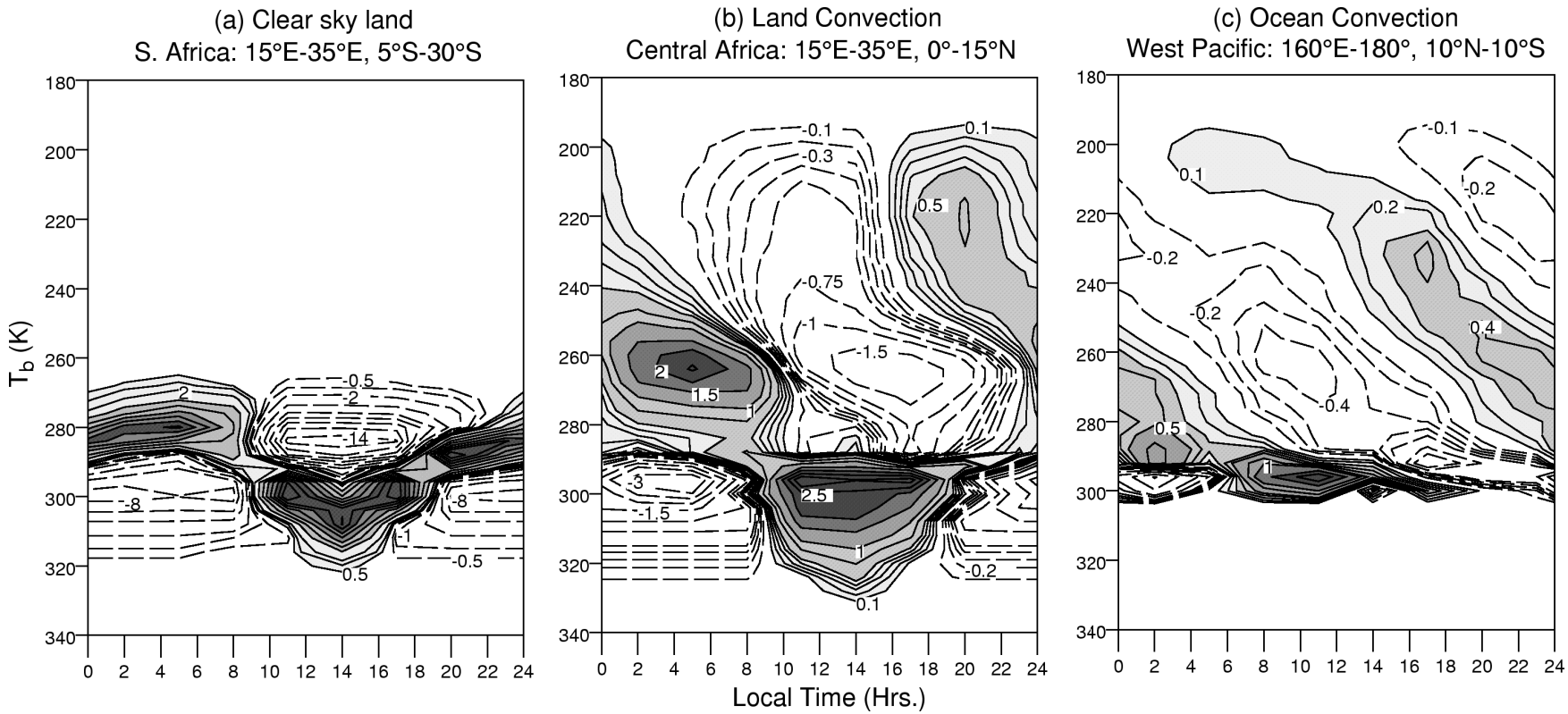

Figure 7: As Figure 6, but for JJA.

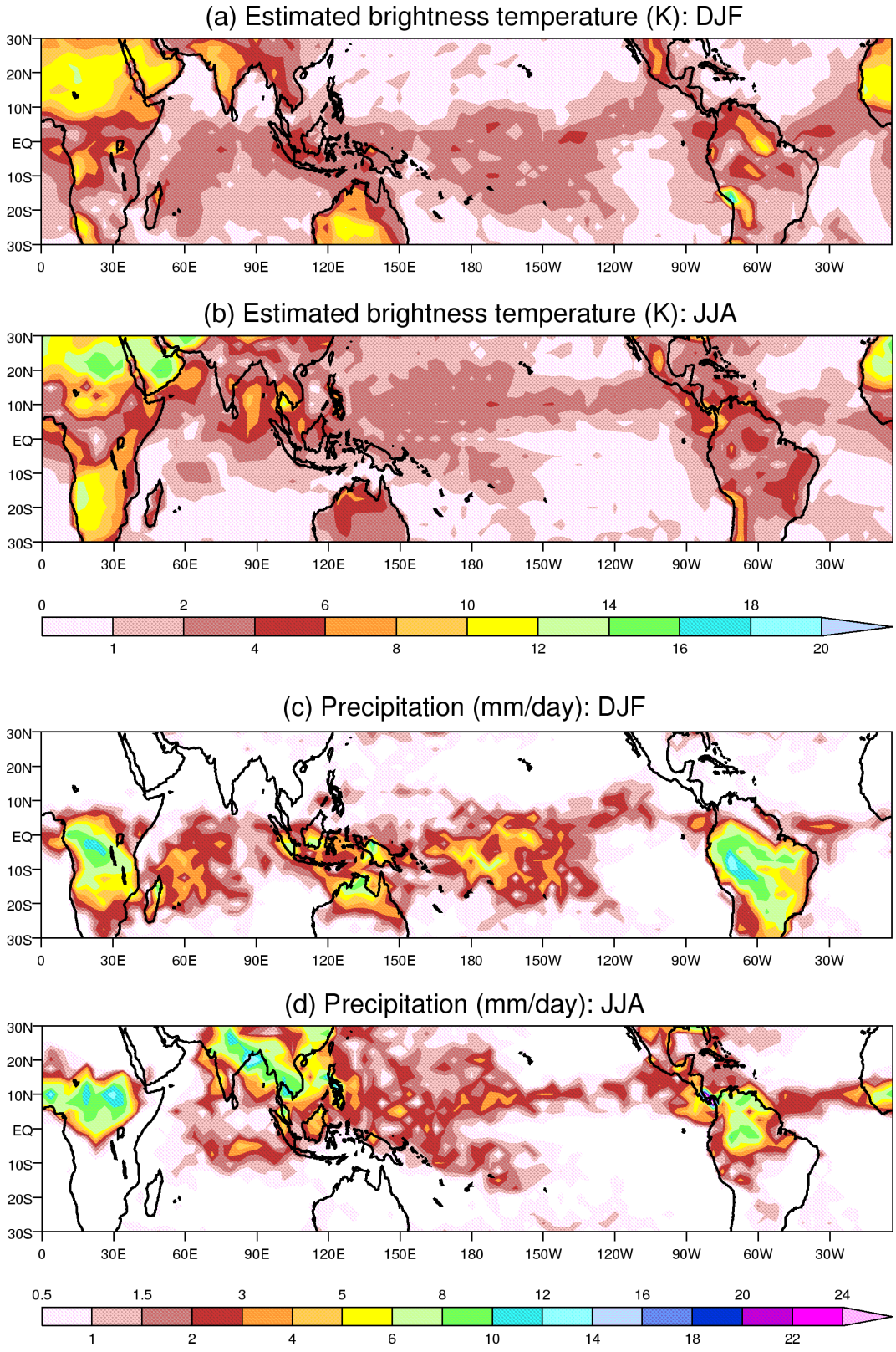

Figure 8: Seasonal means amplitude of the diurnal harmonic of estimated brightness temperature (K) and precipitation (mm day^{-1}) from the L30 version of the Met. Office Unified Model for DJF and JJA.

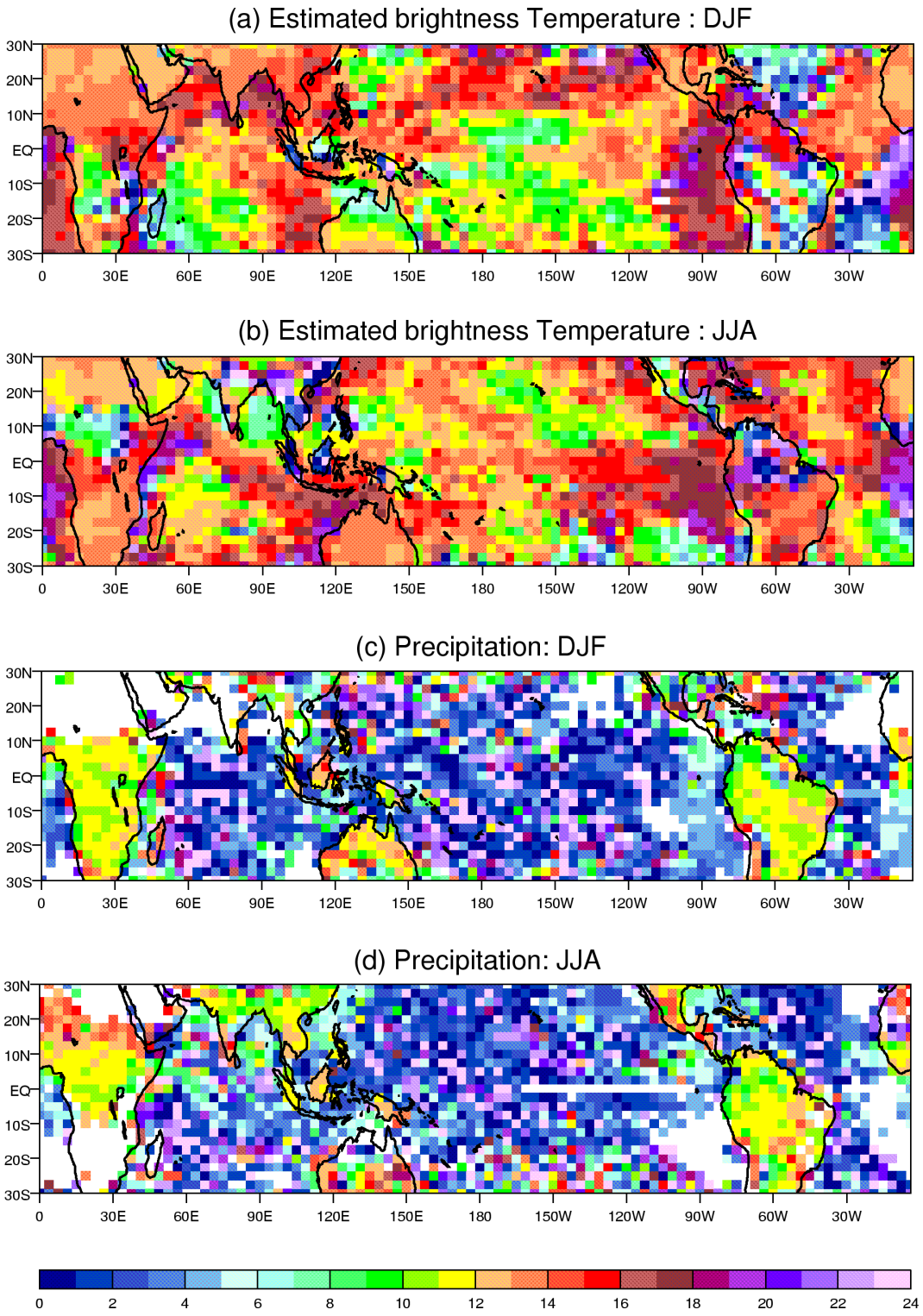

Figure 9: Seasonal mean phase of the diurnal harmonic of estimated brightness temperature and precipitation from the L30 version of the Met. Office Unified Model for DJF and JJA. The local time of maximum is given.

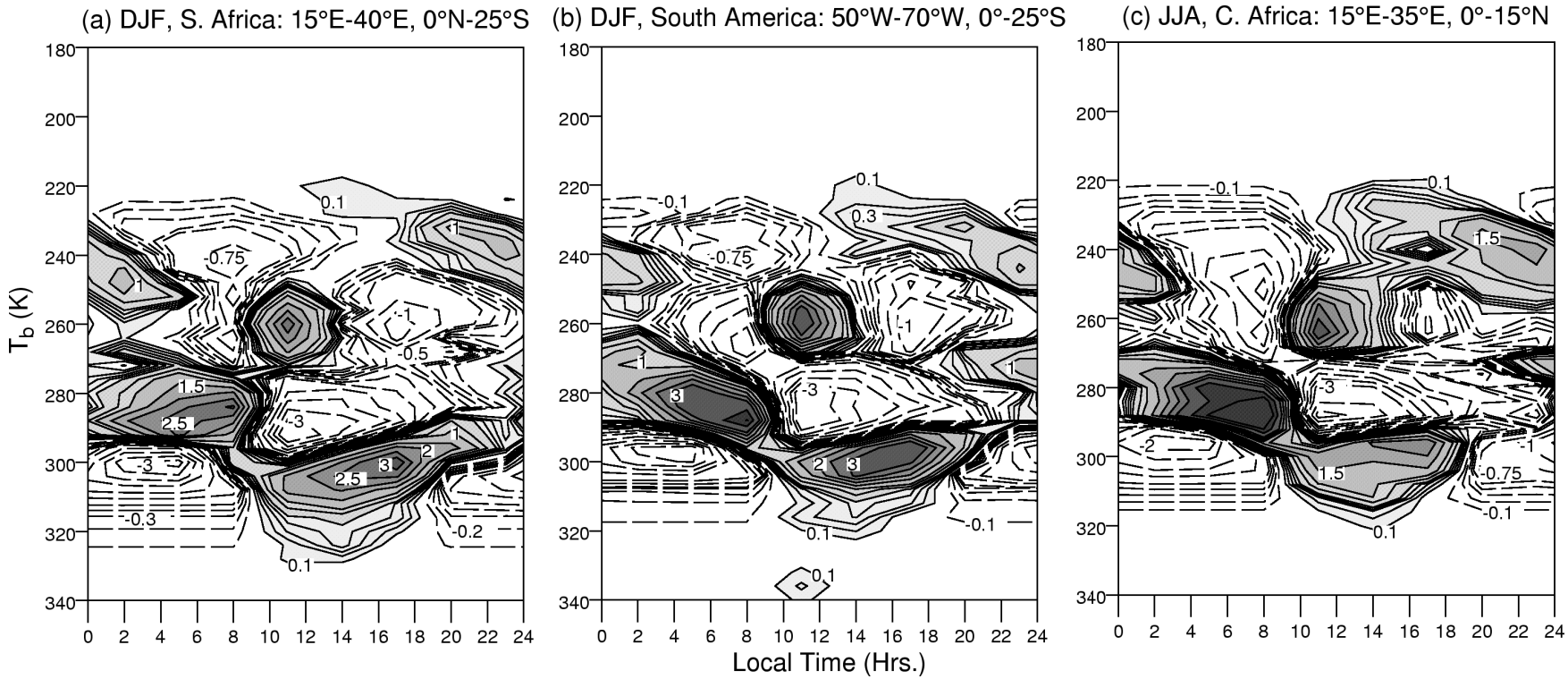

Figure 10: Seasonal mean evolution histograms of the diurnal variation in estimated brightness temperature from the Unified Model for land convective regimes. The contours represent % departures from the daily mean histogram of estimated brightness temperature.

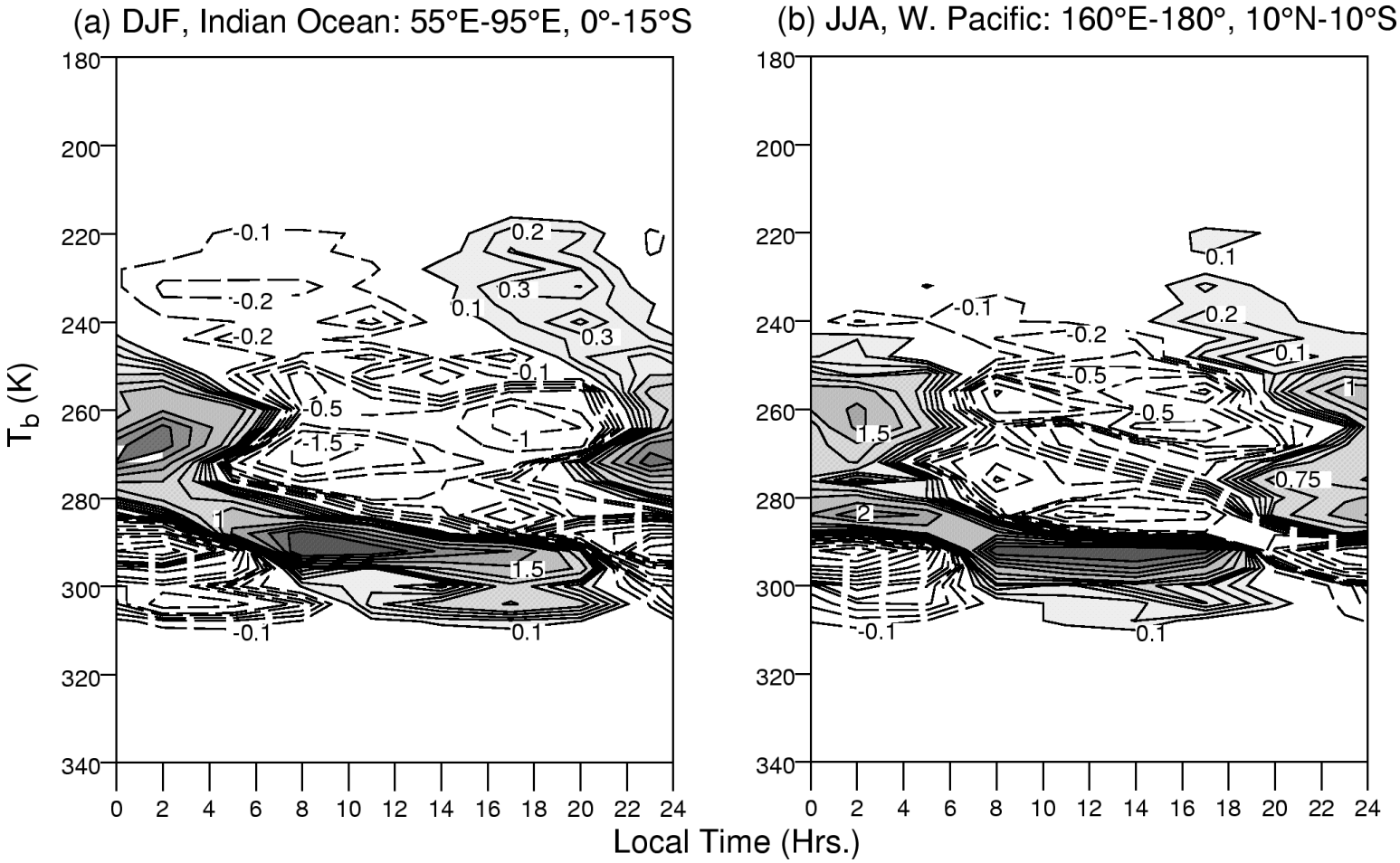

Figure 11: As Figure 10, but for oceanic convective regions.

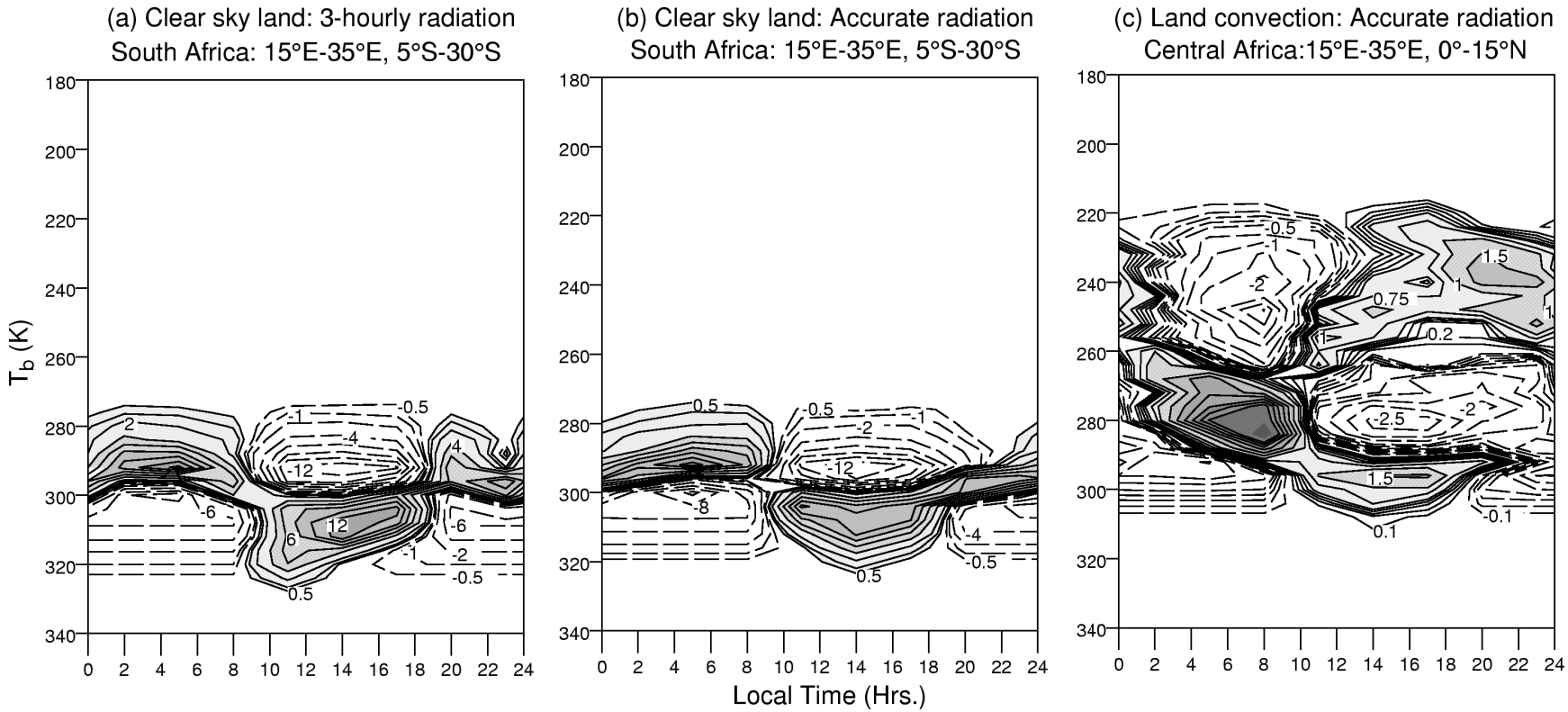

Figure 12: Evolution histograms showing the effect of performing a full radiation calculation every model timestep. (a) and (b) show the evolution of the estimated brightness temperature for a land clear sky regime (South Africa in JJA) for three-hourly and accurate radiation calculations, respectively. (c) shows the evolution of the estimated brightness temperature for a land convective regime (Central Africa in JJA) from the accurate radiation calculation. It can be compared with Figure 10(c).

D Data Dissemination

The mechanism for disseminating the archived data and information about the project whilst it was live was the World Wide Web. NRSC designed and implemented a Web server, running on the same hardware as the processing and archive systems. Customers could log on to this system and find out what data were available, place orders, etc. However, following the end of the project it was decided that, since further funding to operate the commercial web system at NRSC was not available, the simplest way to continue to disseminate the data to the wider scientific (and other) communities was to bank a copy at the British Atmospheric Data Centre.

The following sections describe the components of the CLAUS web system and also CLAUS-VIEW, the suite of space and time software tools developed by LMD to assist customers in using the data.

1 CLAUS Web Server

NRSC, in co-operation with ESSC, designed the CLAUS Web pages containing information on the CLAUS project. This information was registered with EWSE. As the project progressed, this information was updated with both general information on the status of the project and information available to registered users of the CLAUS system. This contains information on ordering products, the processing algorithms used to generate the products and sample images, as well as specific information from each Consortium partner on their role and use of the data.

As one of the design inputs to the design of the CLAUS archive system, NRSC used the CEO Recommendations on Meta-data (Version 1.1) to enable CIP searching *via* the World Wide Web. This allowed for the integration of the CIP search tool into CLAUS to enable users to search and retrieve data through either EWSE (or INFEO as the latter became available).

The introductory CLAUS Web page is shown in Figure 1. From this page, there are links to information about the CLAUS projects as a whole, its use and current status, and to Consortium member pages (Figure 2).

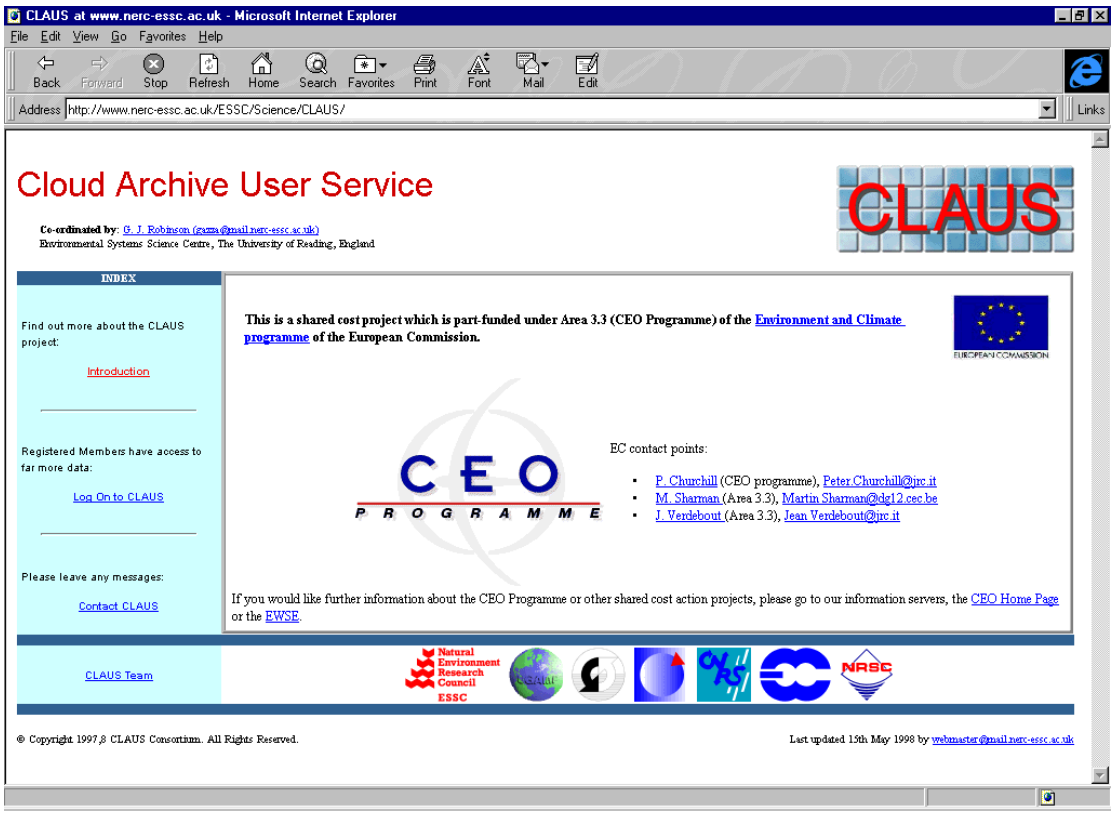

Figure 1: Introductory Page from the CLAUS World Wide Web Server.

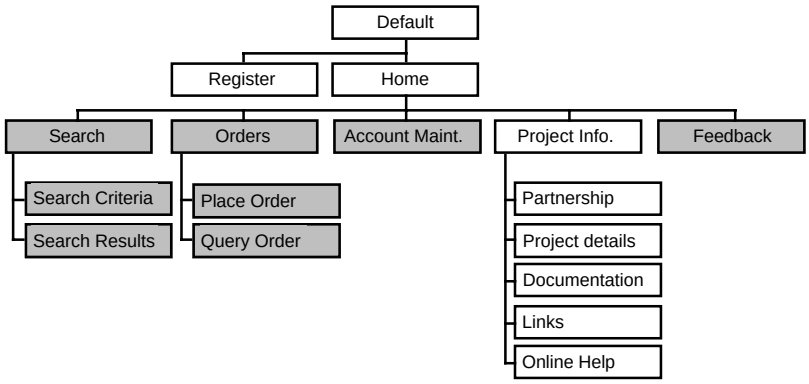

Figure 2: Functional hierarchy of operational CLAUS Web interface. (Functions in shaded boxes are available only to registered CLAUS customers).

2 Space and Time Analysis Tools

LMD developed a space and time analysis software package called CLAUS-VIEW. The specifications are described in the document LMD-CV-SPEC and the user manual is in the document LMD-CV-USM. A demonstration of a beta version of the CLAUS-VIEW package was made at the second Consortium Meeting in Tolouse. A full version of the CLAUS-VIEW software was distributed to all CLAUS partners by the end of May 1998.

The purpose of this package is to provide standard diagnostic tools to users of the CLAUS archive. CLAUS-VIEW comprises several modules and sub-modules:

Data Reliability Module

- Number of interpolated values
- Maximum number of contiguous (in time) interpolated values
- Average data density (%)
- Average viewing angle
- Standard deviation of the viewing angles.

Statistics Module

- Minimum brightness temperature
- Maximum brightness temperature
- Average brightness temperature
- Significance level of the average brightness temperature
- Standard deviation of the brightness temperature
- Mean histogram.

Time Evolution Module

- Temporal evolution of the Brightness Temperature (K)
- Histogram evolution
- Histogram diurnal composite
- Time-space representation (Hovm ller type)

Spectral Module

- Power spectrum for a given region
- Spectral variance maps

Cloud Cluster Module

- Cluster identification
- Cluster size statistic
- Cloud cluster tracking

The CLAUS-VIEW package has been designed to be as portable as possible. It consists of three parts:

The Command Line and Text Interface

The command line and text interface does not require any graphical features so that it can compile and run on almost any Unix platform (and possibly other systems with some minor changes).

By default, CLAUS-VIEW enters the text interface after parsing the command line. Then the user can then enter commands to define or modify the input data-set (GCI database or a sub-set, the parameters, to define the output (text or Postscript), to run modules and display results in ASCII format or as on-screen graphics on screen using the freeware utility 'ghostscript' (Figure1).

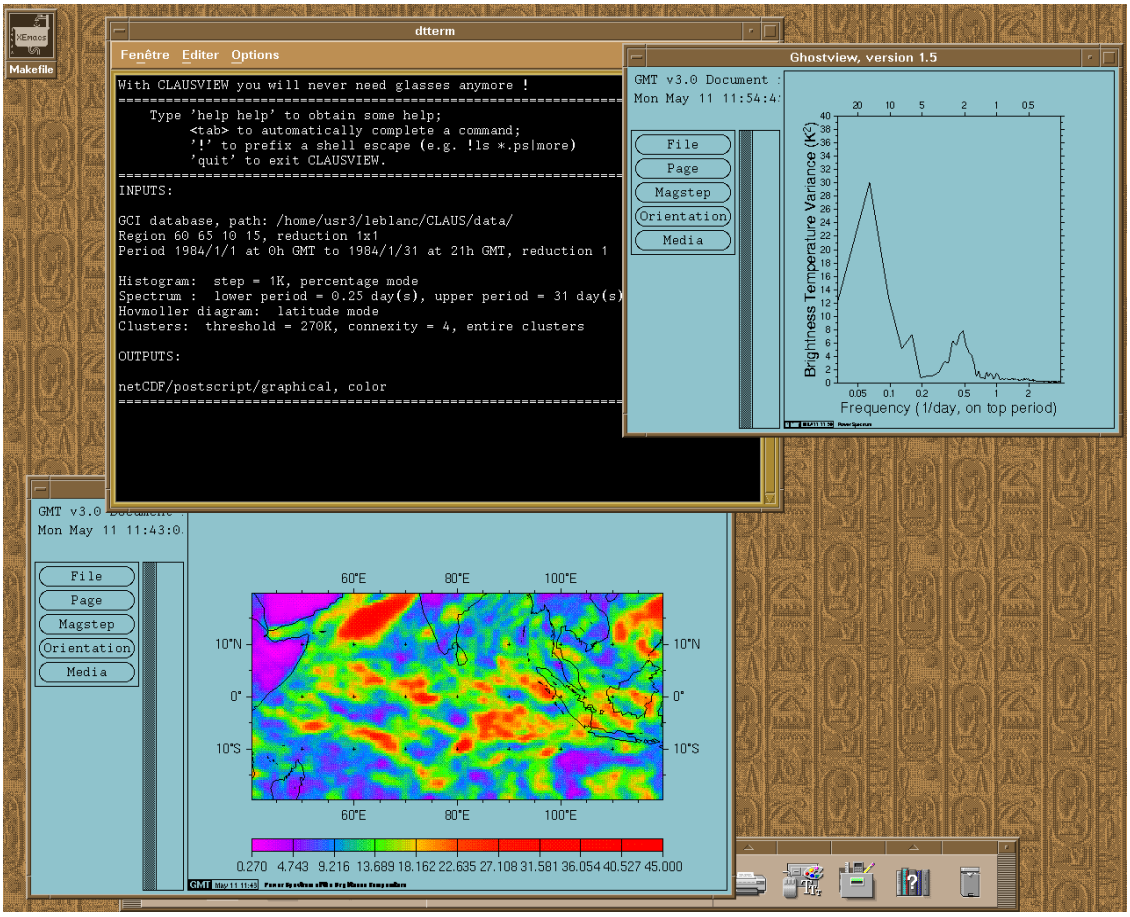

Figure 1: Example of command line interface to CLAUS-VIEW.

The Graphical Interface

The graphical interface runs the CLAUS-VIEW software using a standard Web browser on a Unix or PC platform. However, the CLAUS-VIEW package and the input data-set must first be installed on a Unix platform. This interface can completely replace the CLAUS-VIEW command line and text interface and the graphical output are displayed *via* the browser.

The Programming Interface

The programming interface is designed to make the code more reusable and provide more flexible access to programmers. It allows direct access to the modules using a C library so that it is possible to link the modules with foreign language code, provided that the foreign language allows calls to C functions.

The computer code for CLAUS-VIEW was written in ANSI C++ and C since these compilers are widely available. All the tools needed to compile or run the CLAUS-VIEW package exist in public domain versions or are basic Unix tools. Both the text and graphical interfaces are interactive and provide a common way to call the space and time algorithms. They have the same functionality and differ only in the way parameters are entered. When using the programming interface, the calling program has direct access to the raw output of the modules and does not need to read the ASCII file output.

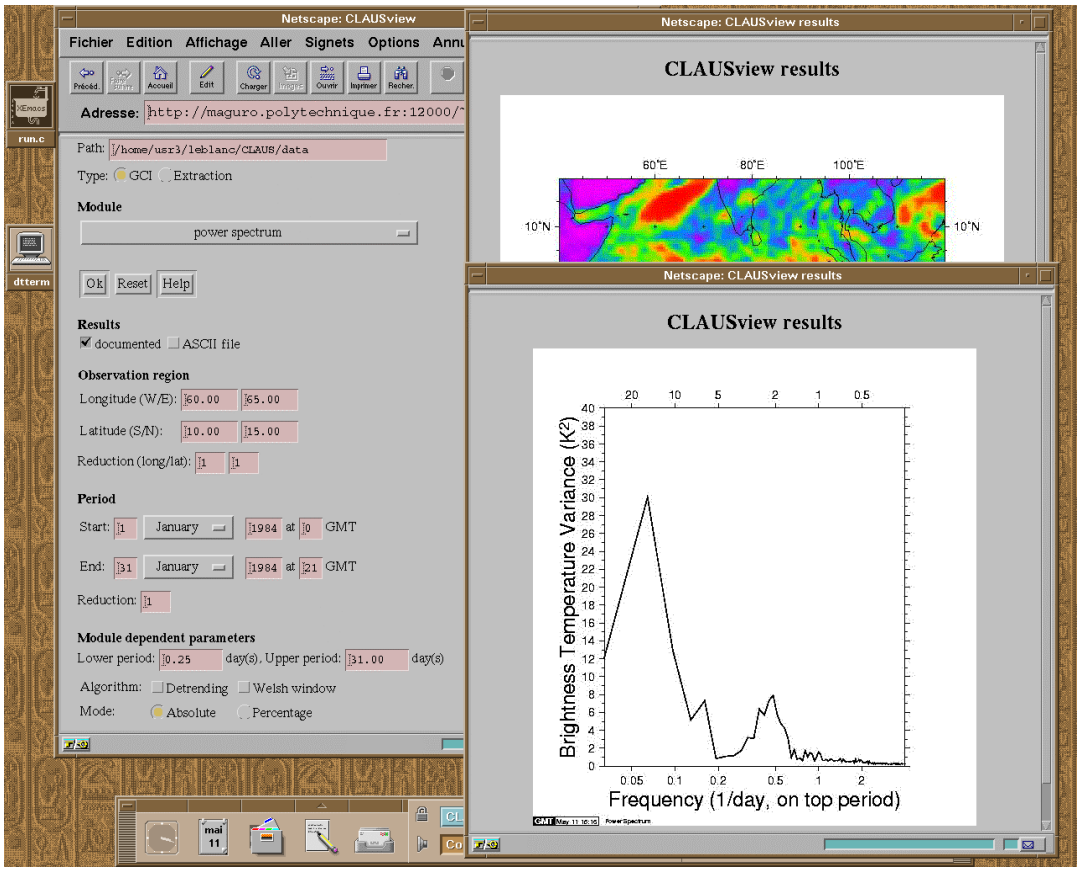

Figure 2: Example of Web browser interface to CLAUS-VIEW.

E Discussion

The following sections discuss how well the project objectives were met.

1 Assessment of the Objectives

By the end of the project all objectives have been satisfied, in some cases in considerable excess of original expectations.

Objective 1: Data Set Provision

This objective was met almost fully, although the data were made available for the validation activities later than scheduled because of operational difficulties. The operational processing system performed better than expected in the absence of tape problems. With hindsight, the system should have been designed to be more fault tolerant, and better Quality Control features should have been included.

Most of the source data available to the project was eventually processed successfully (nine years out of twelve) and placed in an archive for access by the customers involved in the project. Owing to problems with the quality of the source data, the CLAUS data exhibit occasional residual artefacts: the cause of these has been determined will be rectified after the project has ended.

The three-level spatial sampling scheme appears to work extremely well, and coupled with the use of spherical kernel estimators, appears to make optimal use of the data. Temporal interpolation could be improved by implementing the cloud motion correction technique in the operational dataset. Some residual limb darkening artefacts are still present in the final archived data, but these were considered acceptable for the validation activities. It is hoped that the limb darkening and missing data problems can be significantly reduced by using more sophisticated correction procedures; these will be implemented after the project ends.

Although not originally specified as a main deliverable, the production of associated quality information at the same resolution as the brightness temperature data is proving invaluable in helping to interpret the data, especially where the satellite coverage was non-optimal (i.e. missing images), or where unexplained artefacts in the processing were present (for example, mis-calibration of the source data).

Animated one-month sequences of the data proved invaluable in assessing visually the overall quality of the output brightness temperature images; most of the calibration and navigation problems with the source data were identified using this technique.

Objective 2: Validation

Although only a limited sub-set of brightness temperature data was available for the validation activities, the consensus of the testing centres was that the feasibility of using brightness temperature imagery to validate the output of Atmospheric General Circulation Models has been proved conclusively.

Objective 3: Data Access

The brightness temperature data were made available to the testing centres at two stages in the project. Although the main delivery route was ftp, in was found in practice that the

speed of the Internet link to NRSC was too slow for all but small quantities of data. Consequently, most of the data used was transferred via Exbyte tapes.

Information about the CLAUS project was made available for inclusion in the EWSE Web server, which has now been superseded by INFEO.

The Web access mechanism designed and implemented by NRSC was used successfully by all partners, and by one external potential customer. The database query sub-system was also tested by all partners and found to work satisfactorily.

There has been considerable interest in the CLAUS dataset and the project as a whole by groups world-wide. Much of this interest has been generated by personal contacts, presentations at scientific conferences, and more recently through the Internet, e.g. Web pages.

F Conclusions

This project has succeeded in establishing a long-term archive of global brightness temperature imagery and has shown that this data can be used to validate quantitatively the output from Atmospheric General Circulation Models.

Specific conclusions that can de drawn from this work can be grouped under the three main objectives:

Objective 1: Data Set Provision

- The resolution and quality of the brightness temperature imagery generated meets most of the requirements of the testing centres, although higher frequency data would be desirable in the Tropics. Residual artefacts in the brightness temperature imagery do not appear to impact on the results of the validation activities, even over the Indian Ocean where the geostationary satellite coverage is poor.
- The processing techniques used produce results that are qualitatively, and arguably quantitatively, better than that produced by Salby et al.
- Although not originally planned, the provision of quality data at the grid point level, which indicates the confidence with which the data are generated, has proved invaluable in using the brightness temperature imagery. The nature and volume of these data would appear to be unique for a global data product.

Objective 2: Validation

- All of the GCMs investigated were validated successfully using a variety of statistical techniques such as Fourier Analysis, Complex Empirical Orthogonal Functions and Wavelet Analysis.
- Significant new results have been obtained from the validation exercises:

  A The CLAUS data reveal the strong variation in the diurnal cycle across the globe. Over cloud-free continents the maximum surface temperature occurs at around 1400 hours local time, with the largest amplitude. Over convective regimes the diurnal variation is largest and more spatially consistent over continents than oceans. Oceanic convection tends to peak in the early morning, while continental convection tends to peak in the evening.

  B An interesting observation is that the strong diurnal signal over land appears to extend well into neighbouring seas and oceans, leading to substantial variation in oceanic convection and precipitation.

  C The most important result of the validation activities is that all of the GCMs investigated fail to reproduce the diurnal cycle of cloud activity correctly. Although suspected, this has not until now been proven conclusively. Most models predict the factional cloud cover distribution reasonably well, with a few notable differences, such as mis-placing the Monsoon on the wrong side of the Indian sub-continent. However, all models predict the peak of

convective cloudiness (defined by the first harmonic) over land to occur around local noon, in contrast to the observed maximum in the late afternoon or early evening. The explanation for this may lie in incorrect boundary layer and/or land surface process parameterisations.

- The Salby GCI data-set appears to contain a number of artefacts that have been identified independently by two of the testing centres. The CLAUS data appear to be systematically colder than the Salby GCI product. This is probably due to the recent re-calibration of the source data after the latter was created.

Objective 3: Data Access

- Considerable interest has been shown in the Archive by a number of GCM groups and workers in related fields worldwide. At present they have to rely on the ISCCP level C products, which are monthly means and of a lower spatial and temporal resolution than the CLAUS data.

The CLAUS archive provides for the first time a consistent global cloud climatology of the diurnal cycle of tropical convection, cloudiness and surface temperature, which is suitable for climate model evaluation. It is expected that it will become a major tool in the improvement of GCMs over the coming years.

G Appendices

1 References

Albright, M. D., D. R. Mock, E. E. Recker and R. J. Reed, 1981: A diagnostic study of the diurnal rainfall variation in the GATE B-scale area. *J. Atmos. Sci.*, **38**, 1429-1445.

Albright, M. D., E. E. Recker, R. J. Reed, and R. Dang, 1985: The diurnal variation of deep convection and inferred precipitation in the central tropical Pacific during January-February 1979. Mon. Wea. Rev., **113**, 1663-1680.

Arkin, P.A. and B.N. Meisner, 1987: The relationship between large-scale convective rainfall and cold cloud over the western hemisphere during 1982-84. Mon. Weather Rev., 115, 51-74.

Augustine, J. A., 1984: The diurnal variation of large-scale inferred rainfall over the tropical Pacific Ocean during August 1979. *Mon.Wea. Rev.*, **112**, 1745-1751.

Bauer, Stefan, 2000: Validation of Clouds in the ECHAM 4 Model Using a Dynamical Adjustment Technique, PhD. Thesis, Universitaet Hamburg.

Bergman, J. W. and M. L. Salby, 1996: Diurnal variations of cloud cover and their relationship to climatological conditions. *J. Climate*, **9**, 2802-2820.

Betts, A. K. and J. H. Ball, 1995: The FIFE surface diurnal cycle climate. *J. Geophys. Res.*, **100**, 25679-25693.

Brest, C. L., W. B. Rossow and M. Roiter, 1997: Update of Radiance Calibrations for ISCCP, *J. Atmos. Ocean Tech.*, **14**, 1091-1109.

C ron, J.P. and J.F. Gu r my, 1999: Validation of the space-time variability of African Easterly waves simulated by the CNRM GCM. J. Climate, 12, 2831-2855

Chang, A. T. C., L. S. Chiu and G. Yang, 1995: Diurnal cycle of oceanic precipitation from SSM/I data. *Mon. Wea. Rev.*, **123**, 3371-3380.

Chen, S. S., and R. A. Houze, 1997: Diurnal variation and life-cycle of deep convective systems over the tropical Pacific warm pool. *Q. J. R. Meteorol. Soc.*, **123**, 357-388.

Chen, S.S., R.A. Houze Jr. and B.E. Mapes, 1996: Multiscale variability of deep convection in relation to large-scale circulation in TOGA COARE. J. Atmos. Sci., 53, 1380-1409.

Cox, P. M., R. A. Betts, C. B. Bunton, R. L. H. Essery, P. R. Rowntree and J. Smith, 1999: The impact of new land surface physics on the GCM simulation of climate and climate sensitivity. *Climate Dynamics*, **15**, 183-203.

D qu ,M., C. Dreveton,A. Braun, D. Cariolle, 1994: The ARPEGE/IFS atmosphere model: A contribution to the French community climate modelling. *Climate Dyn.*, **10**, 249-266.

Duvel, J.P., 1989: Convection over tropical Africa and Atlantic Ocean during Northern summer. Part I: Interannual and diurnal variations. *Mon. Wea. Rev.*, **117**, 2782-2799.

Duvel, J.P., 1990: Convection over tropical Africa and Atlantic Ocean during Northern summer. Part II: Modulation by easterly waves. *Mon. Wea. Rev.*, **118**, 1855-1868.

Edwards, J. M. and A. Slingo, 1996: Studies with a flexible new radiation code. I: Choosing a configuration for a large-scale model. *Q. J. R. Meteorol. Soc.*, **122**, 689-719.

Ellingson, R. G., and R. R. Ferraro, 1983: An examination of a technique for estimating the longwave radiation budget from satellite radiance observations. *J. Climate Appl. Meteor.*, **22**, 1416-1423.

Fu, R., A. Del Genio, and W. B. Rossow, 1990: Behavior of deep convective clouds in the tropical pacific from ISCCP radiances. *J. Climate*, **3**, 1129-1152

Garreaud, R. D. and J. M. Wallace, 1997: The diurnal march of convective cloudiness over the Americas. *Mon. Wea. Rev.*, **125**, 3157-3171.

Goodman, B., W. P. Menzel, E. C. Cutrim and D. W. Martin, 1993: A non-linear algorithm for estimating three-hourly rain rates over Amazonia from GOES/VISSR observations. *Remote. Sens. Rev.*, **10**, 169-177.

Goulet, L., and J.P. Duvel, 2000: A new approach to detect and characterise intermittent atmospheric oscillations: Application on the Intraseasonal Oscillation, (to appear in the *J. Atmos. Sci.*)

Gray, W. M. and R. W. Jacobson, 1977: Diurnal variation of deep cumulus convection. Mon. Wea. Rev., **105**, 1171-1188.

Gregory, D., R. Kershaw and P. M. Inness, 1997: Parametrization of momentum transport by convection. II: Tests in single-column and general circulation models. *Q. J. R. Meteorol. Soc.*, **123**, 1153-1183.

Harrison, E. F., P. Minnis, B. R. Barkstrom, V. Ramanathan, R. D. Cess and G. G. Gibson, 1990: Seasonal variation of cloud radiative forcing derived from the Earth Radiation Budget Experiment. *J. Geophys. Res.*, **95**, 18687-18703.

Hayashi, Y., 1982: Space-time spectral analysis and its applications to atmospheric waves. J. Meteor. Soc. Japan, **60**, 156-171.

Hendon, H.H. and K. Woodberry, 1993: The diurnal cycle of tropical convection. J. Geophys. Res. - Atmos., 98, 16623-16638.

Hendon, H.H., and K. Woodberry, 1993: The diurnal cycle of tropical convection. *J. Geophys. Res.*, **98**, 16623-16637.

Highwood, E. J. and B. J. Hoskins, 1998: The tropical tropopause. *Q. J. R. Meteorol. Soc.*, **124**, 1579-1604.

Hignett, P. 1991: Observations of the diurnal variation in a cloud-capped marine boundary layer. *J. Atmos. Sci.*, **48**, 1474-1482.

Hodges, K. I. and C. D. Thorncroft, 1997: Distribution and statistics of African mesoscale convective weather systems based on the ISCCP Meteosat imagery. *Mon. Wea. Rev.*, **125**, 2821-2837.

Hodges, K. I., 1996: Spherical non-parametric estimators and their application to the UGAMP AMIP integration: A ten year cyclonic climatology for the northern and southern hemisphere winters. Mon., Weather Rev., 124, pp2914-2932.

Hodges, K., D.W. Chappell, G.J. Robinson and G. Yang, 2000: An improved algorithm for generating global window brightness temperatures from multiple satellite infra-red imagery. *J. Atmos. And Ocean Tech.*, **17**, 1296-1312.

Houze, R. A., S. G. Geotis, F. D. Marks and A. K. West, 1981: Winter monsoon convection in the vicinity of North Borneo. Part I: Structure and time variation of clouds and precipitation. *Mon. Wea. Rev*., **109**, 1595-1614.

Janowiak, J., P. A. Arkin and M. Morrissey, 1994: An examination of the diurnal cycle in oceanic tropical rainfall using satellite and in situ data. *Mon. Wea. Rev.*, **122**, 2296-2311.

Jeuken, A.B.M., Siegmund, P.C., Heijboer, L.C., Feichter, J. and Bengtsson, L. (1996): On the potential of assimilating meteorological analyses in a global climate model for the purpose of model validation. *Journ. Geophys. Res*. **101**, 16 939-16 950

Johnson, R. H. and D. C. Kriete, 1982: Thermodynamic and circulation characteristics of winter monsoon tropical mesoscale convection. *Mon. Wea. Rev.*, **110**, 1898-1911.

Johnson, R. H., T. M. Rickenbach, S. A. Rutledge, P. E. Ciesielski and W. H. Schubert, 1999: Trimodal characteristics of tropical convection. *J. Climate,* **12**, 2397-2418.

Kousky, V. E., 1980: Diurnal rainfall variation in Northeast Brazil. *Mon. Wea. Rev.*, **108**, 488- 498.

Kulkarni, P.L., et al, 1997: On the impact of divergent part of the wind computed from INSAT OLR data on global analysis and forecast fields, *Meteorol. Atmos. Phys*., **64**, 61-82.

Lau, K.M., and P.H. Chan, 1988: Intraseasonal and interannual variations of tropical convection: A possible link between the 40-50 day oscillation and ENSO?, *J. Atmos. Sci.*, **45**, 506-521.

Lenderink, G., van Meijgaard, E., Holtslag, A.A.M. (1998): Evaluation of the ECHAM4 cloud-turbulence scheme for stratocumulus. Preprints 98-13, KNMI, De Bildt, The Netherlands. Submitted to Contributions to Atmospheric Physics.

Liu, C. and M. W. Moncrieff, 1998: A numerical study of the diurnal cycle of tropical oceanic convection. *J Atmos. Sci.*, **55**, 2329-2344.

Mapes, B. E. and R. A. Houze, 1993: Cloud clusters and superclusters over the oceanic warm pool. *Mon. Wea. Rev*., **121**, 1398-1415.

Mapes, B.E. and R.A. Houze Jr., 1993: Cloud clusters and superclusters over the oceanic warm pool. Mon. Weather Rev., 121, 1398-1415.

Matsuno, T., 1966: Quasi-geostrophic motions in the equatorial area. .J. Meteor. Soc. Japan, **44**, 25-43.

McGarry, M. M. and R. J. Reed, 1978: Diurnal variations in convective activity and precipitation during phases II and III of GATE. *Mon. Wea. Rev.*, **106**, 101-113.

Minnis, P. and Harrison, E.F., 1984: Diurnal Variability of Regional Cloud and Clear-sky Radiative Parameters Derived from GOES Data. Part I: Analysis Method, J. of Climate and Appl.Meterology, 23, **7**, 993-1011.

Morcrette, J.- J., 1990: Impact of changes to the radiation transfer parameterizations plus cloud optical properties in the ECMWF model. *Mon. Weather Rev.,* **118**, 847-873.

Morcrette, J.-J. and Fouquart, Y., (1985): On systematic errors in parameterized calculations of longwave radiation transfer. *Quart.J.Roy.Meteor.Soc*., **111**, 691-708

Morcrette, J-J. 1991: Evaluation of model-generated cloudiness: Satellite-observed and model-generated diurnal variability of brightness temperature. *Mon. Wea. Rev.*, **119**, 1205- 1224.

Ohring, G. and A. Gruber, 1984: Satellite determination of the relationship between total longwave radiation flux and infrared window radiance. *J. Clim. Appl. Met.*, **23**, 416-425.

Ohring, G., A. Gruber, and R. Ellingson, 1984: Satellite determinations of the relationship between total longwave radiation flux and infrared window radiance. *J. Climate Appl. Meteor.*, **23**, 416-425.

Phillips, T. J., 1994: A summary documentation of the AMIP models. PCMDI Report No. 18, 343pp. Program for Climate Model Diagnosis and Intercomparison, Lawrence Livermore National Laboratory, Livermore, CA 94550, USA.

Piriou C., 1996: La base de donn es TOGA-COARE du CNRM (deuxi me version). *Note de Travail du Groupe de M t orologie Moyenne Echelle* , No. 45, 242pp.

Pope, V. D., M. L. Gallani, P. R. Rowntree, and R. A. Stratton, 2000: The impact of new physical paramtrizations in the Hadley Centre climate model - HadAM3. *Clim. Dynamics*, **16**, 123-146.

Randall, D. A., Harshvardhan and D. A. Dazlich, 1991: Diurnal variability of the hydrologic cycle in a general circulation model. *J. Atmos. Sci.*, **48**, 40-62.

Ricard, J.L. and J.F. Royer, 1993: A statistical cloud scheme for use in an AGCM. *Ann. Geophys*., **11**, 1095-1115.

Richards, F. and P. A. Arkin, 1981: On the relationship between satellite observed cloud cover and precipitation. *Mon. Wea. Rev.*, **109**, 1081-1093.

Rickenbach, T. M., 1996: Convection in TOGA COARE: Horizontal scale, morphology, and rainfall production. PhD Dissertation, Department of Atmospheric Science Paper No. 630, Colorado State University, Fort Collins, Colorado, USA.

Ringer, M. 1998: Tropical Convective rainfall in the global UM: Initial comparisons with estimates derived from Meteosat Infrared Imagery. Forecasting Research Technical Report, 239, Meteorological Office, London Road, Bracknell, UK.

Roca, R., and V. Ramanathan,1999: Scale dependence of monsoonal convective systems over the Indian Ocean, *J. Climate* (in press).

Roeckner, E. et al. (1996): The Atmospheric General Circulation Model ECHAM4: Model Description and Simulation of Present-Day Climate, Tech. Report. 218. Max-Plank-Institut fuer Meteorologie.

Rossow, W. B., A. Walker and M. Roiter, 1997: International Satellite Cloud Climatology Project (ISCCP): Description of Reduced Resolution Radiance Data. WMO/TD-No. 58, World Meteorological Organization, Geneva.

Rowell, D. P. and J. R. Milford, 1993: On the generation of African squall lines. J. Clim., 6, 1181-1193.

Salby, M. L., H. H. Hendon, K. Woodberry and K. Tanaka, 1991: Analysis of global cloud imagery from multiple satellites. *Bull. Am. Met. Soc.*, **72**, 467-480.

Salby, M.L., and H. Hendon, 1994 : Intraseasonal behavior of clouds, temperature, and motion in the tropics, *J. Atmos. Sci.*, **51**, 2207-2224.

Schulz, J.-P., D-umenil, L. Polcher, J. (1999): The impact of two different land-surface coupling techniques in a single column version of the ECHAM4 atmospheric model, MPI Report 297, Max-Plank-Institut fuer Meteorologie.

Shin, K.-S., G. R. North, Y.-S. Ahn and P. A. Arkin, 1991: Time scales and variability of area-averaged tropical oceanic rainfall. *Mon. Wea. Rev.*, **118**, 1507-1516.

Slingo, J. M., K. R. Sperber, J-J. Morcrette and G. L. Potter, 1992: Analysis of the temporal behavior of convection in the tropics of the European Centre for Medium-range Weather Forecasts model. *J. Geophys. Res.*, **97**, 18119-18135.

Slingo, J. M., M. Blackburn, A. Betts, R. Brugge, K. Hodges, B. Hoskins, M. Miller, L. Steenman-Clark, and J. Thuburn, 1994: Mean climate and transience in the tropics of the UGAMP GCM: Sensitivity to convective parameterization. *Q. J. R. Meteorol. Soc.*, **120**, 881-922

Smith, W. S. and C.-Y. J. Kao, 1996: Numerical simulations of the marine stratocumulus-topped boundary layer and its diurnal variation. *Mon. Wea. Rev.*, **124**, 1803-1816.

Stephenson, D. B., F. Chauvin and J.F. Royer, 1998: Simulation of the Asian summer monsoon and its dependence on model horizontal resolution. *J. Meteorol. Soc. Japan*, **76**, 237-265.

Sui, C.-H., K.-M. Lau, Y. N. Takayabu and D. A. Short, 1997: Diurnal variations in tropical oceanic cumulus convection during TOGA COARE. *J. Atmos. Sci.*, **54**, 639-655.

Toledo Machado, L.A., M. Desbois and J.P. Duvel, 1992: Structural characteristics of deep convective systems over tropical Africa and Atlantic Ocean. *Mon. Wea. Rev*., **120**, 392-406.

Troen, I. and L. Mahrt, 1986: A simple model of the atmospheric boundary layer; sensitivity to surface evaporation. *Bound.-Lay. Meteorol.*, **37**, 129-148.

Velden C., 1994: Geostationary Meteorological Satellite — VIS/IR imagery (McIDAS format)
(http://www.ncdc.noaa.gov/coare/catalog/data/atmosphere_large_scale/gms_bom_exab.html)

Velden C.S. and J.A. Young, 1994: Satellite observations during TOGA COARE: Large-scale descriptive overview. *Monthly Weather Review*, **122**, 2426-2441.

Wallace, J. M., 1975: Diurnal variations in precipitation and thunderstorm frequency over the conterminous United States. *Mon. Wea. Rev.*, **103**, 406-419.

Webster P.J. and R. Lukas, 1992: TOGA COARE: The Coupled Ocean-Atmosphere Response Experiment. *Bulletin of the American Meteorological Society*, **73**, 1377-1416.

Webster, P. J., C. A. Clayson and J. A. Curry, 1996: Clouds, radiation and the diurnal cycle of sea surface temperature in the tropical western Pacific Ocean, *J. Clim.*, **9**, 1712--1730.

Weller, R. A. and S. P. Anderson, 1996: Surface meteorology and air-sea fluxes in the western equatorial Pacific warm pool during the TOGA Coupled Ocean-Atmosphere Response Experiment. *J. Clim.*, **9**, 1959-1990.

Wheeler, M., and G. N. Kiladis, 1999: Convectively-coupled equatorial waves: Analysis of clouds and temperature in the wavenumber-frequency domain. J. Atmos. Sci., **56**, 374-399.

Williams, M. and R. A. Houze, 1987: Satellite-observed characteristics of winter monsoon cloud clusters. *Mon. Wea. Rev.*, **115**, 505-519.

Xie, P. and P. A. Arkin, 1996: Analyses of global monthly precipitation using gauge observations, satellite estimates and numerical model precipitation. *J. Climate*, **9**, 840-858

Yang, G.-Y., and J. Slingo, 2000: The diurnal cycle in the tropics. (Accepted by Mon. Wea. Rev.)

2 Abbreviations

CEO	Centre for Earth Observation
CIP	Catalogue Inter-operability Protocol
CLAUS	Cloud User Archive Service
CGAM	Centre for Global Atmospheric Modelling
CNRM	Centre National de Recherches Météorologiques
ECMWF	European Centre for Medium-Range Weather Forecasts
EOSDIS	Earth Observing System Data and Information System
ESSC	Environmental Systems Science Centre
EWSE	European Wide Service Exchange
ftp	File Transfer Protocol
GCI	Global Cloud Imagery
GCM	General Circulation Model
GISS	NASA Goddard Space Flight Center Institute for Space Studies
GMS	Geostationary Meteorological Satellite
GMT	General Mapping Tools
GOES	Geostationary Operational Environmental Satellite
INFEO	Information on Earth Observation
ISCCP	International Satellite Cloud Climatology Programme
LMD	Laboratoire de Météorologie Dynamique
MJO	Madden-Julian Oscillation
MPEG	Motion Picture Expert Group
MPI	Max-Planck- Institut für Meteorologie
NOAA	National Aeronautical and Atmosphere Administration
NRSC	National Remote Sensing Centre Ltd.
PGM	Portable Grey Map
UGAMP	UK Universities Global Atmospheric Modelling Program
URL	Uniform Resource Locator
WWW	World Wide Web